Molecular Imaging using Strong-Field Processes

Dissertation

zur Erlangung des akademischen Grades eines
Doktors der Naturwissenschaften (Dr. rer. nat.)
im Fachbereich Naturwissenschaften der Universität Kassel

vorgelegt von

Elmar Vincent van der Zwan

Tag der Disputation:
26. Januar 2011

Erstgutachter: Prof. Dr. Manfred Lein
Zweitgutachter: Prof. Dr. Martin Garcia

Molecular Imaging using Strong-Field Processes

Printed in Kassel, 2010

Institut für Physik
Universität Kassel
Heinrich-Plett-Straße 40
D-34109 Kassel
Germany

This thesis was typeset with the LaTeX-system.

Contents

Zusammenfassung

Die vorliegende Arbeit befasst sich mit dem Zusammenhang zwischen einfachen Molekülen und deren Verhalten in starken, kurzen Laserfeldern. Einerseits wird versucht, strukturelle Daten des Moleküls in den Elektronen- und Photonenspektren wiederzuerkennen. Anderseits geht es darum, ein Bild der elektronischen Wellenfunktion aus den spektralen Daten abzuleiten.

Mit Hilfe des Laserfeldes kann ein Elektron dem inneren Bereich des Moleküls entfliehen. Nach der Ionisation wird das nun freie Elektron weiter vom Laserfeld beschleunigt, wobei das Elektron zusätzliche Energie vom Laserfeld aufnimmt. Ein solches hochenergetisches Elektron wird im Laborversuch als ein *above-threshold ionization* (ATI) Elektron wahrgenommen, d.h. ein Elektron, das mehr Photonen absorbiert hat als nötig, um die Ionisationsbarriere zu überwinden. Wenn es vom Laserfeld zurück zum Molekülkern getrieben wird, rekombiniert das Elektron mit einer bestimmten Wahrscheinlichkeit unter Ausstrahlung eines Röntgen- oder UV-Photons zurück in den gebundenen Zustand. Dieser Prozess nennt sich *high-harmonic generation*—Hohe-Harmonischen-Erzeugung—(HHG), da bei einem Laserpuls mit mehreren optischen Zyklen die Frequenzen der erzeugten Photonen höhere Harmonische der Laserfrequenz sind.

Nach der allgemeinen Einleitung im ersten Kapitel, beinhaltet das zweite Kapitel eine Einführung in die Physik der starken und kurzen Laserfelder und deren Wechselwirkung mit Atomen und einfachen Molekülen. Da im Bereich von Laserfeldern, deren Kräfte auf die Elektronen vergleichbar sind mit den inneratomaren Kräften, Störungsrechnungen nicht mehr greifen, ist man für eine theoretische Beschreibung auf andere Methoden angewiesen. Auf der einen Seite ist es für die einfachsten Molekülen mit ein oder zwei Elektronen heutzutage möglich, das gesamte Laser-Molekül-System durch eine numerische Integration der zeitabhängigen Schrödingergleichung (TDSE) exakt zu beschreiben. In dieser Arbeit benutzen wir diese Methode für einfache Modellsysteme mit nur einem Elektron und ein bis zwei räumlichen Koordinaten. Auf der anderen Seite benutzen wir die *strong-field approximation*—Starkfeldnäherung—(SFA) zur analytischen Beschreibung des Gesamtsystems. Hier werden inneratomare Kräfte und durch das Laserfeld entstandene Kräfte jeweils zum Teil vernachlässigt.

Das dritte Kapitel befasst sich mit dem Minimum in HHG-Spektren von diatomaren homonuklearen Molekülen, das dadurch entsteht, dass die Beiträge der beiden Molekülkerne destruktiv interferieren. Dies geschieht, wenn die halbe De-Broglie-Wellenlänge des rekombinierenden Elektrons gleich der internuklearen Distanz parallel

zum Impuls des Elektrons ist. Wir vergleichen das Interferenzminimum eines laserinduzierten HHG-Prozesses mit dem eines Zusammenstoßes zwischen der gebundenen Wellenfunktion und einem künstlich eingebrachten Gaußschen Wellenpaket. Es wird gezeigt, dass das Interferenzminimum des HHG-Prozesses mit dem Minimum des künstlichen Wellenpaketes übereinstimmt, so lange nur eine Elektronenbahn pro Frequenz zum Spektrum beiträgt. In Normalfall tragen aber viele Elektronenbahnen zu einer Frequenz im HHG-Prozess bei. In diesem Fall interferieren die Elektronenbahnen, was dazu führt, dass die Position des Interferenzminimums einer Streuung unterliegt.

Wir zeigen, dass das Coulomb-ähnliche Potential eine signifikante Elliptizität der emittierten Strahlung hervorruft. Beim Interferenzminimum dreht sich die Polarisationsrichtung der emittierten Strahlung um 180°. Der Einfluss des Potentials nimmt für höhere Energien des emittierten Photons ab. Daraus folgt eine geringere Elliptizität und eine schärfere Drehung der Polarisationsrichtung bei hohen Frequenzen. Weiterhin wird gezeigt, dass man das Interferenzminimum auch an der Emissionszeit der HHG-Strahlung erkennen kann.

Im Jahr 2004 wurde gezeigt, dass der HHG-Prozess zur Abbildung von Elektronenorbitalen benutzt werden kann (Itatani et al. [52]). Während der Erzeugung der HHG-Strahlung verbringt das elektronische Wellenpaket eine Zeitdauer in der Größenordnung eines halben optischen Zyklus im freien Raum und breitet sich währenddessen räumlich aus. Deswegen liegt es nahe, das Wellenpaket näherungsweise als eine Summe über ebene Wellen zu beschreiben, die entlang der Laserpolarisationsrichtung gerichtet sind. Dies nennt sich *plane-wave approximation*—Ebene-Wellen-Näherung—(PWA). Die Rekombination des elektronischen Wellenpaketes lässt sich dann durch eine eindimensionale Fourier-Transformation zuzüglich einer zweidimensionalen Projektion des Elektronenorbitals beschreiben. Mit Hilfe eines Referenzatoms und dessen HHG-Strahlung ist es möglich, die Rekombination zu invertieren und ein Bild des Orbitals aus experimentellen Daten zu erhalten. Abgebildet wird hier die Wellenfunktion inklusive ihre Phase, nicht nur die Elektronendichte.

Im vierten Kapitel zeigen wir, dass eine notwendige Bedingung für die tomographische Rekonstruktion eines asymmetrischen Molekülorbitals ist, dass das Wellenpaket sich dem Kern des Moleküls nur von einer Seite aus nähert. Dies ist durch die Verwendung von phasenstabilisierten Laserpulsen mit nur wenigen optischen Zyklen realisierbar. Die exponentielle Abhängigkeit der Ionisierungsrate von der elektrischen Feldstärke des Laserfeldes sorgt dafür, dass die genaue Form des Laserpulses nur bedingt relevant ist. Optimal sind Laserpulse mit 2–3 optischen Zyklen und einer Phase von $\pi/4$ zwischen der Trägerwelle und der Einhüllenden. Die tomographische Rekonstruktion verschiedener, einfacher Moleküle wird numerisch simuliert. Zusätzlich zu der Rekonstruktion in "*length form*" wie in der Originalarbeit (Itatani et al. [52]), führen wir eine Rekonstruktion in "*velocity form*" ein. Sie basiert auf der Beschreibung der Rekombination mit Hilfe des Impulsoperators. Dies hat den Vorteil, dass sich die internukleare Distanz mit ihr besser ermitteln lässt. Die Rekonstruktion in "*length form*" funktioniert nicht in der Nähe einer Knotenebene eines antisymmetrischen Molekülorbitals und auch nicht für asymmetrische Molekülorbitale. Bis jetzt wurde kein Weg gefunden, diese Probleme zu beseitigen.

Im fünften Kapitel beschäftigen wir uns mit dem Lewensteinschen Modell für HHG, welches auf der SFA basiert. Der HHG-Prozess lässt sich im Lewensteinschen Modell als eine Summe über Elektronenbahnen beschreiben. Dies erhalten wir durch eine explizite Evaluation der Integrale über den Impuls, die Ionisations- und die Rekombinationszeit des Elektrons. Wir drücken die exakten und komplexen Ionisations- und Rekombinationszeiten bezüglich der reellen Zeiten des klassischen Modells aus. Dies ermöglicht es, den Beitrag individueller Elektronenbahnen zum HHG-Spektrum numerisch schnell zu berechnen. Auf ähnliche Art berechnen wir die entsprechenden Beiträge zum ATI-Spektrum. Die Ergebnisse werden anschließend verwendet, um eine bessere Bestimmung der Eignung eines Laserpulses zur Benutzung in einer tomographischen Rekonstruktion zu erreichen.

Mit Hilfe der SFA-Rechnungen wird ebenfalls gezeigt, dass bei Benutzung extrem kurzer Laserpulse HHG-Frequenzen mit bestimmten ATI-Impulsen verknüpft werden können. Dies basiert auf der gemeinsamen Ionisationszeit der dominierenden Elektronenbahnen der beiden Prozesse. Wir beschreiben die Verknüpfung zwischen einer HHG-Frequenz und einem ATI-Impuls mit Hilfe der relativen Beiträgen der relevanten Elektronenbahnen. Wir demonstrieren den Zusammenhang zwischen HHG und ATI in eindimensionalen Lösungen der TDSE. Da die PWA in 1D weniger gut zu funktionieren scheint als in 2D oder 3D, erwarten wir eine stärkere Verknüpfung zwischen HHG und ATI in Rechnungen mit einer höheren Anzahl an Dimensionen oder in Experimenten. Solche Rechnungen oder Experimente wurden bis jetzt noch nicht ausgeführt.

Außerdem schlagen wir eine Methode vor, um die tomographische Rekonstruktion mit Informationen aus ATI-Spektren zu ergänzen, während bis jetzt nur HHG-Spektren zur Rekonstruktion benutzt wurden. Dazu wird die Abhängigkeit des ATI-Spektrums von der räumlichen Orientierung eines Moleküls im Vergleich zum ATI-Spektrum des Referenzatoms benutzt, um die Bestimmung des rekombinierenden Wellenpaketes zu verbessern. Angesichts der Tatsache, dass die tomographische Rekonstruktion in eindimensionalen Rechnungen nicht zu funktionieren scheint, haben wir unseren Ansatz zur Verbesserung der Rekonstruktion noch nicht vollständig prüfen können. Die Entwicklung von Lasern mit Wellenlängen länger als 2000 nm und der Fortschritt bei der Erzeugung von geformten Laserpulsen werden möglicherweise dazu beitragen, dass sich in Zukunft die tomographische Rekonstruktion von Molekülorbitalen weiter verbreiten wird.

Im sechsten Kapitel führen wir einen numerischen Algorithmus ein, um die Qualität einer tomographischen Rekonstruktion nachträglich zu verbessern. Im Orts- und Impulsraum werden wiederholt Filter auf das Orbital angewendet, die auf physikalischen Kenntnissen über das Molekül oder den Prozess der tomographischen Rekonstruktion basieren. Im Ortsraum machen wir es uns zu Nutze, dass das Orbital eine begrenzte räumliche Ausdehnung hat, und im Impulsraum beschränken wir die Variation des ursprünglichen Orbitals. Im Idealfall konvergiert der Algorithmus zum exakten Orbital. Es wird gezeigt, dass der Algorithmus manche Kenngrößen eines 2D-Modells des HeH^{2+}-Kations sowie anderer Moleküle reproduzieren kann.

Chapter 1

Introduction

In this thesis we occupy ourselves with atoms and simple molecules subjected to strong laser fields. The main topic is the relationship between atomic and molecular properties such as the geometry of the orbital on the one hand, and their strong-field responses on the other hand. We are interested in molecular imaging, i.e., we aim at researching how much we can find out about a molecule from its strong-field response. Because the strong-field processes take place on femtosecond timescales, they are in principle suitable for the study of ultrafast electronic processes such as chemical reactions. The relatively low cost and easiness of handling of modern lasers adds to the attractiveness of using strong-field processes for molecular imaging. Therefore it is not surprising that in recent years a lot of attention of the atomic physics community has gone in this direction.

To study molecular imaging theoretically, we solve the time-dependent Schrödinger equation (TDSE) numerically and compare the outcome with simple models. In chapter 3, the focus lies on the effect of molecular features on the spectra. By better understanding the complicated behavior already exhibited by very simple molecular models, we hope to pave the way for molecular imaging of more complicated molecules in experiment. Molecular tomography, i.e., recovering a full image of the electronic orbital from the spectra, is the topic of chapter 4. Here we make use of numerical simulations of the experimental procedure and semi-classical calculations that express the strong-field yields in terms of electronic trajectories. We supply the experimentalist with some refinements to the tomographic scheme. In chapter 6 we propose a algorithm that can be used to improve the reconstructed orbital after the experiment has been performed.

Strong-field physics

Under the influence of the laser field, an electron can escape from the core region. Because the laser field is turned on longer than the time scales associated with ionization, the electron can be further accelerated after leaving the core. Such an electron can be experimentally detected in the far field as a so-called above-threshold-ionization (ATI) electron. Instead of simply escaping, many other processes can

occur, especially if the electron gets driven back to the core region by the laser field. Because of the spatial spreading the electron wave packet undergoes while away from the Coulombic potential in the core region, it usually just passes the core region without any interaction. Alternatively, the now highly energetic electron can also recombine into the bound state under the emission of a single highly-energetic photon. These highly-energetic photons are emitted coherently and can therefore be observed experimentally as high-harmonics of the incident laser. This process is called high-harmonic generation (HHG) (Ferray et al. [33]).

The combination of laser parameters and ionization potential of the atom or molecule are chosen such that we are in the high-intensity, low-frequency 'tunneling' regime, which allows for easier and more successful interpretation of spectral characteristics in terms of molecular properties than the low-intensity, high-frequency 'multiphoton' regime. The intensities considered in this thesis will mainly lie in the range of 10^{14} to 10^{15} W/cm^2 at the standard Ti:Sapphire laser wavelength of 780 nm. This amounts to electric field strengths on the order of 0.1 atomic units (a.u.). Expressed in atomic units, the ionization potential of an hydrogen atom is 0.5 a.u. This means that the additional force the charged particles experience because of the laser is comparable to the natural Coulombic forces inside an atom or molecule. Therefore we cannot use any perturbative method to describe the complete system. In order to understand and describe qualitatively and quantitatively the physical processes associated with subjecting an atom or molecule to a strong laser field, we have to consider both the Coulombic and laser forces simultaneously and completely. However, for an understanding of the underlying physics it will prove to be very helpful to separate the generation process into several steps in which either the molecular or laser forces dominate the behavior. Such an approach is provided for example by the strong-field approximation (SFA) (Lewenstein et al. [71]).

In chapter 2 we give a bit more elaborate introduction to the strong-field processes HHG and ATI. Especially noteworthy in this respect is the three-step model for HHG (Corkum [25]), in which the HHG generation process is divided into three steps; in the first step, the electron tunnels out from the Coulombic potential under the influence of the laser field. During the second step the electron is in the continuum, and is accelerated by the laser field only. Thirdly, if the electron comes back to the core region, it can recombine with the parent ion. The Lewenstein model (Lewenstein et al. [71]) is a more quantum-mechanical formulation of the three-step model for HHG. It can be used to explain qualitatively and sometimes quantitatively spectral characteristics and will be used at many places in this thesis.

We will only consider the contribution from the least bound electron to the strong-field processes, i.e., we will adopt the single-active electron (SAE) approximation. Upon returning to the core, the electron can also kick out another electron, leading to a doubly-ionized atom or molecule in a process called nonsequential double ionization. This is an example of a multi-electron process that we will not address in this thesis. Additionally, all electrons of the atom or molecule contribute to some extent to all strong-field processes (Gordon et al. [44]; Patchkovskii et al. [99, 100]; Santra and Gordon [111]; Zhao et al. [137]). For some molecules, under certain conditions the contribution from lower orbitals to the HHG spectrum can even dominate over that of the highest occupied molecular orbital (HOMO) (Smirnova et al. [116]). This

is another aspect of strong-field processes that requires more thorough investigation with molecular imaging in mind, but it is not the subject of this thesis.

HHG spectra

In chapter 3 we mainly study the interference minimum in HHG spectra that arises when the emissions from the two nuclei of a homonuclear diatomic molecule cancel (Lein et al. [67, 68]). The demonstration of this minimum was the first application of HHG towards imaging. We compare the HHG spectra generated by a laser pulse and the harmonics that are created by artificially introducing a Gaussian electron wave packet to a laser-free system in a numerical calculation. This allows us to separate the features in the HHG spectrum that come from either the tunnel ionization or the laser-specific propagation from those that are caused by the Coulombic potential or the recombination (van der Zwan and Lein [143]). We can therefore test models of the harmonic-generation process. We consider not only the intensity, but also the polarization of the emitted harmonics. We find that generally the polarization of the emitted harmonics comes from the recombination step.

Using some very artificial laser pulses we disentangle the contributions from the individual electron trajectories to the spectrum. A single trajectory behaves exactly as classically predicted, but the interferences between multiple trajectories can exhibit themselves in surprising ways. In addition, we consider the harmonics from a molecule with two almost degenerate bound states to study the phase of the continuum wave packet. Next we perform a time-frequency analysis of the emitted harmonics. We observe the two-center interference also in the emission time of the harmonics.

In a calculation where the TDSE is solved numerically, the HHG spectrum is found with a rapidly oscillating time-translation phase superimposed on it. We show that it is possible to remove this additional phase factor. Then the harmonic phase from a numerical calculation follows the expected pattern.

Molecular orbital tomography

Molecular orbital tomography is a method to use HHG spectra to directly image an electronic orbital including its internal phase differences. We devote chapter 4 to this method that takes molecular imaging using strong-field processes to the extreme. It was introduced in 2004 by the Corkum group at the National Research Council of Canada (Itatani et al. [52]). In short, the electronic wave packet spends on the order of half a laser cycle in the continuum—away from the Coulombic potential—for the short HHG trajectories. During this time the electron wave packet will spread out considerably and become much larger than most molecules. In other words, the continuum wave packet effectively only depends on the laser polarization direction and not on the perpendicular direction before recombination.

Additionally ignoring the Coulombic potential on the continuum wave packet comes naturally although still with considerable loss of accuracy. Then the returning con-

tinuum wave packet can be described as a sum over plane waves oriented along the laser polarization axis. This means the interaction between the bound state and the continuum wave packet during recombination becomes similar to a 1D Fourier transform of the bound state. Many 1D Fourier transforms from different orientations of the molecule in the laser field can be combined to obtain a 2D Fourier transform of the orbital. This 2D Fourier transform can be inverted to obtain a 2D projection of the electronic orbital in the spatial domain. The orbital retrieved this way can have positive and negative lobes, or even complex ones in case of a transitional starting state.

We simulate the molecular tomographic scheme by solving the TDSE numerically for different orientations of the molecule in the laser field. In addition to the original *length-form* reconstruction, we introduce a *velocity-form* reconstruction based on momentum matrix elements (van der Zwan and Lein [141]). It has the disadvantage of using only the HHG radiation polarized parallel to the incident laser pulse, thereby possibly reducing the accuracy of the method. However, in the past it was shown that momentum matrix elements (velocity form) are better suited than dipole matrix elements (length form) to extract molecular properties from experimental HHG spectra (Chirilă and Lein [22]). Therefore it lies in the line of expectation that also reconstructing the complete molecular orbital will function better in velocity form than in length form, and indeed we find that we obtain more accurate results using the velocity-form reconstruction equation. The length form tends to overestimate the internuclear distance of a H_2^+-molecular ion.

Reconstruction of asymmetric orbitals

We show that the tomographic reconstruction is actually only possible in two cases; either if the molecular orbital is gerade or ungerade, or if the continuum wave packet approaches the core region from one side only (van der Zwan and Lein [142]). In all other cases the asymmetry of the molecule causes problems. The reason is that contributions from the two directions with which the wave packet can move along the laser polarization axis contribute with nontrivial phases to the spectrum and their contributions cannot be disentangled anymore.

For the reconstruction of a general orbital without symmetry, the desired behavior of the wave packet returning from one side only can be achieved using extremely short laser pulses. We perform a rather simple semi-classical calculation consisting of a sum over classical trajectories weighted with their exponential tunneling rate and a wave-packet-spreading factor from the Lewenstein model. This allows us to make plots showing the probability of return versus the momentum of the returning electron for many different laser pulses. Suitable for reconstructing a general orbital is a continuum wave packet that has a broad spectrum on the positive momentum side, and no contributions with negative momenta, or vice versa.

An extremely short pulse is given by an envelope, that determines the length of the pulse, times a carrier sine wave that oscillates with the fundamental frequency of the pulse. Such a pulse can be characterized by the envelope width, the envelope function

and the carrier-envelope phase (CEP), which determines the offset of a carrier wave peak from the maximum of the envelope. We find that the best pulses for the reconstruction of an asymmetric orbital are few-cycle pulses with a CEP around 0.25π. Experimentally, CEP stabilization is a necessary ingredient for reconstructing asymmetric molecules. The exact parameterization of the envelope function is not so important, due to the exponential dependence on the field strength of the tunneling rate (van der Zwan and Lein [142]).

Continuum wave packet

To perform the tomographic reconstruction, i.e., to obtain the molecular orbital, one needs to have information about the generated HHG spectrum and about the continuum wave packet generated by the laser pulse. Alternatively, one can deduce the composition of a continuum wave packet from the harmonic spectrum and the bound state. One of the biggest challenges before any molecular reconstruction can be made is determining the composition of the molecular continuum wave packet. In the original experiment (Itatani et al. [52]), the known bound-state orbital and measured HHG spectrum of a reference atom were used to calculate the composition of the continuum wave packet for the reference atom. A reference atom with roughly the same ionization potential as the molecule studied was chosen. In the three-step model for HHG, the first two steps (ionization and propagation in the laser field) are then the same for both systems. Consequently, the composition of the continuum wave packet determined from the reference atom was also used for the molecule.

The approximation that a laser pulse generates identical continuum wave packets for an atom and molecule with the same ionization potential is clearly very rough. This can already be seen from the fact that a molecule has an ionization rate that depends on the spatial orientation of the molecule in the laser field, whereas an atom is spherically symmetric. Already in the original work, the tomographic scheme was improved by also incorporating the total orientation-dependent ionization yield into the scheme. This replaces the approximation that the continuum wave packet is the same for the molecule and the reference atom with the approximation that the molecular continuum wave packet has the same frequency dependence for all orientations of the molecule in the laser field.

We present a theoretical analysis of the consequences of using an imperfect continuum wave packet for the reconstruction. The molecular orbital is reconstructed with a complex phase that is easily removed. If the harmonic emission time is different for the atom and molecule, this corresponds to a linear harmonic phase difference between the two. This leads to an additional distortion of the reconstructed orbital.

Link between HHG and ATI

In the traditional case of multi-cycle or even semi-infinite (cw) pulses generating HHG and ATI, both HHG and ATI peaks have complex contributions from many different trajectories. Initially it was thought there would be a direct correspondence

between the two spectra (see Toma et al. [124] and references therein). It is possible to express the harmonic yield as a sum over ATI channels plus recombination (Kuchiev and Ostrovsky [59, 60]). However, to the best of our knowledge no concrete link between individual HHG and ATI peaks exists as in general it is not possible to disentangle the contributions from the different trajectories. For extremely short laser pulses this link turns out to be possible. The reason is that during those pulses only a very limited number of trajectories contribute to each HHG or ATI peak. Taking also advantage of the exponential dependence of the ionization rate on the field strength, we find strong one-to-one links from HHG peaks to ATI peaks for many different pulses and harmonic frequencies. The links are based on shared birth times between HHG and ATI peaks.

Since the orbital geometry also affects the ionization dynamics, the conventional tomographic scheme does not provide us with the optimal continuum wave packet composition. With optimal we do not mean the completely physical description of the continuum wave packet, as for that we would have to go beyond plane waves and the reconstruction becomes impossible, but the plane-wave prefactors that give rise to the best reconstruction possible. We propose a method to incorporate the ATI electrons into the tomographic reconstruction procedure that so far is only based on HHG. We still assume that the atomic and molecular continuum wave packet differ only by real factors. However, it is no longer assumed that the atomic and molecular continuum wave packet share the same frequency dependence. Unfortunately, we found it impossible to test the incorporation of ATI electrons into the tomographic procedure in 1D simulations. We have not yet performed any 2D or 3D simulations to test the method.

SFA expressions

In chapter 5 we use the Lewenstein model to find semi-classical expressions for the HHG and ATI amplitudes containing sums over classical trajectories. For the ATI-case, Milošević et al. performed the integration over the birth time using the saddle-point method (Milošević et al. [87, 88]). In an analogue way we perform the integration over either only the recombination time or over both the birth and recombination time in HHG using the saddle-point method. In the latter case the sum over classical trajectories can be performed without any further complex integrations or other numerically intensive calculations. The saddle-point times, that represent the birth and if applicable the recombination times, are in general complex. To evaluate the saddle-point expressions directly we would therefore need to know the electric field strengths at complex times. The integration over time in the action makes this approach rather complicated. Therefore we expand the full saddle-point expressions around easily calculated classical saddle-point times. We finally arrive at expressions that are very easily calculated numerically, and that can be used to study spectral properties in terms of classical trajectories conveniently.

We use these expressions in determining the link between HHG and ATI spectra, and in investigating the suitability of a laser pulse for molecular orbital tomography. We quantify the suitability of a pulse for conventional tomography. Additionally,

the SFA expressions allow us to quantify the one-to-one links between HHG and ATI peaks and to concretely prescribe the recipe for including ATI electrons in the tomographic reconstruction. Therefore we can also quantify the suitability of a laser pulse for performing tomographic reconstructions with additional information from ATI electrons.

Error reduction

We show that it is possible to improve the quality of the tomographic reconstruction of a molecular orbital using a postprocessing algorithm in chapter 6. The algorithm is based on the algorithms that are widely used for the phase-retrieval problem, i.e., when the amplitude but not the phase of the Fourier transform of an abject are known (Fienup [34]). Iteratively we apply filters to the orbital that represent physical knowledge about either the orbital or the tomographic reconstruction scheme. One of these filters forces the orbital to be nonzero only in an area around the center of the molecule. This area is then dynamically shrunk (Chapman et al. [17]). The error reduction algorithm not only removes density located far away from the center of the molecule that is easily identified as erroneous, but also partially recovers some molecular features in the core region.

Chapter 2

Strong-field physics

Unless noted otherwise, we work in atomic units.

2.1 Time-dependent Schrödinger equation

The quantum-mechanical processes that are the topic of this thesis are governed by the time-dependent Schrödinger equation (TDSE). For the numerical results presented in this thesis we solve the TDSE numerically in either one or two dimensions for a molecular ion with a single electron. For HHG we consider two dimensions because in 2D many of the 3D characteristics of strong field processes are already present, such as the existence of directions perpendicular and parallel to the laser polarization axis. On the other hand, the TDSE can be solved very quickly, allowing the TDSE to be solved for many alignment angles of the molecule in the laser field. If also ATI electrons are considered, we resort to one-dimensional simulations because of the increased numerical effort. The TDSE is solved using the split-operator method (Feit et al. [31]; Fleck et al. [35]), and the ground-state wave function is found by imaginary-time propagation (Kosloff and Tal-Ezer [57]). More details on the numerics can be found in appendix A.1.

For a diatomic molecule in a laser field in the single-active electron approximation, the TDSE for a 2D model reads

$$i\frac{\partial\psi(\mathbf{r},t)}{\partial t} = \hat{H}\psi(\mathbf{r},t), \tag{2.1a}$$

$$\hat{H} = \frac{\hat{\mathbf{p}}^2}{2} + V(\mathbf{r}) + \mathbf{r}\cdot\mathbf{E}(t), \tag{2.1b}$$

$$V(\mathbf{r}) = -\frac{Z_1}{\sqrt{\left(\mathbf{r}-\frac{\mathbf{R}}{2}\right)^2 + a^2}} - \frac{Z_2}{\sqrt{\left(\mathbf{r}+\frac{\mathbf{R}}{2}\right)^2 + a^2}}, \tag{2.1c}$$

where $\hat{\mathbf{p}}$ is the momentum operator, $\mathbf{r} = \binom{x}{y}$, V is a softcore potential with softcore parameter a^2 and nuclear charges Z_1 and Z_2, and $\mathbf{E}(t)$ is the time-dependent electric field of the laser pulse. As we want to study the relationship between molecular characteristics and emitted spectra, we will consider different orientations of the

molecule in the laser field. The internuclear axis $\mathbf{R}$ makes an angle θ with respect to the main laser polarization axis x.

The total harmonic emission spectrum is calculated from the numerical solution of the TDSE as

$$I(\omega) = |\boldsymbol{\alpha}(\omega)|^2, \qquad \boldsymbol{\alpha}(\omega) = \int W(t)\langle\boldsymbol{\alpha}(t)\rangle e^{i\omega t}dt, \tag{2.2a}$$

$$\langle\boldsymbol{\alpha}(t)\rangle = \langle\psi(\mathbf{r},t)|\boldsymbol{\nabla}V(\mathbf{r}) + \mathbf{E}(t)|\psi(\mathbf{r},t)\rangle, \tag{2.2b}$$

where $\langle\boldsymbol{\alpha}(t)\rangle$ is the dipole acceleration and $I(\omega)$ is proportional to the intensity of the emitted radiation at frequency ω. Here $W(t)$ is a standardly used temporal window that prevents high-frequency artifacts at the boundaries of the integration. We use a Welch window

$$W(t) = 1 - \left(\frac{t - T_{\text{prop}}/2}{T_{\text{prop}}/2}\right)^2, \tag{2.3}$$

where T_{prop} is the total propagation time.

In the 1D case the ATI spectrum is also found from the numerical solution of the TDSE. Experimentally, the ATI spectrum is given by the energy distribution of the emitted electrons at the detector. The ATI spectrum is therefore measured far away from the molecule and after the pulse is over. Numerically we can get a good estimate of the ATI spectrum if we consider the Fourier transform of the wave function far away from the nucleus after the laser pulse is over. To also allow slow ATI electrons to leave the nuclear region, we propagate the system for two more laser cycles after the pulse is over. We filter out the bound state from the wave function using

$$\psi_{\text{ATI}}(x) = \begin{cases} 0 & \text{for } |x| \le r_1 \\ \left(\sin\left(\frac{|x|-r_1}{r_2-r_1}\frac{\pi}{2}\right)\right)^2 \psi(x, T_{\text{prop}}) & \text{for } r_1 < |x| < r_2 \\ \psi(x, T_{\text{prop}}) & \text{for } |x| \ge r_2, \end{cases} \tag{2.4}$$

where we set $r_1 = 18$ and $r_2 = 20$. We obtain the ATI momentum spectrum $A(p)$ from $\psi_{\text{ATI}}(x)$ as

$$M(p) = \frac{1}{\sqrt{2\pi}} \int \psi_{\text{ATI}}(x) e^{-ipx} dx, \tag{2.5a}$$

$$A(p) = |M(p)|^2 . \tag{2.5b}$$

If the molecule was ionized completely, the ATI spectrum $A(p)$ would integrate to 1.

2.2 Semi-classical models

The most important characteristic of atomic or small molecular systems subjected to a strong field is the Keldysh parameter (Keldysh [55]). Since laser fields perturb the Coulombic potential, they may cause ionization because of the overlap

between the unperturbed bound state and continuum states in the full potential. There are two pictures to visualize the ionization; firstly we can consider the laser field as quasi-static in which case the electron has time enough to tunnel through any potential barriers. Secondly, we can imagine a quickly-varying laser field that transmits energy to the electron as it absorbs photons from the field. The Keldysh parameter tells us which of these pictures is the more appropriate one. In Keldysh theory (Keldysh [55]), there is an imaginary time associated with the tunneling process that is calculated by inverting the classically-forbidden region. One obtains a real time that is multiplied with i to obtain the imaginary tunneling time.

If we compare the absolute value of the tunneling time with the frequency of the laser pulse, we can approximate whether the electron has enough time to tunnel through the barrier. If this is the case, the first picture is the more accurate one and we are in the 'tunneling' regime, if not, the electron cannot tunnel and we are in the 'multiphoton' regime. To quantify this, we use the Keldysh parameter (Keldysh [55])

$$\gamma = \sqrt{2I_\mathrm{p}}\frac{\omega}{E_0}, \tag{2.6}$$

where ω is the laser frequency, I_p is the ionization potential and E_0 is the peak of the laser electric field. We are in the multiphoton regime if $\gamma > 1$ and we are in the tunneling regime if $\gamma < 1$. This is of course not a black-and-white transition; close to $\gamma = 1$, we might observe features of the radiation that can only be easily explained in the other picture.

2.2.1 Three-step model for HHG

In the tunneling regime, in which we will stay in this thesis, the HHG process can be described remarkably well using a simple semi-classical model that describes it in three distinctive steps and is therefore known as the 'three-step model' or 'simple-man's model' (Corkum [25]). In the first step the electron tunnels out from the Coulombic potential under the influence of the laser field. Ionization takes predominantly place around the peak of the electric field. In Fig. 2.1 we have depicted this situation for the 2D H_2^+ model of section 3.1 placed in a laser field with intensity $I = 5 \times 10^{14}$ W/cm^2 and wavelength $\lambda = 780$ nm. The plot shows the potential as it is seen by the molecule at the peak of the electric field. The blue dotted line is drawn at the bound-state energy -30.2 eV and indicates the tunneling through the potential barrier

The second step of the three-step model is free propagation in the laser field. With 'free' we mean that the electron does not experience the Coulomb attraction from the nucleus in this step. Of course this is an approximation. However, since the electron travels tens or hundreds of atomic units for the laser parameters considered in this thesis, the error we make is acceptable for most harmonic orders. On the other hand, by making this approximation, the propagation in the laser field becomes a classical problem that can be solved easily and that provides us with much physical insight into the process. The third step of the three-step model is recombination into the bound state. It can take place if the laser drives the electron back to the

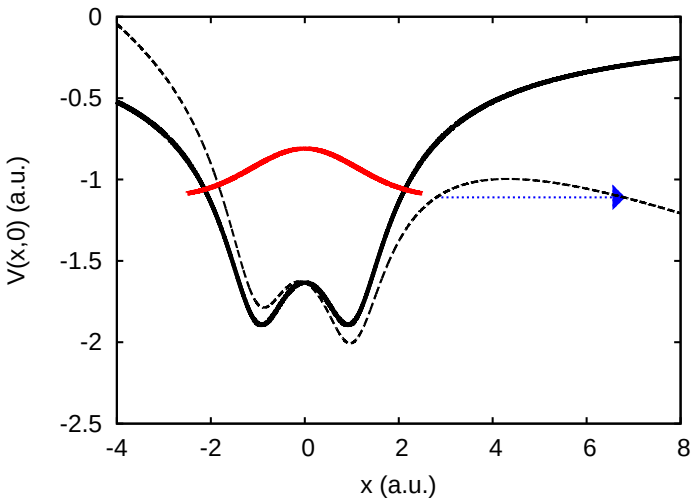

Figure 2.1: (Color online) Coulombic potential (black solid line) and effective potential (black dashed line) for a molecule at the peak of the electric field.

core region. If the electron recombines, it emits the energy it acquired in the laser field as a single high-frequency photon, the high-harmonic.

A harmonic spectrum exhibits a plateau in which the harmonic intensity is almost constant beyond the first few very strong harmonics. This can be seen for instance in Fig. 3.6 on page 30 in which harmonics for a 2D H_2^+ model in different laser pulses and for different alignment angles are plotted. At a certain energy there is a cutoff beyond which the harmonics are strongly suppressed. Depending on the pulse length the plateau region takes different forms; for long pulses and inversion-symmetric molecules the interference between different laser half-cycles leads to the formation of peaks only at odd harmonics[1] (see e.g. Lein and Chirilă [66] and references therein), whereas the interference between short and long trajectories is clearly visible in the harmonic spectrum for shorter pulses (see section 3.2).

Assuming the electrons are born at time at $x = 0$ with $v = 0$ (Corkum [25]), the classical equations of motion for an electron born at time t' up to time t are given

[1] Consider the harmonic emission of a molecule with inversion symmetry subjected to a cw laser field with period T. Since

$$\langle \boldsymbol{\alpha}(t) \rangle = -\langle \boldsymbol{\alpha}(t + T/2) \rangle,$$

the Fourier-transformed dipole acceleration is given by

$$\boldsymbol{\alpha}(\omega) = \int_{-\infty}^{\infty} \langle \boldsymbol{\alpha}(t) \rangle e^{i\omega t} dt = \sum_{n=-\infty}^{\infty} e^{in\omega T} \left(1 - e^{i\omega \frac{T}{2}}\right) \int_0^{T/2} \langle \boldsymbol{\alpha}(t) \rangle e^{i\omega t} dt.$$

Constructive interference between the different half-cycles therefore only occurs at odd multiples of the fundamental laser frequency.

by

$$a(t) = -E(t), \tag{2.7a}$$

$$v(t,t') = -\int_{t'}^{t} E(t'')dt'' = A(t) - A(t'), \tag{2.7b}$$

$$x(t,t') = \int_{t'}^{t} A(t'')dt'' - (t-t')A(t'), \tag{2.7c}$$

$$\tag{2.7d}$$

with the vector potential

$$A(t) = -\int_{-\infty}^{t} E(t')dt'. \tag{2.8}$$

Solving Eqs. (2.7) for the electron in the laser field we obtain the classical trajectories. Details can be found in appendix A.4.1. With the help of such a calculation we can explain many of the features of HHG spectra. Most importantly, the harmonic cutoff is given by the kinetic energy of the most energetic electrons that return to the core region plus the ionization potential, as the electron regains this energy upon recombining. Classically the harmonic energy of the cutoff ω_{cutoff} is given by (Corkum [25])

$$\omega_{\text{cutoff}} = 3.17U_{\text{p}} + I_{\text{p}}, \tag{2.9a}$$

$$U_{\text{p}} = \frac{E_0^2}{4\omega^2}, \tag{2.9b}$$

where U_{p} is the ponderomotive potential or average kinetic energy of a free electron in the laser field. Quantum-mechanically there is a correction to this formula and the cutoff is located at $\omega_{\text{cutoff}} = 3.17U_{\text{p}} + 1.32I_{\text{p}}$ (Lewenstein et al. [71]). In a cw pulse the process repeats itself with opposite sign every half-cycle of the laser pulse.

In the plateau region two dominant trajectories contribute to every harmonic. These are the so-called short and long trajectories. For an electric field given by $E(t) \sim \sin\omega t$, the long trajectories ionize shortly after the peak of the electric field at $t < 0.3T$, where T is the laser period. They recombine at $t > 0.95T$ and therefore spend at least $0.65T$ in the continuum. The short trajectories ionize at $t > 0.3T$, recombine at $t < 0.95T$ and therefore spend shorter than $t = 0.65T$ in the continuum. In the cutoff region the short and long trajectories merge to a single classically forbidden trajectory and the trajectory interferences disappear from the spectrum. In Fig. 2.2 we indicate schematically the short and long trajectories. Especially if the pulse is long, many more returns from trajectories that spend a lot longer in the continuum contribute to the spectrum.

2.2.2 ATI electrons

Most of the electrons that tunnel out under the influence of the laser field, do not recombine with the core, but instead escape forever. These are the so-called above-threshold-ionization (ATI) electrons. The ATI electrons can be relatively easily recorded using an electron spectrometer. The simpleman's model for ATI has two

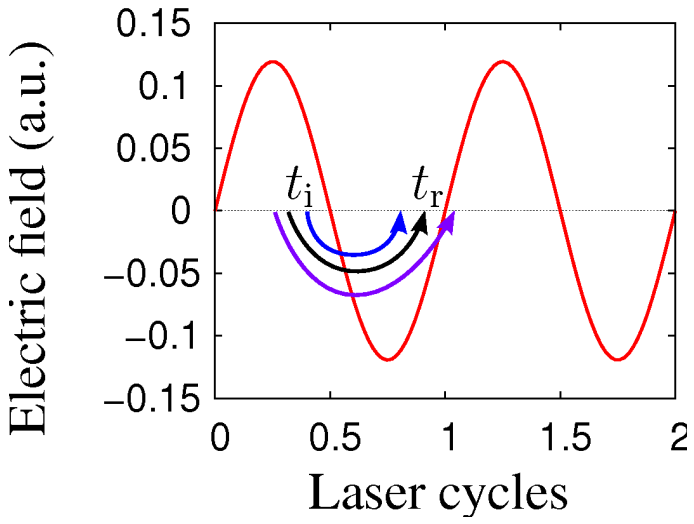

Figure 2.2: (Color online) Sketch of a short (blue upper arrow), long (purple bottom arrow) and most-energetic (black middle arrow) trajectory.

steps; firstly the electrons tunnel out, secondly they freely propagate in the laser field, and after the laser pulse is over they drift with constant momentum toward the observer. They end up at an experimental detector with momentum given by Eq. (2.7b) as

$$v(\infty, t') = -A(t'). \tag{2.10}$$

In words, the momentum of an ATI peak is semi-classically given by the negative of the vector potential at its birth time. For a cw pulse, the electric field is given by

$$E(t) = E_0 \sin(\omega t). \tag{2.11}$$

The amplitude of the vector potential is $A_0 = \frac{E_0}{\omega}$ which means that the maximum energy with which an electron can escape is

$$E_{\max} = \frac{v_{\max}^2}{2} = \frac{E_0^2}{2\omega^2} = 2U_p. \tag{2.12}$$

With Eq. (2.12) we have found the semi-classical cutoff law for the ATI electrons.

In the above analysis we only considered direct ATI electrons, i.e., ATI electrons that after ionization never interact with the core anymore. However, when electrons get driven back to the core, instead of recombining and generating high-harmonics they can also backscatter. This gives rise to a second, much weaker, plateau of rescattering ATI electrons extending up to $10U_p$ (Paulus et al. [102, 103]; Tong et al. [125]).

2.3 High-Harmonic Generation

We now describe the HHG process in more detail. Under the influence of the laser pulse, the total wave function contains a bound part and an ionized continuum part.

Because the continuum part of the wave function moves, the total wave function has a time-dependent electrical dipole moment. Electrodynamics tells us that an accelerated dipole moment oscillating at a single frequency generates electromagnetic radiation with the same frequency and with its phase conserved. The oscillating dipole in HHG contains many different frequencies leading to the emission of a superposition of frequencies.

Consider a molecular system in a laser field polarized in the x-direction. The harmonic radiation for a 2D molecule in the xy-plane oriented with θ with respect to the x-axis is then characterized by

$$I_\theta(\omega) = \omega^4 |\mathbf{D}_\theta(\omega)|^2, \tag{2.13a}$$

$$\Phi_\theta(\omega) = \arg[\mathbf{D}_\theta(\omega)], \tag{2.13b}$$

where $I_\theta(\omega)$ is proportional to the harmonic intensity and $\Phi_\theta(\omega)$ the phase of a harmonic with frequency ω. The Fourier transformed dipole moment $\mathbf{D}(\omega)$ is given by the expression (for simplicity we drop the angle dependence)

$$\mathbf{D}(\omega) = \int \langle \mathbf{d}(t) \rangle e^{i\omega t} dt, \tag{2.14a}$$

$$\langle \mathbf{d}(t) \rangle = \langle \psi(\mathbf{r}, t)| - e\mathbf{r}|\psi(\mathbf{r}, t)\rangle, \tag{2.14b}$$

where $\mathbf{r} = \binom{x}{y}$ and $-e$ is the electron charge ($e = 1$ in a.u.).

With the semi-classical picture of the harmonic generation process in mind we split the time-dependent wave function ψ in two parts as $\psi(\mathbf{r}, t) = \psi_0(\mathbf{r}, t) + \psi_c(\mathbf{r}, t)$, where $\psi_0(\mathbf{r}, t)$ is a bound-state wave function and $\psi_c(\mathbf{r}, t)$ is the continuum wave packet. We employ the three-step model and therefore ignore the influence of the laser on the bound state. The time evolution of the bound state is given by

$$\psi_0(\mathbf{r}, t) = \psi_0(\mathbf{r}) e^{iI_\mathrm{p} t}, \tag{2.15}$$

where $\psi_0(\mathbf{r})$ is a time-independent bound state of the system (with arbitrary global phase) and I_p is its ionization potential. For the continuum wave packet we use several simplifications from the three-step model. Firstly, we consider only electron momenta parallel to the laser polarization axis x. That means we can write

$$\psi_c(\mathbf{r}) = \int_{-\infty}^{\infty} a(k) e^{ikx} dk, \tag{2.16}$$

where the $a(k)$ are complex amplitudes. In addition, we ignore the influences of the Coulomb potential and the laser field on the evolution of $\psi_c(\mathbf{r})$. This leads to the plane-wave approximation (PWA) for the continuum wave packet, i.e., we describe the continuum wave packet as a superposition of plane waves whose time evolution is given by

$$\psi_c(\mathbf{r}, t) = \int_{-\infty}^{\infty} a(k) e^{ikx} e^{-i\frac{k^2}{2}t} dk. \tag{2.17}$$

If the total probability in the continuum wave packet is sufficiently small, the tran-

sition dipole moment in the time domain $\langle \mathbf{d}(t) \rangle$ is described by

$$\begin{aligned} \langle \mathbf{d}(t) \rangle &\simeq -\langle \psi_0(\mathbf{r},t)|\mathbf{r}|\psi_c(\mathbf{r},t)\rangle - \langle \psi_c(\mathbf{r},t)|\mathbf{r}|\psi_0(\mathbf{r},t)\rangle, \\ &= -\iint \psi_0(\mathbf{r}) e^{-iI_\mathrm{p}t}\mathbf{r} \int_{-\infty}^{\infty} a(k) e^{ikx} e^{-i\frac{k^2}{2}t} dk d^2\mathbf{r} \\ &\quad - \iiint_{-\infty}^{\infty} a^*(k) e^{-ikx} e^{i\frac{k^2}{2}t} dk\, \mathbf{r}\, \psi_0(\mathbf{r}) e^{iI_\mathrm{p}t} d^2\mathbf{r}, \end{aligned} \tag{2.18}$$

where we assumed that the ground state is real, as is always a possible choice for a bound state of a real-valued Hamiltonian. In the frequency domain this becomes

$$\begin{aligned} \mathbf{D}(\omega) = &-\int_{-\infty}^{\infty} a(k) \iint \psi_0(\mathbf{r}) \mathbf{r} e^{ikx} d^2\mathbf{r}\, 2\pi\delta(\omega - I_\mathrm{p} - \frac{k^2}{2}) dk \\ &- \int_{-\infty}^{\infty} a^*(k) \iint \psi_0(\mathbf{r}) \mathbf{r} e^{-ikx} d^2\mathbf{r}\, 2\pi\delta(\omega + I_\mathrm{p} + \frac{k^2}{2}) dk. \end{aligned} \tag{2.19}$$

To evaluate the Dirac δ-function we split the integration over k into two parts as $\int_{-\infty}^{\infty} dk = \int_{-\infty}^{0} dk + \int_{0}^{\infty} dk$ and then we change the integration variable from k to $u = \frac{k^2}{2}$, with $k = \pm\sqrt{2u}$ and $dk = \frac{dk}{du} du = \pm\frac{du}{\sqrt{2u}}$. If we restrict ourselves to physically measurable positive harmonic frequencies ω, we obtain

$$\begin{aligned} \mathbf{D}(\omega) = &-\int_{0}^{\infty} a(\sqrt{2u}) \iint \psi_0(\mathbf{r}) \mathbf{r} e^{i\sqrt{2u}x} d^2\mathbf{r}\, 2\pi\delta(\omega - I_\mathrm{p} - u) \frac{du}{\sqrt{2u}} \\ &- \int_{0}^{\infty} a(-\sqrt{2u}) \iint \psi_0(\mathbf{r}) \mathbf{r} e^{-i\sqrt{2u}x} d^2\mathbf{r}\, 2\pi\delta(\omega - I_\mathrm{p} - u) \frac{du}{\sqrt{2u}}. \end{aligned} \tag{2.20}$$

Performing the integration over u explicitly, for $\omega \geq I_\mathrm{p}$ we reach the following expression for HHG from the three-step model

$$I(\omega) = \omega^4 |\mathbf{D}(\omega)|^2, \tag{2.21a}$$

$$\begin{aligned} \mathbf{D}(\omega) = &-\frac{2\pi\, a[k(\omega)]}{k(\omega)} \iint \psi_0(\mathbf{r}) \mathbf{r} e^{ik(\omega)x} d^2\mathbf{r} \\ &- \frac{2\pi\, a[-k(\omega)]}{k(\omega)} \iint \psi_0(\mathbf{r}) \mathbf{r} e^{-ik(\omega)x} d^2\mathbf{r}, \end{aligned} \tag{2.21b}$$

with the wave number $k(\omega) = \sqrt{2(\omega - I_\mathrm{p})}$.

The main theme of this thesis is to obtain molecular properties from this and similar equations, e.g., by completely inverting it as in the molecular tomographic process. In order to retrieve ψ_0, we need to combine the two terms on the right-hand side of Eq. (2.21b) to one term. There are two cases in which this is possible. The first case is when the orbital ψ_0 is symmetric or anti-symmetric under the combined operations $x \to -x$ and $y \to -y$, i.e., when the orbital is (un-)gerade. In this case the Fourier transformed dipole moment is given by

$$\mathbf{D}(\omega) = -\frac{2\pi\, a'[k(\omega)]}{k(\omega)} \iint \psi_0(\mathbf{r}) \mathbf{r} e^{-ik(\omega)x} d^2\mathbf{r}, \tag{2.22}$$

where $a'[k(\omega)] = a[-k(\omega)] - a[k(\omega)]$ for gerade orbitals and $a'[k(\omega)] = a[k(\omega)] + a[-k(\omega)]$ for ungerade orbitals. In case we consider a cw-pulse this reduces to $a'[k(\omega)] = 2a[-k(\omega)]$ for both gerade and ungerade orbitals.

The second possibility to allow for recovery of ψ_0 from HHG is when $a(k) = 0$ for $k > 0$ (or $k < 0$). Physically this means that the returning electron wave packet approaches the nucleus from only one side. It is this case that we will focus on mostly in this thesis. In case the electrons only return from the positive side (i.e., with negative momentum) the Fourier transformed dipole moment is given by

$$\mathbf{D}(\omega) = \frac{-2\pi\, a[-k(\omega)]}{k(\omega)} \iint \psi_0(\mathbf{r}) \mathbf{r} e^{-ik(\omega)x} d^2\mathbf{r} \tag{2.23}$$

for $\omega \geq I_\mathrm{p}$.

To this simplified picture we add the fact that high harmonics seem to be better described numerically when one neglects the effect of the ionization potential on the incoming wave momentum (see e.g. Lein et al. [67]) by replacing our equation for $k(\omega)$ with $k(\omega) = \sqrt{2\omega}$. This replacement is supported by tests that we have performed. Physically the replacement amounts to saying that if we want to describe the returning electron wave packet as a plane wave, we should take into account that at the moment of recombination it has already reabsorbed the ionization potential into its kinetic energy. In other words, the molecular potential will lead to an increase of the kinetic energy, which in turn leads to an increase of the wave numbers in a plane wave expansion of the wave packet.

2.3.1 HHG in velocity and acceleration form

In addition to the length form description used so far, we can describe the HHG process also in velocity or acceleration form, using $\langle \mathbf{p}(t) \rangle = \frac{\partial}{\partial t} \langle \mathbf{d}(t) \rangle$ or $\langle \boldsymbol{\alpha}(t) \rangle = \frac{\partial^2}{\partial t^2} \langle \mathbf{d}(t) \rangle$, respectively. By means of two simple partial integrations starting from Eqs. (2.13) and (2.14a), it is easy to derive for HHG in acceleration form

$$I(\omega) = |\boldsymbol{\alpha}(\omega)|^2, \qquad \boldsymbol{\alpha}(\omega) = \int \langle \boldsymbol{\alpha}(t) \rangle e^{i\omega t} dt. \tag{2.24}$$

The only difference with the expression used in the numerical HHG calculation (as given by Eq. (2.2a)) is the addition of the Welch window $W(t)$ to prevent high-frequency artefacts from the numerical evaluation. Using the Ehrenfest theorem, the explicit expression for the dipole acceleration given in Eq. (2.2b) can be derived from the dipole moment (Eq. (2.14b)). Our choice for the acceleration form in the numerical calculations is based on (Burnett et al. [13]), who showed it is the most suited for this task.

Alternatively, we can perform a single partial integration to describe the harmonic generation in velocity form as

$$I(\omega) = \omega^2 \left| \mathbf{P}(\omega) \right|^2, \tag{2.25a}$$

$$\mathbf{P}(\omega) = \int \langle \mathbf{p}(t) \rangle e^{i\omega t} dt, \tag{2.25b}$$

$$\langle \mathbf{p}(t) \rangle = -\langle \psi(\mathbf{r}, t) | \hat{\mathbf{p}} | \psi(\mathbf{r}, t) \rangle. \tag{2.25c}$$

In the simplified model introduced above we have that

$$\begin{aligned}\langle \mathbf{p}(t)\rangle \simeq &- \iint \psi_0(\mathbf{r}) e^{-iI_\mathrm{p}t}\hat{\mathbf{p}} \int a(k) e^{ikx} e^{-i\frac{k^2}{2}t} dk d^2\mathbf{r} \\ &- \iiint a^*(k) e^{-ikx} e^{i\frac{k^2}{2}t} dk\, \hat{\mathbf{p}}\, \psi_0(\mathbf{r}) e^{iI_\mathrm{p}t} d^2\mathbf{r}.\end{aligned} \tag{2.26}$$

If we plug in that $\hat{\mathbf{p}} = -i\frac{\partial}{\partial \mathbf{r}}$ we obtain

$$\begin{aligned}\langle \mathbf{p}(t)\rangle \simeq &- \iiint \begin{pmatrix} k \\ 0 \end{pmatrix} \psi_0(\mathbf{r}) e^{-iI_\mathrm{p}t} a(k) e^{ikx} e^{-i\frac{k^2}{2}t} dk d^2\mathbf{r} \\ &- \iiint \begin{pmatrix} k \\ 0 \end{pmatrix} a^*(k) e^{-ikx} e^{i\frac{k^2}{2}t} dk\, \psi_0(\mathbf{r}) e^{iI_\mathrm{p}t} d^2\mathbf{r},\end{aligned} \tag{2.27}$$

where we used the hermiticity of the momentum operator for the second term. In similar lines as before we reach the following expression for the HHG process in velocity form

$$I(\omega) = \omega^2 \left|\mathbf{P}(\omega)\right|^2, \tag{2.28a}$$

$$\begin{aligned}\mathbf{P}(\omega) = &- \begin{pmatrix} 1 \\ 0 \end{pmatrix} 2\pi\, a[k(\omega)] \iint \psi_0(\mathbf{r}) e^{ik(\omega)x} d^2\mathbf{r} \\ &+ \begin{pmatrix} 1 \\ 0 \end{pmatrix} 2\pi\, a[-k(\omega)] \iint \psi_0(\mathbf{r}) e^{-ik(\omega)x} d^2\mathbf{r}.\end{aligned} \tag{2.28b}$$

Note that—unlike in length form—the two contributing terms have opposite signs.

For a symmetric molecule Eq. (2.28b) can be simplified to

$$\mathbf{P}(\omega) = \begin{pmatrix} 1 \\ 0 \end{pmatrix} 2\pi\, a'[k(\omega)] \iint \psi_0(\mathbf{r}) e^{-ik(\omega)x} d^2\mathbf{r}, \tag{2.29}$$

where for gerade orbitals $a'[k(\omega)] = a[-k(\omega)] - a[k(\omega)]$ and for ungerade orbitals $a'[k(\omega)] = a[-k(\omega)] + a[k(\omega)]$. In case $a(k) = 0$ for $k > 0$ Eq. (2.28b) reduces to

$$\mathbf{P}(\omega) = \begin{pmatrix} 1 \\ 0 \end{pmatrix} 2\pi\, a[-k(\omega)] \iint \psi_0(\mathbf{r}) e^{-ik(\omega)x} d^2\mathbf{r}, \tag{2.30}$$

Also in the case of a velocity form description of the HHG process, best results are obtained if an adapted dispersion relationship $k(\omega)$ with $k(\omega) = \sqrt{2\omega}$ is used.

2.3.2 Pulse polarization

The acceleration dipole moments associated with HHG are found numerically as complex numbers representing the amplitude and phase of the emission for a certain frequency ω. The numerical data can however be converted into a more intuitive representation in terms of the polarization angle, ellipticity and a complex prefactor incorporating the global phase and amplitude. This information is also needed if we want to compare physical properties like the ellipticity of the generated harmonics between different systems or as a function of harmonic order. Regularly, pulses

are characterized using Stokes parameters. Stokes parameters do not provide information on the absolute phase with which a pulse is emitted. This information is however needed by us to obtain the relative phase between harmonics, needed to compare the emission time t_e of different harmonics (as $t_e = \frac{\partial \Phi}{\partial \omega}$) or of harmonics by different systems. In contrast with the method described below, Stokes parameters can be used to determine the coherence of the radiation. As the harmonic emission process is completely coherent, we expect fully coherent radiation (Zhou et al. [139]) and we do not need information about the coherence of the emitted radiation.

We can write the emitted radiation field $\mathbf{E}_{\mathrm{em}}(t)$ as

$$\mathbf{E}_{\mathrm{em}}(t) = \int_{-\infty}^{\infty} \frac{c(\omega)}{\sqrt{1+(\epsilon(\omega))^2}} \left(\mathbf{e}_{\mathrm{p}}(\omega) + i\epsilon(\omega)\mathbf{e}_{\mathrm{o}}(\omega)\right) e^{-i\omega t} \frac{d\omega}{2\pi}, \tag{2.31}$$

where c is a complex function and ϵ is the ellipticity as a function of frequency ω. Here ϵ can be either positive or negative, $\epsilon = 0$ represents linearly polarized light, and $\epsilon = \pm 1$ represent positively and negatively circularly polarized light, depending on the choice of propagation direction. Furthermore, $\mathbf{e}_{\mathrm{p}}$ is the unit vector in the main polarization direction, and $\mathbf{e}_{\mathrm{o}}$ is the unit vector in the perpendicular direction. At a given ω, all possible types of coherent plane-wave radiation can be uniquely described by the parameters (ϕ, ϵ, c). Coherent non-plane-wave radiation would require position-dependent (ϕ, ϵ, c).

By inverting Eq. (2.24) and identifying $\langle \boldsymbol{\alpha}(t) \rangle$ with the emitted pulse $\mathbf{E}_{\mathrm{em}}(t)$ (omitting any proportionality factors), we find

$$\boldsymbol{\alpha}(\omega) = \frac{c(\omega)}{\sqrt{1+(\epsilon(\omega))^2}} \left(\mathbf{e}_{\mathrm{p}}(\omega) + i\,\epsilon(\omega)\mathbf{e}_{\mathrm{o}}(\omega)\right). \tag{2.32}$$

Next we write $\mathbf{e}_{\mathrm{p}}$ and $\mathbf{e}_{\mathrm{o}}$ in terms of a polarization angle ϕ with respect to the polarization axis of the fundamental field (or any other reference) as

$$\mathbf{e}_{\mathrm{p}} = \begin{pmatrix} \cos(\phi(\omega)) \\ \sin(\phi(\omega)) \end{pmatrix}, \tag{2.33a}$$

$$\mathbf{e}_{\mathrm{o}} = \begin{pmatrix} -\sin(\phi(\omega)) \\ \cos(\phi(\omega)) \end{pmatrix}. \tag{2.33b}$$

Similarly to the angle θ between the molecular axis and the laser polarization axis, a counterclockwise rotation corresponds to a positive ϕ. Because $\phi \to \phi + \pi$ is the same as $c \to -c$, we use the range $\phi\,\epsilon\,[0, \pi)$. In other words, ϕ is defined modulo π, and not modulo 2π as suggested by Eq. (2.33)!

The measured acceleration dipole moments can be expressed in terms of the laser parameters (ϕ, ϵ, c) as

$$\alpha_x(\omega) = \frac{c(\omega)}{\sqrt{1+(\epsilon(\omega))^2}} (\cos(\phi(\omega)) - i\,\epsilon(\omega)\sin(\phi(\omega))), \tag{2.34a}$$

$$\alpha_y(\omega) = \frac{c(\omega)}{\sqrt{1+(\epsilon(\omega))^2}} (\sin(\phi(\omega)) + i\,\epsilon(\omega)\cos(\phi(\omega))). \tag{2.34b}$$

For an experimentalist the most practical way to measure the polarization angle and ellipticity of the emitted radiation is to pass the harmonics through a polarization filter and measuring the emitted intensity for many polarization directions. The direction of greatest emission corresponds to the main polarization direction, and the emission in the orthogonal direction is a measure for the ellipticity of the emitted radiation (Zhou et al. [139]). Only under considerable effort for the experimentalist, the harmonic phase can be measured interferometrically as a function of alignment angle (McFarland et al. [84]; Smirnova et al. [116]) or as a function of harmonic order (Mairesse et al. [76]). Theoretically one has easy access to the harmonic phase. Using the phase information, Eq. (2.34) can be inverted to deduce the polarization parameters ϕ, ϵ, and the complex number c from the complex-valued α_x and α_y. In appendix A.2, the details of the inversion process can be found.

2.3.3 Multi-electron and many-particle contributions

Although HHG is predominantly a single-electron process (Figueira de Morisson Faria et al. [90]), multi-electron contributions can become important. For N_2 a significant contribution of the HOMO-1 to the harmonic spectrum was observed experimentally (McFarland et al. [84]) and theoretically (Le et al. [62]). Contributions to the harmonic spectrum from laser-induced ion dynamics during the excursion of the free electron are also observed (Mairesse et al. [79]).

In CO_2, the molecular alignment angle determines whether the ionization takes predominantly place from the HOMO, the HOMO-1 or the HOMO-2 (Smirnova et al. [117]). In a combined experimental and theoretical work, it was shown that the interference between the HOMO and HOMO-2 even may cause destructive interference depending on the electron excursion time (Smirnova et al. [116]). The minimum in the harmonic spectrum therefore shifts not only with the alignment angle (see section 3.1), but also with the laser intensity (Torres et al. [126]; Wörner et al. [135]).

Under normal experimental conditions, many molecules or atoms will contribute to the HHG process (see e.g. Gaarde et al. [39]; Priori et al. [105]; Tosa et al. [127]). Because of the spatial and temporal beam profile of the laser pulse, the effective laser intensity that these particles experience depends on both space and time. All these contributions interfere in the far-field, which has an influence on the observed radiation. The difference between the single-particle and many-particle responses is called the propagation effect. The experimentalist can influence the phase-matching between the different contributing particles by changing the location of the laser focus with respect to the particle source, and thereby select either the short or long trajectories (Gaarde and Schafer [38]; Salières et al. [109]).

2.3.4 Nuclear contributions

In this thesis—as in most work done on HHG—we ignore the effect of nuclear motion on the harmonic spectrum. This is based on the consideration that nuclei are much heavier than electrons. The typical time scale associated with nuclear motion is picoseconds, i.e., much longer than the few-femtosecond electronic dynamics in HHG,

and therefore the nuclei are approximated as fixed during the HHG process. Only for the extremely light molecules H_2 and D_2 a significant effect of nuclear motion on the ratio of harmonic intensities has been observed experimentally (Baker et al. [2]). Theoretically, using an extension of the Lewenstein model (see chapter 5) to include nuclear motion, a similar effect was seen for the ratio of harmonic intensities of CH_4 and CD_4 (Madsen et al. [75]).

Chapter 3

High-harmonic generation

3.1 Two-center interference minimum

In this chapter we will focus on 2D H_2^+ with fixed nuclei. The potential is given by Eq. (2.1c) with $Z_1 = Z_2 = 1$ and we use $a^2 = 0.5$ such that the ionization potential is given by $I_p = 30.2$ eV. For H_2^+, one observes a minimum in the spectrum of emitted radiation polarized in the x-direction because of interference between the two centers of the molecule (Lein et al. [68]). Using the plane-wave approximation for the returning electron, the (first and usually only observable) minimum occurs when the x-projection of the internuclear distance as seen by the returning wave packet is equal to half the de Broglie wavelength. This is illustrated in Fig. 3.1 ($R_{\text{eff}} = \frac{\lambda}{2} = \frac{\pi}{k}$). Because the de Broglie wavelength decreases with harmonic order, the minimum will shift toward higher harmonics for higher angles θ between the laser polarization and molecular axis. Since it is a structural minimum that depends only on the geometry of the bound state, one expects to see no shifts in the location of the minimum when different laser pulses are used or when instead Gaussian wave packets are used to generate harmonics in a laser-field-free electron-ion collision (Lein et al. [68]). Such a structural minimum can also be observed in the harmonic spectra of for instance H_2, O_2 and to some extent CO_2, although there multi-electron contributions are important also (see section 2.3.3) (Le et al. [64]).

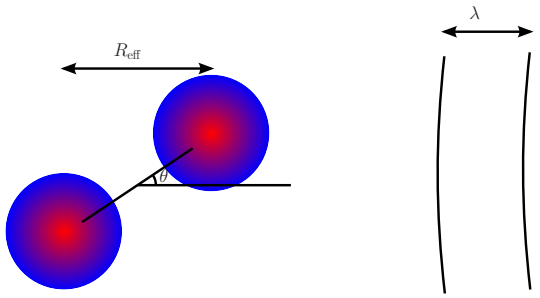

Figure 3.1: (Color online) Illustration of the two-center interference minimum in H_2^+ when half the de Broglie wavelength of the returning electron matches the effective internuclear distance.

In the three-step model (see section 2.2.1) or its quantum-mechanical formulation in terms of the strong-field approximation (SFA) (see section 5.1), the continuum wave packet formed by tunnel ionization carries practically no signature of the bound-state orbital. Therefore, the molecular characteristics imprinted on the emitted spectra must come from the recombination step (or from multiorbital interference). When studying molecular properties from harmonic spectra, the influence of the laser field on the recombination step and also the effect of the Coulombic potential on the propagation step are typically ignored (see e.g. Itatani et al. [52]; Lein et al. [68]). To study the effects of these approximations, in this chapter we perform a numerical comparison between the harmonics emitted in a normal laser-induced HHG process and harmonics emitted when an artificially prepared wave packet collides with the molecular ion in the absence of any laser pulse (Lein et al. [68]). Additionally, we compare the harmonics generated by both physical and artificial laser pulses to disentangle the influence of the different harmonic trajectories. We show that elliptically polarized HHG radiation from linearly polarized generating pulses occurs near the two-center interference. Elliptical polarization of harmonics from linearly polarized generating pulses was also found in recent experiments (Zhou et al. [139]).

For the wave-packet simulation without laser field the grid dimensions are given by $L_x \times L_y$. The center of the potential is placed in the middle of the grid at $(x, y) = (0, 0)$, and the Gaussian wave packet is introduced with its center at position $(x_0 = L_x/4, 0)$. The initial wave packet $\psi(\mathbf{r})$ is given by the superposition

$$\psi(\mathbf{r}) = \psi_0(\mathbf{r}) + \psi_\mathrm{G}(\mathbf{r}), \tag{3.1a}$$

$$\psi_\mathrm{G}(\mathbf{r}) = \sqrt{C}\sqrt{\frac{c_x c_y}{\pi}} e^{-\frac{1}{2}\left(c_x^2\left(x-\frac{L_x}{4}\right)^2 + c_y^2 y^2\right) + ik_0 x}, \tag{3.1b}$$

where $\psi_0(\mathbf{r})$ is the ground-state wave function, and c_x, c_y quantify the momentum spread of the Gaussian wave packet in the x- and y-directions. The wave packet moves with a central momentum $k_0 < 0$ toward the molecular core. The norm of the Gaussian wave packet C should be set small to mimic the situation of HHG at the typically used intensities. We use $C = 10^{-6}$. The momentum-spread parameter in the y-direction is chosen as

$$c_y = r_k |k_0|, \tag{3.2}$$

where a tuning parameter r_k is used to study the effects of different types of Gaussian wave packets and can be set to simulate the character of the continuum wave packet as generated by a laser pulse. The momentum-spread parameter in the x-direction c_x is set relatively large to allow for many harmonics to be probed by one wave packet. The propagation time is chosen such that a classical particle with momentum k_0 moves from $(L_x/4, 0)$ to $(-L_x/4, 0)$ during the propagation. As a result, the strongest emission is expected at the middle of the propagation. This way little distortion is introduced from using window function $W(t)$ in the temporal Fourier transform for obtaining the power spectrum using Eq. (2.2a). As an example, for $r_k = 0.01$ and $k_0 = -1.78$, the grid dimensions are $L_x = 383$ a.u. and $L_y = 1006$ a.u. Here we use 2304×6144 spatial grid points and 2000 time steps, i.e., the same time step as for a laser-induced HHG calculation at a comparable energy. The propagation time equals the optical period of a laser field with a 780-nm wavelength. More details on the calculation can be found in appendix A.1.1.

For the simulation of the laser-induced HHG process we use a laser pulse linearly polarized in the x-direction, simplifying Eq. (2.1b) to

$$\hat{H} = \frac{\hat{\mathbf{p}}^2}{2} + V(\mathbf{r}) + xE(t). \tag{3.3}$$

The initial state is set to the ground state $\psi_0(\mathbf{r})$. The time-dependent wave function is propagated for the laser pulse duration and two additional cycles after the end of the laser pulse to minimize distortions from the dipole acceleration window and to allow the wave packets to return to the nucleus. For the laser-induced calculations we use a grid measuring 280×84 a.u. with 1536×512 grid points and 2000 time steps per optical cycle.

3.1.1 Harmonic intensity

The laser wavelength for the calculations of laser-induced HHG is $\lambda = 780$ nm. For the Gaussian-wave-packet collisions, the same energy scale in units of harmonics of a 780-nm laser pulse is used. In Fig. 3.2 we show the spectrum of the emitted radiation polarized along the x-direction on the left-hand side and the alignment dependence of harmonic 49 on the right-hand side. We compare a Gaussian wave packet with $k_0 = -1.78$ and $r_k = 0.01$ to laser pulses with an intensity of $I = 5 \times 10^{14}$ W/cm^2 and different lengths. The laser pulses have a $\sin^2$ envelope of either three or five cycles, or a trapezoidal envelope of fifteen cycles length with five-cycle ramps. The electric field of a linearly-polarized $\sin^2$-pulse is given by

$$E(t) = (-1)^{N_{\text{cycles}}} E_0 \sin^2\left(\frac{\pi t}{N_{\text{cycles}} T}\right) \cos(\omega t + \phi_{\text{CEP}}), \tag{3.4}$$

where E_0 is the maximum field amplitude, T is the laser period, N_{cycles} is the number of cycles in the pulse and ϕ_{CEP}, the carrier-envelope phase (CEP), is the phase between the carrier wave and the envelope. The linearly-polarized trapezoidal pulse has a $\sin(\omega t)$-carrier that is multiplied with a trapezoidal envelope. We use $\phi_{\text{CEP}} = \frac{\pi}{4}$ for the shortest pulse, and $\phi_{\text{CEP}} = 0$ for the five-cycle $\sin^2$-pulse. In preparing the alignment-dependent curves on the right-hand side, the numerical data were integrated over one harmonic order.

The harmonic spectra in Fig. 3.2 feature the plateau region and cutoff introduced in section 2.2.1. Semi-classically for a cw-pulse the cutoff should be around harmonic 76 from $\omega_{\text{cutoff}} = 3.17U_{\text{p}} + I_{\text{p}}$ (Eq. (2.9a)). Because the three-cycle pulse is extremely short, its harmonic spectrum has a first cutoff well below this value (see section 4.6.1). The Gaussian wave packet gives rise to a mostly structureless spectrum, whereas for the three-cycle pulse the trajectory interferences and for the fifteen-cycle pulse the formation of peaks at odd harmonics are visible (see section 2.2.1). The two-center minima are visible in the plateau region around harmonic 45–50. The figure shows that the different laser pulses give rise to minima that are near, but not exactly at, the minimum position of the Gaussian wave packet.

In Fig. 3.3 we plot the positions of the minima θ_{min} in the alignment dependence versus harmonic order for different laser pulses and for the Gaussian wave packet

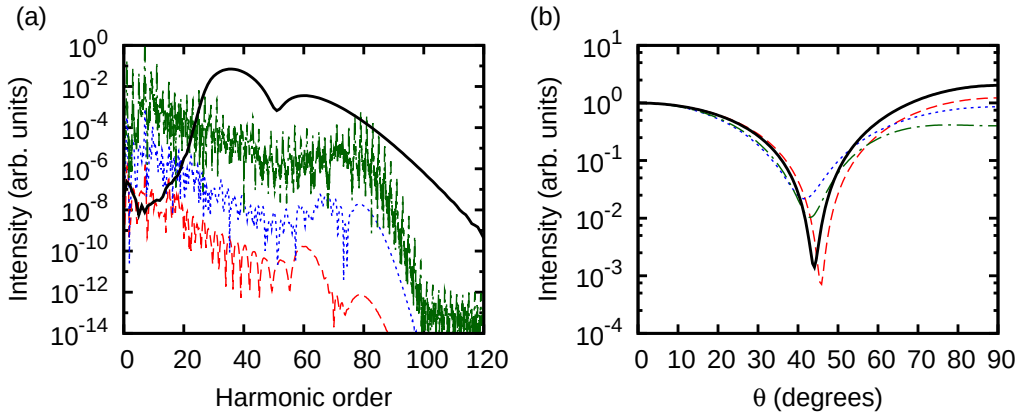

Figure 3.2: (Color online) (a) Intensity vs harmonic order for alignment angle $\theta = 45°$ (curves shifted for clarity) and (b) intensity of harmonic 49 vs θ. A Gaussian wave packet (black solid line) is compared to a three-cycle $\sin^2$-pulse (red dashed line), a five-cycle $\sin^2$-pulse (blue dotted line) and a fifteen-cycle trapezoidal pulse (green dot-dashed line).

from Fig. 3.2b. Also indicated in the figure are the curves that are predicted for the two-center minimum ($R_{\text{eff}} = R\cos\theta_{\text{min}}$) (Lein et al. [67]) using either the energy-conserving relationship $k(\omega) = \sqrt{2(\omega - I_{\text{p}})}$ from the Lewenstein model (Lewenstein et al. [71]), or using the I_{p}-corrected relationship $k(\omega) = \sqrt{2\omega}$ that has been adopted previously for molecular imaging (Itatani et al. [52]; Lein et al. [68]), see section 2.2.1. From Fig. 3.3 it is clear that the Gaussian wave packet gives rise to a very smooth shift of the minimum as a function of alignment angle θ. The laser pulses produce minima that follow the same trend as the Gaussian wave packet, but are scattered around the general trend. The results for short and longer pulses are scattered differently, but not less or more. The differences between relatively long ten- and fifteen-cycle pulses pulses are small. This is expected, since both pulses are effectively almost cw-like. Even for the fifteen-cycle pulse the depletion of the ground state remains below 6%. The results suggest that when using the plane-wave approximation for the returning electron in molecular imaging applications, a dispersion relationship in between the Lewenstein and I_{p}-corrected relationships should be used (Gonoskov and Ryabikin [43]; Levesque et al. [70]).

3.1.1.1 Effect of the propagation step

We compare the positions of interference minima for different types of Gaussian wave packets in Fig. 3.4. We vary the momentum spread of the wave packet in the perpendicular direction, the central momentum of the wave packet and the position at which the wave packet starts. The striking and important observation is that all curves lie very close together. Apparently the position of the minimum is insensitive to the momentum distribution of the continuum wave packet. Only for the lowest harmonics can we observe some difference between the different kinds of continuum wave packets. Small differences appear there between wave packets starting far away and those starting close to the nucleus, due to the effect of the

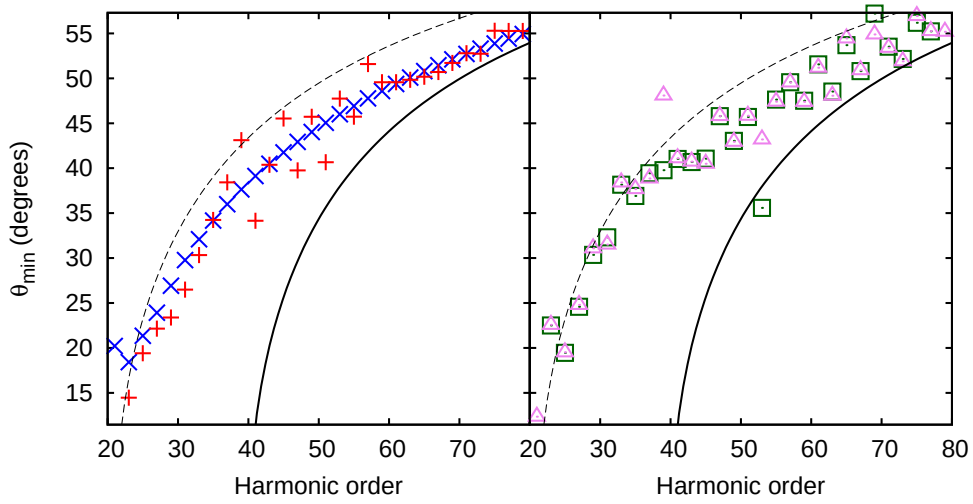

Figure 3.3: (Color online) Location of the minimum in the alignment dependence of the harmonic intensity polarized along the x-direction. (Left) Blue crosses are for the Gaussian wave packet and red plusses for the three-cycle pulse of Fig. 3.2. (Right) Green squares are for the fifteen-cycle pulse of Fig. 3.2 and violet triangles are for a ten-cycle trapezoidal pulse. The black solid line displays the two-center interference based on the SFA relation $k(\omega) = \sqrt{2(\omega - I_\mathrm{p})}$ and the black dashed line is the I_p-corrected result based on the relation $k(\omega) = \sqrt{2\omega}$.

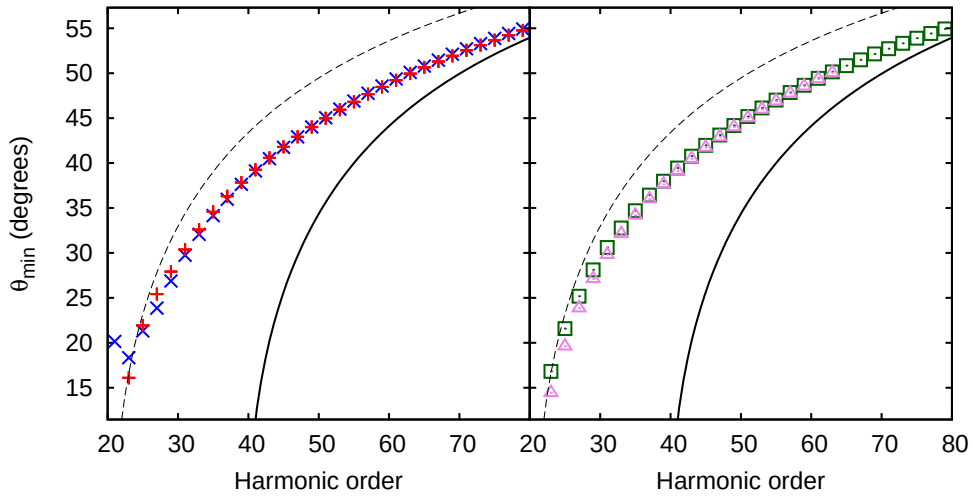

Figure 3.4: (Color online) (Left) Same as Fig. 3.3 for a broad Gaussian wave packet starting far from the nucleus (blue crosses) and a broad Gaussian wave packet starting close to the nucleus (red plusses). (Right) A narrow Gaussian wave packet starting close to the nucleus (green squares) and a broad Gaussian wave packet starting far from the nucleus but with less energy (violet triangles). The blue crosses and red plusses have $r_k = 0.03$ and $k_0 = -1.78$, the violet triangles have the same r_k but $k_0 = -1.38$. The red plusses and green squares start at $x_0 = 20$ a.u., the blue crosses correspond to an initial position of $x_0 = 95.8$ a.u. and the green squares to $x_0 = 74.1$ a.u.

long-range binding potential. Our findings suggest that in terms of the three-step model, the propagation step has little effect on the observed position of the minimum and cannot account for the big fluctuations observed in Fig. 3.3.

3.1.1.2 Effect of the recombination step

In the three-step model (see section 2.2.1), the laser field during the recombination step and possible interferences between different parts of the continuum wave packet are ignored. In reality, the electronic wave packet does not recombine under laser-field-free conditions, and different trajectories recombine at different times with different phases. To study the effect on the recombination process, we resort to a comparison of the minimum positions using artificial pulses. The pulses are four-cycle sinusoidal pulses with a constant envelope corresponding to an intensity of $I = 5 \times 10^{14}$ W/cm^2, i.e., a section of a cw laser field. At $t = 0$, the electric field is $E(0) = 0$. Optionally, we employ either or both of two methods to influence the recombination step: (i) setting the dipole acceleration to 0 after some point in time during the propagation and (ii) turning off the laser field for the inner region near the nuclei after some point in time.

Every half laser cycle, both a short and long classical electronic trajectory contribute to every harmonic peak (Lewenstein et al. [71]), as discussed in section 2.2.1. As a reminder, the distinction between short and long trajectories is based on whether the electron spends shorter or longer than $0.65T$ in the continuum, where T is the laser period. Setting the dipole acceleration to 0 beyond $t = T_\alpha$ using a temporal width ΔT_α (Smirnova et al. [116]), Eq. (2.2a) becomes

$$\boldsymbol{\alpha}(\omega) = \int_0^L W'(t)\langle\boldsymbol{\alpha}(t)\rangle e^{i\omega t}dt, \tag{3.5a}$$

$$W'(t) = W(t)S(t), \tag{3.5b}$$

$$S(t) = \begin{cases} 1 & \text{for } t \leq t_1 \\ \cos^2\left(\frac{t-t_1}{t_2-t_1}\frac{\pi}{2}\right) & \text{for } t_1 < t < t_2 \\ 0 & \text{for } t \geq t_2, \end{cases} \tag{3.5c}$$

where L is the propagation length, $t_1 = T_\alpha - \frac{\Delta T_\alpha}{2}$ and $t_2 = T_\alpha + \frac{\Delta T_\alpha}{2}$. We use $\Delta T_\alpha = 0.1T$. We set the dipole acceleration to 0 at either $T_\alpha = 0.95T$, the return time of the most energetic trajectory, or at $T_\alpha = 1.182T$, the time at which the return momentum of the first half-cycle's long trajectory matches that of the second half-cycle's short trajectory. Thus with $T_\alpha = 0.95T$ we take into account only the short trajectories from the first half-cycle, and $T_\alpha = 1.182T$ is the optimal point in time for selecting only a single pair of short and long trajectories.

Additionally, we optionally turn off the laser field in the inner region at time $t = T_\text{l}$. To prevent artifacts, the field is turned off gradually in both space and time. The laser interaction is completely turned off for $r = \sqrt{x^2 + y^2} < 4$, undisturbed for $r > 6$, and we use a $\sin^2$-transition between these two extremes. In the time domain, we use a smoothened step function (convolution of a Gaussian with a step function)

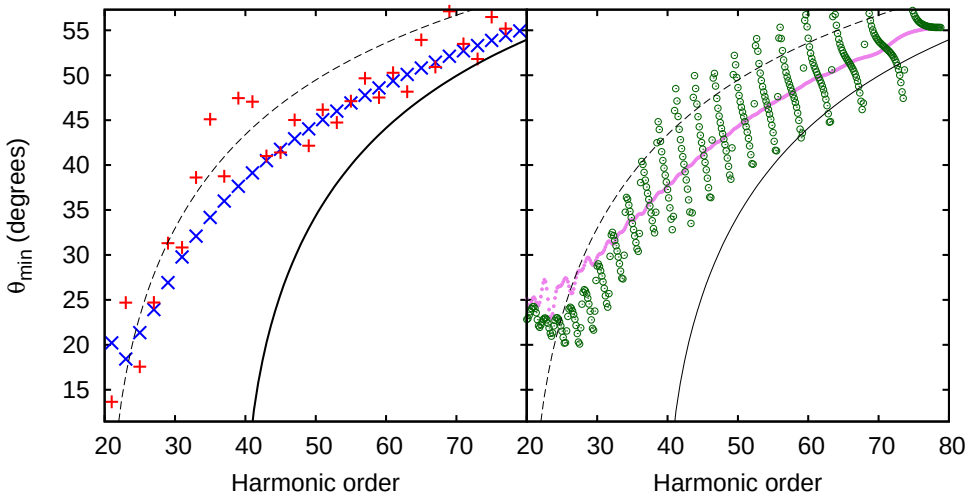

Figure 3.5: (Color online) (Left) Same as Fig. 3.3 for a broad Gaussian wave packet starting far from the nucleus (blue crosses) and for harmonics generated from a sinusoidal laser pulse (red plusses). (Right) Harmonics from sinusoidal pulses with $T_\alpha = 1.182T$ (green circles) and with $T_\alpha = 0.95T$ (violet points).

with a width of $0.1T$. In formula, the Hamiltonian in Eq. (2.1b) or Eq. (3.3) is replaced by

$$\hat{H} = \frac{\hat{\mathbf{p}}^2}{2} + V(\mathbf{r}) + Z(\mathbf{r},t)\cdot xE(t), \tag{3.6a}$$

$$Z(\mathbf{r},t) = F(\mathbf{r}) + (1-F(\mathbf{r}))R(t), \tag{3.6b}$$

$$F(\mathbf{r}) = \begin{cases} 0 & \text{for } r \le 4 \\ \sin^2(\frac{\pi}{4}(r-4)) & \text{for } 4 < r < 6 \\ 1 & \text{for } r \ge 6, \end{cases} \tag{3.6c}$$

$$R(t) = \frac{1}{2}\left(1 - \operatorname{erf}\left((t-T_\mathrm{l}) \,/\, \left(\sqrt{2}\cdot 0.1T\right)\right)\right). \tag{3.6d}$$

When $T_\mathrm{l} = 0.5T$ is used, this special setup allows us to compare near-physical harmonics to those generated in an identical setup where only trajectories starting during the first half-cycle contribute and with the laser field completely turned off during all recombinations. This method could be easily extended to filter out either the short or long trajectories.

In Fig. 3.5 we compare the scattering around the Gaussian-wave-packet results from the sinusoidal pulse (red plusses) with those from setting the dipole acceleration to 0 at $T_\alpha = 1.182T$ (green circles) and from setting the dipole acceleration to 0 at $T_\alpha = 0.95T$ (violet points). With $T_\alpha = 1.182T$ the interference between the long and short trajectories leads to a strong, but regular oscillation of the laser-induced results around the Gaussian-wave-packet results. The same interference between the short and long trajectories can be seen in an associated harmonic spectrum as the top, black solid line in Fig. 3.6. When every harmonic peak is caused by a single trajectory (violet points in Fig. 3.5), the interference disappears completely and the

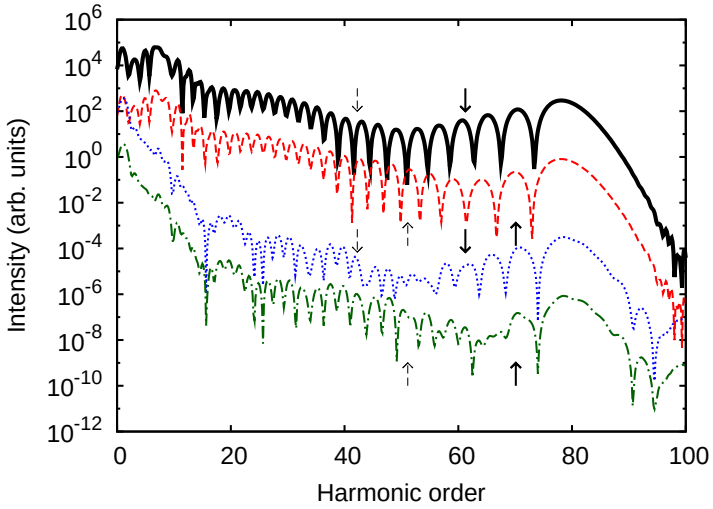

Figure 3.6: (Color online) Harmonic intensity polarized in the x-direction for the green circles from Fig. 3.5 for $\theta = 45°$ (black solid line) and $\theta = 50°$ (red dashed line). Also for the violet points from Fig. 3.7 for $\theta = 45°$ (blue dotted line) and $\theta = 50°$ (green dot-dashed line). Solid and dashed arrows indicate spectral minimum positions predicted using $k(\omega) = \sqrt{2(\omega - I_\mathrm{p})}$ and $k(\omega) = \sqrt{2\omega}$, respectively.

result is almost as smooth as that from the Gaussian wave packet. Under normal circumstances, additional later returns from the same trajectories contribute to the spectrum. For a finite pulse length, different half-cycles also contribute differently because of the pulse envelope. Additionally, for a numerical calculation the dipole acceleration window $W(t)$ also changes the contributions between different half-cycles. All of these together then smoothen but irregularize the oscillation of the green circles in Fig. 3.5, leading to the scattering of the laser-induced data points observed in Fig. 3.3. The interference between the short and long trajectories can probably also explain the scattering of the two-center minimum as a function of intensity as found by (Gonoskov and Ryabikin [43]).

The fact that the results for a single harmonic trajectory (violet points in Fig. 3.5) lie so close to the Gaussian-wave-packet result, means that the laser field has no significant influence on the amplitude of the recombination matrix elements. This supports using HHG for molecular imaging (Haessler et al. [46]; Itatani et al. [52]; Lein et al. [67, 68]), as in a typical experimental setup only short trajectories contribute to the harmonic spectrum. Interestingly, however, in Fig. 3.7 we show that turning off the laser field during the recombination does have a significant effect on the interference between the short and long trajectories. In the figure, the green circles are copied from Fig. 3.5. Additionally, we show the case where there is only a single set of short and long trajectories with additionally the laser pulse turned off in the inner region at $T_\mathrm{l} = 0.5T$ (violet points). The strong reduction in scattering amplitude for the violet points in Fig. 3.7 can be understood from Fig. 3.6, where we plot the harmonic spectra for molecular alignment angles 45° and 50° for the case of the green circles (violet points) in Fig. 3.7 as the top (bottom) two curves. For the unmodified laser pulse we observe a significant shift of the trajectory interference positions in

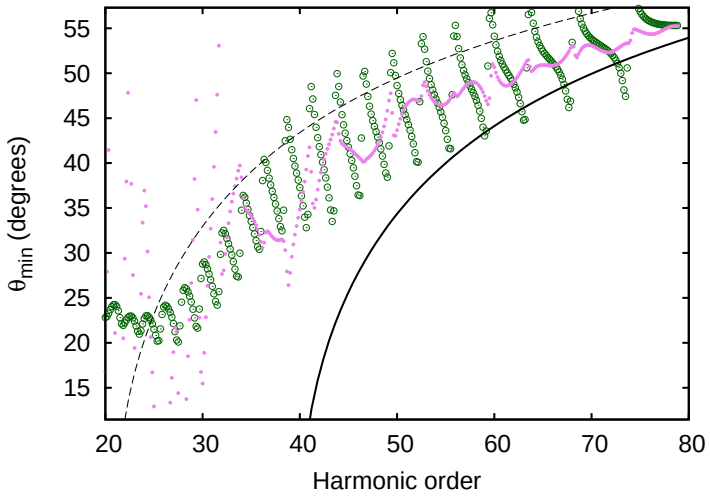

Figure 3.7: (Color online) Same as Fig. 3.3 for harmonics from a sinusoidal laser pulse with $T_\alpha = 1.182T$ (green circles) and additionally with $T_\mathrm{l} = 0.5T$ (violet points).

the harmonic spectrum when going from alignment at 45° to 50°. Although at first sight the bottom two curves in Fig. 3.6 look more distinct from one another, a closer look reveals that the alignment dependence of the trajectory interference minima is actually a lot smaller with the laser field turned off in the inner region, as there is no shift visible. The strong scattering at low harmonics for the violet points in Fig. 3.7 is caused by the fact that the finite temporal widths of the filters $R(t)$ and $S(t)$ suppress the complete lower end of the spectrum.

3.1.2 Harmonic phase

The two-center minimum in the harmonic spectrum is accompanied by a phase jump in the harmonic phase. Using the plane-wave approximation, this should be a sharp π-phase jump (Lein et al. [67]). However, in experiments a smaller and smoother phase jump is observed (Boutu et al. [11]). Such deviations can be attributed to nonclassical momenta (Chirilă and Lein [23]) and to effects of the Coulombic potential (Ciappina et al. [24]). Similarly, a phase jump is observable when one considers a fixed harmonic as a function of θ. The phase of harmonic 49 for emission polarized along x is shown in Fig. 3.8. The same set of laser pulses and Gaussian wave packet is used as in Fig. 3.2. The curves have been shifted such that for $\theta = 0$ the phase is 0. The figure shows that both the Gaussian wave packet and the extremely short three-cycle laser pulse give rise to a mostly constant phase as a function of θ with a phase jump slightly smaller than π at the location of the minimum. The longer pulses have a more smeared-out phase jump. In the neighborhood of the minimum their jump is a lot smaller than π but over the complete θ-range the jump seems to be bigger than π. This behavior for the longer pulses is probably an effect of more, and longer, trajectories contributing to the harmonics. Different trajectories are associated with different Coulomb corrections

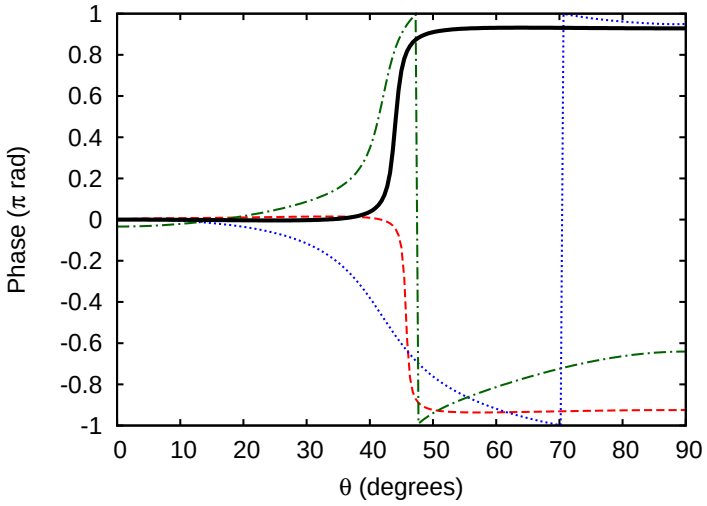

Figure 3.8: (Color online) Phase of the harmonic emission polarized along x for harmonic 49 generated by a Gaussian wave packet (black solid line) and generated by a three-cycle $\sin^2$-pulse (red dashed line), a five-cycle $\sin^2$-pulse (blue dotted line), and a fifteen-cycle trapezoidal pulse (green dot-dashed line).

and therefore the harmonic phase becomes smeared out. This is in accordance with the shallower intensity minima in the right-hand side of Fig. 3.2 for the longer pulses.

It is interesting to investigate the phase jump for the different Gaussian wave packets of Fig. 3.4. This is plotted in Fig. 3.9 for a smaller range of θ for clarity. The broad Gaussian wave packet starting closing to the nucleus (red dashed line) starts out with small perpendicular momentum components. Because of the short propagation time before the interaction with the core, both Coulomb effects on the momentum distribution and perpendicular momentum components will be relatively small in this scenario. As a result we observe a sharp almost-π-phase jump. To some extent, the difference with the narrow Gaussian wave packet (green dot-dashed line) is that the latter experiences roughly the same Coulomb effects, but starts out with much larger perpendicular momentum components. This leads to a much smoother phase jump. Independent of the central momentum of the wave packet, a broad wave packet starting far away from the nucleus (black solid and blue dotted lines) experiences a smoother phase jump because of Coulomb effects and the associated increased nonparallel momentum components.

3.1.3 Polarization direction

In the following two subsections we use the procedure outlined in section 2.3.2 and appendix A.2 to express the numerically calculated radiative emission in terms of the polarization parameters (ϕ, ϵ, c). The two-center interference minimum can then also be observed in the polarization direction ϕ of the harmonics. Because the emission in the direction parallel to the laser polarization direction is strongly suppressed at the minimum, we expect a $\frac{\pi}{2}$-jump toward the minimum. The π-jump for the harmonic

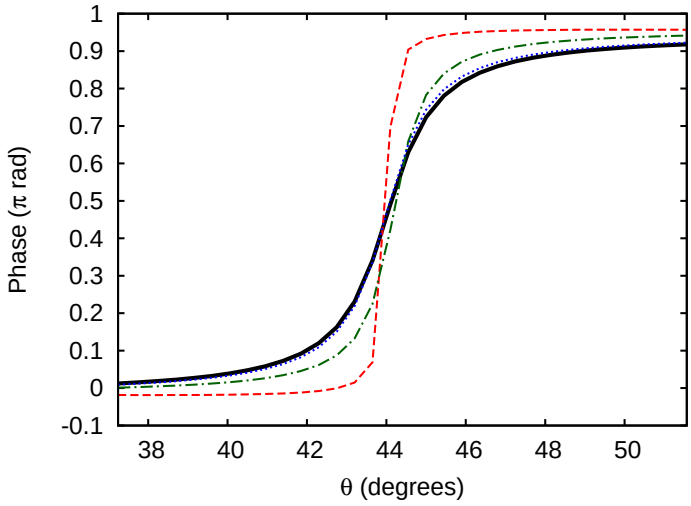

Figure 3.9: (Color online) Phase of the harmonic emission polarized along x for harmonic 49 generated by a broad Gaussian wave packet starting far from the nucleus (solid black line), a broad Gaussian wave packet starting close to the nucleus (red dashed line), a narrow Gaussian wave packet starting close to the nucleus (green dot-dashed line), and a broad Gaussian wave packet starting far from the nucleus but with less energy (blue dotted line).

phase in the x-direction in Fig. 3.8 translates to a full π-rotation for ϕ. This is exactly what is observed for a Gaussian wave packet and harmonics generated by different laser pulses in Fig. 3.10. The polarization direction of the emitted radiation was averaged over one harmonic order using the total emitted intensities as weights.

The phase jump in the x-direction at the two-center interference minimum becomes smoother for low harmonics (Boutu et al. [11]; Chirilă and Lein [23]; Ciappina et al. [24]). In the following we investigate how the jump in the polarization direction depends on harmonic order. We plot the main polarization direction for different harmonics in Fig. 3.11. Here we plot the polarization data points corresponding to the exact harmonics, i.e., no averaging was done. The right-most curves for high harmonics show a simple polarization-direction jump around the two-center minimum. For the lowest harmonics (on the left-hand side) the behavior becomes more complicated. To explain this finding, we also plot the phase difference δ between α_y and α_x for harmonic 31 (black crosses). The intensity ratio $\frac{|\alpha_y|}{|\alpha_x|}$ equals 1 for $\theta = 16°$ and $\theta = 37°$, and it reaches a maximum of $\frac{|\alpha_y|}{|\alpha_x|} = 2$ at $\theta = 25°$. For a given ratio $\frac{|\alpha_y|}{|\alpha_x|}$, the main polarization direction is aligned more along the laboratory-frame (x or y) direction with the higher amplitude if the phase difference δ between the laboratory-frame directions is far from 0 or π. We can observe this effect clearly in Fig. 3.11: at θ equal to 20°–25° for harmonic 31, where δ is around $\frac{\pi}{2}$ and $|\alpha_y|$ is bigger than $|\alpha_x|$, the relatively slow increase in the polarization direction shows the tendency that the polarization is clamped toward the y-direction ($\phi = \frac{\pi}{2}$).

We fit the jump observed in Fig. 3.10 with a smoothened step function to determine

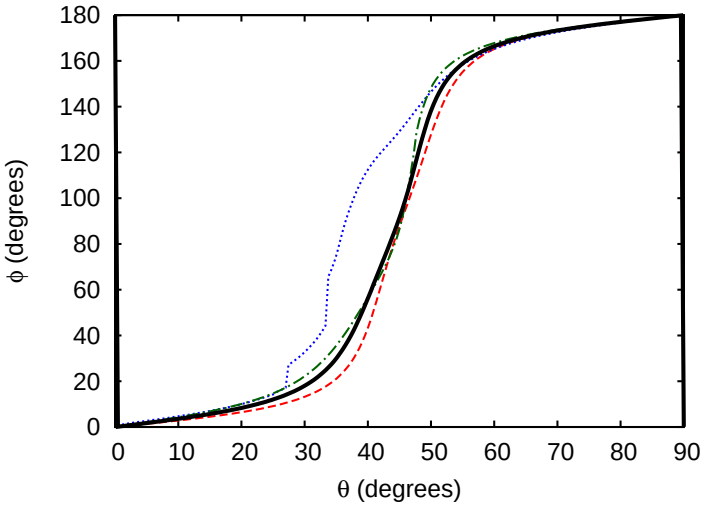

Figure 3.10: (Color online) Main polarization direction ϕ for harmonic 49 generated by a Gaussian wave packet (black solid line) and generated by a three-cycle $\sin^2$-pulse (red dashed line), a five-cycle $\sin^2$-pulse (blue dotted line), and a fifteen-cycle trapezoidal pulse (green dot-dashed line).

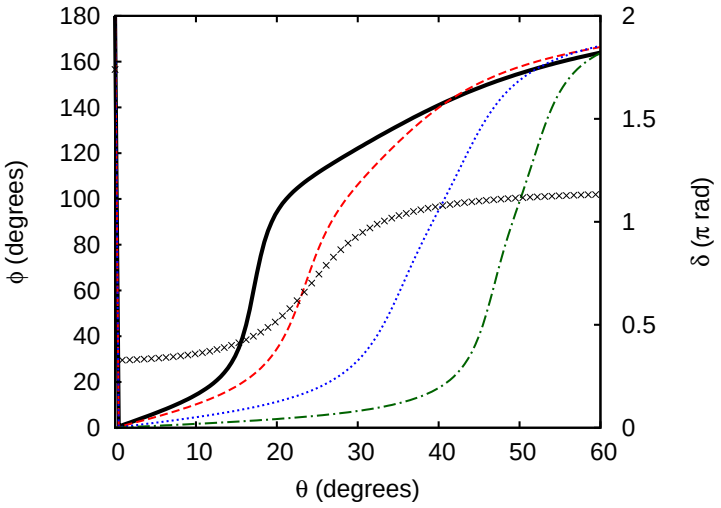

Figure 3.11: (Color online) Main polarization direction ϕ for harmonic 31 (black solid line), harmonic 41 (red dashed line), harmonic 51 (blue dotted line), and harmonic 61 (green dot-dashed line). The black crosses show the phase difference δ between the x- and y-components for harmonic 31. A three-cycle $\sin^2$-pulse was used.

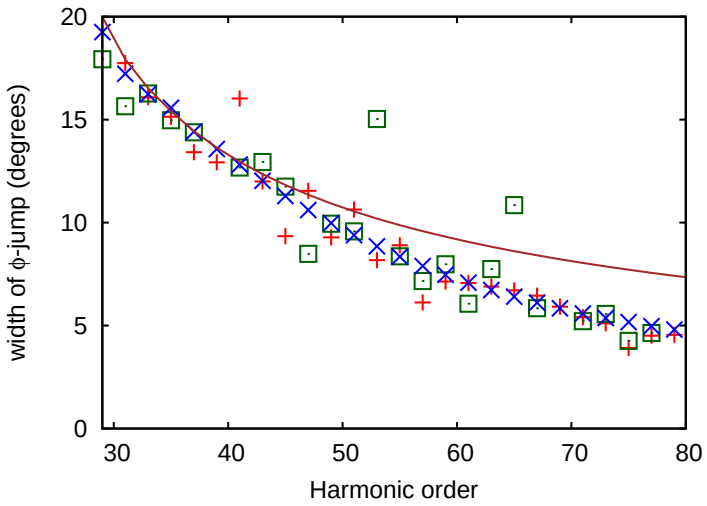

Figure 3.12: (Color online) Width of the jump in ϕ. Blue crosses are for the Gaussian wave packet, red plusses for the three-cycle pulse, and green squares for the fifteen-cycle pulse. The brown line shows the curve expected from purely geometric considerations.

the location θ_p and the width $\Delta\theta$ of the polarization-direction jump. When one plots the location θ_p as a function of harmonic order, one obtains a curve very similar to that shown in Fig. 3.3. In Fig. 3.12 we plot the width $\Delta\theta$ as a function of harmonic order for a Gaussian wave packet and different laser pulses. Again, the results for the different laser pulses are scattered around the Gaussian-wave-packet result. The width of the jump for ϕ as a function of harmonic order does not depend on the laser pulse length. One observes that the width of the jump decreases with increasing harmonic order. An important part of this decrease is due to a purely geometric effect: with increasing harmonic order, the minimum moves to higher θ leading to a narrower interference pattern as a function of θ.

In the absence of Coulomb effects, i.e., when α_x and α_y have the same phases apart from π-jumps for symmetric molecules, the polarization direction ϕ is given by $\tan\phi = \frac{\alpha_y}{\alpha_x}$ (see Eq. (A.38b)). We assume that α_y is alignment independent over the range of the two-center minimum, as also indicated by numerical tests that we have performed, and that the alignment dependence of α_x comes purely from the two-center interference with the phase lag $kR\cos\theta$, i.e., $\alpha_x = \alpha_x^{(0)}\cos\left(\frac{1}{2}kR\cos\theta\right)$ (Ciappina et al. [24]; Zhou et al. [138]). Then the variation $\Delta\phi$ of the polarization direction on varying θ in the vicinity of θ_p is proportional to $\Delta(kR\cos\theta) \simeq (\pi/\cos\theta_\mathrm{p})\,\Delta(\cos\theta)$. Thus the width $\Delta\theta$ should be such that $\Delta(\cos\theta)\,/\cos\theta_\mathrm{p}$ is independent of harmonic frequency, provided that $\alpha_y/\alpha_x^{(0)}$ is frequency independent. The brown line in Fig. 3.12 is obtained for $\Delta\theta$ if we set $\Delta(\cos\theta)\,/\cos\theta_\mathrm{p}$ arbitrarily equal to 0.185 using $\Delta(\cos\theta) \simeq \cos\left(\theta_\mathrm{p} - \frac{\Delta\theta}{2}\right) - \cos\left(\theta_\mathrm{p} + \frac{\Delta\theta}{2}\right)$. A comparison between the brown line and the other curves shows that at the high end of the spectrum the decrease in $\Delta\theta$ cannot be explained any more exclusively by the geometric effect. Since θ_p varies very slowly in this range, we expect only a slow variation in $\alpha_y/\alpha_x^{(0)}$. This suggests that decreasing Coulomb effects play a role, in accordance

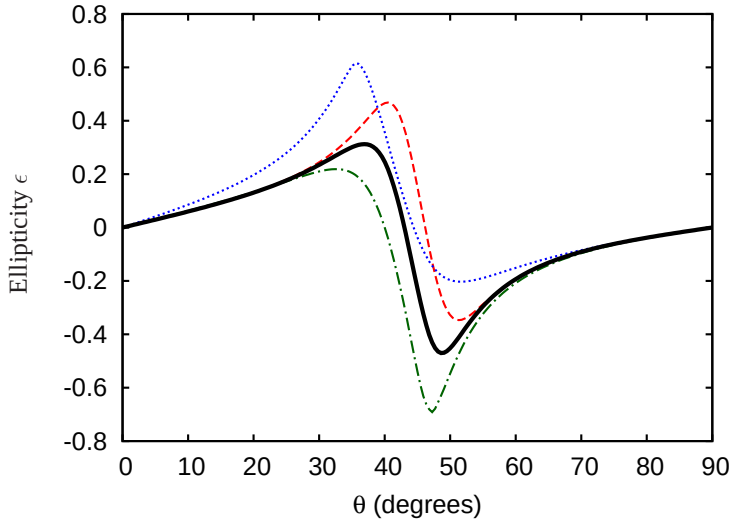

Figure 3.13: (Color online) Ellipticity of the harmonic emission for harmonic 49 generated by a Gaussian wave packet (black solid line) and generated by a three-cycle $\sin^2$-pulse (red dashed line), a five-cycle $\sin^2$-pulse (blue dotted line), and a fifteen-cycle trapezoidal pulse (green dot-dashed line).

with Fig. 3.3, where for harmonics 50–80 we observe a transition toward the curve predicted by the SFA dispersion relationship, also indicating decreasing Coulomb effects in this range.

3.1.4 Ellipticity

In Fig. 3.13 we plot the ellipticity ϵ of the emitted radiation for harmonic 49 as a function of θ. Again the polarization data was averaged over one harmonic order using the intensities as weights. The plot shows that both a Gaussian wave packet and different laser pulses give rise to both significant and varying elliptical emission. Nonzero ellipticity means that the harmonics in the x and y-directions are emitted with different phases. Using the plane-wave approximation for the returning electron, one would not expect to see any ellipticity for a symmetric molecule (Levesque et al. [69]). Since the ionization and propagation step are identical for the two components of the radiation, the ellipticity must come from the recombination step. Therefore, this result confirms that the Coulomb effects can lead to significant ellipticity. The ellipticity for parallel or perpendicular alignment is zero, because at these alignment angles, the perpendicular component of the emitted radiation vanishes. The ellipticity goes through zero at some intermediate alignment angle. If we plot the angle of zero ellipticity as a function of harmonic order, we arrive at Fig. 3.14. This plot shows that in the close vicinity of the two-center interference minimum, the ellipticity goes through zero. This is as expected, because at the location of the minimum, the x-component of the emitted radiation is very small. Because the x-component has opposite signs before and after the minimum, the ellipticity changes handedness through the minimum.

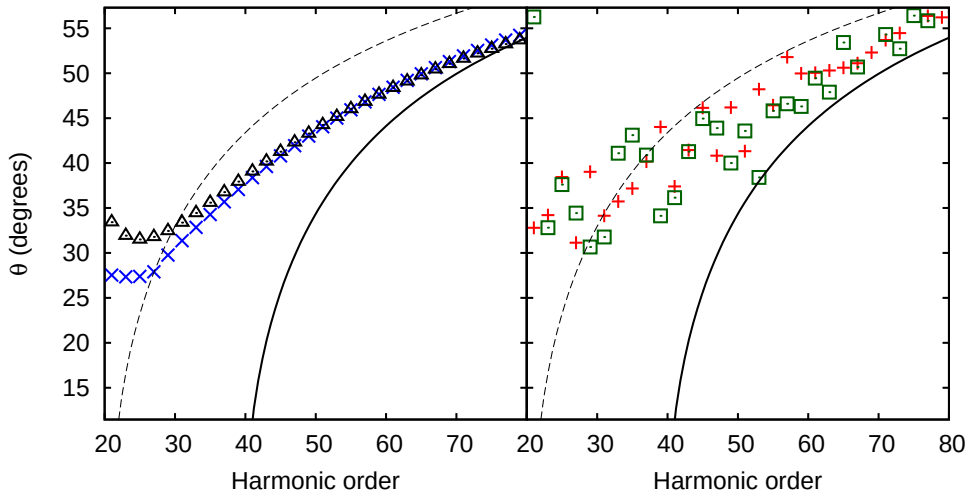

Figure 3.14: (Color online) Alignment angles of zero ellipticity. (Left) Blue crosses are for a broad Gaussian wave packet starting far from the nucleus and black triangles for a narrow Gaussian wave packet starting close to the nucleus. (Right) Red plusses for the three-cycle pulse and green squares for the fifteen-cycle pulse.

For each harmonic, we can also plot the extrema of the ellipticity that can be reached and the alignment angles at which those extrema are reached. The results are shown in Figs. 3.15 and 3.16, respectively. We observe that for sufficiently high harmonic orders, the ellipticity extrema become smaller in absolute value and move closer to the two-center interference minimum with increasing harmonic order. Since the ellipticity is an indicator of non-plane-wave character, the decreasing ellipticity is another signature of decreasing Coulomb effects for higher harmonic orders, which correspond to higher return momenta.

3.2 Harmonic phase

Numerically we obtain the harmonic spectrum through a discrete Fourier transform of $\langle \boldsymbol{\alpha}(t) \rangle$, according to Eq. (2.2a). The discrete Fourier transform assumes $t = 0$ for the first data point. Numerically the harmonic emission does not occur at $t = 0$, but at some different point in time somewhere around the peak of the pulse. Therefore, $\boldsymbol{\alpha}(\omega)$ will acquire a complex phase factor that represents the time translation[1]. Assuming that the emission in the directions x,y is centered around $t = a_{x,y}$, we numerically recover $\boldsymbol{\alpha}(\omega)$ with the phase

$$\arg\left(\boldsymbol{\alpha}(\omega)\right) = \boldsymbol{\Phi}_\alpha(\omega) + \mathbf{a}\,\omega. \tag{3.7}$$

[1] A basic property of Fourier transforms is that for a function $f(t)$ and its Fourier transform $\hat{f}(\omega) = \int f(t) e^{i\omega t} dt$ we have that

$$\hat{f}'(\omega) = \int f(t - t_0) e^{i\omega t} dt = e^{i\omega t_0} \hat{f}(\omega).$$

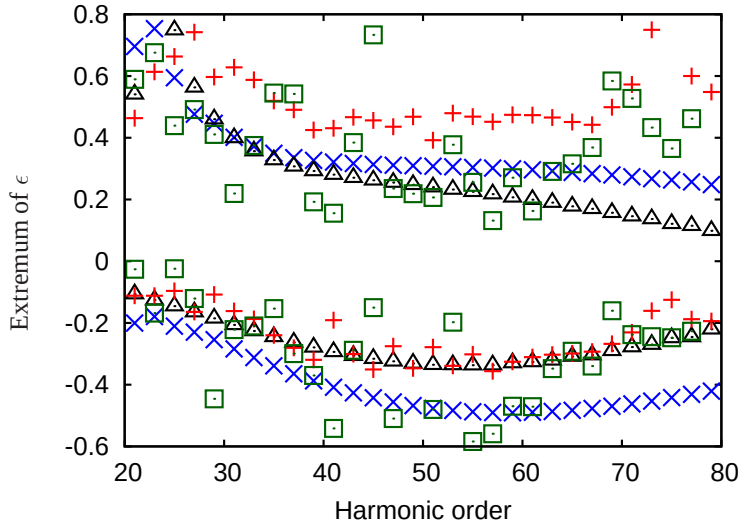

Figure 3.15: (Color online) Extrema of ellipticity as a function of harmonic order. Blue crosses represent a broad Gaussian wave packet starting far from the nucleus, black triangles a narrow Gaussian wave packet starting close to the nucleus, red plusses a three-cycle pulse, and green squares a fifteen-cycle pulse.

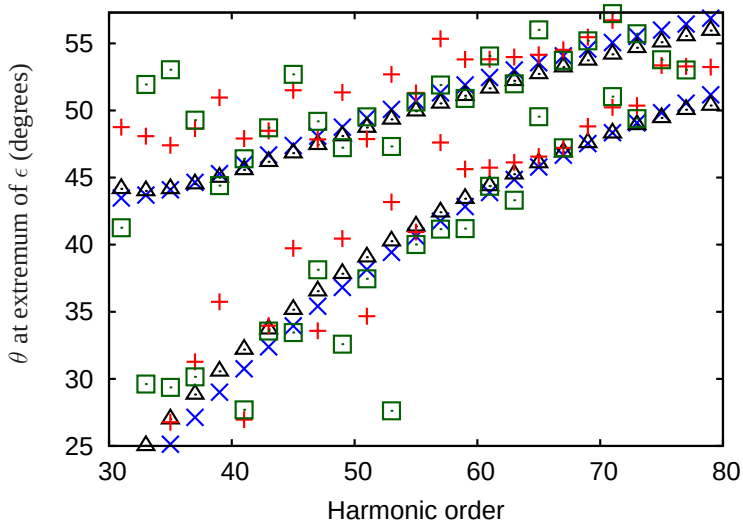

Figure 3.16: (Color online) Alignment angles for extrema from Fig. 3.15. Same wave packets and pulses as in Fig. 3.15.

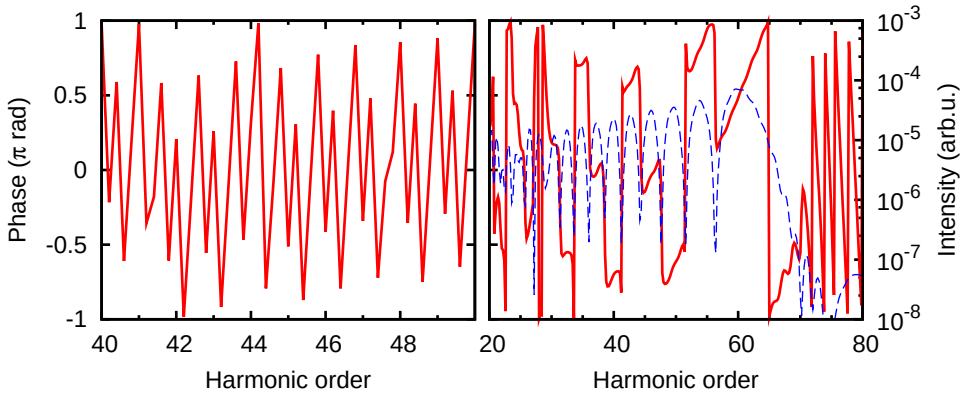

Figure 3.17: (Color online) The red lines represent the phase of the emitted harmonics polarized along the x-direction. The left graph is the rough numerical result and the right graph is after applying Eq. (3.9). The blue line is the harmonic intensity polarized in the x-direction. Note the difference in harmonic range between the graphs.

Here $\mathbf{\Phi}_\alpha(\omega)$ is the 'internal' phase of $\boldsymbol{\alpha}(\omega)$, i.e., the part of $\arg(\boldsymbol{\alpha}(\omega))$ that does not depend on the time reference.

We attempt to remove the numerical time-translation phase $\mathbf{a}$ at least for the x-direction by the following procedure. We search for a' that minimizes the error

$$T(a') = \sum_i |\Phi_{\alpha_x}(\omega_i) - \Phi_{\alpha_x}(\omega_{i-1})| \,. \tag{3.8}$$

Here the sum runs over all numerical data points up to the semi-classical cutoff and we need to take into account that the phase is defined modulo 2π. The method is motivated by the fact that experimentally a quadratic dependence of the harmonic phase on the frequency is observed (see e.g. Boutu et al. [11]), whereas numerically typically wild oscillations are seen. Therefore we assume that for a' that minimizes $T(a')$ in Eq. (3.8), we have that $a_x = a'$. We find a' numerically using a bisect algorithm. Then we (partially) remove the time-translation phase from the numerical results using

$$\boldsymbol{\alpha}(\omega) \to \boldsymbol{\alpha}'(\omega) = \boldsymbol{\alpha}(\omega) e^{-i\omega a'} . \tag{3.9}$$

In Fig. 3.17 we plot the harmonic phase for 2D H_2^+ with $I_p = 30.2$ eV aligned parallel to the laser polarization direction (see section 3.1). We use a laser intensity of $I = 5 \times 10^{14}$ W/cm^2 and a laser wavelength of $\lambda = 780$ nm. The pulse is the three-cycle $\sin^2$-pulse from section 3.1. On the left we plot the numerical harmonic phase for a small frequency range, and on the right we plot the harmonic phase for a much broader frequency range after applying $a' = 1.39T$ according to Eq. (3.9). Here T is the laser period. The plots show that one can largely remove the artificial time-translation phase from the numerical calculation. More information on the effects of the time-translation phase on molecular orbital tomography can be found in section 4.2. The algorithm is not used for the molecular-orbital-tomography simulations presented in chapter 4.

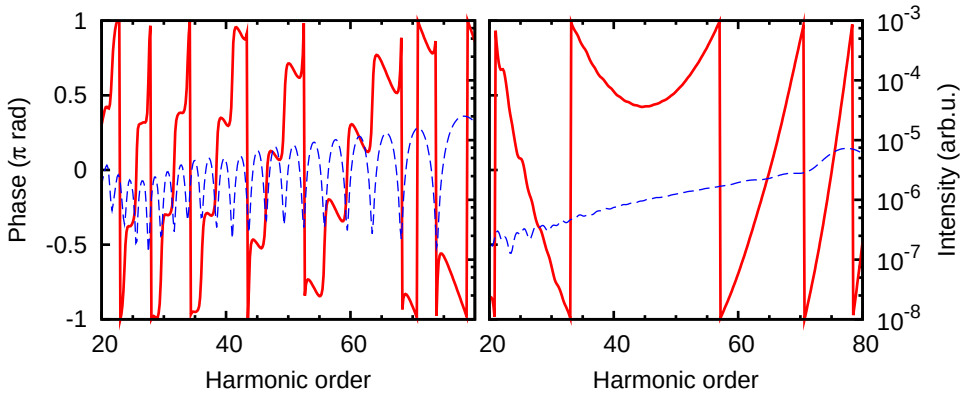

Figure 3.18: (Color online) Same as the right graph of Fig. 3.17 for a sinusoidal pulse with $T_\alpha = 1.182T$ (left) or $T_\alpha = 0.95T$ (right).

Interestingly, on top of a relatively flat background there are some jumps of almost-π magnitude present in Fig. 3.17. The blue line in the same graph shows the harmonic spectrum and we observe that the jumps coincide with minima in the spectrum. These minima are caused by the interference of short and long trajectories. Because the contributions of the two families of trajectories have unequal amplitudes, the observed jump is smaller than π. To confirm that the jumps in the harmonic phase of the translated spectrum are due to interference between short and long trajectories, we employ one of the artificial pulses from section 3.1.1.2; in Fig. 3.18 we plot the harmonic phase and harmonic intensity in the x-direction for a sinusoidal pulse with a flat envelope for which the dipole acceleration is set to 0 after either $T_\alpha = 1.182T$ (left) or $T_\alpha = 0.95T$ (right), giving rise to a single set of short and long trajectories, and a single set of short trajectories contributing to the spectrum, respectively. In case $T_\alpha = 1.182T$, the regular interference between the short and long trajectories becomes the dominant feature of both the harmonic intensity and phase. The phase jumps at the harmonic minima become noticeably smaller with increasing harmonic order. With the long trajectories removed ($T_\alpha = 0.95T$), the harmonic spectrum becomes structureless and the phase jumps disappear. The harmonic phase initially has a negative slope and at the high end of the spectrum a rapid positive slope, i.e., a substantial second derivative with respect to the harmonic frequency exists, representing the harmonic chirp of the short trajectories.

In Fig. 3.19 we consider the harmonic phase of a 44-cycle trapezoidal pulse with two-cycle ramps and the same wavelength and intensity as before. In this case, many half-cycles contribute to the harmonic emission and all harmonics are emitted at many different times. Therefore it no longer makes sense to talk about a central point in time at which the emission occurs and we do not perform the time translation as given by Eq. (3.9). The repetitive character of the harmonic emission combined with the gerade symmetry of the H_2^+ molecule gives rise to harmonic emission at odd harmonic orders and vanishing intensity at other frequencies (see section 2.2.1). In Fig. 3.19 the apparent completely chaotic behavior of the phase and the concentration of the harmonic intensity around the harmonic peaks are clearly visible.

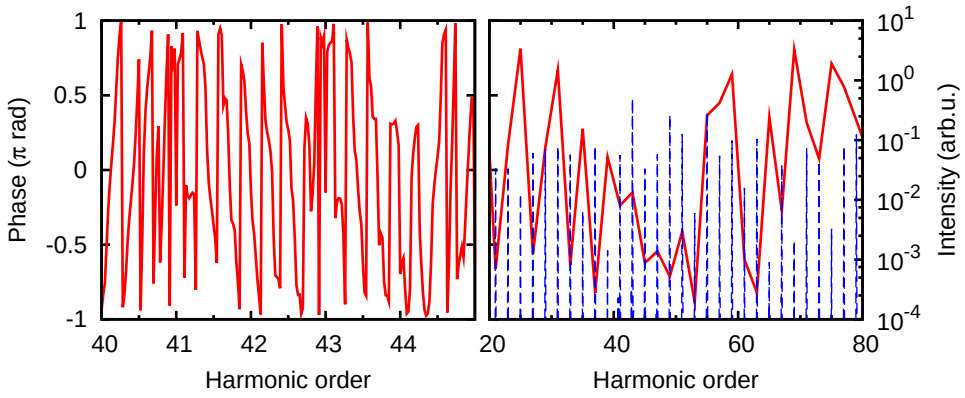

Figure 3.19: (Color online) Same as the left graph of Fig. 3.17 (no time translation) for a 44-cycle trapezoidal pulse. In the left graph all data points are shown, in the right graph only the data points exactly at the odd harmonics are shown. Note the difference in harmonic range between the graphs.

Since the odd harmonic peaks form spectrally and partially temporally separated contributions to the harmonic spectrum and associated attosecond pulse train, it makes sense to compare their individual contributions. In the left graph of Fig. 3.20 we plot the harmonic phase difference between each odd harmonic peak ω and its respective lower-lying peak $\omega - 2\omega_L$, where ω_L is the fundamental laser frequency. Because the behavior of two adjacent odd harmonic peaks is very similar, the resulting plot is a lot less chaotic than the right graph of Fig. 3.19. For all data points in the neighborhood of several odd harmonic peaks we plot the phase difference with the corresponding data points at a $2\omega_L$-lower frequency in the right graph of Fig. 3.20. The data points are spectrally separated by $\simeq 0.022\omega_L$. We observe that in the vicinity of the odd harmonics all curves can be quite well approximated by a slightly sloped linear relationship. This reflects that the harmonic phase behaves very similarly around all odd harmonic peaks, underlining the fact that all harmonic peaks underly roughly the same physical process. The slopes of the curves reflect the slight emission-time differences between the harmonics. Since many trajectories contribute to each harmonic, and because the harmonic emission is not centered around $t = 0$, the emission time as a function of harmonic does not follow the simple behavior displayed in the right graph of Fig. 3.18.

3.3 Harmonic phases from two close-lying states

To study the high-harmonic generation process, it will prove interesting to study the harmonics generated by two almost degenerate states. Since for our numerical simulations we are restricted to one-electron systems and we wish to study HHG in the tunneling regime, we resort to a very artificial potential to obtain two deep- and close-lying states. The potential is best described as extended H_2^+ with $R = 14$ a.u. and two modifications; firstly, at the origin we add a potential peak to separate the two lobes. Since this strongly reduces the quantum-mechanical overlap between the two atomic lobes of H_2^+, the gerade ground and ungerade first excited state

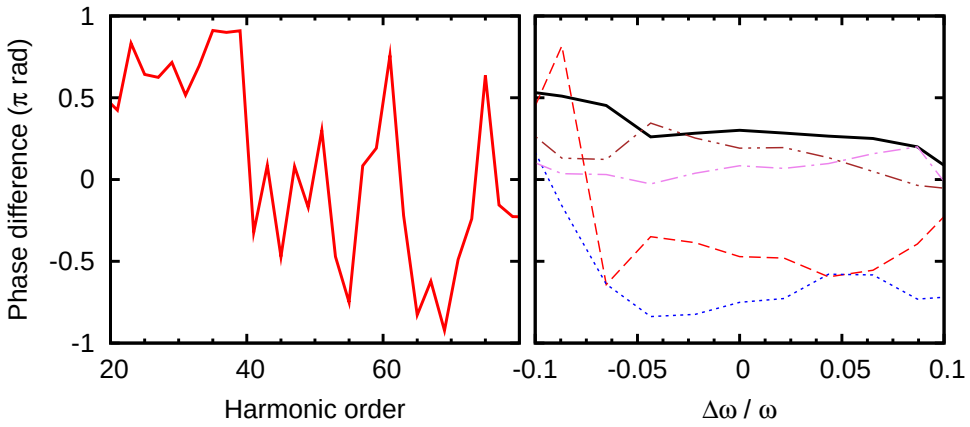

Figure 3.20: (Color online) Harmonic phase differences for the pulse from Fig. 3.19. From the harmonic phase at frequency ω we subtracted the harmonic phase at $\omega - 2\omega_L$. The left graph contains data points at the odd harmonic orders, the right graph shows the area around the harmonic peak for harmonic orders 51 (black solid line), 53 (red dashed line), 55 (blue dotted line), 57 (violet dot-dashed line), and 59 (brown dot-dot-dashed line).

are almost degenerate. Secondly, we add a ring-like potential barrier around the molecule to prevent depletion during the pulse. We consider linearly polarized laser light aligned along the internuclear axis. The potential is given by

$$V(\mathbf{r}) = -\frac{1}{\sqrt{(\mathbf{r}-\frac{\mathbf{R}}{2})^2+a^2}} - \frac{1}{\sqrt{(\mathbf{r}+\frac{\mathbf{R}}{2})^2+a^2}} + b_c e^{-(|\mathbf{r}|-b_r)^2/b_w^2} + p_c e^{-(x^2+0.01y^2)/p_w^2}, \tag{3.10}$$

with $a^2 = 0.5$, peak parameters $p_c = 2.0$, $p_w = 4$ and $b_c = 0.7$ and barrier parameters $b_r = 14$, and $b_w = 1.5$. The ground ($n = 0$) and first excited ($n = 1$) state energies are both -13.57 eV with $\frac{E_1 - E_0}{|E_0|} < 10^{-8}$. For the numerical calculation we used $I = 1.5 \times 10^{14}$ W/cm^2, $\lambda = 2000$ nm and the three-cycle sin^2-pulse with $\phi_{\mathrm{CEP}} = 1.25\pi$. In Fig. 3.21 we plot the potential and in Fig. 3.22 we show a cut through the potential at $y = 0$. Also indicated in this plot is the situation at the maximum of the electric field.

In Fig. 3.23 we plot the phase difference between the two close-lying state for harmonics polarized along the x-direction. We also show the Fourier transforms of the two orbitals and the harmonic frequencies corresponding to I_p, and to V_0, the maximum of the potential peak at $x = y = 0$. For low harmonic energies, both at the tunneling step and the recombination step V_0 is too high to overcome, and the $n = 0$- and $n = 1$-states give rise to identical spectra as there is no interference possible between the lobes. This is an illustration of the fact that the continuum wave packet carries the phase of the ionizing lobe. At recombination the harmonic phase is determined by the phase difference between the continuum and bound states, which is equal for the two close-lying states. Above harmonic 80, where the recombining electron has enough energy to overcome the V_0, interferences can occur at the recombination step. The phase difference becomes quite chaotic there, but some jumps observable seem to correspond to jumps in the Fourier transforms of the individual

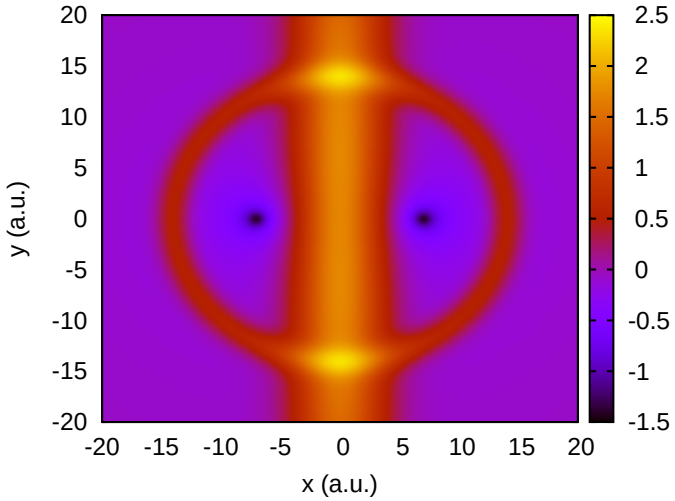

Figure 3.21: (Color online) Density plot of the potential used in section 3.3.

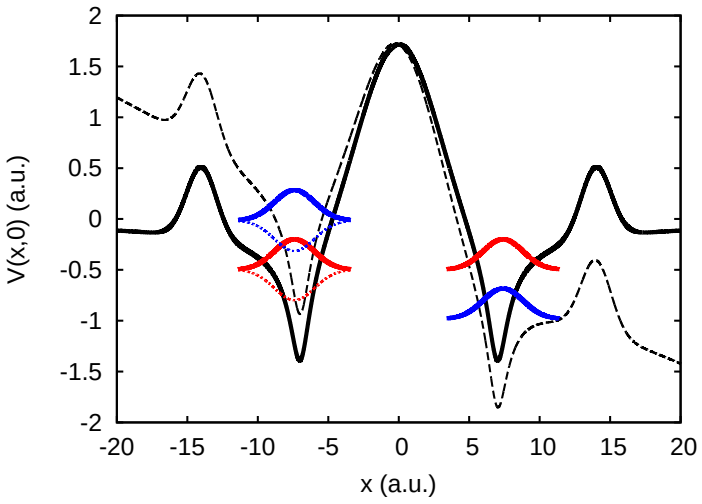

Figure 3.22: (Color online) Cut through the potential at $y = 0$ for the laser-free situation (black solid line) and at the maximum of the electric field (black dashed line). Schematically indicated are also the two lobes of the wave function in both situations; for the laser-free situation with red lines, at the peak of the electric field with blue lines, the dotted lines indicate the lobe for the $n = 1$-state.

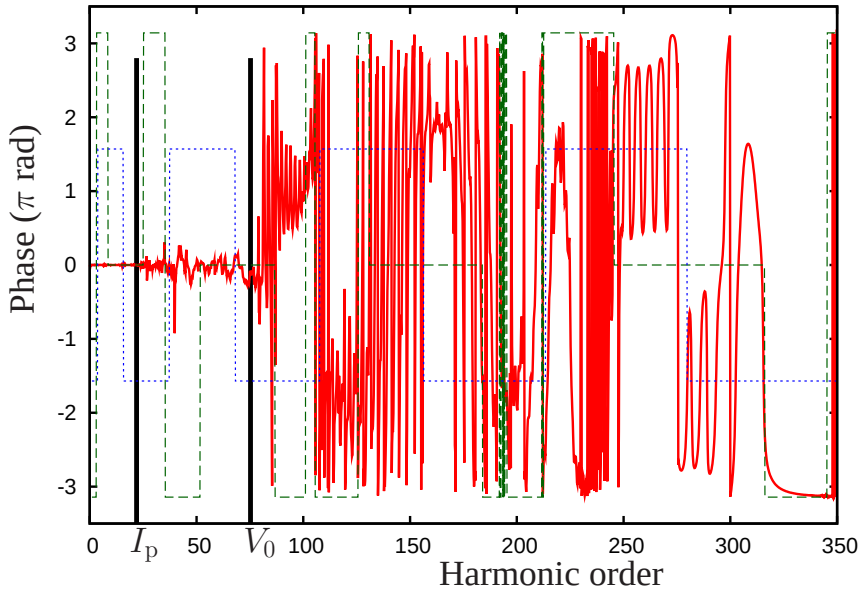

Figure 3.23: (Color online) Harmonic phase difference for the two close-lying states as a function of harmonic order. The green dashed and blue dotted lines are the Fourier transforms of the $n = 0$ and $n = 1$ states, respectively.

states.

3.4 Time-frequency analysis

Using the method developed by our former group member Ciprian Chirilă we analyze the temporal characteristics of the HHG process from our numerical results (Chirilă et al. [20]). In short, instead of performing a Fourier transform to obtain the harmonic spectrum from $\langle \boldsymbol{\alpha}(t) \rangle$, we perform a Gabor transform (Gabor [40]) to obtain time-frequency information. We replace Eq. (2.2a) with

$$\boldsymbol{\alpha}_G(\omega, t) = \int \langle \boldsymbol{\alpha}(t') \rangle \frac{\exp(-(t'-t)^2/2\sigma^2)}{\sigma\sqrt{2\pi}} e^{i\omega t'} dt'. \tag{3.11}$$

We use here $\sigma = 1/(3\omega_L)$, with ω_L being the central laser frequency. The parameter σ sets the balance between the resolutions in the temporal and frequency domains. In the limit $\sigma \to \infty$, all the temporal information is lost, and the Fourier transform is recovered up to a prefactor that depends on σ.

Using Eq. (3.11) one obtains the quantum-mechanical emission-time distribution for all harmonic orders. If we take the maxima of $|\boldsymbol{\alpha}_G(\omega, t)|$ as a function of t for different ω, we obtain the classical emission times (see Chirilă et al. [20]). In Fig. 3.24 we plot the classical emission times for different alignment angles of the 2D H_2^+ model of section 3.1. The intensity is $I = 5 \times 10^{14}$ W/cm^2 with $\lambda = 800$ nm. For plot '(a)' we use a pulse with eight cycles and a trapezoidal envelope with ramps of two cycles. We perform the analysis on trajectories that are born in the first

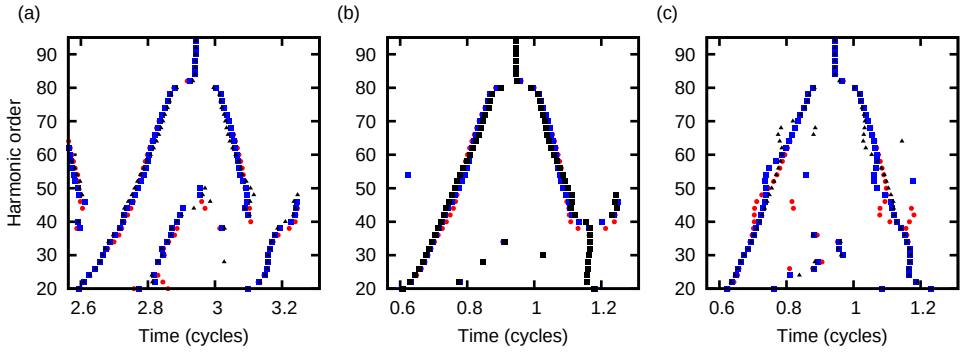

Figure 3.24: (Color online) Harmonic-order emitted as a function of time for 2D H_2^+. Red circles are for $\theta = 40°$, blue squares are for $\theta = 45°$ and black triangles are for $\theta = 50°$. (a) a standard laser pulse, (b) a ramp-less pulse and (c) additionally has trajectories from later half-cycles suppressed.

half-cycle of the plateau. The short (left branch) and long (right branch) trajectories are clearly visible. The experimental parameters are such that the two-center interference minimum is expected to move through the plateau. At the interference minimum, we expect an emission-time shift because of the relationship between the harmonic phase and the emission time t_e

$$t_e = \frac{\partial \Phi}{\partial \omega}, \tag{3.12}$$

where Φ is the harmonic phase (Chirilă et al. [20]). The above relationship follows from the Fourier-transform property in the footnote on page 37. Such an emission-time shift was also observed experimentally for CO_2 (Boutu et al. [11]).

In plot '(a)' we can observe the emission-time shift move along the plateau as a function of θ, but not very clearly. The reason is that there are many processes going on in Fig. 3.24a that obscure the view. We show here that we can use some of the ideas of section 3.1.1.2 to clean the picture. In plot '(b)' we use a laser pulse that does not have a ramp-on, i.e., the electric field starts with the full intensity. This way returns from trajectories that started during the ramp-on are removed. As a result, the short and long trajectories stand out better in the plot. Also we can now observe the interference minimum shift along the plateau much clearer for the short trajectories. In plot '(c)' we turn off the laser pulse in the inner region after the first half-cycle, i.e., we set $T_1 = 0.5T$ in Eq. (3.6). This additionally suppresses trajectories born during the second half-cycle. Some of these can interfere with long trajectories born during the first half-cycle (see section 3.1.1.2). The features of the short and long trajectories stand out even more now from an almost zero background as most of the other processes are suppressed. As a result, we can see the two-center interference minimum move along the plateau very clearly for both the short and long trajectories in Fig. 3.24c.

Chapter 4

Molecular orbital tomography

This chapter is devoted to molecular orbital tomography, i.e., the most extreme form of molecular imaging. It was introduced in December 2004 by the Corkum group at the National Research Council of Canada (Itatani et al. [52]). Instead of inferring molecular characteristics from HHG spectra as we have occupied ourselves with in chapter 3, in molecular orbital tomography—also referred to as molecular tomography or orbital tomography—we image the full (one-electron) electronic wave function with the help of HHG spectra. The method was shown to work for N_2 by (Itatani et al. [52]) using *a priori* information about the harmonic phases. The experiment for N_2 has been repeated using measured harmonic phases by (Haessler et al. [46]). At the moment it is unclear whether the tomographic reconstruction works for CO_2 (Haessler [45]). So far no experimental reconstructions for other molecules have been reported.

We ask the reader to view the density plots in this chapter in the color version of this thesis. The differences between the orbitals are a lot clearer in that version.

4.1 Derivation

4.1.1 Length form reconstruction

For an orientation θ of the bound state $\psi_{0,\theta}(\mathbf{r})$ we consider the Fourier elements

$$\mathbf{d}_\theta[\omega(k)] \equiv \iint \psi_{0,\theta}(\mathbf{r})\mathbf{r}e^{-ikx}d^2\mathbf{r} \tag{4.1}$$

inside the definition of $\mathbf{D}_\theta[\omega(k)]$ for positive harmonic frequencies and negative momentum of the returning electron in Eq. (2.23). In other words, we focus on the case that $a(k) = 0$ for $k > 0$ to allow for inversion of Eq. (2.21b). Here $\omega(k)$ is the harmonic frequency corresponding to return momentum k. Since we are interested in recovering the molecular orbital from 1D Fourier elements, it makes sense to consider k and not ω the independent variable in the following. Since we consider only returns with negative momentum, there exists a one-to-one mapping between

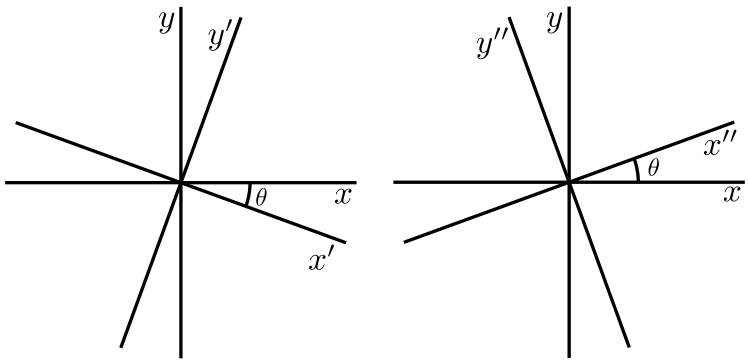

Figure 4.1: Coordinate frames.

k and ω. Through a dispersion relationship such as $k(\omega) = \sqrt{2\omega}$ we can go back to a frequency-based picture in the end.

Using rotations given by (see Fig. 4.1)

$$A_\theta = \begin{pmatrix} \cos\theta & -\sin\theta \\ \sin\theta & \cos\theta \end{pmatrix} \tag{4.2}$$

$$A_\theta{}^{-1} = \begin{pmatrix} \cos\theta & \sin\theta \\ -\sin\theta & \cos\theta \end{pmatrix} \tag{4.3}$$

$$\mathbf{r}'_\theta = \begin{pmatrix} x' \\ y' \end{pmatrix} = A_\theta \begin{pmatrix} x \\ y \end{pmatrix} = \begin{pmatrix} x\cos\theta - y\sin\theta \\ x\sin\theta + y\cos\theta \end{pmatrix} \tag{4.4}$$

$$\mathbf{r}''_\theta = \begin{pmatrix} x'' \\ y'' \end{pmatrix} = A_\theta{}^{-1} \begin{pmatrix} x \\ y \end{pmatrix} = \begin{pmatrix} x\cos\theta + y\sin\theta \\ -x\sin\theta + y\cos\theta \end{pmatrix} \tag{4.5}$$

we define

$$\psi_{0,\theta}(\mathbf{r}) = \psi_0(A_\theta{}^{-1}\mathbf{r}) = \psi_0(x\cos\theta + y\sin\theta, -x\sin\theta + y\cos\theta) \tag{4.6}$$

and

$$\mathbf{d}_\theta[\omega(k)] = \iint \psi_0(\mathbf{r})\mathbf{r}'_\theta(\mathbf{r})e^{-ik(x\cos\theta - y\sin\theta)}d^2\mathbf{r}. \tag{4.7}$$

Now define the more general Fourier transform

$$\mathbf{g}(k_1,k_2) = \begin{pmatrix} g_1(k_1,k_2) \\ g_2(k_1,k_2) \end{pmatrix} = \iint \psi_0(\mathbf{r})\mathbf{r}e^{-i(k_1x+k_2y)}d^2\mathbf{r}, \tag{4.8}$$

of which both components can be inverted to reach

$$\psi_0(\mathbf{r})\,\mathbf{r} = \frac{1}{(2\pi)^2}\iint \mathbf{g}(k_1,k_2)e^{i(k_1x+k_2y)}dk_1dk_2. \tag{4.9}$$

Note that $\mathbf{d}_0[\omega(k)] = \mathbf{g}(k,0)$. This is also predicted by the Fourier Slice Theorem (Lichtenbelt [73]), which states that a Fourier transform of a 1D projection of a multidimensional function is the same as a line through a two-dimensional Fourier

transform of that function in the same direction. We write $k_1 = k\cos\vartheta$ and $k_2 = -k\sin\vartheta$. Next we change the integration variables to k, ϑ with

$$dk_1 dk_2 = \left|\det\left(\begin{bmatrix}\frac{dk_1}{dk} & \frac{dk_1}{d\vartheta}\\ \frac{dk_2}{dk} & \frac{dk_2}{d\vartheta}\end{bmatrix}\right)\right| dkd\vartheta = kdkd\vartheta, \tag{4.10}$$

where $k \geq 0$ and $\vartheta\,\epsilon\,[0, 2\pi)$. Eq. (4.9) then becomes

$$\psi_0(\mathbf{r})\mathbf{r} = \frac{1}{(2\pi)^2}\int_0^{2\pi}\int_0^{\infty}\mathbf{g}(k\cos\vartheta, -k\sin\vartheta)e^{ik(x\cos\vartheta - y\sin\vartheta)}kdkd\vartheta. \tag{4.11}$$

From now the integration boundaries will be left out for ease of notation. We can insert the following equality

$$\begin{aligned} {A_\theta}^{-1}\mathbf{d}_\theta[\omega(k)] &= \begin{pmatrix} \iint \psi_0(\mathbf{r})[\cos\theta(x\cos\theta - y\sin\theta) \\ +\sin\theta(x\sin\theta + y\cos\theta)]e^{-ik(x\cos\theta - y\sin\theta)}d^2\mathbf{r} \\ \\ \iint \psi_0(\mathbf{r})[-\sin\theta(x\cos\theta - y\sin\theta) \\ +\cos\theta(x\sin\theta + y\cos\theta)]e^{-ik(x\cos\theta - y\sin\theta)}d^2\mathbf{r} \end{pmatrix} \\ &= \begin{pmatrix} \iint \psi_0(\mathbf{r})xe^{-ik(x\cos\theta - y\sin\theta)}d^2\mathbf{r} \\ \iint \psi_0(\mathbf{r})ye^{-ik(x\cos\theta - y\sin\theta)}d^2\mathbf{r} \end{pmatrix} \\ &= \mathbf{g}(k\cos\theta, -k\sin\theta), \end{aligned} \tag{4.12}$$

into this formula to reach

$$\psi_0(\mathbf{r})\mathbf{r} = \frac{1}{(2\pi)^2}\iint {A_\vartheta}^{-1}\mathbf{d}_\vartheta[\omega(k)]e^{ik(x\cos\vartheta - y\sin\vartheta)}kdkd\vartheta. \tag{4.13}$$

In the experimental implementation (Itatani et al. [52]), the molecules are aligned along directions within the xy-plane, with an angle θ between the molecular axis and the electric field. Therefore we replace $\vartheta \to \theta$ and we rewrite Eq. (4.13) into two distinct equalities for $\psi_0(\mathbf{r})$ as

$$\psi_0(\mathbf{r}) = \frac{1}{x}\frac{1}{(2\pi)^2}\iint (d_{\theta,x}[\omega(k)]\cos\theta + d_{\theta,y}[\omega(k)]\sin\theta)e^{ik(x\cos\theta - y\sin\theta)}kdkd\theta, \tag{4.14a}$$

$$\psi_0(\mathbf{r}) = \frac{1}{y}\frac{1}{(2\pi)^2}\iint (-d_{\theta,x}[\omega(k)]\sin\theta + d_{\theta,y}[\omega(k)]\cos\theta)e^{ik(x\cos\theta - y\sin\theta)}kdkd\theta. \tag{4.14b}$$

It is expected that a good estimation for ψ_0 can then be attained using both equalities to obtain

$$\begin{aligned} \psi_0(\mathbf{r}) = \frac{1}{2(2\pi)^2}\Bigg\{ &\frac{1}{x}\iint (d_{\theta,x}[\omega(k)]\cos\theta + d_{\theta,y}[\omega(k)]\sin\theta)e^{ik(x\cos\theta - y\sin\theta)}kdkd\theta \\ &+ \frac{1}{y}\iint (-d_{\theta,x}[\omega(k)]\sin\theta + d_{\theta,y}[\omega(k)]\cos\theta)e^{ik(x\cos\theta - y\sin\theta)}kdkd\theta\Bigg\}. \end{aligned} \tag{4.15}$$

Finally, we convert the above expression back to frequency space. This is the more natural choice as in a HHG experiment photon energies are being measured. Let us consider the general dispersion relationship

$$k(\omega) = \sqrt{2(\omega - c_{\mathrm{I}}(\omega) I_{\mathrm{p}})}, \tag{4.16}$$

where $c_{\mathrm{I}}(\omega)$ is an arbitrary function of ω. A change of integration variables gives $kdk = k\frac{dk(\omega)}{d\omega}d\omega = \left(1 - \frac{dc_{\mathrm{I}}(\omega)}{d\omega} I_{\mathrm{p}}\right) d\omega$. Therefore the reconstruction equation becomes

$$\begin{aligned}\psi_0(\mathbf{r}) = \frac{1}{2(2\pi)^2}\Bigg\{ & \frac{1}{x}\iint (d_{\theta,x}(\omega)\cos\theta + d_{\theta,y}(\omega)\sin\theta) \\ & \times e^{ik(\omega)(x\cos\theta - y\sin\theta)} \left(1 - \frac{dc_{\mathrm{I}}(\omega)}{d\omega} I_{\mathrm{p}}\right) d\omega d\theta \\ & + \frac{1}{y}\iint (-d_{\theta,x}(\omega)\sin\theta + d_{\theta,y}(\omega)\cos\theta) \\ & \times e^{ik(\omega)(x\cos\theta - y\sin\theta)} \left(1 - \frac{dc_{\mathrm{I}}(\omega)}{d\omega} I_{\mathrm{p}}\right) d\omega d\theta \Bigg\}.\end{aligned} \tag{4.17}$$

Energy conservation for the returning electron in the Lewenstein model gives $c_{\mathrm{I}}(\omega) = 1$. On the other hand, as explained at the end in section 2.3, molecular characteristics are often derived from HHG spectra using $c_{\mathrm{I}}(\omega) = 0$ (Itatani et al. [52]; Lein et al. [67]). Typically a constant $c_{\mathrm{I}}(\omega)$ is used and $\frac{dc_{\mathrm{I}}(\omega)}{d\omega}$ vanishes. In that case the reconstruction equation simplifies to

$$\begin{aligned}\psi_0(\mathbf{r}) = \frac{1}{2(2\pi)^2}\Bigg\{ & \frac{1}{x}\iint (d_{\theta,x}(\omega)\cos\theta + d_{\theta,y}(\omega)\sin\theta) e^{ik(\omega)(x\cos\theta - y\sin\theta)} d\omega d\theta \\ & + \frac{1}{y}\iint (-d_{\theta,x}(\omega)\sin\theta + d_{\theta,y}(\omega)\cos\theta) e^{ik(\omega)(x\cos\theta - y\sin\theta)} d\omega d\theta \Bigg\}.\end{aligned} \tag{4.18}$$

Compared to the original work (Itatani et al. [52]), our additional factor of $\frac{1}{2}$ can be related to their summation of θ only running from 0 to π. This is a simplification for symmetric orbitals. The fact that they only use the real part of their reconstructed orbital is probably because they lack phase information in their measurements, so this was done in an attempt to reduce the reconstruction error. When $\mathbf{d}_\theta$ is known, and the original orbital is real, taking the real part in the reconstruction has no effect. Apart from these observations there still seems to be a sign error in the exponent of the reconstruction equation in (Itatani et al. [52]).

Experimentally both the amplitude and the phase of $\mathbf{D}_\theta(\omega)$ can be obtained from measuring the intensities and relative phases of the high harmonics, although in (Itatani et al. [52]) only the intensities were measured. They solved this problem by adding phase information from *a priori* considerations. There are two unknowns in our equation for $\mathbf{D}_\theta(\omega)$, namely $a[-k(\omega)]$ and $\psi_{0,\theta}(\mathbf{r})$. The idea is to solve this problem by looking at an atomic system for which $\psi_0^{(a)}(\mathbf{r})$ is known and $a^{(a)}[k(\omega)]$ is very similar to $a[k(\omega)]$. If the atomic and molecular system share the same ionization potential, and the same intensity-dependent ionization probability, the first step of

the three step model (ionization) is similar, as the systems respond similarly to strong fields. The saddle point through which the electrons tunnel acts as a spatial filter, so the second step (propagation in the laser field) is also the same for the two systems. Therefore the atomic system can be used to determine $a[-k(\omega)]$ (Levesque et al. [70]), after which $\psi_0(\mathbf{r})$ can be determined. It has been pointed out that the polarizability of the system plays an important role in the multi-photon regime, and therefore the size of the system influences the intensity-dependent ionization rate if the Keldysh parameter (Eq. (2.6)) is not much smaller than 1 (Chin and Golovinski [18]; Liang et al. [72]). Therefore extra care should be given if the Keldysh parameter $\gamma \sim 1$.

Some experimental schemes to determine the harmonic phase might not be able to distinguish between $\mathbf{D}^*(\omega)$ and $\mathbf{D}(\omega)$ as they cannot measure the sign of a phase difference. In case the orbital is accidently reconstructed using $\mathbf{D}^*(\omega)$ instead of $\mathbf{D}(\omega)$, the consequences depend on the phase of the Fourier components of the reference atom. If the Fourier transform of the reference atom is purely real or imaginary, the reconstructed orbital is rotated by 180° and complex conjugated. On the other hand, if the phase of the reference atom shows more complex behavior, i.e., if the reference atom is not symmetric, additional distortions to the reconstructed orbital result.

4.1.2 Velocity form reconstruction

Instead of inverting Eq. (2.23) to obtain a reconstruction formula in length form, we can also invert Eq. (2.30). Let us consider the Fourier elements

$$p_\theta[\omega(k)] \equiv \iint \psi_{0,\theta}(\mathbf{r}) e^{-ikx} d^2\mathbf{r} \tag{4.19}$$

in that equation. We define the generalized Fourier transform

$$l(k_1, k_2) = \iint \psi_0(\mathbf{r}) e^{-i(k_1 x + k_2 y)} d^2\mathbf{r}, \tag{4.20}$$

for which

$$p_\theta[\omega(k)] = l(k\cos\theta, -k\sin\theta) = \frac{1}{2\pi\, a'(k)} P_{\theta,x}[\omega(k)]. \tag{4.21}$$

The inverse of this transform is

$$\psi_0(\mathbf{r}) = \frac{1}{(2\pi)^2} \iint l(k_1, k_2) e^{i(k_1 x + k_2 y)} dk_1 dk_2. \tag{4.22}$$

We change the integration variables $dk_1 dk_2 \rightarrow k dk d\theta$, where $k_1 = k\cos\theta$ and $k_2 = -k\sin\theta$, to arrive at

$$\begin{aligned} \psi_0(\mathbf{r}) &= \frac{1}{(2\pi)^2} \iint k\, p_\theta[\omega(k)] e^{ik(x\cos\theta - y\sin\theta)} dk d\theta \\ &= \frac{1}{(2\pi)^2} \iint p_\theta(\omega) e^{ik(\omega)(x\cos\theta - y\sin\theta)} d\omega d\theta. \end{aligned} \tag{4.23}$$

For the last equality we assumed a simple dispersion relationship with a constant $c_I(\omega)$.

4.2 Phase of reconstructed orbital

In this section we look at the phase with which the orbital is reconstructed in a numerical simulation of the molecular-orbital-tomography scheme. The conclusion is derived for length-form reconstructions, but equally valid for velocity-form reconstructions. The simulation starts with the determination of the reference quantities $\mathbf{D}^{(a)}(\omega)$ and $\mathbf{d}^{(a)}(\omega)$. The Fourier-transformed dipole moment $\mathbf{D}^{(a)}(\omega)$ is numerically most reliably calculated from the dipole acceleration, but effectively calculated according to Eq. (2.14a) as

$$\mathbf{D}^{(a)}(\omega) = \int \langle \mathbf{d}^{(a)}(t) \rangle e^{i\omega t} dt. \tag{4.24}$$

Since the harmonic emission does not occur at $t = 0$, but at some different point in time, $\mathbf{D}^{(a)}(\omega)$ will acquire a complex phase factor that represents the time translation (see section 3.2). Assuming that the emission in the directions x and y is centered around $t = a_{1_{x,y}}$, respectively, we numerically recover $\mathbf{D}^{(a)}(\omega)$ with the phase

$$\arg\left(\mathbf{D}^{(a)}(\omega)\right) = \mathbf{\Phi}_D^{(a)}(\omega) + \mathbf{a}_1\,\omega, \tag{4.25}$$

where $\mathbf{\Phi}_D^{(a)}(\omega)$ is the 'internal' phase of $\mathbf{D}^{(a)}(\omega)$, i.e., the part of $\arg\left(\mathbf{D}^{(a)}(\omega)\right)$ that does not depend on the time reference. It incorporates the physically relevant phase jumps between the harmonics, including the chirp of the emitted radiation. On the other side, the reconstruction matrix element $\mathbf{d}^{(a)}(\omega)$ has the phase

$$\arg\left(\mathbf{d}^{(a)}(\omega)\right) = \mathbf{\Phi}_d^{(a)}(\omega) + c_{\mathrm{F}}\mathbf{I}, \tag{4.26}$$

where $\mathbf{\Phi}_d^{(a)}(\omega)$ contains the physically relevant phase jumps between the momentum components, $\mathbf{I}$ is the two-dimensional identity matrix and c_{F} with $0 \leq c_{\mathrm{F}} < 2\pi$ represents the arbitrary phase that the reference ground state has when determining its Fourier transform. Normally $c_{\mathrm{F}} = 0$ is used, but it will prove insightful to explicitly keep c_{F}. Since the continuum wave packet is given by $(a[-k(\omega)]$ is to be understood as a linear combination in the long-pulse-symmetric-molecule case, see Eq. (2.22))

$$a[-k(\omega)] = -\frac{k(\omega) D_x^{(a)}(\omega)}{2\pi d_x^{(a)}(\omega)}, \tag{4.27}$$

its argument is given by

$$\arg\left(a[-k(\omega)]\right) = \pi + \Phi_{D_x}^{(a)}(\omega) + a_{1_x}\omega - \Phi_{d_x}^{(a)}(\omega) - c_{\mathrm{F}}. \tag{4.28}$$

Next in the tomographic scheme is the determination of the reconstruction matrix elements $\mathbf{d}_\theta^{(\mathrm{tom})}(\omega)$ as

$$\mathbf{d}_\theta^{(\mathrm{tom})}(\omega) = -\frac{k(\omega)\mathbf{D}_\theta(\omega)}{2\pi a[-k(\omega)]}, \tag{4.29}$$

where with the superscript '(tom)' we explicitly denote matrix elements as recovered by the tomographic procedure. This means that the argument of $\mathbf{d}_\theta^{(\mathrm{tom})}(\omega)$ is given

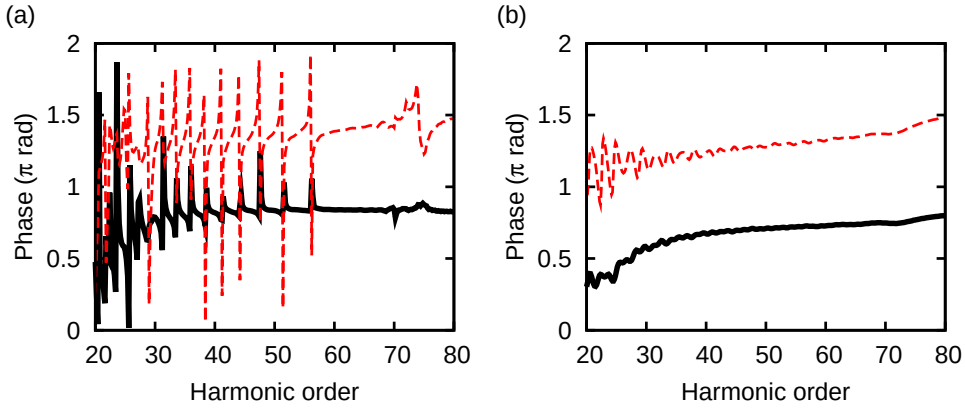

Figure 4.2: (Color online) Harmonic phase difference between H_2^+ and He^+ (solid black line), and between shielded He^+ and He^+ (red dashed line) for harmonics polarized in the x-direction; (a) using a three-cycle $\sin^2$ pulse, (b) using an artificial pulse with only short trajectories.

by

$$\arg\left(\mathbf{d}_\theta^{(\mathrm{tom})}(\omega)\right) = \pi\mathbf{I} + \mathbf{\Phi}_D(\theta,\omega) + \mathbf{a}_2(\theta)\omega - \left(\pi + \Phi_{D_x}^{(a)}(\omega) + a_{1_x}\omega - \Phi_{d_x}^{(a)}(\omega) - c_{\mathrm{F}}\right)\mathbf{I}, \tag{4.30}$$

where $\mathbf{a}_2$ is analogous to $\mathbf{a}_1$ but for the molecule. One of the main assumptions behind molecular orbital tomography is that the propagation step of the three-step model is identical for the molecule and the reference. Therefore within the three-step model the only difference between the harmonic phases is given by the recombination matrix elements, i.e.,

$$\mathbf{\Phi}_D(\theta,\omega) - \mathbf{\Phi}_d(\theta,\omega) = \mathbf{\Phi}_D^{(a)}(\omega) - \mathbf{\Phi}_d^{(a)}(\omega). \tag{4.31}$$

This means we can write

$$\arg\left(\mathbf{d}_\theta^{(\mathrm{tom})}(\omega)\right) = \mathbf{\Phi}_d(\theta,\omega) + \left(\mathbf{a}_2(\theta) - a_{1_x}\mathbf{I}\right)\omega + c\mathbf{I}. \tag{4.32}$$

The fact that $\mathbf{a}_1$ and $\mathbf{a}_2$ do not cancel out in the above expression reflects the influence of any emission time difference between the reference and molecule on the reconstructed orbital. Such an emission time difference can arise for instance due to a difference in Coulomb fields between the reference and molecule.

4.2.1 Demonstration central emission time

As a demonstration of the fact that different atoms and molecules are associated with different emission times, we plot the difference in harmonic phase in the x-direction between different atoms and molecules as a function of harmonic order in Fig. 4.2. The solid black lines are for the phase difference between 2D H_2^+ and He^+. The laser wavelength is $\lambda = 780$ nm and the laser intensity is $I = 5 \times 10^{14}$ W/cm^2. The model for H_2^+ was the same as in chapter 3; the ground state was modeled using a 2D softcore potential with softcore parameter $a^2 = 0.5$ to give an ionization

potential of 30.2 eV. He^+ was modeled using a 2D softcore potential with $Z = 2$ and $a^2 = 0.9207$ to give the same ionization potential. The red lines are for the phase difference between 'shielded' He^+ and He^+. We modeled 'shielded' He^+ using a 2D softcore potential with $Z = 1.5$ and $a^2 = 0.2952$ and $I_p = 30.2$ eV. The left plot was created using a laser pulse with a three-cycle $\sin^2$ envelope with a carrier-envelope phase of 1.25π, as was also used in chapter 3. The interference between the short and long trajectories that we also observed in section 3.1.1.2 is clearly visible here. For the right plot we use a cw-like pulse and set the dipole acceleration to 0 at $t = 0.95T$ to select only a single set of short trajectories, using the method proposed in section 3.1.1.2. This gets rid of most of the interference patterns and cleans the picture significantly.

For both plots in Fig. 4.2 the phase difference between 'shielded' He^+ and He^+ is linear in ω in the harmonic plateau, with the trajectory interference pattern superimposed for the normal pulse on the left. Since the two model systems are so similar, their harmonic spectra are very similar. This results in only a small difference in the center time of emission and therefore in a small value for $a_{2,x} - a_{1_x}$, which means the harmonic phase difference in the x-direction only has a small linear slope. Any effect from the extension of the molecule or trajectory length would be frequency-dependent. All frequency-dependent emission-time differences would show up as higher than linear orders in Fig. 4.2. As there is no higher than linear order visible for the trend of the red dashed lines, the emission time shift is apparently identical for all harmonic orders.

As far as the harmonic phase difference between H_2^+ and He^+ (black solid lines in Fig. 4.2) is concerned, a quadratic contribution to the trend does seem to appear additionally to a small linear contribution from a difference in central emission time. A probable explanation is that the difference in character between the two-center H_2^+ and the one-center He^+ has a significant influence on the propagation. The low harmonics are influenced more by the Coulombic potential during the propagation than the high harmonics. Therefore it makes sense that the low harmonics experience a larger emission time shift between H_2^+ and He^+ than the high harmonics, which is visible as the steeper curve for the low harmonics.

4.2.2 Reconstruction equation

Using the above analysis, and considering that an adapted dispersion relationship without I_p ($c_I(\omega) = 0$) was used for the reconstruction, the reconstruction equation

Eq. (4.18) becomes

$$\psi_0(\mathbf{r}) = \frac{e^{ic_\mathrm{F}}}{2(2\pi)^2}\Bigg\{\frac{1}{x}\iint (d_{\theta,x}(\omega)e^{ia_{2_x}(\theta)\frac{k^2}{2}}\cos\theta + d_{\theta,y}(\omega)e^{ia_{2_y}(\theta)\omega}\sin\theta) \times e^{-ia_{1_x}\omega}e^{ik(\omega)(x\cos\theta - y\sin\theta)}d\omega d\theta + \frac{1}{y}\iint (-d_{\theta,x}(\omega)e^{ia_{2_x}(\theta)\omega}\sin\theta + d_{\theta,y}(\omega)e^{ia_{2_y}(\theta)\omega}\cos\theta) \times e^{-ia_{1_x}\omega}e^{ik(\omega)(x\cos\theta - y\sin\theta)}d\omega d\theta\Bigg\}. \quad (4.33)$$

Here the phase of the reconstruction matrix elements $\mathbf{d}_\theta(\omega)$ is taken to incorporate only the physically relevant phase jumps between the harmonics. The above equation shows that in principle the molecular orbital is reconstructed with the same phase c_F as was used for the reference orbital. However, both errors from the determination of $\mathbf{d}_\theta$, e.g., because of the plane-wave approximation used, and the finite harmonic range available lead to errors in the reconstructed orbital. In general, these errors can make the reconstructed orbital a complex object without a well-defined single global phase. In practice, the errors can introduce a combination of small complex disturbances and an overall global phase to the reconstructed orbital.

Furthermore, the fact that the harmonic emission might occur at slightly different times for the different systems and cartesian directions might lead to an additional distortion of the reconstructed orbital in the numerical simulation of molecular orbital tomography. To the extent that $\mathbf{a}_2(\theta) \neq a_{1_x}\mathbf{I}$ for one of the two components, there is a 'chirp' of the reconstructed orbital for the orientation θ. Since $\omega = k^2/2$ in Eq. (4.33), the high momentum components are translated in space further than the low components if $\mathbf{a}_2(\theta) \neq a_{1_x}\mathbf{I}$.

Experimentalists sometimes remove the time translation phase from the recombination matrix elements (see e.g. Boutu et al. [11]). If the actual emission times are used for the reference and molecule, this can be used to circumvent the distortion from an emission time shift between the reference and molecule. However, if the three-step model is used to determine the emission time, any emission time difference between the reference and molecule will survive and the reconstructed orbital will be distorted.

4.2.3 Rotation of reconstructed orbital in complex plane

The above analysis shows that the orbital might be reconstructed with a nonzero global phase. The best guess for the orbital is therefore obtained by rotating the reconstructed orbital in the complex plane in such a way that the density in the real domain is maximized. In formula, for the rotated wave function

$$\psi_0'(\mathbf{r}) = \psi_0(\mathbf{r})e^{-i\phi}, \quad (4.34)$$

we are looking for the angle ϕ that maximizes

$$a_\mathrm{D}'(\phi) = \iint \left(\mathrm{Re}(\psi_0'(\mathbf{r}))\right)^2 d^2\mathbf{r}. \quad (4.35)$$

Simple algebra shows that the condition for an extremum of the density in the real domain is given by

$$\frac{da'_{\mathrm{D}}(\phi)}{d\phi} = (b_{\mathrm{D}} - a_{\mathrm{D}}) \sin 2\phi + 2c_{\mathrm{D}} \cos 2\phi = 0, \tag{4.36a}$$

$$a_{\mathrm{D}} = \iint (\mathrm{Re}(\psi_0(\mathbf{r})))^2 \, d^2\mathbf{r}, \tag{4.36b}$$

$$b_{\mathrm{D}} = \iint (\mathrm{Im}(\psi_0(\mathbf{r})))^2 \, d^2\mathbf{r}, \tag{4.36c}$$

$$c_{\mathrm{D}} = \iint (\mathrm{Re}(\psi_0(\mathbf{r}))\mathrm{Im}(\psi_0(\mathbf{r}))) \, d^2\mathbf{r}. \tag{4.36d}$$

This is easily solved for ϕ to obtain

$$\phi = \frac{1}{2} \arctan\left(\frac{2c_{\mathrm{D}}}{a_{\mathrm{D}} - b_{\mathrm{D}}}\right). \tag{4.37}$$

Now we need to check whether multiplying the wave function with $e^{-i\phi}$ minimizes or maximizes the density in the real domain. In the former case, we need to move the density from the imaginary domain to the real domain. The densities in the real and imaginary domains of the rotated wave function are given by, respectively,

$$a'_{\mathrm{D}} = a_{\mathrm{D}} \cos^2\phi + b_{\mathrm{D}} \sin^2\phi + c_{\mathrm{D}} \sin 2\phi, \tag{4.38a}$$

$$b'_{\mathrm{D}} = a_{\mathrm{D}} \sin^2\phi + b_{\mathrm{D}} \cos^2\phi - c_{\mathrm{D}} \sin 2\phi. \tag{4.38b}$$

If $b'_{\mathrm{D}} > a'_{\mathrm{D}}$, which simplifies to

$$(b_{\mathrm{D}} - a_{\mathrm{D}}) \cos 2\phi - 2c_{\mathrm{D}} \sin 2\phi > 0, \tag{4.39}$$

we move the density from the imaginary to the real domain by adding $\frac{\pi}{2}$ to ϕ.

In a real experiment, the molecular orbital is reconstructed with more complicated errors than just a rotation in the complex plane. The less ideal the experimental parameters (e.g., complexity of the orbital, laser wavelength and intensity), the bigger these errors are and the more they also manifest themselves as the appearance of significant density far away from the molecular core. In such a case maximizing the density in the real domain might be equivalent to maximizing the errors in the real domain, as the outer regions dominate the core region in the above procedure. Therefore sometimes it is necessary to limit the integration range in the above procedure. In that case, the orbital parameters in Eq. (4.36) become

$$a_{\mathrm{D}} = \iint_{r \le R_{\mathrm{c}}} (\mathrm{Re}(\psi_0(\mathbf{r})))^2 \, d^2\mathbf{r}, \tag{4.40a}$$

$$b_{\mathrm{D}} = \iint_{r \le R_{\mathrm{c}}} (\mathrm{Im}(\psi_0(\mathbf{r})))^2 \, d^2\mathbf{r}, \tag{4.40b}$$

$$c_{\mathrm{D}} = \iint_{r \le R_{\mathrm{c}}} (\mathrm{Re}(\psi_0(\mathbf{r}))\mathrm{Im}(\psi_0(\mathbf{r}))) \, d^2\mathbf{r}, \tag{4.40c}$$

where $r = \sqrt{x^2 + y^2}$ and R_{c} limits the range of the integration to the molecular core region and should be set equal to a couple of bohr.

4.3 Simulation

As far as possible the experimental procedure (Itatani et al. [52]) was followed. In velocity form, the procedure is as follows; firstly we calculate the continuum wave packet function $a(k)$, which acts as a container function as it is combines many different factors to form an effective plane-wave continuum decomposition. In case the laser pulse gives rise to essentially one-sided returns, as is the case for the pulses that are used in this section as will be shown in section 4.6.1, it is approximated as (see Eq. (2.30))

$$a_\theta[-k(\omega)] = \frac{P_x^{(a)}(\omega)}{2\pi\, p^{(a)}(\omega)} \sqrt{\frac{P_{\mathrm{I}}(\theta)}{P_{\mathrm{I}}^{(a)}}}, \tag{4.41}$$

where with the (a)-superscript we denote reference quantities and P_{I} is the total ionization probability, experimentally relatively easily accessible as the total solid angle- and momentum-integrated photoelectron spectrum. As a reference system we use a 2D softcore atom with a nuclear charge equal to the total nuclear charge of the molecule and the softcore parameter chosen such that its ionization potential is equal to that of the molecule. Secondly we determine the reconstruction matrix elements as

$$p_\theta(\omega) = \frac{P_{\theta,x}(\omega)}{2\pi\, a_\theta[-k(\omega)]}. \tag{4.42}$$

Finally the molecular orbital is reconstructed using Eq. (4.23).

The reconstruction works best if many different orientations N_θ are used, as otherwise artifacts in the reconstructed orbital can arise. In formula, we use $N_\theta = \frac{100}{\min(\Delta x, \Delta y)}$, where Δx, Δy are the spatial resolutions in the x- and y-directions, respectively. As an example, for a typical spatial resolution of $\Delta x = \Delta y = 0.17$ a.u. this leads to $N_\theta \simeq 600$, which is definitely on the safe side. In practice usually less angles need to be measured, as symmetries of the orbital reduce the number of independent orientations. Nonetheless, for typical laser intensities of $2-5\times10^{14}$ W/cm^2 at a wavelength of 780 nm the simulation is quite resource-intensive. Therefore numerical tomographic simulations are at the moment practical only on massively parallel machines. Because the numerical solution of the time-dependent Schrödinger equation for each orientation angle is independent, and only at the very end of the simulation we need to combine data from all the different angles to perform the reconstruction, not much communication between the different processes is needed and the simulation is highly parallelizable. Therefore no high-performance computer is needed but a cluster of normal PCs suffices.

After some initial numerical experiments, the above formula for N_θ was chosen to be on the safe side always. Usually it should be possible to reduce this number significantly without decreasing the quality of the reconstruction. It is probably also possible to calculate the harmonics for even significantly less angles, and calculate the rest by interpolation from the calculated angles. One complication for such an interpolation procedure are the strongly varying complex phases factors in any numerical HHG calculation that will partially survive in the reconstructed matrix elements, see the analysis in section 4.2. We have not experimented with such an interpolation procedure. In a recent tomographic experiment where only 8 harmonic

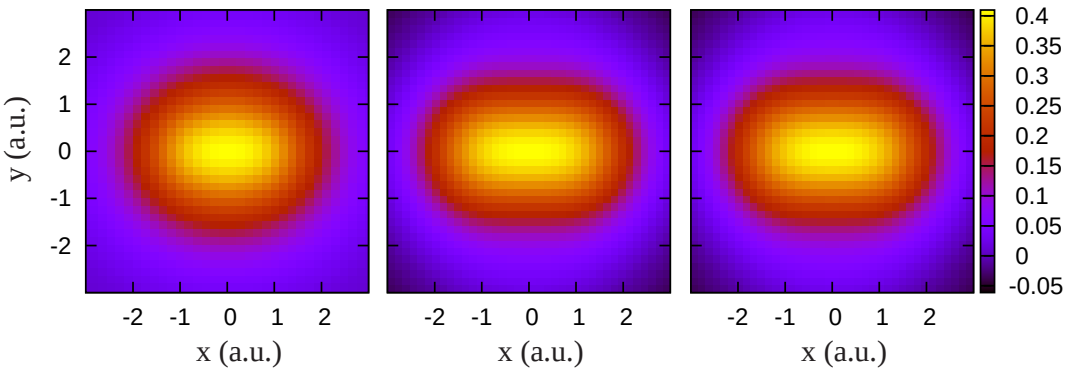

Figure 4.3: (Color online) Tomographic reconstruction of the ground state of 2D H_2^+. From left to right the exact orbital, the real part of the reconstructed orbital and the real part of the reconstructed after rotation in the complex plane are shown.

orders were used for the reconstruction, no significant improvement was reported in going beyond $\Delta\theta = \frac{360}{N_\theta} = 10^\circ$ (Haessler [45]). The low requirement on the angular resolution reported there is probably related to the slow angular variation for σ- and π-orbitals.

Before performing the reconstruction, we diffuse the matrix elements by convoluting them with a Gaussian filter to flatten artificial spikes that arise when the molecule and the reference system exhibit trajectory interferences at slightly different frequencies. The Gaussian filter has a $1/e$-width of $6\omega_\mathrm{L}$. After diffusing the matrix elements, we use the frequency range

$$\max\left(\omega_\mathrm{L}, 0.05I_\mathrm{p}\right) < \omega < 1.05 \times \left(3.17U_\mathrm{p} + I_\mathrm{p}\right) \tag{4.43}$$

for the reconstruction. In words, for a 780-nm pulse and $I_\mathrm{p} = 30.2$ eV all measured frequencies above the fundamental are used, and to take into account that the quantum-mechanical cutoff lies beyond the classical one, we use the classical cutoff times 1.05. We have also experimented with not using the lowest harmonics for the reconstruction. The results strongly depended on the molecule considered in that case; both improvements and detoriations of reconstructed orbitals were seen and no general guideline was found. In (Haessler [45]) it was reported that if only a limited frequency range is available for the reconstruction, best results are obtained if one makes sure the used frequency range is not too one-sided with respect to the characteristic momentum/-a of the reconstructed orbital, even if that means not using part of the available frequency range.

Even in the relatively straightforward case of the ground state of 2D H_2^+, the rotation procedure from section 4.2.3 brings a slight improvement, as demonstrated in Fig. 4.3. The laser wavelength is $\lambda = 780$ nm and the laser intensity is $I = 5 \times 10^{14}$ W/cm^2. The laser pulse had a three-cycle $\sin^2$ envelope with a carrier-envelope phase of $\phi_\mathrm{CEP} = 1.25\pi$. The 2D softcore model for H_2^+ included a softcore parameter $a^2 = 0.5$ and internuclear distance $R = 2$ to give an ionization energy of 30.2 eV. As a reference we used a softcore model for He^+ with $Z = 2$ and $a^2 = 0.9207$ to give the same I_p. The left-most density plot in Fig. 4.3 shows the exact ground state and in the middle the real part of the reconstructed orbital in velocity form is

shown. The right-most density plot shows the real part of the reconstructed orbital rotated in the complex plane by $\phi \simeq 0.12$ rad to maximize the total density in the real domain ($R_c = \infty$ suffices here). Although the difference is small, after rotation in the complex plane the reconstructed orbital is more oval and less rectangular and thereby resembles the exact orbital a bit better.

For a length-form reconstruction, we proceed analogously. Here the continuum wave packet is approximated from the parallel emission of the atomic reference system as (see Eq. (2.23))

$$a_\theta[-k(\omega)] = -\frac{k(\omega) D_x^{(a)}(\omega)}{2\pi\, d_x^{(a)}(\omega)} \sqrt{\frac{P_{\mathrm{I}}(\theta)}{P_{\mathrm{I}}^{(a)}}}. \tag{4.44}$$

The reconstruction matrix elements are retrieved using

$$\mathbf{d}_\theta(\omega) = -\frac{k(\omega)\mathbf{D}(\omega)}{2\pi\, a_\theta[-k(\omega)]}, \tag{4.45}$$

and the molecule is reconstructed using Eq. (4.18).

In the above we considered the case that $a(k) = 0$ for $k > 0$ allowing for the reconstruction of general molecules. In case one uses a long pulse to reconstruct an (un-)gerade molecule, the procedure is exactly the same. The only difference is that evaluation of the righthand sides of Eq. (4.41) or Eq. (4.44) does not give the momentum components of the continuum wavepacket as defined in Eq. (2.16), but instead an effective container function $a'[k(\omega)]$ is obtained. The analysis around Eqs. (2.22) and (2.29) showed us that for either a length or velocity-form reconstruction $a'[k(\omega)] = a[-k(\omega)] - a[k(\omega)]$ for gerade orbitals and $a'[k(\omega)] = a[k(\omega)] + a[-k(\omega)]$ for ungerade orbitals.

4.4 Length versus velocity form

In Fig. 4.4 we present the results of a numerical simulation of molecular orbital tomography using length and velocity forms. The parameters are the same as for Fig. 4.3. Although the orbital has a $k = 0$-component that cannot be retrieved using the tomographic procedure, the reconstruction procedure seems to work quite well. The negative part of the reconstructed orbital is located at large r and does not destroy the reconstruction of the inner region. The length-form reconstructed orbital shown in the middle overestimates the nuclear dimensions significantly, but its shape seems to be closer to the exact orbital on the left than the velocity-form reconstructed orbital shown on the right. It has been reported before that in a length form description of HHG the nuclear dimension is stretched (Chirilă and Lein [22]).

In Fig. 4.5 the results of a tomographic simulation for an ungerade orbital are shown. We use the first excited state of H_2^+, but with an adapted softcore parameter of $a^2 = 0.0681$ to keep I_p constant. The laser parameters are the same as for Fig. 4.4. The length-form reconstruction breaks down around the $x = 0$-symmetry axis because of the $1/x$-term in Eq. (4.18). The velocity form gives a reasonable reconstruction, although some erroneous density outside of the core region is visible.

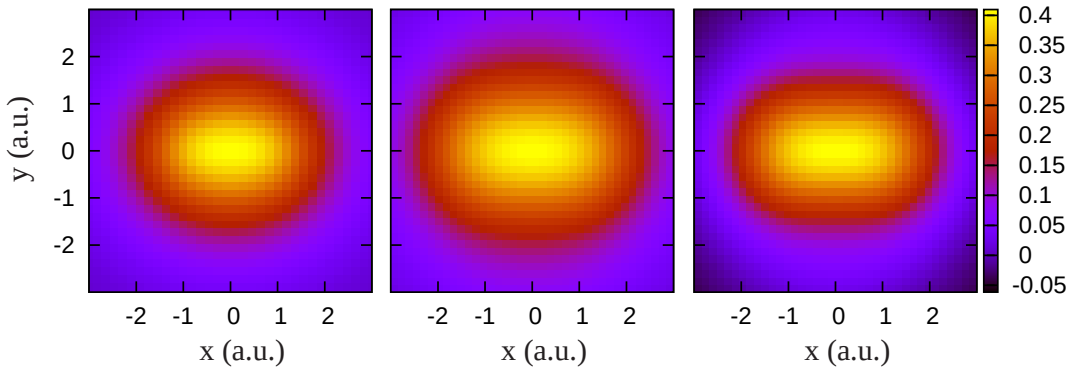

Figure 4.4: (Color online) Tomographic reconstruction of the ground state of 2D H_2^+. From left to right the exact orbital, the real part of the reconstructed orbital using length-form reconstruction and using velocity-form reconstruction are shown.

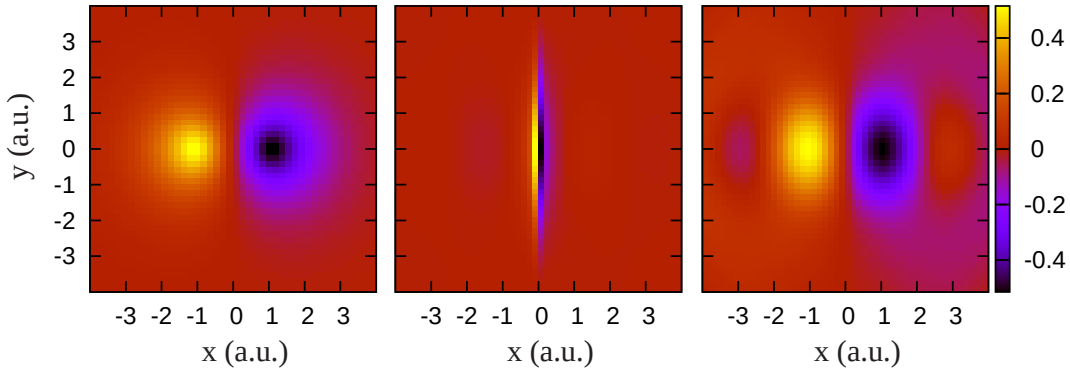

Figure 4.5: (Color online) Tomographic reconstruction of the first excited state of 2D H_2^+. From left to right the exact orbital, the real part of the reconstructed orbital using length-form reconstruction and using velocity-form reconstruction are shown.

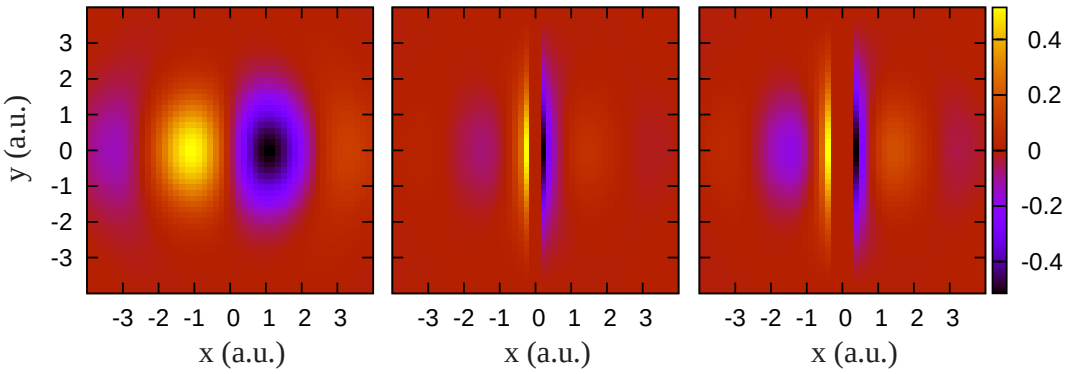

Figure 4.6: (Color online) Alternative length form tomographic reconstructions of the first excited state of 2D H_2^+. From left to right the real part of the reconstructed orbital using only the $1/y$-term, using $R_- = 0.1$ and using $R_- = 0.3$ are shown.

In Fig. 4.6 we explore some possibilities to improve the length-form reconstruction of an ungerade orbital. If only the $1/y$- and not the $1/x$-term of Eq. (4.18) is used (left panel), the reconstruction is comparable to the velocity-form reconstruction. This shows that the problem in length form can be overcome by avoiding the problem-causing term in Eq. (4.18). Of course a general prescription is hard to give here, but by considering both terms in Eq. (4.18) independently it is possible to reconstruct an ungerade orbital. Problems will persist where two antisymmetry axes cross, e.g., at the origin of a π_g-orbital. Alternatively, we could set the orbital to 0 if $|x| < R_-$. The results for $R_- = 0.1$ and $R_- = 0.3$ in Fig. 4.6 show that the results still show the artifacts, but the shape of the reconstructed orbital outside the region where x is small becomes visible.

If the reconstructed orbital was not centered around the origin, but all electron density would be placed at for instance positive x, y, the problem would not occur. Using adapted matrix elements we obtain a perfect length-form reconstruction. However, in length form and using the plane-wave approximation, the correspondence between the translated molecule and the harmonic spectrum is lost. This leads to the introduction of new errors to the reconstructed orbital in the molecular tomography scheme. Since these errors are frequency-dependent, and not bound to a small spatial region, it is probably not beneficial to translate the molecule before a length-form reconstruction. The adapted length-form matrix elements corresponding to a translated orbital can also not be obtained from the normal length-form matrix elements without knowledge of the orbital.

4.4.1 Biegert-type length-form reconstruction

Very recently an alternative length-form reconstruction equation was proposed by the Biegert group (Hijano et al. [49]). It consists of a trick to get rid of the $1/x$-, $1/y$-problems except at the origin by multiplying ψ with $\frac{x^2+y^2}{x^2+y^2}$. The idea here is to use the two terms in Eq. (4.18) independently as equalities for ψ as in Eq. (4.14).

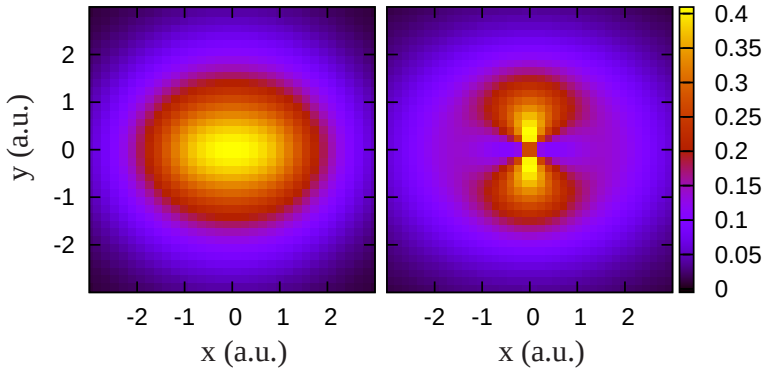

Figure 4.7: (Color online) Tomographic reconstruction of the ground state of 2D H_2^+. On the left side the exact orbital, and on the right side the real part of the Biegert-type length-form reconstructed orbital are shown.

The length-form reconstruction equation then becomes

$$\psi_0(\mathbf{r}) = \frac{x f_x(\mathbf{r}) + y f_y(\mathbf{r})}{x^2 + y^2}, \tag{4.46a}$$

$$f_x(\mathbf{r}) = \frac{1}{(2\pi)^2} \left\{ \iint (d_{\theta,x}(\omega)\cos\theta + d_{\theta,y}(\omega)\sin\theta) e^{ik(\omega)(x\cos\theta - y\sin\theta)} d\omega d\theta \right\}, \tag{4.46b}$$

$$f_y(\mathbf{r}) = \frac{1}{(2\pi)^2} \left\{ \iint (-d_{\theta,x}(\omega)\sin\theta + d_{\theta,y}(\omega)\cos\theta) e^{ik(\omega)(x\cos\theta - y\sin\theta)} d\omega d\theta \right\}. \tag{4.46c}$$

Using exact matrix elements the authors obtained very good results with Eq. (4.46) (see Hijano et al. [49]).

Unfortunately, in our numerical simulations their method does not perform so well. In Fig. 4.7 we show the Biegert-type length-form reconstruction for the case of Fig. 4.4. Although the ground state can be reconstructed quite well using the original reconstruction equation Eq. (4.18), we plot the result for Eq. (4.46) to show its effect. There is a very clear distortion of the reconstructed orbital around the origin. This is probably related to an inequality between f_x/x and f_y/y combined with a rapidly changing ratio x/y around the origin. Using exact matrix elements, f_x/x and f_y/y are equal (see Eq. (4.14)).

As a reference, in Fig. 4.8 we plot the obtained reconstructions for the case of Fig. 4.5 using exact matrix elements, but limited to the experimental harmonic range of a 780-nm pulse with an intensity of 5×10^{14} W/cm^2. The Biegert-type length-form reconstruction using Eq. (4.46) (middle plot) performs quite well here. The divergent axis of normal length form (left plot) has been reduced to a single point, the origin. Apart from the origin, the accuracy of the reconstruction is comparable to the velocity-form result (right plot). However, using matrix elements obtained from the numerical tomographic simulation, Biegert-type length-form reconstruction brings no real improvement compared to normal length-form reconstruction, as shown in Fig. 4.9. This is in line with what we saw in Fig. 4.7. Like in Fig. 4.8 we obtain a point-like divergence around the origin instead of a line-shaped one. The problem is that even if we set all points with $|x| < 0.1$ or $|y| < 0.3$ to 0 ($R_- = 0.3$, right plot),

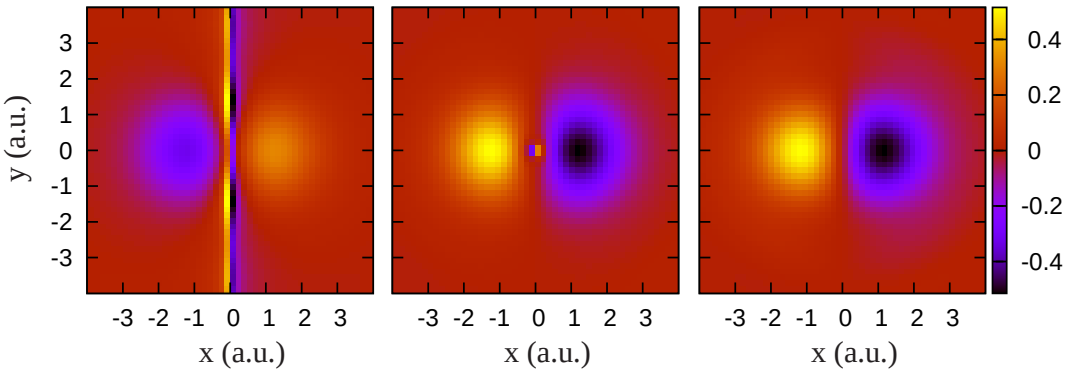

Figure 4.8: (Color online) Tomographic reconstruction of the first excited state of 2D H_2^+ using exact matrix elements. From left to right the real part of the orbital using length-form reconstruction, using length-form Biegert-type reconstruction and using velocity-form reconstruction are shown.

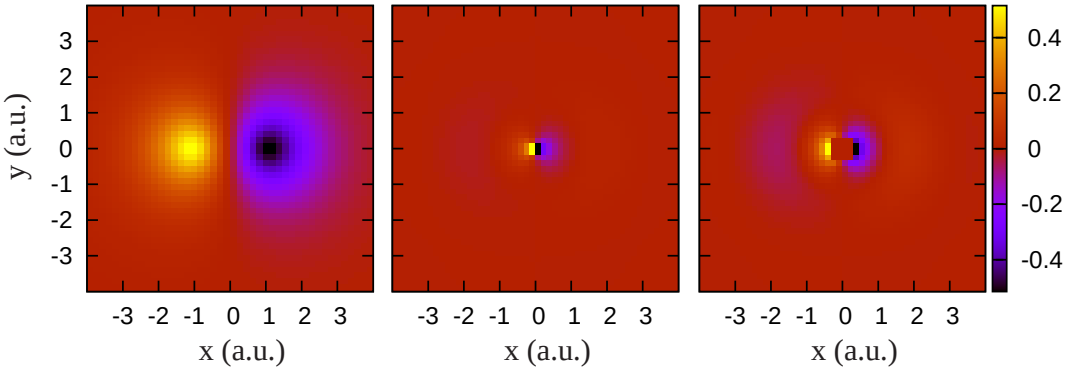

Figure 4.9: (Color online) Tomographic reconstruction of the first excited state of 2D H_2^+. From left to right the exact orbital, the real part of the reconstructed orbital using a Biegert-type length-form reconstruction, and the same with $R_- = 0.3$ are shown.

there is no improvement. The dominant behavior in the plot is still that of artificial peaks at the origin.

The derivation of Eq. (4.46) depended on the equality between f_x/x and f_y/y as in Eq. (4.14). However, in a real tomographic experiment (or its numerical simulation), both will contain different errors. In the area around the origin where the density is low, these errors can be substantial and Eq. (4.46) breaks down.

4.5 Orbital symmetry and signs

Using linearly-polarized HHG, one cannot measure the absolute phase of an orbital in the complex plane. The reason is that when one multiplies the orbital with a complex phase factor, the continuum wave acquires the same extra phase and the harmonic spectrum and phases are not altered. This makes physical sense as the absolute overall phase of an wave function has no physical meaning. Problems result

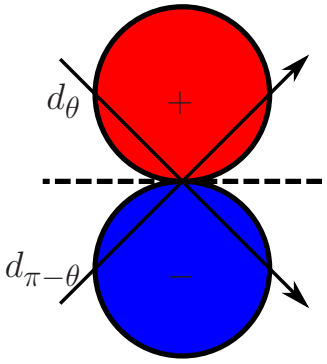

Figure 4.10: (Color online) Typical 2D projection of an ungerade orbital with antisymmetry around the yz-plane (depicted by the dashed line). The x-direction is from bottom to top.

when reconstructing orbitals that contain some symmetry.

Consider for instance an ungerade orbital. An example with one nodal plane is depicted in Fig. 4.10. The sign difference between matrix elements mirrored with respect to the nodal plane becomes clear from the figure. For this orbital a rotation by 180° is equivalently described by a multiplication by -1. Physically, the orientation angles 0° and 180° cannot be distinguished and lead to identical harmonics. Therefore the matrix elements obtained within the tomography scheme at 180° need to be multiplied by -1 to take into account the antisymmetry.

For the typical cases of mirror symmetries with respect to the laboratory frame axes x and y, we will give the symmetry relationships in the following. First we consider a mirror symmetry S_x with respect to the x-axis, i.e., $\psi_0(x,-y) = S_x\,\psi_0(x,y)$ with $S_x = \pm 1$. The following equations can be used to determine the reconstruction matrix elements

$$\begin{aligned}\mathbf{d}_{-\theta}(\omega) &= \iint \psi_0(\mathbf{r}) \begin{pmatrix} x\cos\theta + y\sin\theta \\ -x\sin\theta + y\cos\theta \end{pmatrix} e^{-ik(\omega)(x\cos\theta + y\sin\theta)} d^2\mathbf{r} \\ &= \iint \psi_0(x,-y) \begin{pmatrix} x\cos\theta - y\sin\theta \\ -x\sin\theta - y\cos\theta \end{pmatrix} e^{-ik(\omega)(x\cos\theta - y\sin\theta)} d^2\mathbf{r} \qquad (4.47a) \\ &= S_x \begin{pmatrix} d_{\theta,x}(\omega) \\ -d_{\theta,y}(\omega) \end{pmatrix}, \\ p_{-\theta}(\omega) &= S_x\, p_\theta(\omega). \qquad (4.47b)\end{aligned}$$

Equivalently, in case of a mirror symmetry S_y with respect to the y-axis ($\psi_0(-x,y) = S_y\,\psi_0(\mathbf{r})$), the following hold

$$\mathbf{d}_{\pi-\theta}(\omega) = S_y \begin{pmatrix} d_{\theta,x}(\omega) \\ -d_{\theta,y}(\omega) \end{pmatrix}, \qquad (4.48a)$$

$$p_{\pi-\theta}(\omega) = S_y\, p_\theta(\omega). \qquad (4.48b)$$

We observe that the length form x-components behave as the velocity form components and follow the sign of the symmetry, whereas the length-form y-components

show the inverse behavior. In other words, the length-form dipole operator changes the sign of the mirror symmetry for the y-component. Every mirror symmetry reduces the range of orientations that both needs to be measured and carries independent physical information by 50%.

In the orbital reconstructions published so far, the information about the symmetry came from *a priori* considerations. However, there has been some limited success in measuring the orbital symmetry directly. Although this is not possible using linearly-polarized pulses for the reason mentioned above, there have been some alternative methods proposed. By considering the alignment-dependent total ionization rate, nodal planes can be identified and an indication of the symmetry can be obtained (Levesque et al. [69]). The four most common molecular symmetries can also be distinguished visually by considering a polarization map that shows the polarization angle as a function of alignment and harmonic order (Hijano et al. [49]). Alternatively we can generate high-harmonics using elliptically polarized pulses to determine the molecular symmetry (Mairesse et al. [77]; Niikura et al. [93]). Semi-classically this can be understood as studying trajectories that ionize from one lobe and then recombine in another to determine the relative phase between these two lobes. Elliptically polarized pulses can also be used to perform a tomographic reconstruction directly (Shafir et al. [115]).

4.5.1 Asymmetric orbitals

Consider the case where the molecular orbital has lobes with different signs but they are not associated with any symmetries. Also in this case the continuum wave packet will start out with the phase of the lobe that dominates the ionization at a certain orientation, and this initial phase will work its way through the final phase with which the continuum wave packet recombines. This leads to a π-jump in the phase of the continuum wave packet at the transition between orientations corresponding to two lobes with a sign difference that is not taken into account in the current procedure for determining $a_\theta[-k(\omega)]$. An improvement should therefore be expected if we artificially multiply the reconstruction matrix elements with -1 appropriately at such a transition.

We performed a tomographic simulation for the first excited state of HeH^{2+} using a laser intensity of $I = 3 \times 10^{14}$ W/cm^2 and a laser wavelength of $\lambda = 780$ nm. The softcore parameter was chosen as $a^2 = 0.7581$ to set the ionization potential at 30.2 eV. For a discussion of asymmetric orbitals and more details on HeH^{2+} see section 4.6. The results of the simulation are shown in Fig. 4.11. The exact orbital on the left shows the two lobes with their sign difference. The difference between the velocity-form reconstructed orbitals in the middle and on the right is that for the right-most plot we multiplied $p_\theta(\omega)$ with -1 for $\frac{\pi}{2} < \theta < \frac{3\pi}{2}$, roughly corresponding to the orientations where the transition between the two lobes take place. A clear improvement in reconstruction is seen between the right-most and middle plots. Because the positive lobe is larger and has higher amplitude than the negative lobe, probably the reconstructed orbital would look better if $p_\theta(\omega)$ was multiplied with -1 for a slightly smaller range.

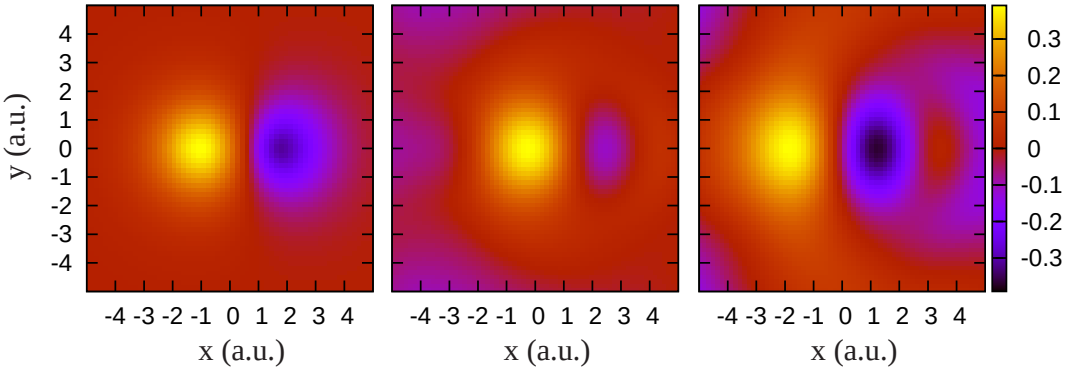

Figure 4.11: (Color online) Tomographic reconstruction of the first excited of 2D HeH^{2+}. From left to right the exact orbital, the real part of the reconstructed orbital and the real part of the reconstructed orbital when the matrix elements for $\frac{\pi}{2} < \theta < \frac{3\pi}{2}$ are multiplied with -1 are shown.

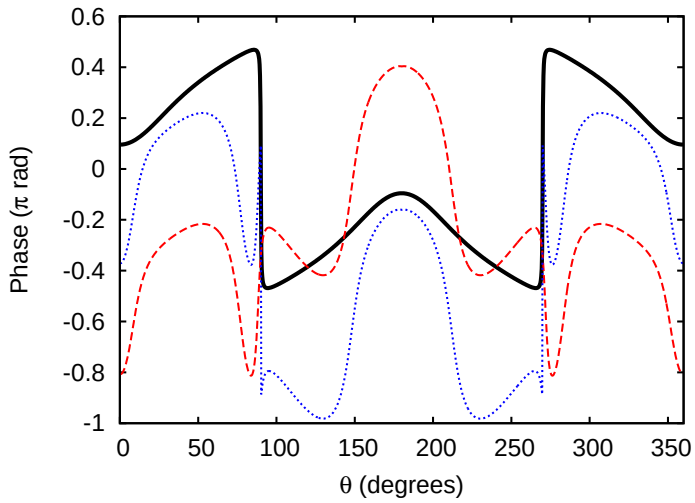

Figure 4.12: (Color online) Phase of $p_\theta(\omega)$ for harmonic 49 as a function of θ for the exact orbital (black solid line), for the reconstructed orbital (red dashed line) and for the reconstructed orbital with $p_\theta(\omega) \rightarrow -p_\theta(\omega)$ for $\frac{\pi}{2} < \theta < \frac{3\pi}{2}$ (blue dotted line).

The physical reason why the reconstruction can be improved like this can be seen in Fig. 4.12. Here we show the phase of $p_\theta(\omega)$ for harmonic 49 as a function of orientation angle for the three different plots of Fig. 4.11. The different curves in Fig. 4.12 include the complex phase factors with which the reconstructed orbitals were multiplied to maximize the density in the real domain, for which we used $R_c = 3$ a.u. In this case using $R_c = \infty$ produces very bad results because of the density far away from the origin. The curve of the exact orbital (black line) shows sharp π-jumps at 90° and 270° orientation, although the orbital is not (un-)gerade and $p_\theta(\omega)$ is therefore not purely real or imaginary. Because the initially obtained matrix elements (red dashed line) do not include these jumps, the adapted matrix elements (blue dotted line) follow the exact curve much better.

4.6 Reconstruction of asymmetric orbitals

As derived in section 2.3, when the studied molecule is not gerade or ungerade a reconstruction of the molecular orbital is only possible if the electronic wave packet approaches the molecule from one side only. This can be achieved using extremely short pulses, as will be shown in the following sections. Furthermore, for a molecule that has no internal symmetries, obviously one cannot use the equalities from section 4.5 to reduce the number of angles for which one needs experimental (or in the simulation, numerical) data. In principle, however, we could use the a priori knowledge that the reconstructed orbital can be chosen real to reduce the number of needed angles by 50% as

$$\begin{aligned}\mathbf{d}_{\pi+\theta}(\omega) &= \iint \psi_0(\mathbf{r}) \begin{pmatrix} -x\cos\theta + y\sin\theta \\ -x\sin\theta - y\cos\theta \end{pmatrix} e^{-ik(\omega)(-x\cos\theta + y\sin\theta)} d^2\mathbf{r}, \\ &= -\mathbf{d}^*_\theta(\omega), \end{aligned} \tag{4.49a}$$

$$p_{\pi+\theta}(\omega) = p^*_\theta(\omega). \tag{4.49b}$$

However, it turns out that in practice the orbital is reconstructed with a nonzero phase introduced by the different errors of the tomographic scheme as we saw in section 4.2. Therefore using Eq. (4.49) might produce unwanted and strange effects. We have observed numerically that a reconstruction using Eq. (4.49) becomes unreliable for more adverse reconstruction conditions (complicated orbital, low intensity, etc), i.e., when the overall error of the reconstruction increases.

4.6.1 Semi-classical pulse characterization

In general, recolliding electrons with both positive and negative momenta contribute to the generation of the same harmonic generation, each through their own recombination matrix element. The reconstruction of an arbitrary orbital therefore requires that the wave packets approach the core from one side only as we saw in section 2.3. We propose achieving this behavior of the continuum wave packet by using extremely short tailored laser pulses for high-harmonic generation. By stabilization and control of the carrier-envelope phase (CEP), the returning wave packet can be tailored.

Because of the very-few-cycle character of the pulse, the CEP can be chosen such that classical trajectories in the unwanted direction are effectively suppressed.

4.6.1.1 Return probability

To characterize the returning wave packet we calculate semi-classically the probability that an electron returns with momentum k. We sample the ionization time with 3000 points per laser cycle. At each ionization time t_i, the electron tunnels with tunneling probability

$$p_\mathrm{I} \sim \exp\left(-\frac{4I_\mathrm{p}\sqrt{2I_\mathrm{p}}}{3|E(t_\mathrm{i})|}\right). \tag{4.50}$$

The above factor can be found also in the Lewenstein model (Lewenstein et al. [71]) as we will see in section 5.1.3.2. After tunnelling, the electron follows a classical trajectory, starting with zero velocity at position zero. Every classical return receives a weight based on the tunnelling probability and a factor τ^{-3}, where τ is the time the electron spends in the continuum until the time of return. This factor reflects the effect of wave-packet spreading and comes from the Lewenstein model (Lewenstein et al. [71]). With experiments in mind, we consider here a full three-dimensional world. We then add the contributions from the different trajectories to arrive at the probability that the electron returns to the core with a momentum k in the range $k_\mathrm{i} - \Delta k/2 < k \leq k_\mathrm{i} + \Delta k/2$, where k_i is the momentum of the i'th momentum bin and Δk is the width of a bin. In contrast with the full Lewenstein model as treated in section 5.1, interferences between the different paths leading to the same harmonic are not included in this model. Therefore slightly more accurate results are obtained by using the approach of section 5.3.1, at the cost of added complexity. However, to observe the general trend and assess the suitability of different pulses for the reconstruction of general molecules the approach in this section suffices.

We consider two types of analytical representations for extremely short and linearly-polarized laser pulses. The first type are 3-cycle pulses with a $\sin^2$-envelope for which the electric field is given by Eq. (3.4). We choose a laser wavelength of $\lambda = 780$ nm and an intensity of $I = 5 \times 10^{14}$ W/cm^2 for both pulses. The length of such a pulse in terms of the full width at half maximum of the intensity (FWHM) is 2.84 fs. The second type are pulses with a Gaussian envelope. These pulses are in principle infinitely long but for the semi-classical calculation we consider only the center 4 cycles of the pulses

$$E(t) = E_0 \exp\left(-1.5\frac{(t-2T)^2}{T^2}\right)\cos(\omega t + \phi_\mathrm{CEP}). \tag{4.51}$$

These pulses have a FWHM of 2.50 fs. Both mentioned values of the FWHM are comparable to one laser cycle (2.6 fs). The choice of simple analytical expressions for the time-dependent field strength leads to small but unimportant violations of the rule $\int E(t)dt = 0$ for the pulses with a Gaussian envelope.

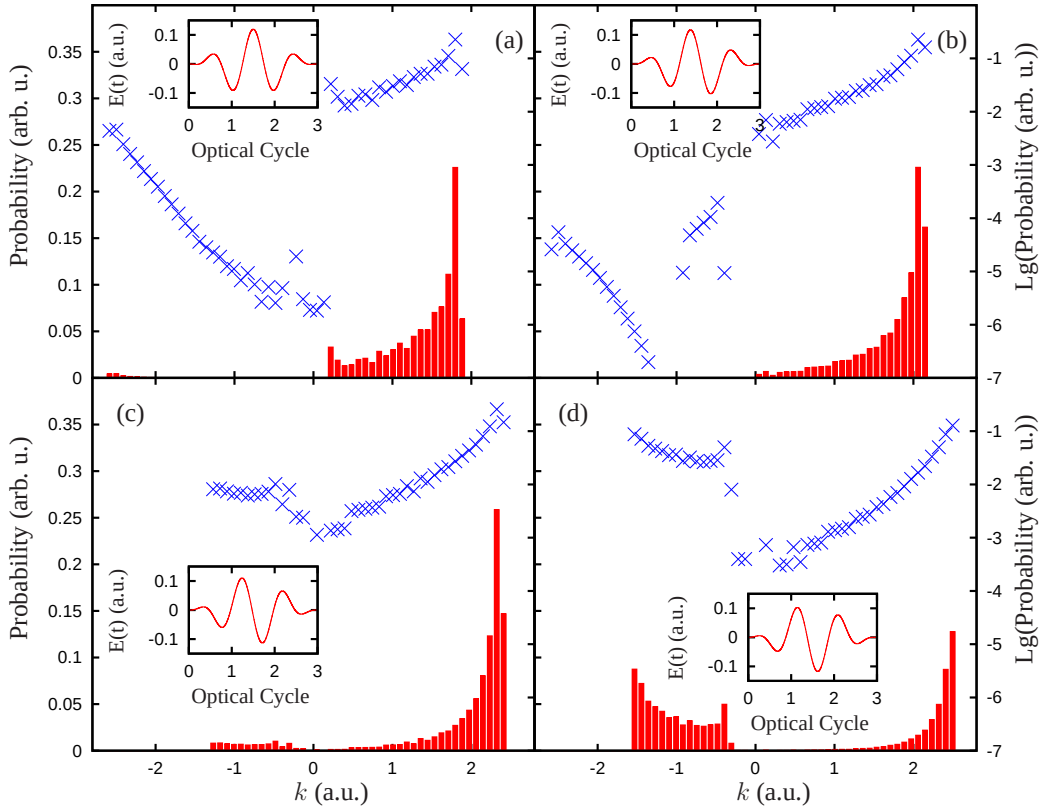

Figure 4.13: (Color online) Returning electron momentum distributions for the 3-cycle $\sin^2$-pulses. (a) $\phi_{\mathrm{CEP}} = 0$ rad, (b) $\phi_{\mathrm{CEP}} = 0.25\pi$ rad, (c) $\phi_{\mathrm{CEP}} = 0.55\pi$ rad and (d) $\phi_{\mathrm{CEP}} = 0.75\pi$ rad. The distributions are shown on a linear scale (bars), and on a logarithmic scale (crosses).

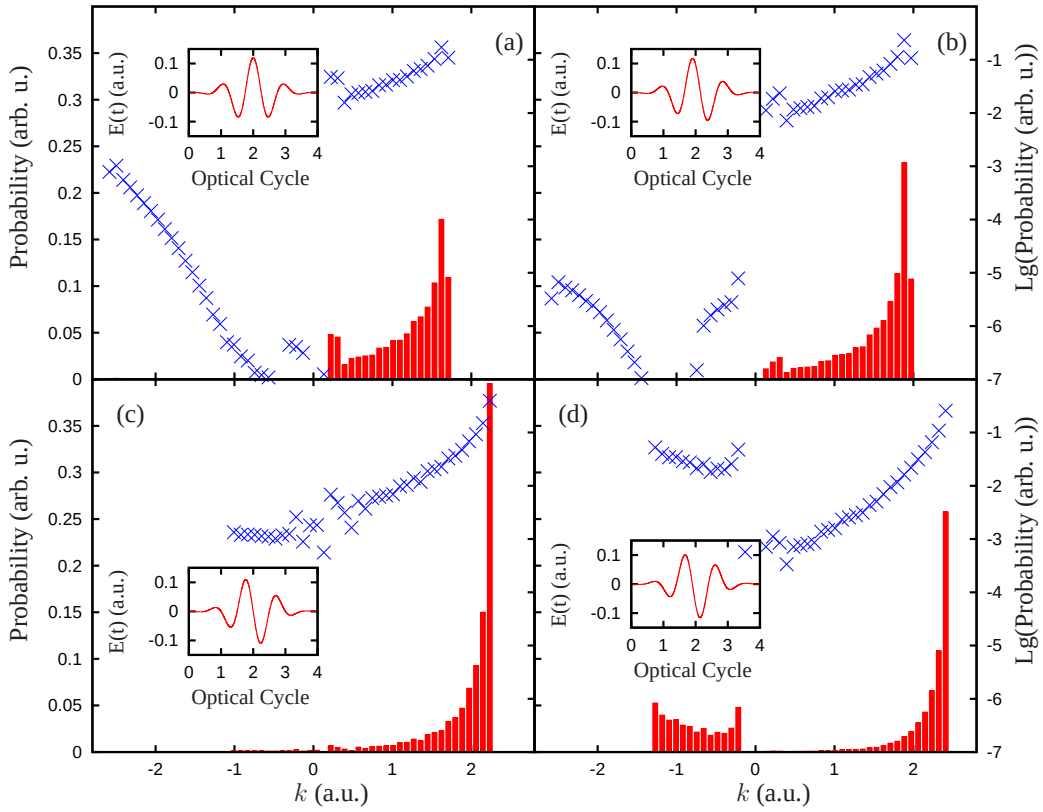

Figure 4.14: (Color online) Returning electron momentum distributions for the Gaussian pulses. (a) $\phi_{\mathrm{CEP}} = 0$ rad, (b) $\phi_{\mathrm{CEP}} = 0.2\pi$ rad, (c) $\phi_{\mathrm{CEP}} = 0.5\pi$ rad and (d) $\phi_{\mathrm{CEP}} = 0.7\pi$ rad. The distributions are shown on a linear scale (bars), and on a logarithmic scale (crosses).

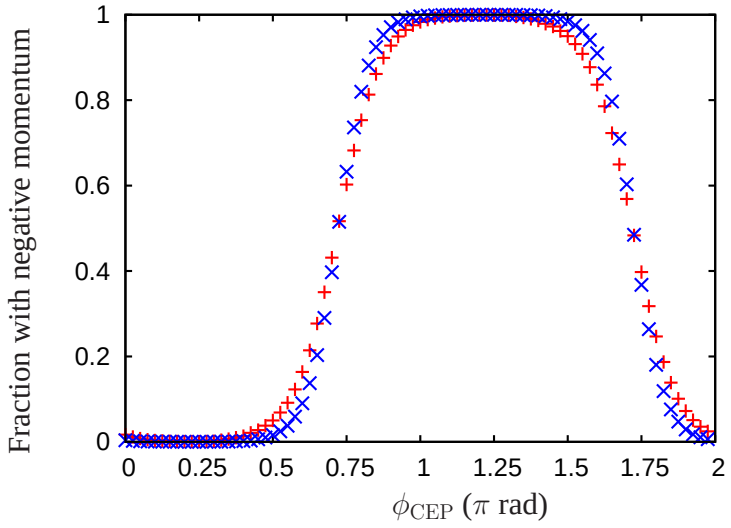

Figure 4.15: (Color online) Fraction of electrons returning with negative momentum as a function of ϕ_{CEP}. Red plus symbols correspond to the 3-cycle $\sin^2$-pulse, blue crosses to the Gaussian pulse.

4.6.1.2 Results

We set $I_p = 30.2$ eV in accordance with the 2D model system for H_2^+ that we used in section 3.1 and elsewhere. In Figs. 4.13 and 4.14 the probability that an electron returns with momentum k is depicted for the two different pulse types and different CEPs. The bars reflect that probability on a linear scale, the crosses on a logarithmic scale. For each pulse the sum of the probabilities is normalized to 1. The insets show the laser pulse used to generate the data. Subjected to an infinitely long pulse of the mentioned intensity and wavelength, the fastest returning electrons would have an energy of $3.17U_p$ corresponding to $k \simeq \pm 2.57$ a.u. The figures show that the CEP of an extremely short pulse has a very large influence on the characteristics of the returning wave packet, and that tuning of the CEP allows one to select the characteristics that one desires. This is also apparent in Fig. 4.15, which shows the fraction of the electrons returning with negative momentum as a function of ϕ_{CEP} for the two pulses. For $\phi_{CEP} = 0$ rad, the pulses have their main ionizing half-cycle in the positive direction, which means that the electrons leave toward the negative direction. As a consequence, most electron returns occur with positive momentum.

An optimal pulse for use with the molecular orbital tomography has to meet two requirements: (i) all returning electrons should come from the same side, i.e., zero probability for electrons returning with the opposite momentum sign and (ii) the energy spectrum of the returning electrons should be broad, so that the Fourier transform of the orbital can be accurately extracted from the HHG spectra. The results show that a large range of CEPs that are suitable for molecular orbital tomography can be found for both pulses. For both pulses the results are very similar. This indicates that many types of phase-stabilized extremely short laser pulses will be suitable for the procedure. These pulses should have an ionizing half-cycle where the amplitude of the electric field is significantly higher than everything earlier, and the following half-cycle in the opposite direction should be comparable to the ionizing half-cycle in strength, to force the electrons to return. Everything after the 'returning'-half-cycle should be significantly lower in amplitude, otherwise electrons return from the other side with a significant probability. The reason that these effects can be achieved with the few-cycle pulses proposed in this section, is that the ionization rate depends exponentially on the field amplitude. A nice demonstration that small field-amplitude changes can have large influence on harmonic spectra can be found in (Cao et al. [14]). Because of this effect, we expect no problems with experimental pulses that have more smeared out tails, or with pre- and postpulses. For a different I_p the qualitative behavior will be the same, as I_p has no influence on the classical trajectories. Small differences in relative ionization rates might lead to a slightly different CEP being optimal for a different I_p though.

4.6.1.3 Harmonic spectra

A quantum-mechanical signature of the above-mentioned effects can be found in the high-harmonic spectra generated with these pulses. We consider a 2D He^+ model

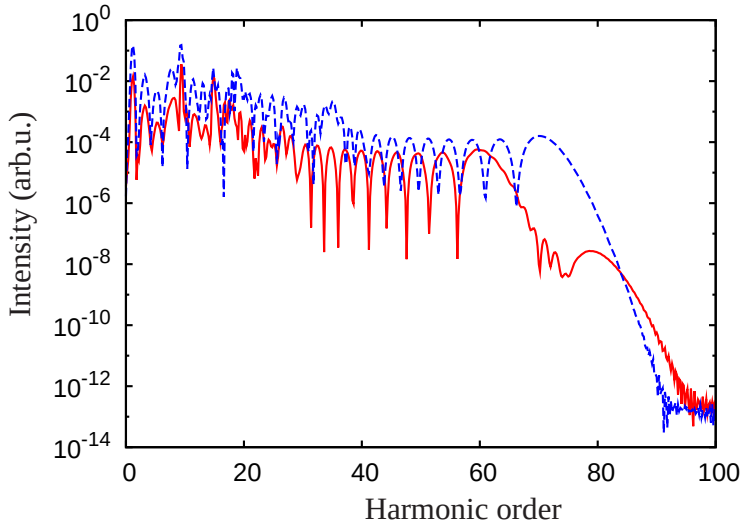

Figure 4.16: (Color online) Harmonic spectra calculated using 3-cycle $\sin^2$-pulses with $\phi_{\mathrm{CEP}} = 0.25\pi$ rad (red solid line) and $\phi_{\mathrm{CEP}} = 0.55\pi$ rad (blue dashed line). The latter spectrum was multiplied with a factor 10 to separate the two curves graphically.

ion with the soft-core potential

$$V(\mathbf{r}) = -\frac{2}{\sqrt{\mathbf{r}^2 + a^2}} \tag{4.52}$$

with the softness parameter a^2 adjusted such that $I_{\mathrm{p}} = 30.2$ eV. In Fig. 4.16 harmonic spectra associated with two values of the CEP for the 3-cycle $\sin^2$-pulse are shown. In both spectra, the low-frequency part is rather irregular due to the interference of several trajectories, while the high-frequency part shows the typical regular pattern of interference between short and long trajectories (Milošević and Becker [85]). The latter is the pattern that we expect for uni-directional recollisions.

For the case of $\phi_{\mathrm{CEP}} = 0.25\pi$ rad, the transition to the regular interference pattern occurs at roughly the 28th harmonic. To relate the energy of an emitted photon Ω with the momentum of the returning electron k, we use the energy-conserving dispersion relationship $\Omega = k^2/2 + I_{\mathrm{p}}$. The 28th harmonic then corresponds to $k \simeq \pm 1$ a.u. As can be seen in Fig. 4.13, $|k| \simeq 1$ a.u. is exactly the limit above which contributions come only from electrons with positive momentum. Also the cutoff at the 60th harmonic can be related to the classical picture, corresponding to the cutoff of $k \simeq 2.2$ a.u. for electrons with positive momentum. The second cutoff comes from the less-likely events involving electrons with negative momentum, and clearly extends a couple of harmonics beyond the classically calculated and expected cutoff at the 76th harmonic, corresponding to $k \simeq -2.57$ a.u.

In the case of $\phi_{\mathrm{CEP}} = 0.55\pi$ rad, the classical picture suggests a single cutoff at $k \simeq 2.4$ a.u., corresponding to the 68th harmonic. This is exactly what we see in Fig. 4.13. However, there is a small discrepancy between the TDSE and classical result concerning the location of the transition to a more regular spectrum. In the classical calculation, the fastest electrons with negative momentum have $k \simeq$

−1.3 a.u. This would correspond to a transition in the spectrum around the 33th harmonic. The TDSE result shows this transition around the 37th harmonic, which may be due to modifications of the electron trajectories by the Coulombic potential.

4.6.2 Alternative approaches

In this thesis we show that for the tomographic reconstruction of general molecules one needs that $a(k) = 0$ for $k > 0$ or alternatively for $k < 0$. In the previous sections we presented a calculation that shows that extremely short laser pulses can exhibit this behavior for the generated continuum wave packet. In attosecond physics, many people have worked on similar problems; the generated harmonics combine to an attosecond pulse that can be used for applications. In a long pulse, every laser half-cycle the generation process is repeated and one obtains an attosecond pulse train (Paul et al. [101]; Tzallas et al. [129]). A few experimental groups have isolated single attosecond pulses (Drescher et al. [28]; Hentschel et al. [48]), or focussed on generating as short as possible attosecond pulses (Mairesse et al. [76]; Sola et al. [119]). Single attosecond pulses correspond to harmonics being generated during a single half-cycle, which in practice amounts to the same requirements as one-sided returns. Very short attosecond pulses require broad and preferably Fourier-limited harmonics, something also very useful for molecular imaging. For both isolating and shortening attosecond pulses, at the moment the best results are obtained using spectral filtering of the lowest harmonics. However, for tomographic imaging the low harmonics are very important too and should not be ignored. To some extent the requirements for generating a single or short attosecond pulse are therefore less strong than those for successful molecular imaging of asymmetric molecules, and the methods reported in this section cannot be directly applied to imaging of asymmetric molecules.

Single attosecond pulses can also be obtained using polarization gating (Corkum et al. [26]). Here two circularly polarized pulses with opposite handedness are combined. High-harmonics are generated only in the linearly-polarized region in the meeting point of the pulses, because under circular polarization the continuum wave packet never returns to the core (Dietrich et al. [27]). Therefore the requirements on the individual pulses are less stringent. Twelve femtosecond generating pulses can be used to generate a single attosecond pulse if one uses a double optical gating (DOG) method that combines polarization gating with two-color gating where a weak second-harmonic field is added to the fundamental (Mashiko et al. [83]). The generalized double optical gating method (GDOG) takes it even one step further by replacing the circularly polarized pulses by elliptically polarized pulses. Then single attosecond pulses can be generated from 20–30 femtosecond infrared pulses that are widely available nowadays (Feng et al. [32]; Gilbertson et al. [42]). Alternatively, a linearly polarized 30-fs 800-nm pulse can be combined with a parallelly polarized 40-fs 1300-nm pulse to generate single attosecond pulses without the need for CEP stabilization (Takahashi et al. [121]).

4.6.3 Helium-hydrogen cation

To demonstrate the molecular tomographic method in case of an asymmetric molecule, we make use of a 2D version of the doubly-charged Helium-Hydrogen cation (HeH^{2+}). From a theorist point-of-view, this is the simplest asymmetric molecule conceivable, consisting of one singly-charged and one doubly-charged nucleus, and a single electron. For an experimentalist the cation poses a much bigger challenge. Despite the very strong repulsion between the nuclei, a bound state exists. The ground state is repulsive, but the first excited state ($2p\sigma$) has a potential well that is 0.849 eV deep and has a minimum around $R = 3.89$ a.u. It supports around 15 vibrational states, each associated with a different life time before decaying via an electronic dipole transition to the $1s\sigma$-ground state. Depending on the temperature of the source used, in practice a distribution of vibrational states is occupied in a real experiment.

The existence of a bound state in HeH^{2+} was first predicted by Bates and Carson (Bates and Carson [6]). This results was verified by Winter et al. (Winter et al. [134]), who also showed that from the first 20 excited states of the cation, three are bound. Experimental evidence of the existence of at least one bound state was given by Ben-Itzhak et al. (Ben-Itzhak et al. [9]). A similar group of people later measured the average life time of the cation to be on the order of a few ns (Ben-Itzhak et al. [8]) and studied the contributions of the different vibrational states for different HeH^{2+}-isotopes in more detail (Ben-Itzhak et al. [7]). The life time on the order of a few ns makes it difficult but not impossible to perform experiments on the HeH^{2+}-cation.

4.7 Projected 3D orbital

The harmonic spectra used so far were based on the solution of the time-dependent Schrödinger equation in two dimensions, i.e., on a 2D slice of the true 3D orbital. However, the experimentally observed harmonic spectra involve the whole 3D orbital, such that the double integral in for instance Eq. (4.1) becomes a triple integral over all space dimensions x, y and z. Since only ψ_0 depends on z in that and the following equations, Eq. (4.18) becomes

$$\begin{aligned}\psi_0(\mathbf{r}) &= \int_{-\infty}^{\infty} \psi_0^{3D}(x,y,z)dz \\ &= \frac{1}{2}\{\frac{1}{x}\frac{1}{(2\pi)^2}\iint (d_{\theta,x}(\omega)\cos\theta + d_{\theta,y}(\omega)\sin\theta)e^{ik(\omega)(x\cos\theta - y\sin\theta)}d\omega d\theta \\ &+ \frac{1}{y}\frac{1}{(2\pi)^2}\iint (-d_{\theta,x}(\omega)\sin\theta + d_{\theta,y}(\omega)\cos\theta)e^{ik(\omega)(x\cos\theta - y\sin\theta)}d\omega d\theta\}, \quad (4.53)\end{aligned}$$

where from now on with $\psi_0^{3D}(x,y,z)$ we denote the unrotated three dimensional orbital, and with $\psi_0(\mathbf{r})$ its projection on the xy-plane. This equation shows that from experimental spectra we can only directly reconstruct ψ_0 and not ψ_0^{3D}. If we assume rotational symmetry of the molecule around the x-axis, i.e., the internuclear axis, we can however retrieve the 3D orbital from its projection. The reason is that

in this case the projected orbital contains all physical information about the full orbital and the first equality of Eq. (4.53) becomes an Abel transform (Weisstein [132]). More details about the procedure can be found in appendix A.3.

4.8 ATI electrons

4.8.1 Molecular tomography including ATI electrons

In principle ATI electrons contain information about $a_\theta[-k(\omega)]$ that can be used for the tomographic reconstruction of a molecular orbital. However, so far no practical link between HHG and ATI electrons exists. For the case of extremely short pulses, this link turns out to be possible, as we will show in section 5.3.2. In the simple-man's model (see section 2.2.2), the momentum of ATI electrons is completely determined by the vector potential at their moment of birth. This time of birth can be related to specific harmonics (specific components of $a_\theta[-k(\omega)]$). If both relationships are unique, ATI electrons can improve the tomographic reconstruction.

Schematically, in the simple-man's model the ATI intensity A at electron momentum p is given by (assuming one trajectory per ATI peak)

$$A^{(a)}(p) = \left|T^{(a)}(t_\mathrm{b}(p))\right|^2 \times \left|p_\mathrm{A}(t_\mathrm{b}(p))\right|^2, \tag{4.54a}$$

$$A_\theta(p) = \left|T_\theta(t_\mathrm{b}(p))\right|^2 \times \left|p_\mathrm{A}(t_\mathrm{b}(p))\right|^2, \tag{4.54b}$$

where the first line is for the reference atom and the second line is for the molecule. Here $t_\mathrm{b}(p)$ is the birth time of the trajectory leading to momentum p and p_A describes the propagation including for example angular spreading. The complex amplitude T describes the continuum wave packet just after ionization. This means that

$$\left|T^{(a)}(t_\mathrm{b}(p))\right| = \frac{\sqrt{A^{(a)}(p)}}{\left|p_\mathrm{A}(t_\mathrm{b}(p))\right|}, \tag{4.55a}$$

$$\left|T_\theta(t_\mathrm{b}(p))\right| = \frac{\sqrt{A_\theta(p)}}{\left|p_\mathrm{A}(t_\mathrm{b}(p))\right|}. \tag{4.55b}$$

Similarly, in the three-step model for HHG the continuum wave packet is given by (assuming one trajectory per HHG peak)

$$a^{(a)}[-k(\omega)] = T^{(a)}(t_\mathrm{b}[p^{(\mathrm{A})}(\omega)]) \times p_\mathrm{H}(t_\mathrm{b}[p^{(\mathrm{A})}(\omega)]), \tag{4.56a}$$

$$a_\theta[-k(\omega)] = T_\theta(t_\mathrm{b}[p^{(\mathrm{A})}(\omega)]) \times p_\mathrm{H}(t_\mathrm{b}[p^{(\mathrm{A})}(\omega)]), \tag{4.56b}$$

where p_H describes the free propagation of the electron in the laser field for the HHG process and $p^{(\mathrm{A})}(\omega)$ is the ATI momentum that shares its birth time with the harmonic frequency ω. This means that we can express the continuum wave packet

as

$$\begin{aligned} a_\theta[-k(\omega)] &= a^{(a)}[-k(\omega)]\frac{T_\theta(t_\mathrm{b}[p^{(\mathrm{A})}(\omega)])}{T^{(a)}(t_\mathrm{b}[p^{(\mathrm{A})}(\omega)])} \\ &= a^{(a)}[-k(\omega)]\frac{\left|T_\theta(t_\mathrm{b}[p^{(\mathrm{A})}(\omega)])\right| e^{i\phi_\theta^{(T)}(t_\mathrm{b}[p^{(\mathrm{A})}(\omega)])}}{\left|T^{(a)}(t_\mathrm{b}[p^{(\mathrm{A})}(\omega)])\right| e^{i\phi_{(a)}^{(T)}(t_\mathrm{b}[p^{(\mathrm{A})}(\omega)])}} \\ &\simeq a^{(a)}[-k(\omega)]\sqrt{\frac{A_\theta[p^{(\mathrm{A})}(\omega)]}{A^{(a)}[p^{(\mathrm{A})}(\omega)]}}, \end{aligned} \tag{4.57}$$

where $\phi^{(T)}$ is the phase of T in the complex plane. The approximation $\phi_\theta^{(T)}(t) = \phi_{(a)}^{(T)}(t)$ for the last equality is based on the fact that the tunneling process is usually and quite accurately described by a real tunneling factor (Smirnova et al. [117]). In the Lewenstein model (Lewenstein et al. [71]), the contribution from a trajectory is proportional to a real ionization rate and inherits the phase from the lobe of the bound state it ionized from (see e.g., Eq. (5.109)). Multiplication of $a_\theta[-k(\omega)]$ with a global phase is irrelevant for the reconstruction. Therefore, in the Lewenstein model we can consider $\phi_0^{(T)}(t) = \phi_{(a)}^{(T)}(t)$ as fulfilled if the reference atom and molecule share I_p. The approximation $\phi_\theta^{(T)}(t) = \phi_0^{(T)}(t)$ also holds as long as we do not consider symmetric ionizing lobes with opposite signs. This shows that using ATI electrons we cannot overcome the limitation of conventional molecular orbital tomography that orbital symmetries cannot be measured (see the discussion in section 4.5).

To use Eq. (4.57), we need to know the best mapping from ATI peaks to harmonics peaks for a given pulse. Therefore we will derive an analytical expression for both processes in terms of sums over classical trajectories in chapter 5. In section 5.3.2 an ATI peak will be uniquely linked to every harmonic peak through the birth time of the electron giving rise to both peaks in the three-step model. In this model, an electron returning with momentum k will give rise to a harmonic order $\left(\frac{k^2}{2} + I_\mathrm{p}\right)/\omega_\mathrm{L}$. Therefore there are no links to ATI peaks available for harmonic peaks with an energy lower than I_p. For those low-energy peaks, as well as for other peaks for which no suitable link to an ATI peak can be found, the original relationship between the atomic and molecular $a(k)$ should be used. In this relationship, $\sqrt{\frac{A_\theta[p^{(\mathrm{A})}(\omega)]}{A^{(a)}[p^{(\mathrm{A})}(\omega)]}}$, the square root of the relative strength of an ATI peak, is replaced by the square root of the relative total ionization probabilities.

Starting from the simple-man's model for HHG, one needs to make two basic approximations for standard molecular tomography. Firstly, and most importantly, it is assumed that the tunneling step is identical for the atom and the molecule, independent of the alignment angle of the molecule in the laser field. Secondly, it is assumed that the propagation step for HHG is the same for the atom and the molecule. If instead we perform the molecular tomography including ATI electrons as proposed in this section, these assumptions are replaced with four, but much weaker, approximations. The first approximation is that the propagation step for HHG is the same for the atom and the molecule. The second approximation is that the same holds for the propagation step of ATI, i.e., that the propagation step for ATI is the same for the atom and the molecule.

The third assumption is that the tunneling amplitude T has the same phase for the atom and the molecule, as the ratio between the two tunneling amplitudes is assumed to be real. The tunneling itself is usually described by a real factor, so only a small error is expected here. However, T also includes the phase of the bound state with which the wave packet starts in the continuum. As a result, both the original and adapted tomography from this section cannot measure the symmetry of an orbital, as this phase then cancels out in the recombination. Furthermore it was recently found that for multi-electron systems nonadiabatic multi-electron rearrangements can produce an extra phase factor (Mairesse et al. [79]). The gravest assumption in the newly proposed technique is that there exists a one-to-one mapping for every harmonic peak to an ATI peak. As will be shown later, extremely short laser pulses can fulfill this last assumption, thereby opening the door for molecular tomography with additional information from ATI electrons.

4.8.2 Demonstration link between ATI and HHG

The formulas in section 4.8.1 can also be used to demonstrate the link between ATI and HHG as a fundamental phenomenon in strong-field physics. Comparing Eqs. (4.54) and (4.56), we see that for any atom or molecule we can write

$$\frac{\left|a^{(i)}[-k(\omega)]\right|}{\sqrt{A^{(i)}(p^{(\mathrm{A})}(\omega))}} = \frac{\left|p_{\mathrm{H}}(t_{\mathrm{b}}[p^{(\mathrm{A})}(\omega)])\right|}{\left|p_{\mathrm{A}}(t_{\mathrm{b}}[p^{(\mathrm{A})}(\omega)])\right|}, \tag{4.58}$$

where with the superscript '(i)' we label the atom or molecule. The right-hand side of equation (4.58) is independent of the system considered, as it only depends on the propagation properties of the electron in the laser field. Therefore plotting the left-hand side expression should produce a curve that is a measure of the laser pulse used, and not of the system subjected to that laser field. This means that if we plot the left-hand side as a function of ω for different molecules, the extent to which these curves are identical is a measure of the extent to which the one-to-one mapping between HHG and ATI works. Unfortunately it seems the plane-wave approximation for HHG is not justified in 1D, as we will see in section 4.9. Therefore it does not make much sense to compare $\left|a^{(i)}[-k(\omega)]\right| / \sqrt{A^{(i)}(p^{(\mathrm{A})}(\omega))}$ for different molecules in a 1D simulation. As at the moment of writing we did not perform any 2D or 3D simulations that incorporate ATI electrons, we will leave this to a later time.

4.8.2.1 Birth time

Instead, we demonstrate the links between HHG and ATI for extremely short pulses for a single molecule with the help of the procedure introduced in section 3.1.1.2 on page 28 to artificially turn off the pulse in the inner region gradually in space and time. We employ a 1D version of Eq. (3.6) with the following parameters. The laser pulse is completely turned off for $|x| \leq 8$ and left unaltered for $|x| \geq 10$. In the temporal domain we again use a characteristic temporal width of $0.1T$, where T is the laser period. In Fig. 4.17 we plot the normalized amplitudes of $a[-k(\omega)]$ and $\sqrt{A^{(i)}(p^{(\mathrm{A})}(\omega))}$ for three different harmonics ω and corresponding ATI momenta

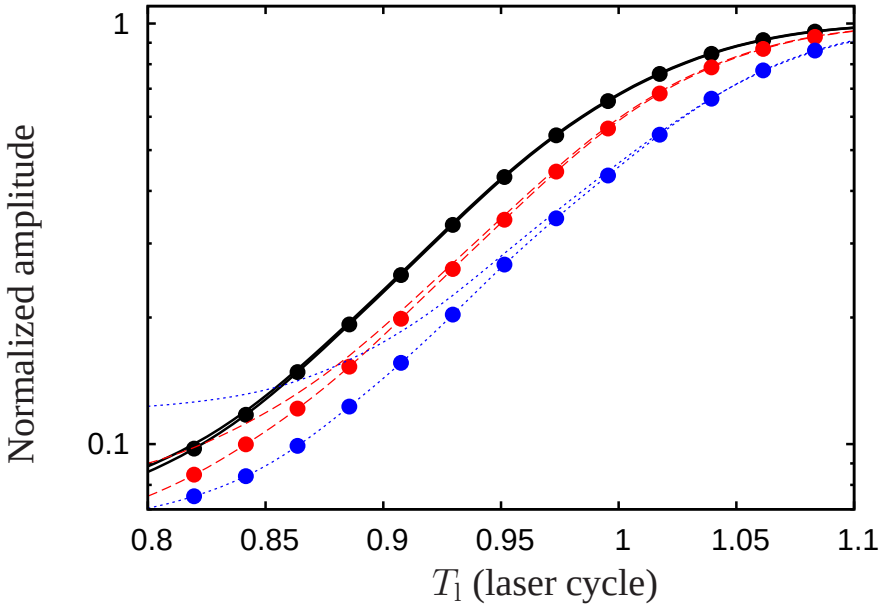

Figure 4.17: (Color online) Normalized $|a[-k(\omega)]|$ (linespoints) and $\sqrt{A(p^{(\mathrm{A})}(\omega))}$ (lines) as a function of T_l. We consider harmonic orders 100 (black solid lines), 150 (red dashed lines), and 200 (blue dotted lines).

$p^{(\mathrm{A})}(\omega)$ as a function of the turn-off time T_l. We use a laser intensity of 2×10^{14} W/cm^2 and a wavelength of 2000 nm. The pulse is a two-cycle sin^2-pulse with $\phi_{\mathrm{CEP}} = 1.25\pi$ rad. We consider here 1D H_2^+. The potential is given by

$$V(x) = -\frac{Z_1}{\sqrt{\left(x - \frac{R}{2}\right)^2 + a^2}} - \frac{Z_2}{\sqrt{\left(x + \frac{R}{2}\right)^2 + a^2}}. \tag{4.59}$$

We use $Z_1 = Z_2 = 0.730883$ a.u., $R = 2$ a.u. and $a^2 = 0.5$ to obtain a ground state with $I_\mathrm{p} = 30.2$ eV. The amplitudes of the continuum function $a[-k(\omega)]$ were convoluted with a Gaussian with a $1/e$-width of 6 harmonic orders and the ATI momentum spectrum was convoluted with a Gaussian with a $1/e$-width of 0.135 a.u.

The harmonic orders considered are 100, 150, and 200. From the SFA calculation that we will present in chapter 5 we find that these are associated with ATI momenta $p^{(\mathrm{A})}(\omega)$ equal to -1.49218, -1.83006, and -2.23151 a.u., respectively. We define $Q^{(h)}_{1\mathrm{to}1}(\omega)$ as the extent to which the trajectories born at $t_\mathrm{b}[p^{(\mathrm{A})}(\omega)]$ determine the spectra at harmonic ω and ATI momentum $p^{(\mathrm{A})}(\omega)$. Here $Q^{(h)}_{1\mathrm{to}1}(\omega) = 0$ means there is no link between the two spectra and $Q^{(h)}_{1\mathrm{to}1}(\omega) = 1$ means trajectories born at $t_\mathrm{b}[p^{(\mathrm{A})}(\omega)]$ completely determine both spectral peaks. We postpone the exact definition of $Q^{(h)}_{1\mathrm{to}1}(\omega)$ and a detailed discussion on how to find the links to section 5.3.2. For the three HHG-ATI pairs of Fig. 4.17, we have $Q^{(h)}_{1\mathrm{to}1} = 0.997$, $Q^{(h)}_{1\mathrm{to}1} = 0.986$, and $Q^{(h)}_{1\mathrm{to}1} = 0.802$, respectively.

Initially, for low T_l, the three HHG and ATI peaks are all suppressed. For later T_l, first harmonic order 100, then harmonic order 150 and finally harmonic order

200 revives. We observe that the ATI peaks are revived at the same time and with the same speed as their corresponding HHG peaks. This demonstrates clearly the shared birthtimes between the ATI and HHG peaks.

4.8.2.2 Variation CEP

The links between HHG and ATI peaks can be used to express the variation of the amplitude of an ATI peak in terms of the variation of a HHG peak upon varying the laser pulse used. Specifically, based on Eq. (4.58), we expect that

$$\frac{\Delta\left(\left|a^{(i)}[-k(\omega)]\right|\right)}{\left|a^{(i)}[-k(\omega)]\right|} = \frac{\Delta\left(\frac{\left|p_{\mathrm{H}}(t_{\mathrm{b}}[p^{(\mathrm{A})}(\omega)])\right|}{\left|p_{\mathrm{A}}(t_{\mathrm{b}}[p^{(\mathrm{A})}(\omega)])\right|}\sqrt{A^{(i)}(p^{(\mathrm{A})}(\omega))}\right)}{\frac{\left|p_{\mathrm{H}}(t_{\mathrm{b}}[p^{(\mathrm{A})}(\omega)])\right|}{\left|p_{\mathrm{A}}(t_{\mathrm{b}}[p^{(\mathrm{A})}(\omega)])\right|}\sqrt{A^{(i)}(p^{(\mathrm{A})}(\omega))}}, \tag{4.60}$$

where the Δ is taken on a small variation of the laser pulse. Even if Eq. (4.58) holds only up to an additional factor that changes slowly upon a variation of the laser pulse, Eq. (4.60) can be used to predict the variation of an ATI peak based on the variation of the amplitude of the corresponding HHG peak.

In Fig. 4.18a we plot the right-hand side of Eq. (4.60) as a function of the left-hand side of Eq. (4.60) for 100 different two-cycle 2000-nm pulses with an intensity of 2×10^{14} W/cm^2. The laser pulses have $\phi_{\mathrm{CEP}} = 0$–π rad and the molecule is the same as in section 4.8.2.1. We consider sets of HHG and ATI peaks that fulfill the criteria

$$\omega \geq 100\omega_{\mathrm{L}}, \tag{4.61a}$$

$$|p^{(\mathrm{A})}| \geq 1.05, \tag{4.61b}$$

$$\left|\frac{\Delta\left(p^{(\mathrm{A})}\right)}{p^{(\mathrm{A})}}\right| \leq 0.01, \tag{4.61c}$$

$$Q_{1\mathrm{to}1}^{(h)} \geq 0.95, \tag{4.61d}$$

where $\Delta\left(p^{(\mathrm{A})}\right)$ is the variation of the ATI momentum upon varying ϕ_{CEP}. For Fig. 4.18 we evaluate p_{H} and p_{A} using the SFA expressions for the HHG and ATI yields that we will derive in chapter 5. More specifically, we approximate p_{H} as everything after $d_{\mathrm{ion},\theta}$ in Eq. (5.108) and p_{A} as the two terms after $d_{\mathrm{ion},\theta}$ in Eq. (5.129). We would like to stress that in Fig. 4.18a the variations of the spectral amplitudes are calculated with respect to the previous CEP-value, and not with respect to a common reference.

From Fig. 4.18 the correlation between the HHG and ATI amplitude variations is clear; there is a strong correspondence between the behavior of the HHG and ATI amplitudes as a function of ϕ_{CEP}. In Fig. 4.18b we show that this correspondence cannot be explained through the norms of the two spectra. Plotted here are the square root of the harmonic intensities summed over the complete harmonic range and the square root of $A(p)$ summed over the complete momentum range, both scaled. As a function of ϕ_{CEP}, the norm of the HHG spectrum is almost constant

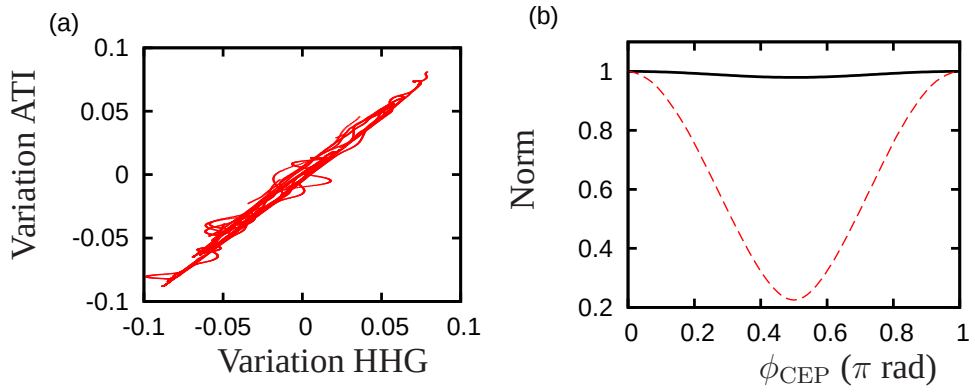

Figure 4.18: (Color online) (a) Right-hand side of Eq. (4.60) versus left-hand side of Eq. (4.60) for small CEP variations. (b) Scaled norms of the HHG spectrum (black solid line) and ATI spectrum (red dashed line) as a function of ϕ_{CEP}.

compared to the norm of the ATI spectrum. This shows that it is not possible to quantitatively predict the variation of an ATI peak based solely on the norm of the entire HHG spectrum.

4.8.2.3 Variation internuclear separation

Alternatively, we demonstrate the links between HHG and ATI for different molecules using the approximation that the recombination matrix element has the same amplitude for these molecules. We consider 1D H_2^+ with varying internuclear distances from $R = 1.6$–3.2 a.u. The molecules have $Z_1 = Z_2 = 0.730883$ a.u. and the softness parameter adjusted such that $I_{\mathrm{p}} = 30.2$ eV. We approximate Eq. (4.58) as

$$\frac{\left|\alpha^{(i)}(\omega)\right|}{\sqrt{A^{(i)}(p^{(\mathrm{A})}(\omega))}} \simeq z(\omega), \tag{4.62}$$

where $z(\omega)$ is independent of the molecule. In Fig. 4.19 we plot the normalized amplitudes of $\alpha^{(i)}(\omega)$ and $\sqrt{A^{(i)}(p^{(\mathrm{A})}(\omega))}$ as a function of internuclear distance R for the same set of harmonics and ATI peaks as in Fig. 4.17. The amplitudes of $\alpha^{(i)}(\omega)$ were convoluted with a Gaussian with a $1/e$-width of 6 harmonic orders.

The approximation that the amplitude of the recombination matrix element is independent of R is not well justified and it introduces errors. Nonetheless we observe the relationship between the HHG and ATI peaks in Fig. 4.19. The amplitude of harmonic order 100 and its corresponding ATI peak increase as a function of R. In contrast, harmonic order 200 first increases, and then decreases as a function of R, just like its corresponding ATI peak. Harmonic order 150 and its corresponding ATI peak show intermediate behavior. A modulation of the yields is visible superimposed on the trends. Note that the modulation of an ATI peak has the same phase and strength as the modulation of the corresponding HHG peak. This shows that it is the ionization rate that is modulated as a function of R. Trajectory interferences cannot play a role as $Q_{1\mathrm{to}1}^{(h)} \sim 1$ means only a single trajectory contributes to both

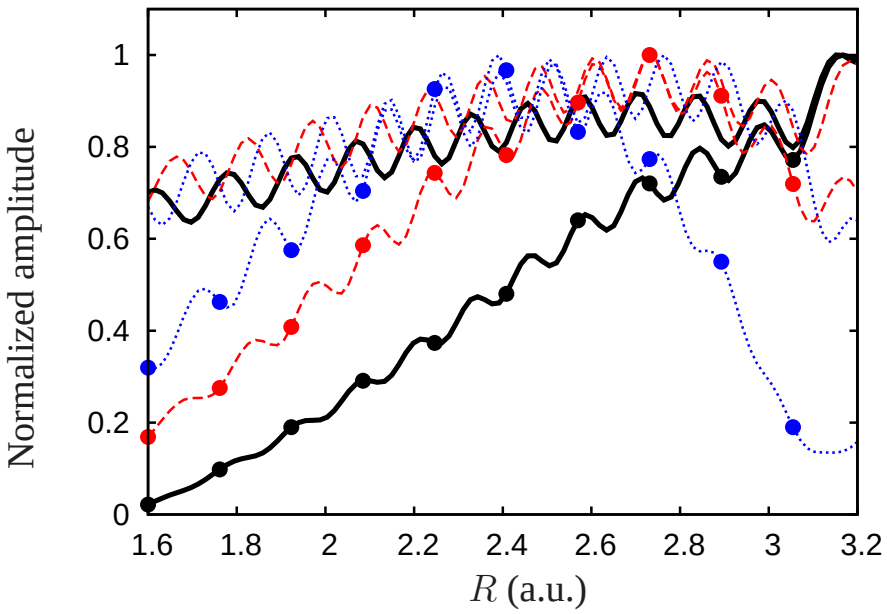

Figure 4.19: (Color online) Normalized $|\alpha^{(i)}(\omega)|$ (linespoints) and $\sqrt{A^{(i)}(p^{(\mathrm{A})}(\omega))}$ (lines) as a function of R for the harmonics and ATI peaks from Fig. 4.17.

HHG and ATI. The reason behind the ionization rate modulation is unknown at the moment. We have confirmed it is not related to the spatial grid spacing.

If instead one uses $\left|a^{(i)}[-k(\omega)]\right|$ in either length or velocity form, one observes wild behavior as a function of R and no correlation between the HHG and ATI peaks can be seen (not shown). This is probably related to the fact that the plane-wave approximation is not well justified in 1D. Artificial peaks are introduced to $a^{(i)}[-k(\omega)]$ when a minimum in the matrix element does not coincide with a minimum in the spectrum.

4.9 1D Molecular orbital tomography

In 1D molecular orbital tomography takes a slightly different form than in 2D. The length-form matrix element Eq. (4.1) in 1D is given by

$$d_j[\omega(k)] = \int \psi_0(x)(jx)e^{-jikx}dx, \tag{4.63}$$

where $j = \pm$. The derivation in section 4.1.1 reduces to inverting a single 1D Fourier transform and the tomographic reconstruction Eq. (4.17) simplifies to

$$\psi_0(x) = \frac{1}{2\pi}\frac{1}{x}\int \frac{d_+(\omega)e^{ik(\omega)x} - d_-(\omega)e^{-ik(\omega)x}}{k(\omega)}\left(1 - \frac{dc_{\mathrm{I}}(\omega)}{d\omega}I_{\mathrm{p}}\right)d\omega. \tag{4.64}$$

For a constant $c_{\mathrm{I}}(\omega)$ this reduces to

$$\psi_0(x) = \frac{1}{2\pi}\frac{1}{x}\int \frac{d_+(\omega)e^{ik(\omega)x} - d_-(\omega)e^{-ik(\omega)x}}{k(\omega)}d\omega. \tag{4.65}$$

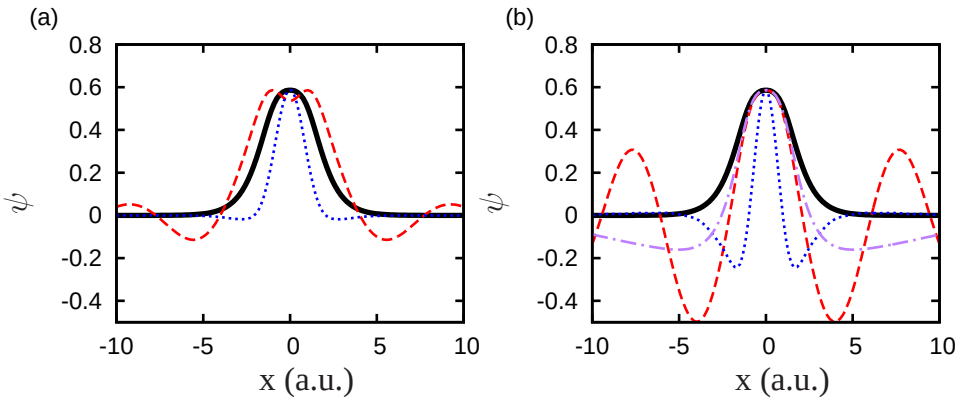

Figure 4.20: (Color online) Ground state of 1D H_2^+ (black solid line) and tomographic reconstruction using $k(\omega) = \sqrt{2\omega}$ (red dashed line) and $k(\omega) = \sqrt{2(\omega - I_p)}$ (blue dotted line); (a) using length-form reconstruction, (b) using velocity-form reconstruction. In plot (b) we also show a reconstruction using exact matrix elements (purple dot-dashed line).

The velocity-form matrix element Eq. (4.19) in 1D is given by

$$p_j[\omega(k)] = \int \psi_0(x) e^{-jikx} dx. \tag{4.66}$$

The velocity-form reconstruction Eq. (4.23) reduces to.

$$\psi_0(x) = \frac{1}{2\pi} \int \frac{p_+(\omega) e^{ik(\omega)x} + p_-(\omega) e^{-ik(\omega)x}}{k(\omega)} d\omega, \tag{4.67}$$

where we assumed a constant $c_I(\omega)$. In case of a mirror symmetry S with respect inverting x ($\psi_0(-x) = S\,\psi_0(x)$), Eq. (4.48) still holds as

$$d_-(\omega) = S\, d_+(\omega), \tag{4.68a}$$
$$p_-(\omega) = S\, p_+(\omega). \tag{4.68b}$$

In Fig. 4.20 we plot the result of a tomographic simulation for the 1D H_2^+-model with $R = 2$ a.u. from section 4.8.2. For the reconstruction we employ a three-cycle $\sin^2$-pulse with $\phi_{CEP} = 1.25\pi$ rad at an intensity of $I = 2 \times 10^{14}$ W/cm^2 and wavelength $\lambda = 2000$ nm. The reference atom is 1D He with $Z = 1.46177$ and $a^2 = 0.85527$, and possesses an identical ionization potential. On the left in Fig. 4.20 we plot the result for length-form reconstruction and on the right for velocity-form reconstruction, in both cases for two different dispersion relationships. For the given experimental parameters the frequency range used for the reconstruction runs from harmonic 2.5 to harmonic 452, as given by Eq. (4.43).

It is clear that the reconstructions are disappointing, especially considering the long wavelength used. Velocity-form reconstruction seems to tend to a too localized function at the origin for $k(\omega) = \sqrt{2(\omega - I_p)}$ and a nonlocalized state for $k(\omega) = \sqrt{2\omega}$. Only length-form reconstruction with $k(\omega) = \sqrt{2\omega}$ provides something that resembles the original orbital, but still with rather large errors. Using exact plane-wave

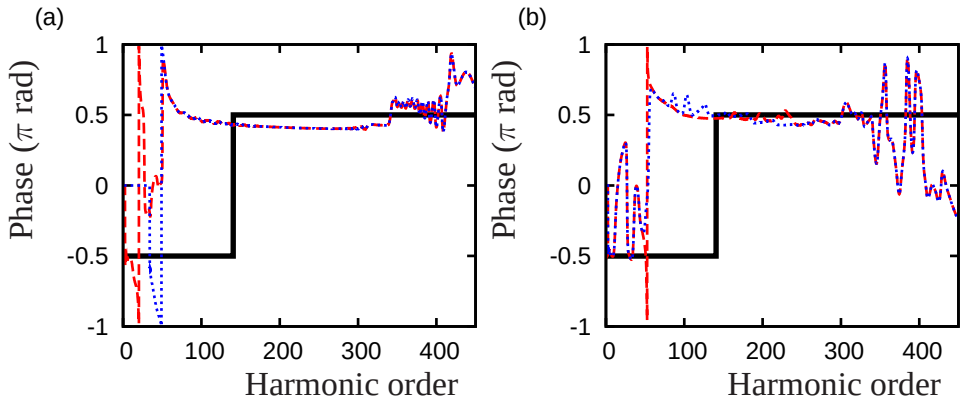

Figure 4.21: (Color online) Phase of $d(\omega)$ for the ground state of Fig. 4.20 (black solid line) and retrieved from the tomographic reconstruction; (a) using $k(\omega) = \sqrt{2\omega}$ (red dashed line) and using $k(\omega) = \sqrt{2(\omega - I_\mathrm{p})}$ (blue dotted line), (b) using $k(\omega) = \sqrt{2\omega}$ and 10 two-cycle pulses (red dashed line) and additionally incorporating ATI electrons (blue dotted line).

matrix elements limited to the experimental harmonic range, the length-form reconstruction is almost perfect (not shown), whereas the velocity-form reconstruction already contains significant errors. The problem with 1D tomography might be related to the lack of the perpendicular dimension. The electron wave packet can only spread out in the polarization direction. Therefore its approximation as a sum of plane waves loses validity and its interaction with the molecular core is less well described by a Fourier transform of the bound state orbital.

We tried to improve the reconstruction by employing 10 different two-cycle 2000-nm pulses with ϕ_CEP ranging from 0.0–0.9π rad at the same intensity of 2×10^{14} W/cm^2, following the prescription that will be given in section 5.3.1.2. We obtained only a marginal—if any—improvement to the reconstruction (not shown). Also there was no difference visible if we added information from ATI electrons to the 10-pulse reconstruction, following the prescription that will be given in section 5.3.2.2 (also not shown). There are probably two reasons for these observations.

Firstly, in 1D tomographic reconstruction does not really seem to work, as we saw in Fig. 4.20. This can also be seen in Fig. 4.21, where we plot the phase of the length-form recombination matrix element as a function of harmonic order. The exact phase is flat with a π-jump around harmonic 140. Independent of the dispersion relationship, there is no phase jump reproduced around harmonic order 140 (left plot). Even though both 10-pulse reconstructions flatten the phase over some harmonic ranges, the location of the phase jump is not altered and therefore the reconstruction not significantly improved. The reason the curve for $k(\omega) = \sqrt{2(\omega - I_\mathrm{p})}$ has non-zero values below I_p is that also for the 1D case we convolute the matrix elements with a Gaussian filter with a $1/e$-width of $6\omega_\mathrm{L}$. There seems to be a problem with 1D tomography or our implementation of it that is too fundamental to be corrected by the rather subtle methods employed here. The incorporation of ATI electrons into the reconstruction can only improve the amplitude but not the phase of the reconstruction matrix elements (see Eq. (4.57)).

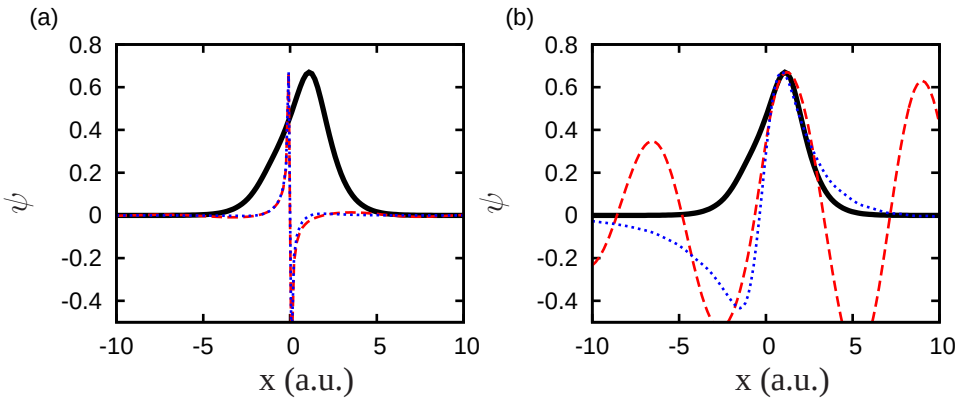

Figure 4.22: (Color online) Same as Fig. 4.20 for the ground state of 1D HeH^{2+}.

The second reason is specifically related to the lack of improvement from incorporating ATI electrons in the 1D case. ATI inclusion adds to standard tomography an orientation-dependence of the ω-dependent ionization rate. In other words, in standard molecular tomography the same ionization probability $P_1(\theta)$ is used for all harmonics. In a 1D symmetric molecule, there is only one orientation and therefore no variation of the harmonic-dependent ionization rate as a function of θ. Therefore a big advantage of ATI-included tomography over standard tomography is lost in a 1D simulation of the scheme. A small correction from an improved determination of the ω-dependent ionization rate should still be present.

For completeness we plot in Fig. 4.22 the result of a tomographic simulation for 1D HeH^{2+}. Its potential is given by $R = 2.5$ a.u., $Z_1 = 0.487255$ a.u., $Z_2 = 0.974511$ a.u. and $a^2 = 0.477255$. As a reference state we use the same state as for 1D H_2^+. The antisymmetric component of the asymmetric orbital causes the length-form reconstructions on the left to diverge at the origin. However, just as in the previous case, also the velocity-form reconstructions are not accurate.

4.10 Multi-electron contributions

Up to now we have assumed that there was only a single electron contributing to HHG. In other words, our analysis and simulations so far are all based on the single-active-electron approximation (SAE). Although the SAE can be very useful in understanding HHG, contributions from more deeply bound electrons to the spectra can be found, as discussed in section 2.3.3. For molecular tomography it has been claimed that in a multi-electron system one does not retrieve the HOMO, but instead one obtains a Dyson orbital plus exchange correction terms (Patchkovskii et al. [99, 100]; Santra and Gordon [111]). In length form, the dipole matrix elements Eq. (4.1) are replaced by

$$\mathbf{d}[\omega(k)] = \langle \psi^{\mathrm{D}}(\mathbf{r}_n)|\mathbf{r}_n|\chi(x_n)\rangle + \mathbf{d}^{\mathrm{ex}}, \tag{4.69a}$$

$$\psi^{\mathrm{D}}(\mathbf{r}_n) = \sqrt{n}\langle \Psi_0(\mathbf{r}_1,\ldots,\mathbf{r}_n)|\Psi^+(\mathbf{r}_1,\ldots,\mathbf{r}_{n-1})\rangle. \tag{4.69b}$$

Here we consider an n-electron system and $\mathbf{r}_i$ is the electron coordinate of the i-th electron. The one-electron Dyson orbital ψ^{D} is given by the overlap between the n-electron ground state of the neutral Ψ_0 and the $n-1$-electron ground state of the ion Ψ^+. The continuum wave function $\chi(x_n)$ is a plane wave under the plane-wave approximation. Furthermore $\mathbf{d}^{\mathrm{ex}}$ is an exchange correction that corresponds to the indistinguishability of the n electrons.

The above multi-electron correction to Eq. (4.1) can be put in a physically insightful form under two assumptions; firstly we assume that Ψ_0 and Ψ^+ can be represented using single Slater determinants, i.e., as antisymmetrized products of single-electron orbitals (the Hartree-Fock framework). Secondly, we assume that the ion does not relax after removal of one electron, i.e., Ψ^+ is built with the same single-electron orbitals ψ_i as Ψ_0 consists of except for the active orbital ψ_n (Koopmans' approximation). Then the contributions to $\mathbf{d}[\omega(k)]$ take the form

$$\psi^{\mathrm{D}}(\mathbf{r}_n) \simeq \psi_n(\mathbf{r}_n), \tag{4.70a}$$

$$\mathbf{d}^{\mathrm{ex}} \simeq \langle \sum_{i=1}^{n} \mathbf{d}_{ii}\psi_n(\mathbf{r}_n) - \sum_{i=1}^{n-1} \mathbf{d}_{in}\psi_i(\mathbf{r}_n) | \chi(x_n) \rangle, \tag{4.70b}$$

$$\mathbf{d}_{ij} = \langle \psi_i | \mathbf{r} | \psi_j \rangle. \tag{4.70c}$$

Note that the exchange correction term results from taking the plane-wave approximation; $\mathbf{d}^{\mathrm{ex}}$ vanishes under the above approximations for an exact continuum wave $\chi(x_n)$.

An inversion of Eq. (4.70) (Patchkovskii et al. [99]) shows that in the Hartree-Fock framework and under the Koopmans' approximation, the reconstructed quantity $\psi_0(\mathbf{r})\mathbf{r}$ in Eq. (4.13) is replaced with

$$\psi_0(\mathbf{r})\mathbf{r} \to \psi^{\mathrm{D}}(\mathbf{r})\mathbf{r} + \sum_{i=1}^{n} \mathbf{d}_{ii}\psi_n(\mathbf{r}) - \sum_{i=1}^{n-1} \mathbf{d}_{in}\psi_i(\mathbf{r}). \tag{4.71}$$

From Eq. (4.71) we see that there is an exchange correction to the reconstructed orbital from the total permanent dipole moment of the molecule (second term), and also from the transition dipole moments between the HOMO and occupied lower-lying one-particle orbitals (third term). The total permanent dipole vanishes for (un-)gerade orbitals, so that for those molecules we are only left with the correction from the transition dipole moments. Since the exchange correction is a vector, the deviation of the reconstructed orbital from the HOMO depends on the component of Eq. (4.71) considered. For N_2 the experimentally reconstructed orbital more closely resembles the theoretical prediction from Eq. (4.71) than the pure HOMO (Patchkovskii et al. [99]).

The exchange correction vanishes for directions perpendicular to an axis on which the projection of the angular momentum vanishes for all occupied orbitals (Patchkovskii et al. [100]). The number of components of Eq. (4.71) could be extended from two (x and y) to three (x, y and z) by repeating the experiment appropriately after either rotating the molecules in a plane other than the xy-plane, or using a probe beam propagating in the x- or y-directions. In a system where only a limited of orbitals

contribute, and the exchange corrections vanish for certain components, it might be possible to reconstruct the full electronic wave function by just considering HHG from the HOMO (Patchkovskii et al. [99]); the Dyson orbital, closely resembling the HOMO, is obtained from a component with vanishing exchange correction. Then the Dyson orbital can be subtracted from the other components to retrieve some of the lower-lying orbitals.

Alternatively, molecular tomography can be extended to reconstruct not only the HOMO but also some lower-lying orbitals if the contributions to the spectrum of these orbitals are strong but separable because of symmetry reasons (Zhao et al. [136, 137]). This has been demonstrated experimentally for N_2 in an experiment where the HOMO was reconstructed and signatures from the HOMO-1 were seen (Haessler et al. [46]).

4.11 Experimental considerations

In achieving a molecular tomographic reconstruction an experimentalist has to overcome many technical difficulties. In this section we will stipulate a few for the understanding of a theorist, or as a basic overview.

4.11.1 Molecular orientation and alignment

The difference between orientation and alignment is that under alignment one does not distinguish between molecules oriented at $\theta = 0°$ or $\theta = 180°$. It has been shown that orientation of nonpolar molecules cannot be achieved using one-color pulses (Gershnabel et al. [41]; Ohmura et al. [97]). On the other hand, it has also been shown that a molecule with a permanent dipole moment can be oriented in three-dimensional space (Tanji et al. [122]). In this subsection we focus on the for molecular imaging typical case of two-dimensional alignment of symmetric molecules. Here the alignment distribution along an azimuthal angle—typically around the laser polarization direction—is left undisturbed. For symmetric molecules there is no difference between alignment and orientation. Such a molecule also never possesses a permanent dipole, forcing the experimentalist to attempt to align molecules using laser-induced dipole moments.

If the polarizability tensor of the molecule is anisotropic, the interaction of an induced dipole with the laser field produces a potential well in the direction of the most-polarizable axis (for linear molecules the internuclear axis). This potential is known as the angular AC Stark shift. Averaged over one laser cycle its depth is proportional to the difference in polarizability between the most- and second-most-polarizable axis and to the laser intensity (Friedrich and Herschbach [36]). Classically, the torque that the molecules experiences is related to the angle θ its most polarizable axis makes with the laser polarization direction. Quantum-mechanically this corresponds to the excitation of a coherent superposition of rotational eigenstates. The alignment can be done adiabatically or non-adiabatically (for an excellent review see Haessler [45] and references therein).

The standard measure for the achieved degree of alignment is $\langle\cos^2\theta\rangle$. Here maximum alignment corresponds to $\langle\cos^2\theta\rangle = 1$ and maximum anti-alignment to $\langle\cos^2\theta\rangle = 0$. For linear molecules such as H_2^+ and HeH^{2+}, the force on the molecules works in the plane formed by the internuclear and the laser polarization axes. For an initially isotropic distribution of linear molecules, the cylindrical symmetry around the laser polarization direction is conserved. For such molecules anti-alignment therefore means that the internuclear axes are oriented in a disk-shaped distribution at $\theta = \pi/2$. An isotropic distribution corresponds to $\langle\cos^2\theta\rangle = 1/3$.

In adiabatic alignment, a low-intensity laser pulse with a minimum length on the order of a rotational period of the molecule is used (Friedrich and Herschbach [36]; Larsen et al. [61]; Sakai et al. [108]; Seideman [113]). During such a pulse, the molecules are slowly aligned along the laser polarization axis, but the alignment is lost after the pulse is over. Experiments on aligned molecules can therefore only be done in the presence of the laser field that perturbs the molecules. Much better for molecular imaging experiments is the use of non-adiabatic alignment. Here a relatively intense pulse (typically 10^{13}–10^{14} W/cm^2) with a length much shorter than the rotational period (typically 20–100 fs) is used to impulsively align the molecules (Rosca-Pruna and Vrakking [107]; Seideman [114]). Because of the coherence of the rotational wave packet created, revivals of the molecular alignment occur at multiples of the rotational period (on the order of picoseconds for small molecules), allowing for the actual imaging processes to take place in laser-field-free situations. Typical molecular imaging experiments use a pump-probe setup, where the pump aligns the molecules and the stronger probe pulse, that is delayed by one rotational period of the molecule studied, initiates strong-field processes.

There have been several methods proposed to improve the experimentally achieved degree of alignment, which also depends on the initial rotational temperature of the sample. It is possible to combine the adiabatic and non-adiabatic alignment techniques (Poulsen et al. [104]). Using two almost parallel aligning pulses, planes of alignment are created (Mairesse et al. [78, 81]). The high-harmonics from these planes are predominantly emitted at certain diffraction angles, effectively creating much better alignment of the molecules. Furthermore, evolutionary algorithms can be employed to optimize the alignment (Horn et al. [50]). Instead of aligning molecules, we can also take advantage of a preferred ionization direction—if present—by using two orthogonally polarized pulses to achieve directional sensitivity, thereby avoiding the experimental difficulties associated with aligning molecules altogether (Kitzler and Lezius [56]).

4.11.2 Phase-locked few-cycle pulses

A laser cavity can amplify light whose wavelength fits an integer times in a round trip through the cavity. Therefore a laser does not emit light of a single frequency, but instead many different frequency modes are supported. For the simplest case of an empty Fabry-Pérot (parallel and flat mirrors) cavity with length L, the modes are separated by angular frequency $\Delta\omega = \frac{\pi c}{L}$. Depending on the bandwidth of the gain medium, between a few and on the order of a million cavity modes are excited. High gain-bandwidth media, such as the nowadays omnipresent titanium-doped sapphire

(Ti:Sapph) crystals, can be used for the generation of ultrashort pulses because of the broad frequency range and many cavity modes excited. Normally the cavity modes operate independently and have no fixed phase relationships, leading to a randomly fluctuating output intensity. To generate ultrashort pulses, the cavity modes have to be phase locked in a process called *mode locking*. Mode locking can be done actively or passively, but for the generation of ultrashort pulses in the femtosecond regime only passive mode locking is suitable, as no fast enough active methods are available.

Passive mode locking is based on a saturable absorber inside the laser cavity that becomes satisfied when a strong pulse passes and thereby effectively stimulates the formation of short pulses, i.e., the concentration of pulse energy. The difference in absorption during the pulse and at other times can be small (e.g., 1%) because of the many passes of the light in the cavity. There are many ways to make a saturable absorber, for example semiconductor mirrors can be used, but for the generation of ultrashort pulses Kerr lenses are most common. When propagating in a medium, a strong laser pulse affects the refractive index of the material through which it travels by polarizing it. In strong-field physics especially the second-order term, the *Kerr* effect, is important. It is given by

$$\Delta n = n_2 \, I, \tag{4.72}$$

where I is the laser intensity and n is the refractive index. When a strong pulse propagates through a medium, the spatial center of the beam profile experiences the highest intensity, and therefore the highest local refractive index, as normally $n_2 > 0$. As a result the wave front is deformed, and the beam self-focusses. This is then combined with a small aperture or a narrow pump beam to achieve the formation of ultrashort pulses by relative attenuation of the non-peak-intensity-part at every loop through the cavity. A nice introduction and reference for laser technology is the online encyclopedia provided by RP Photonics Consulting GmbH (Paschotta [98]).

To further compress the pulse from roughly 20–200 fs to the few-cycle regime ($\lesssim 8$ fs), usually a hollow-fiber compression technique is used (see for example the excellent review by Nisoli and Sansone [94]). Propagation inside a gas-filled hollow fiber leads to spectral broadening (Nisoli et al. [95, 96]). In a medium with $n_2 > 0$ the center of the pulse envelope is dynamically delayed compared to the leading and trailing edges due to the Kerr effect, a process called *self-phase modulation*. Initially the output pulse after a hollow-fiber can be even longer than the input pulse, but because of its broader bandwidth pulse compression can be achieved by removing the well-behaved chirp[1] introduced by the fiber using linear chromatic dispersion, e.g., using two prisms (see e.g. Paschotta [98]). Sub-5-fs pulses have been generated using tapered hollow fibers with smaller output than input diameter (Caumes et al. [15]), and 3.8-fs pulses were generated using two gas-filled hollow fibers and ultrabroadband dispersion compensation using a liquid-crystal spatial light modulator that in combination with (for example) two gratings allows for

[1] The chirp of a laser pulse is the time-dependence of its instantaneous frequency. A linear positive chirp corresponds for instance to a pulse where the instantaneous frequency increases linearly with time.

complete spectral phase control (Schenkel et al. [112]). High-energy 5.4-fs pulses that could be focussed up to an estimated 5×10^{18} W/cm^2 have been obtained using a hollow fiber with a pressure gradient (Bohman et al. [10]; Suda et al. [120]).

For few-cycle pulses the exact evolution of the electric field—and not just its envelope—becomes important. The electric field of such a pulse can be described by a real envelope times a carrier wave as

$$E(t) = f(t)e^{i(\omega t+\phi_{\mathrm{CEP}})}, \tag{4.73}$$

where ω is the central frequency of the pulse and $f(t)$ is its real envelope. Chromatic dispersion ($n = n(\lambda)$) and nonlinear effects lead to variations from pulse to pulse. The pulse-to-pulse variations correspond to variations in the carrier-envelope phase ϕ_{CEP} that are encoded in the spectrum as an offset ω_0 of the frequency comb. This can be seen by considering a frequency comb $\omega_n = n\omega_{\mathrm{rep}} + \omega_0$ with $\omega_{\mathrm{rep}} = \frac{2\pi}{T}$. Here T is the time between two pulses (the cavity roundtrip time). The electric field of a pulse can then be written in terms of the electric field of the previous pulse as[2]

$$E(t+T) = e^{i\frac{\omega_0}{\omega_{\mathrm{rep}}}2\pi}E(t) = f(t)e^{i\left(\omega t+\phi_{\mathrm{CEP}}+\frac{\omega_0}{\omega_{\mathrm{rep}}}2\pi\right)}. \tag{4.74}$$

The last equality shows that an offset ω_0 leads to $\Delta\phi_{\mathrm{CEP}} = \frac{\omega_0}{\omega_{\mathrm{rep}}}2\pi$, where $\Delta\phi_{\mathrm{CEP}}$ is the pulse-to-pulse CEP variation.

The CEP can be stabilized either actively or passively (Nisoli and Sansone [94]). Active stabilization works by spreading the frequency spectrum over a full octave, and then frequency-doubling the low end of the spectrum to let it interfere with the high end of the spectrum in a f-to-$2f$ interferometer (Apolonski et al. [1]; Jones et al. [53]; Telle et al. [123]). The resulting lowest-frequency beat signal has frequency ω_0. A feedback loop is used to control the CEP using some means of active phase stabilization, e.g., via the pump power, by slightly tilting a resonator mirror, or by inserting a glass wedge to a variable extent (Paschotta [98]). The f-to-$2f$ setup itself causes a slow CEP drift that can be monitored and corrected using a second f-to-$2f$ interferometer (Baltuška et al. [5]). Then residual phase fluctuations can be kept below 100 mrad. On the other hand, passive CEP stabilization works by difference frequency generation from two parts of the spectrum (Baltuška et al. [4]; Vozzi et al. [130]). The resulting lower frequency pulse automatically has $\phi_{\mathrm{CEP}} = 0$.

4.11.3 Measurement of harmonic phases

As mentioned in section 4.1.1, the initial experiment on molecular orbital tomography was performed without measuring the harmonic phases, which were added

[2] The frequency comb $\omega_n = n\omega_{\mathrm{rep}} + \omega_0$ corresponds to an electric field

$$E(t) = \sum_{n=1}^{\infty} \tilde{E}_n e^{i\omega_n t},$$

where $\tilde{E}_n$ is the complex amplitude of the n-th frequency component. One pulse later the electric field is given by

$$E(t+T) = \sum_{n=1}^{\infty} \tilde{E}_n e^{i(n\omega_{\mathrm{rep}}+\omega_0)(t+\frac{2\pi}{\omega_{\mathrm{rep}}})} = e^{i\frac{\omega_0}{\omega_{\mathrm{rep}}}2\pi}E(t).$$

by hand from *a priori* considerations (Itatani et al. [52]). Although possible, it is far from trivial for an experimentalist to measure harmonic phases, or equivalently, if also the harmonic spectrum is considered at the same time, the time profile of the emitted radiation. The reason is that the radiation takes place on an attosecond time scale. Normally time profiles of physical processes are obtained using a measurement device that operates faster than the characteristic time scale of the process. In this case such faster-operating measurement tools are very rare and are associated with large energy bandwidths[3]. Therefore alternative approaches are used to measure the harmonic phases.

As an introduction to these alternative approaches, consider the characterization of femtosecond pulses. Here many of the same problems in measuring the electric field already occur. Two widespread techniques are *Frequency-Resolved Optical Gating* (FROG) and *Spectral Phase Interferometry for Direct Electric-Field Reconstruction* (SPIDER) (Nisoli and Sansone [94]). An autocorrelation of the pulse can be measured using two copies of the pulse with a variable delay interacting with a nonlinear medium, for example a second-harmonic-generation crystal. This however only provides a rough measure of the length of the pulse, and no details of the electric field are obtained. If instead of only measuring the total intensity emitted by a nonlinear medium as a function of the delay time between the two pulses (a standard autocorrelation), one measures the nonlinear emission spectrally resolved, one obtains a FROG trace (Trebino [128]). In contrast to the 1D autocorrelation, the 2D FROG trace contains enough information to completely characterize the optical pulse. The retrieval process iteratively converges to the unique solution that satisfies all the constraints and can be done for example using the widely-spread PCGPA-algorithm (Kane [54]).

Alternatively, SPIDER works by creating two copies of the pulse that are delayed and then mixed with a chirped picosecond pulse in a nonlinear medium (Iaconis and Walmsley [51]). This creates a frequency offset between the two copies of the femtosecond pulse given by the delay between the two copies. Then a spectrogram of the two frequency-shifted femtosecond-pulse copies is recorded. If the pulses are delayed by a time τ much larger than the length of the pulse, in the spectrogram fringes with a period of roughly $\frac{2\pi}{\tau}$ appear[4]. Here τ is chosen such that multiple fringes per independent frequency component appear. The spectral shear between the two copies leads to an interference between two frequency-shifted components of the original pulse at each frequency component. The phase differences between neighboring frequency components and thereby the phases of the Fourier components of the pulse are encoded in the deviations from the nominal fringe spacing if the spectral shear is chosen small enough. The inversion requires only two 1D Fourier transforms to fully characterize the electric field of the femtosecond pulse (Iaconis

[3] From the Heisenberg uncertainty relationship

$$\Delta E \Delta t \geq \frac{\hbar}{2} \overset{\text{a.u.}}{=} \frac{1}{2}$$

it follows that a time resolution of $\Delta t = 1$ a.u. $\simeq 24.2$ as is associated with an energy uncertainty of $\Delta E = \frac{1}{2}$ a.u. $= 13.6$ eV.

[4] In Fourier analysis, a signal with a periodicity of τ has contributing terms with angular frequencies $n\frac{2\pi}{\tau}$, where n is an integer.

and Walmsley [51]). In other words, compared to FROG, in SPIDER the nonlinear generating medium is replaced by a frequency shear between the two copies (normally requiring a nonlinear medium to produce) and no variable time delay between the two copies is needed.

In the case we consider relatively long generating pulses that generate attosecond pulse trains, *Resolution of Attosecond Beating by Interference of Two-photon Transitions* (RABITT) can be used to measure the harmonic phases (Paul et al. [101]). RABITT works by delaying a low intensity branch of the generating optical pulse and mixing it with the generated high harmonics, and then subjecting a second atomic system to the combined field. The delay-time dependent photo-electron spectrum is recorded. This spectrogram shows sidebands between the odd harmonics at the even harmonics. These sidebands are periodic with half the fundamental (=generating) laser period as a function of the delay time. The interference at each sideband between contributions coming from the higher- and from the lower-lying harmonic can be used to retrieve the phase difference between the two neighboring harmonics, and thereby to retrieve the harmonic phases up to an irrelevant global phase (Haessler [45]). RABITT can be considered as a specific case of SPIDER tuned for harmonic spectra with only odd-harmonic peaks (Muller [92]). It was recently found that because of spatiotemporal intensity fluctuations, under realistic experimental conditions RABITT underestimates the pulse duration (Kruse et al. [58]). The reason is that intensity differences lead to differences in the relative contributions of short and long trajectories, and therefore to spatiotemporal differences in the chirp. The chirps of different intensities then average out to a relatively flat phase in the measurement.

The harmonic phases generated by laser pulses of any length, so also those generated by very short pulses, can be measured using the *Frequency-Resolved Optical Gating for the Complete Reconstruction of Attosecond Bursts* (FROG CRAB) method (Mairesse and Quéré [80]). Here the attosecond pulse (train) is used to ionize an atom in the presence of a low-frequency field (e.g., the fundamental field) that functions as a gate. Then the intensity and energy of the photo-electrons for different delays between the two pulses are recorded, to arrive at the so-called Crab trace. This trace is very similar to a FROG trace and it contains information about both the gate pulse and the attosecond pulse that can be retrieved quite robustly because of the redundancy present. For a single attosecond burst and its generating field the method works like an attosecond streak camera; the time-dependent energy of the electrons appears in the Crab trace. For long dressing fields, the 'Rabbitt'-effect of sidebands between the harmonics becomes important and the oscillations of these sidebands becomes visible in the trace. In the intermediate case, the trace is continuous (with overall oscillation) for high electron energies, and discrete with time-oscillation in the lower part (Mairesse and Quéré [80]). This is because for high energies a single trajectory dominates, whereas for low energies many half-cycles contribute.

4.12 Discussion

The most important question in a discussion on molecular tomography is: why does it work so well? Many approximations are made that theorists would not dream of making when calculating molecular properties for a single molecule, and still experimentally one obtains a good reconstruction. How can it be that the errors from ignoring the Coulombic field on the propagation (the plane-wave approximation), from ignoring the laser-field on the recombination process and from ignoring completely all electronic interactions do not completely destroy the reconstruction? We think the answer lies in the fact that in the tomographic procedure one compares two different systems (molecule and reference atom), and therefore many of the errors are simply 'divided out' by making the same approximations in both systems.

The wave function $\psi_c(\mathbf{r}) = \int_{-\infty}^{\infty} a(k)e^{ikx}dk$ with the experimentally obtained $a(k)$ is not an accurate description of the continuum wave packet. However, when comparing the two systems, $a(k)$ is an effective plane-wave prefactor for the Fourier-components of the reconstructed orbital. If one attempts a (plane-wave) tomographic molecular reconstruction using exact matrix elements, it does not work (Walters et al. [131]), because no cancellation of errors can take place here. However, in molecular orbital tomography the same plane-wave approximation is made for both the atom and the molecule, with very similar effects.

Using longer wavelengths, the possibility for molecular tomography improves because lower intensities can be used and still higher frequency bandwidths can be achieved (Le et al. [65]). This is because of the λ^2-dependence of the ponderomotive potential U_p, and thus of the energy of the returning electrons (see section 2.2.1).

Instead of improving the description of the continuum wave packet with the help of ATI electrons, also an XUV pulse can be used to measure the wave packet directly (Smirnova et al. [118]). This way corrections to the simple-man's model and the Lewenstein model can be measured. A future reconstruction method might include the measured effects.

Tomographic reconstructions might be improved using iterative schemes. One could use an iterative approach to go beyond the plane-wave approximation (Patchkovskii et al. [100]). After reconstruction with plane waves, the potential and a new basis set are calculated. Then using a mean-root-square method a new orbital is calculated that corresponds the best to this new basis set and the measured dipole moments. This then continues iteratively.

Alternatively, we have considered an iterative approach where the potential is obtained from the reconstructed orbital using the time-independent Schrödinger equation as

$$V = \frac{(E - \hat{T})\psi}{\psi}, \tag{4.75}$$

where $\hat{T}$ is the kinetic energy operator and E is the bound state energy. In theory one can then optimize the reconstruction in an iterative way by calculating the bound state and associated harmonics of the retrieved potentials. However, the problem

here is that the potential cannot be obtained accurately enough from Eq. (4.75) around zero-crossings of the wave function.

Chapter 5

SFA calculations

In this chapter we derive semi-classical expressions for HHG and ATI amplitudes in terms of classical trajectories using the strong-field approximation (SFA). For HHG, we start from the Lewenstein model (Lewenstein et al. [71]). We perform integrals over birth, and if applicable, recombination times analytically. The resulting expressions are very fast to evaluate numerically. This allows us to evaluate them for many different experimental parameters (e.g., laser intensity, wavelength, pulse length). The HHG expressions derived in section 5.1.3 and the corresponding ATI expression of section 5.2 are used to derive many of the HHG and ATI properties presented in this thesis.

5.1 High-harmonic generation

The dipole acceleration $\alpha(\omega)$ in the Lewenstein model for linearly polarized pulses reads

$$\begin{aligned}\boldsymbol{\alpha}_\theta(\omega) = -\omega \int_0^{T_p} dt \int_0^t dt'\, \mathbf{v}^*_{\mathrm{rec},\theta}(k_\mathrm{s}(t,t') + A(t)) e^{-iS(t,t')+i\omega t} \\ \times d_{\mathrm{ion},\theta}(k_\mathrm{s}(t,t') + A(t'), t') \left[\frac{2\pi}{\epsilon + i(t-t')}\right]^{3/2},\end{aligned} \tag{5.1}$$

where the laser pulse is turned on after $t = 0$ and turned off some sensible time before $t = T_p$. The matrix elements are defined as

$$d_{\mathrm{ion},\theta}(k,t) = \frac{1}{(2\pi)^{3/2}} \iint \psi_{0,\theta}(\mathbf{r})(E(t)\cdot x) e^{-ikx} d^2\mathbf{r}, \tag{5.2a}$$

$$\mathbf{v}_{\mathrm{rec},\theta}(k) = \frac{1}{(2\pi)^{3/2}} \iint e^{-ikx}(i\nabla)\psi_{0,\theta}(\mathbf{r}) d^2\mathbf{r}. \tag{5.2b}$$

The prefactors come from the integration over three spatial dimensions, where one spatial dimension is already integrated over for $\psi_0(\mathbf{r})$ (see Eq. (4.53)). The semi-classical action is given by

$$S(t,t') = \frac{1}{2}\int_{t'}^t dt''\, [k_\mathrm{s}(t,t') + A(t'')]^2 + I_\mathrm{p}(t-t'). \tag{5.3}$$

The momentum appearing from performing the saddle-point method for the momentum integral in the Lewenstein model, the so-called saddle-point momentum k_{s}, is given by

$$k_{\mathrm{s}}(t,t') = -\int_{t'}^{t} A(t'')dt''/(t-t'). \tag{5.4}$$

It is equal to the canonical momentum $p = v(t,t') - A(t)$ such that a classical electron starting at time t' returns to its starting point at time t, where $v(t,t')$ is the electron velocity. This reflects the fact that the dominant contributions come from classical trajectories that start and recombine close to the origin. The electron cannot emit a photon in vacuum because the difference in dispersion relationships between photons and electrons forbids simultaneous momentum and energy conservation. Instead, the electron will recombine predominantly in the vicinity of a nuclear core, where a nucleus can absorb most of the electron momentum. For an atom this means the recombination and classically also the ionization take place at the origin. In case of a molecule the multiple nuclear centers allow for an electron ionizing and recombining at different cores. For molecules with very large internal distances on the order of $\alpha = \frac{E_0}{\omega^2}$ (e.g., ~ 35 a.u. for $I = 5 \times 10^{14}$ W/cm^2 and $\lambda = 780$ nm) this can lead to a significant increase in the cutoff energy that is beyond the standard SFA model, as discussed in section 2.2.2 (Chirilă and Lein [21]; Moreno et al. [89]).

The influence of the binding potential on the propagation is neglected in the SFA. This allowed for defining k_{s} as a canonical momentum that is conserved during the propagation. In other words, for an electron that ionizes at time t' and returns to the core at time t, the velocity at time $t'' > t'$ is given by

$$v_t(t'',t') = k_{\mathrm{s}}(t,t') + A(t''). \tag{5.5}$$

The factor $[2\pi/(\epsilon + i(t-t'))]^{3/2}$ describes the spreading of the wave packet during the propagation in the continuum. Mathematically, it arises from performing the integration over the momentum of the electron using the saddle-point approximation. A second order Taylor expansion of the action around the momentum saddle points gives a factor $[2\pi/(\epsilon + i(t-t'))]^{1/2}$ for every spatial dimension (Lewenstein et al. [71]). Therefore in numerical simulations one should adapt the power of the factor to the dimensionality of the model system.

5.1.1 Saddle point method for the recombination time

We perform the integral over t using the saddle-point method. Because the exponent is rapidly oscillating, the only contributions to the integral come from around the saddle points t_0 that are defined as

$$\frac{d}{dt}\left[S(t,t') - \omega t\right]_{t=t_0} = 0. \tag{5.6}$$

To find the saddle points, we consider that

$$\frac{d}{dt}S(t,t') = \frac{\partial k_{\mathrm{s}}}{\partial t}\frac{\partial S(t,t')}{\partial k_{\mathrm{s}}} + \frac{\partial}{\partial t}S(t,t') = \frac{1}{2}[k_{\mathrm{s}}(t,t') + A(t)]^2 + I_{\mathrm{p}}, \tag{5.7}$$

where we have used that by definition the first derivative of the action with respect to the saddle-point momentum k_s vanishes. The saddle times t_0 are given by

$$\frac{[k_\mathrm{s}(t_0,t')+A(t_0)]^2}{2}=\omega-I_\mathrm{p}, \tag{5.8}$$

or

$$v_\mathrm{rec}\equiv v_{t_0}(t_0,t')=k_\mathrm{s}(t_0,t')+A(t_0)=\pm\sqrt{2(\omega-I_\mathrm{p})}, \tag{5.9}$$

where for the first equality we used Eq. (5.5). This shows that the condition found is the energy-conservation relation for the returning electrons; they should have return momentum $v_\mathrm{rec}=\pm\sqrt{2(\omega-I_\mathrm{p})}$.

Now we expand $S(t,t')-\omega t$ around the saddle times as

$$\begin{aligned}S(t,t')-\omega t=S(t_0,t')-\omega t_0+\frac{d}{dt}[S(t,t')-\omega t]_{t=t_0}(t-t_0)\\+\frac{1}{2}\frac{d^2}{dt^2}[S(t,t')-\omega t]_{t=t_0}(t-t_0)^2+\mathcal{O}((t-t_0)^3).\end{aligned} \tag{5.10}$$

We plug in that

$$\begin{aligned}\frac{d^2}{dt^2}[S(t,t')-\omega t]&=\frac{d}{dt}[\frac{[k_\mathrm{s}(t,t')+A(t)]^2}{2}+I_\mathrm{p}-\omega]\\&=-(k_\mathrm{s}(t,t')+A(t))\left(\frac{k_\mathrm{s}(t,t')+A(t)}{t-t'}+E(t)\right),\end{aligned} \tag{5.11}$$

where we used that

$$\frac{d}{dt}k_\mathrm{s}(t,t')=\frac{-A(t)(t-t')+\int_{t'}^{t}A(t'')dt''}{(t-t')^2}=-\frac{k_\mathrm{s}(t,t')+A(t)}{t-t'}. \tag{5.12}$$

We arrive at

$$\begin{aligned}S(t,t')-\omega t\simeq S(t_0,t')-\omega t_0\\-\frac{1}{2}(k_\mathrm{s}(t_0,t')+A(t_0))\left(\frac{k_\mathrm{s}(t_0,t')+A(t_0)}{t_0-t'}+E(t_0)\right)(t-t_0)^2.\end{aligned} \tag{5.13}$$

Approximating the integral over the return times in the dipole acceleration $\boldsymbol{\alpha}_\theta(\omega)$ by the saddle-point method we reach

$$\begin{aligned}\boldsymbol{\alpha}_\theta(\omega)\simeq-\omega\int_0^{T_p}dt'\sum_{t_0>t'}\int_{-\infty}^{\infty}dt\,\mathbf{v}^*_{\mathrm{rec},\theta}[k_\mathrm{s}(t_0,t')+A(t_0)]\left[\frac{2\pi}{\epsilon+i(t_0-t')}\right]^{3/2}\\\times d_{\mathrm{ion},\theta}(k_\mathrm{s}(t_0,t')+A(t'),t')e^{-i(S(t_0,t')-\omega t_0)}\\\times e^{\frac{1}{2}i(k_\mathrm{s}(t_0,t')+A(t_0))\left(\frac{k_\mathrm{s}(t_0,t')+A(t_0)}{t_0-t'}+E(t_0)\right)(t-t_0)^2}.\end{aligned} \tag{5.14}$$

Here we approximate the integral of the action over t around one saddle-point t_0 as an integral of the second order expansion of the action over all t. We take the

dominant contributions at $t = t_0$ for $\mathbf{v}^*_{\mathrm{rec},\theta}$ and $d_{\mathrm{ion},\theta}$. The result for $\boldsymbol{\alpha}_\theta(\omega)$ is

$$\begin{aligned}\boldsymbol{\alpha}_\theta(\omega) = -\omega \int_0^{T_p} dt' \sum_{t_0>t'} \mathbf{v}^*_{\mathrm{rec},\theta}(v_{\mathrm{rec}}) \left[\frac{2\pi}{\epsilon + i(t_0 - t')}\right]^{3/2} \\ \times d_{\mathrm{ion},\theta}(k_{\mathrm{s}}(t_0,t') + A(t'),t') e^{-i(S(t_0,t')-\omega t_0)} \sqrt{\frac{2\pi i}{\frac{2(\omega - I_{\mathrm{p}})}{t_0 - t'} + E(t_0) v_{\mathrm{rec}}}}.\end{aligned} \tag{5.15}$$

If we consider only such pulses that the wave packet returns with negative momentum, the dipole acceleration equals

$$\begin{aligned}\boldsymbol{\alpha}_\theta(\omega) = -\omega\, \mathbf{v}^*_{\mathrm{rec},\theta}(-\sqrt{2(\omega - I_{\mathrm{p}})}) \int_0^{T_p} dt' \sum_{t_0>t'} \left[\frac{2\pi}{\epsilon + i(t_0 - t')}\right]^{3/2} \\ \times d_{\mathrm{ion},\theta}(k_{\mathrm{s}}(t_0,t') + A(t'),t') e^{-i(S(t_0,t')-\omega t_0)} \sqrt{\frac{2\pi i}{\frac{2(\omega - I_{\mathrm{p}})}{t_0 - t'} - E(t_0)\sqrt{2(\omega - I_{\mathrm{p}})}}}.\end{aligned} \tag{5.16}$$

Because

$$\boldsymbol{\alpha}_\theta(\omega) = \int_{-\infty}^{\infty} (\partial_t^2 \langle \mathbf{d}_\theta(t)\rangle) e^{i\omega t} dt = -i\omega \int_{-\infty}^{\infty} (\partial_t \langle \mathbf{d}_\theta(t)\rangle) e^{i\omega t} dt = -i\omega \mathbf{P}_\theta(\omega), \tag{5.17}$$

the SFA short-pulse result can be expressed as

$$\begin{aligned}\mathbf{P}_\theta(\omega) = -i\, \mathbf{v}^*_{\mathrm{rec},\theta}(-\sqrt{2(\omega - I_{\mathrm{p}})}) \int_0^{T_p} dt' \sum_{t_0>t'} \left[\frac{2\pi}{\epsilon + i(t_0 - t')}\right]^{3/2} \\ \times d_{\mathrm{ion},\theta}(k_{\mathrm{s}}(t_0,t') + A(t'),t') e^{-i(S(t_0,t')-\omega t_0)} \sqrt{\frac{2\pi i}{\frac{2(\omega - I_{\mathrm{p}})}{t_0 - t'} - E(t_0)\sqrt{2(\omega - I_{\mathrm{p}})}}}.\end{aligned} \tag{5.18}$$

5.1.1.1 Integration into molecular orbital tomography

We can convert this equation to the notation of chapter 4 if we use $\mathbf{v}^*_{\mathrm{rec},\theta}(-k(\omega)) = \frac{1}{(2\pi)^{3/2}} \iint \psi_{0,\theta}(\mathbf{r})(i\nabla) e^{-ik(\omega)x} d^2\mathbf{r} = \frac{k(\omega)}{(2\pi)^{3/2}} \mathbf{p}_\theta(\omega)$ to reach

$$\begin{aligned}\mathbf{P}_\theta(\omega) = -i \frac{k(\omega)}{(2\pi)^{3/2}} \mathbf{p}_\theta(\omega) \int_0^{T_p} dt' \sum_{t_0>t'} \left[\frac{2\pi}{\epsilon + i(t_0 - t')}\right]^{3/2} \\ \times d_{\mathrm{ion},\theta}(k_{\mathrm{s}}(t_0,t') + A(t'),t') e^{-i(S(t_0,t')-\omega t_0)} \sqrt{\frac{2\pi i}{\frac{2(\omega - I_{\mathrm{p}})}{t_0 - t'} - E(t_0) k(\omega)}},\end{aligned} \tag{5.19}$$

where we used $k(\omega) = \sqrt{2(\omega - I_{\mathrm{p}})}$. If we can compare this with the harmonic relationships for velocity-form reconstruction

$$I_\theta(\omega) = \omega^2 \left|\mathbf{P}_\theta(\omega)\right|^2, \tag{5.20a}$$

$$\mathbf{P}_\theta(\omega) = 2\pi\, a_\theta[-k(\omega)]\, \mathbf{p}_\theta(\omega), \tag{5.20b}$$

we see that the velocity-form continuum wave packet decomposition $a_\theta[-k(\omega)]$ in the SFA is given by

$$a_\theta[-k(\omega)] = -i\frac{k(\omega)}{(2\pi)^{5/2}}\int_0^{T_p} dt' \sum_{t_0>t'}\left[\frac{2\pi}{\epsilon + i(t_0-t')}\right]^{3/2} \times d_{\mathrm{ion},\theta}(k_\mathrm{s}(t_0,t') + A(t'),t')e^{-i(S(t_0,t')-\omega t_0)}\sqrt{\frac{2\pi i}{\frac{2(\omega-I_\mathrm{p})}{t_0-t'} - E(t_0)k(\omega)}}. \tag{5.21}$$

For length-form reconstruction we have to replace the velocity-form reconstruction matrix element $\mathbf{v}_{\mathrm{rec},\theta}(k)$ in Eq. (5.18) with the length-form matrix element $\mathbf{d}_{\mathrm{rec},\theta}(k) = \frac{1}{(2\pi)^{3/2}}\iint \psi_{0,\theta}(\mathbf{r})(-\mathbf{r})e^{-ikx}d^2\mathbf{r}$ to obtain the Fourier transformed dipole acceleration. It is given by

$$\boldsymbol{\alpha}_\theta(\omega) = i\omega^2\,\mathbf{d}^*_{\mathrm{rec},\theta}(-\sqrt{2(\omega-I_\mathrm{p})})\int_0^{T_p} dt' \sum_{t_0>t'}\left[\frac{2\pi}{\epsilon + i(t_0-t')}\right]^{3/2} \times d_{\mathrm{ion},\theta}(k_\mathrm{s}(t_0,t') + A(t'),t')e^{-i(S(t_0,t')-\omega t_0)}\sqrt{\frac{2\pi i}{\frac{2(\omega-I_\mathrm{p})}{t_0-t'} - E(t_0)\sqrt{2(\omega-I_\mathrm{p})}}}. \tag{5.22}$$

Now we use that $\mathbf{d}^*_{\mathrm{rec},\theta}[-k(\omega)] = \frac{1}{(2\pi)^{3/2}}\iint \psi_{0,\theta}(\mathbf{r})(-\mathbf{r})e^{-ik(\omega)x}d^2\mathbf{r} = -\frac{1}{(2\pi)^{3/2}}\mathbf{d}_\theta(\omega)$ to reach

$$\mathbf{D}_\theta(\omega) = \frac{i}{(2\pi)^{3/2}}\mathbf{d}_\theta(\omega)\int_0^{T_p} dt' \sum_{t_0>t'}\left[\frac{2\pi}{\epsilon + i(t_0-t')}\right]^{3/2} \times d_{\mathrm{ion},\theta}(k_\mathrm{s}(t_0,t') + A(t'),t')e^{-i(S(t_0,t')-\omega t_0)}\sqrt{\frac{2\pi i}{\frac{2(\omega-I_\mathrm{p})}{t_0-t'} - E(t_0)\sqrt{2(\omega-I_\mathrm{p})}}}. \tag{5.23}$$

We can compare this with the harmonic relationships for length form as found earlier

$$I_\theta(\omega) = \omega^4|\mathbf{D}_\theta(\omega)|^2, \tag{5.24a}$$

$$\mathbf{D}_\theta(\omega) = -\frac{2\pi\, a_\theta[-k(\omega)]}{k(\omega)}\mathbf{d}_\theta[\omega(k)]. \tag{5.24b}$$

In the SFA, the continuum wave packet decomposition in length form $a_\theta[-k(\omega)]$ is then given by

$$a_\theta[-k(\omega)] = \frac{-ik(\omega)}{(2\pi)^{5/2}}\int_0^{T_p} dt' \sum_{t_0>t'}\left[\frac{2\pi}{\epsilon + i(t_0-t')}\right]^{3/2} \times d_{\mathrm{ion},\theta}(k_\mathrm{s}(t_0,t') + A(t'),t')e^{-i(S(t_0,t')-\omega t_0)}\sqrt{\frac{2\pi i}{\frac{2(\omega-I_\mathrm{p})}{t_0-t'} - E(t_0)k(\omega)}}. \tag{5.25}$$

This shows that in the SFA the continuum wave packet decomposition is exactly the same in length or velocity form. Note that in (van der Zwan et al. [140]) $a(k)$ has a prefactor of 2π compared to what is presented here.

5.1.2 Saddle point method for both emission and recombination time

We can perform the integrations over both times in Eq. (5.1) analytically using the saddle-point method. Contributions come from the points where there is no rapid phase oscillation, i.e., points where the derivatives of $S(t,t') - \omega t$ with respect to both times vanish. The saddle point conditions are

$$\frac{d}{dt}\left[S(t,t') - \omega t\right]_{\substack{t=t_\mathrm{s} \\ t'=t'_\mathrm{s}}} = 0, \tag{5.26a}$$

$$\frac{d}{dt'}\left[S(t,t') - \omega t\right]_{\substack{t=t_\mathrm{s} \\ t'=t'_\mathrm{s}}} = 0. \tag{5.26b}$$

By redefining v_rec as

$$v_\mathrm{rec} \equiv k_\mathrm{s}(t_\mathrm{s}, t'_\mathrm{s}) + A(t_\mathrm{s}), \tag{5.27a}$$

Eq. (5.26a) again leads to

$$\frac{v_\mathrm{rec}^2}{2} = \omega - I_\mathrm{p}. \tag{5.27b}$$

Analogous to Eq. (5.7) we use for the second condition that

$$\frac{d}{dt'}S(t,t') = -\frac{1}{2}[k_\mathrm{s}(t,t') + A(t')]^2 - I_\mathrm{p}. \tag{5.28}$$

Eq. (5.26b) then leads to the condition

$$\frac{[k_\mathrm{s}(t_\mathrm{s}, t'_\mathrm{s}) + A(t'_\mathrm{s})]^2}{2} = -I_\mathrm{p}. \tag{5.29}$$

We define v_i as the initial momentum with which the electron is born at time t'_s. Using

$$v_\mathrm{i} = k_\mathrm{s}(t_\mathrm{s}, t'_\mathrm{s}) + A(t'_\mathrm{s}), \tag{5.30}$$

we rewrite Eq. (5.29) as

$$\frac{v_\mathrm{i}^2}{2} = -I_\mathrm{p}. \tag{5.31}$$

At real times the laser electric field is real, which means that the purely imaginary initial momentum can only be obtained using complex saddle-point times $t_\mathrm{s}, t'_\mathrm{s}$. We now divide the two saddle point conditions (5.27) and (5.29) by $2U_\mathrm{p}$, to arrive at the rewritten conditions

$$\frac{[k_\mathrm{s}(t_\mathrm{s}, t'_\mathrm{s}) + A(t'_\mathrm{s})]^2}{4U_\mathrm{p}} = \frac{-I_\mathrm{p}}{2U_\mathrm{p}}, \tag{5.32a}$$

$$\frac{(k_\mathrm{s}(t_\mathrm{s}, t'_\mathrm{s}) + A(t_\mathrm{s}))^2}{4U_\mathrm{p}} = \frac{\omega - I_\mathrm{p}}{2U_\mathrm{p}}. \tag{5.32b}$$

Using $\gamma = \sqrt{\frac{I_\mathrm{p}}{2U_\mathrm{p}}}$, we introduce the functions $f(\gamma)$ and $g(\gamma)$ as

$$f(\gamma) \equiv k_\mathrm{s}(t_\mathrm{s}, t'_\mathrm{s}) + A(t'_\mathrm{s}) = S_\mathrm{Ip} 2i\sqrt{U_\mathrm{p}}\gamma, \tag{5.33a}$$

$$\begin{aligned} g(\gamma) &\equiv k_\mathrm{s}(t_\mathrm{s}, t'_\mathrm{s}) + A(t_\mathrm{s}) = v_\mathrm{rec} = S_\mathrm{vrec}\sqrt{4U_\mathrm{p}(\frac{\omega}{2U_\mathrm{p}} - \gamma^2)} \\ &= S_\mathrm{vrec}\sqrt{2\omega}\sqrt{1 - \frac{2U_\mathrm{p}}{\omega}\gamma^2} \simeq S_\mathrm{vrec}\sqrt{2\omega}(1 - \frac{1}{2}\frac{2U_\mathrm{p}}{\omega}\gamma^2 - \frac{1}{8}(\frac{2U_\mathrm{p}}{\omega}\gamma^2)^2) + \mathcal{O}(\gamma^6), \end{aligned} \tag{5.33b}$$

where S_Ip and S_vrec are ± 1. The physical meaning of S_vrec is the sign of the returning electron momentum v_rec. Only one possibility for S_Ip is physical for a given trajectory, as we will find when we determine S_Ip later on.

For $\gamma \to 0$, the saddle-point conditions become equal to

$$f(0) = k_\mathrm{s}(t_0, t'_0) + A(t'_0) = 0, \tag{5.34a}$$

$$g(0) = k_\mathrm{s}(t_0, t'_0) + A(t_0) = S_\mathrm{vrec}\sqrt{2\omega} \equiv v_0. \tag{5.34b}$$

Combined with the condition that the electron returns to its starting point from the momentum saddle-point equation (Eq. (5.4)), these saddle-point conditions show that for $\gamma \to 0$ we need to consider classical trajectories with $v_\mathrm{i} = 0$ (Eq. (5.34a)) and $\frac{v_\mathrm{rec}^2}{2} = \omega$ (Eq. (5.34b)). The last condition physically means that concerning energy conservation of the recombination process we need to use an adapted dispersion relationship that takes into account that $I_\mathrm{p} \to 0$ for $\gamma \to 0$.

As a side-remark, we would like to stress that using Eq. (5.34a), we can express the canonical saddle-point momentum for a classical trajectory as

$$k_\mathrm{s}(t_0, t'_0) = -A(t'_0). \tag{5.35}$$

This equality simplifies the numerical calculation.

Since γ is smaller than 1 for the cases we are interested in, it makes sense to expand the saddle times $t_\mathrm{s}, t'_\mathrm{s}$ around t_0, t'_0 as

$$t'_\mathrm{s}(\gamma) = t'_0 + \sum_{n=1}^{\infty} \frac{1}{n!} a_n \gamma^n, \tag{5.36a}$$

$$t_\mathrm{s}(\gamma) = t_0 + \sum_{n=1}^{\infty} \frac{1}{n!} b_n \gamma^n. \tag{5.36b}$$

It should be noted that t_0 is redefined here with respect to section 5.1.1. We will determine the coefficients a_i and b_i up to second order. We start by also expanding $f(\gamma)$ and $g(\gamma)$ around $\gamma = 0$ as

$$f(\gamma) = f(0) + \sum_{n=1} \frac{1}{n!} \left[\frac{d^n f(\gamma)}{d\gamma^n}\right]_{\gamma=0} \gamma^n, \tag{5.37a}$$

$$g(\gamma) = g(0) + \sum_{n=1} \frac{1}{n!} \left[\frac{d^n g(\gamma)}{d\gamma^n}\right]_{\gamma=0} \gamma^n. \tag{5.37b}$$

When we compare with Eq. (5.33) we find the conditions

$$\left[\frac{df(\gamma)}{d\gamma}\right]_{\gamma=0} = S_{\mathrm{Ip}} 2i\sqrt{U_{\mathrm{p}}}, \tag{5.38a}$$

$$\left[\frac{d^n f(\gamma)}{d\gamma^n}\right]_{\gamma=0} = 0 \qquad \text{for } n \geq 2, \tag{5.38b}$$

$$\left[\frac{dg(\gamma)}{d\gamma}\right]_{\gamma=0} = 0 \qquad \text{for } n \text{ is odd}, \tag{5.38c}$$

$$\left[\frac{d^2 g(\gamma)}{d\gamma^2}\right]_{\gamma=0} = -v_0 \frac{2U_{\mathrm{p}}}{\omega}. \tag{5.38d}$$

For the first condition we write

$$\left[\frac{df(\gamma)}{d\gamma}\right]_{\gamma=0} = \left[\frac{dt'_{\mathrm{s}}}{d\gamma}\frac{\partial f(\gamma)}{\partial t'_{\mathrm{s}}} + \frac{dt_{\mathrm{s}}}{d\gamma}\frac{\partial f(\gamma)}{\partial t_{\mathrm{s}}}\right]_{\gamma=0}, \tag{5.39a}$$

$$\frac{dt'_{\mathrm{s}}}{d\gamma} = a_1 + a_2\gamma + \mathcal{O}(\gamma^2), \tag{5.39b}$$

$$\frac{dt_{\mathrm{s}}}{d\gamma} = b_1 + b_2\gamma + \mathcal{O}(\gamma^2), \tag{5.39c}$$

$$\frac{\partial f(\gamma)}{\partial t'_{\mathrm{s}}} = \frac{k_{\mathrm{s}}(t_{\mathrm{s}}, t'_{\mathrm{s}}) + A(t'_{\mathrm{s}})}{t_{\mathrm{s}} - t'_{\mathrm{s}}} + \frac{\partial A(t'_{\mathrm{s}})}{\partial t'_{\mathrm{s}}}, \tag{5.39d}$$

$$\frac{\partial f(\gamma)}{\partial t_{\mathrm{s}}} = -\frac{k_{\mathrm{s}}(t_{\mathrm{s}}, t'_{\mathrm{s}}) + A(t_{\mathrm{s}})}{t_{\mathrm{s}} - t'_{\mathrm{s}}}. \tag{5.39e}$$

Using Eq. (5.34) we arrive at

$$-a_1\, E(t'_0) - \frac{b_1\, v_0}{t_0 - t'_0} = S_{\mathrm{Ip}} 2i\sqrt{U_{\mathrm{p}}}. \tag{5.40}$$

Similarly we find from

$$\left[\frac{dg(\gamma)}{d\gamma}\right]_{\gamma=0} = \left[\frac{dt'_{\mathrm{s}}}{d\gamma}\frac{\partial g(\gamma)}{\partial t'_{\mathrm{s}}} + \frac{dt_{\mathrm{s}}}{d\gamma}\frac{\partial g(\gamma)}{\partial t_{\mathrm{s}}}\right]_{\gamma=0}, \tag{5.41a}$$

$$\frac{\partial g(\gamma)}{\partial t'_{\mathrm{s}}} = \frac{k_{\mathrm{s}}(t_{\mathrm{s}}, t'_{\mathrm{s}}) + A(t'_{\mathrm{s}})}{t_{\mathrm{s}} - t'_{\mathrm{s}}}, \tag{5.41b}$$

$$\frac{\partial g(\gamma)}{\partial t_{\mathrm{s}}} = -\frac{k_{\mathrm{s}}(t_{\mathrm{s}}, t'_{\mathrm{s}}) + A(t_{\mathrm{s}})}{t_{\mathrm{s}} - t'_{\mathrm{s}}} + \frac{\partial A(t_{\mathrm{s}})}{\partial t_{\mathrm{s}}}, \tag{5.41c}$$

that

$$\left(-\frac{v_0}{t_0 - t'_0} - E(t_0)\right) b_1 = 0. \tag{5.42}$$

Since this condition holds generally, we must have that

$$b_1 = 0. \tag{5.43}$$

From Eq. (5.40) it then follows that

$$a_1 = -\frac{S_{\mathrm{Ip}} 2i\sqrt{U_{\mathrm{p}}}}{E(t'_0)}, \tag{5.44a}$$

$$a_1^2 = -\frac{4U_{\mathrm{p}}}{(E(t'_0))^2}. \tag{5.44b}$$

To determine a_2 and b_2 we have to consider the second order terms in the expansions of $f(\gamma)$ and $g(\gamma)$. Using *Mathematica*, Eq. (5.34) and $b_1 = 0$, we verify that

$$\left[\frac{d^2 f(\gamma)}{d\gamma^2}\right]_{\gamma=0} = \frac{-b_2 v_0}{t_0 - t_0'} + \frac{-a_1^2 - a_2(t_0 - t_0')}{t_0 - t_0'} E(t_0') - a_1^2 E'(t_0'), \tag{5.45a}$$

$$\left[\frac{d^2 g(\gamma)}{d\gamma^2}\right]_{\gamma=0} = -\frac{b_2(v_0 + (t_0 - t_0')E(t_0)) + a_1^2 E(t_0')}{t_0 - t_0'}. \tag{5.45b}$$

Combining these equations with the requirements in Eq. (5.38) leads to

$$a_2 = \frac{4U_\mathrm{p}}{(E(t_0'))^2}\left(\frac{E(t_0) - E(t_0')}{v_0 + (t_0 - t_0')E(t_0)} + \frac{E'(t_0')}{E(t_0')}\right), \tag{5.46a}$$

$$b_2 = \frac{2v_0(t_0 - t_0')\frac{U_\mathrm{p}}{\omega} + \frac{4U_\mathrm{p}}{E(t_0')}}{v_0 + (t_0 - t_0')E(t_0)}. \tag{5.46b}$$

5.1.2.1 Gaussian integral for return time

To perform the integration over both times, we expand $S(t,t') - \omega t$ around the saddle points $(t_\mathrm{s}, t_\mathrm{s}')$ as

$$\begin{aligned} S(t,t') - \omega t =& S(t_\mathrm{s}, t_\mathrm{s}') - \omega t_\mathrm{s} + \frac{1}{2}\frac{d^2}{dt^2}\left[S(t,t') - \omega t\right]_{\substack{t=t_\mathrm{s}\\ t'=t_\mathrm{s}'}} (t - t_\mathrm{s})^2 \\ &+ \frac{d}{dt}\frac{d}{dt'}\left[S(t,t') - \omega t\right]_{\substack{t=t_\mathrm{s}\\ t'=t_\mathrm{s}'}} (t - t_\mathrm{s})(t' - t_\mathrm{s}') \\ &+ \frac{1}{2}\frac{d^2}{dt'^2}\left[S(t,t') - \omega t\right]_{\substack{t=t_\mathrm{s}\\ t'=t_\mathrm{s}'}} (t' - t_\mathrm{s}')^2. \end{aligned} \tag{5.47}$$

Using Eq. (5.12) and

$$\frac{d}{dt'} k_\mathrm{s}(t,t') = \frac{k_\mathrm{s}(t,t') + A(t')}{t - t'}, \tag{5.48}$$

it is easily verified that

$$\frac{d^2}{dt^2}\left[S(t,t') - \omega t\right] = (k_\mathrm{s}(t,t') + A(t))\left(\frac{-k_\mathrm{s}(t,t') - A(t)}{t - t'} - E(t)\right), \tag{5.49a}$$

$$\frac{d}{dt}\frac{d}{dt'}\left[S(t,t') - \omega t\right] = (k_\mathrm{s}(t,t') + A(t'))\frac{k_\mathrm{s}(t,t') + A(t)}{t - t'}, \tag{5.49b}$$

$$\frac{d^2}{dt'^2}\left[S(t,t') - \omega t\right] = -(k_\mathrm{s}(t,t') + A(t'))\left(\frac{k_\mathrm{s}(t,t') + A(t')}{t - t'} - E(t')\right). \tag{5.49c}$$

In the dipole acceleration $\boldsymbol{\alpha}_\theta(\omega)$ we again take the dominant contributions at $(t = t_\mathrm{s}, t' = t_\mathrm{s}')$ for the prefactors of the action. Furthermore, we replace $k_\mathrm{s}(t_\mathrm{s}, t_\mathrm{s}') +$

$A(t_\mathrm{s})$ by v_rec to reach

$$\begin{aligned}\boldsymbol{\alpha}_\theta(\omega) \simeq -\omega \sum_{t_0,t_0'} \mathbf{v}^*_{\mathrm{rec},\theta}(v_\mathrm{rec}) d_{\mathrm{ion},\theta}(k_\mathrm{s}(t_\mathrm{s},t_\mathrm{s}')+A(t_\mathrm{s}'),t_\mathrm{s}') \left[\frac{2\pi}{\epsilon+i(t_\mathrm{s}-t_\mathrm{s}')}\right]^{\frac{3}{2}} e^{-iS(t_\mathrm{s},t_\mathrm{s}')+i\omega t_\mathrm{s}} \\ \times \int_{-\infty}^{\infty} dt \int_{-\infty}^{\infty} dt'\, e^{-\frac{1}{2}i(k_\mathrm{s}(t_\mathrm{s},t_\mathrm{s}')+A(t_\mathrm{s})\left(\frac{-k_\mathrm{s}(t_\mathrm{s},t_\mathrm{s}')-A(t_\mathrm{s})}{t_\mathrm{s}-t_\mathrm{s}'}-E(t_\mathrm{s})\right))(t-t_\mathrm{s})^2} \\ \times e^{-i(k_\mathrm{s}(t_\mathrm{s},t_\mathrm{s}')+A(t_\mathrm{s}'))\frac{k_\mathrm{s}(t_\mathrm{s},t_\mathrm{s}')+A(t_\mathrm{s})}{t_\mathrm{s}-t_\mathrm{s}'}(t-t_\mathrm{s})(t'-t_\mathrm{s}')} \\ e^{+\frac{1}{2}i(k_\mathrm{s}(t_\mathrm{s},t_\mathrm{s}')+A(t_\mathrm{s}'))\left(\frac{k_\mathrm{s}(t_\mathrm{s},t_\mathrm{s}')+A(t_\mathrm{s}')}{t_\mathrm{s}-t_\mathrm{s}'}-E(t_\mathrm{s}')\right)(t'-t_\mathrm{s}')^2},\end{aligned} \tag{5.50}$$

where again the integrals over t' or t around the saddle points are approximated as integrals over all t' or t of the expanded action. Rewriting the exponent from the form at^2+bt+c to the form $a(t+\frac{b}{2a})^2-\frac{b^2}{4a}+c$ and shifting the integration variables, we reach

$$\begin{aligned}\boldsymbol{\alpha}_\theta(\omega) = -\omega \sum_{t_0,t_0'} \mathbf{v}^*_{\mathrm{rec},\theta}(v_\mathrm{rec}) d_{\mathrm{ion},\theta}(k_\mathrm{s}(t_\mathrm{s},t_\mathrm{s}')+A(t_\mathrm{s}'),t_\mathrm{s}') \left[\frac{2\pi}{\epsilon+i(t_\mathrm{s}-t_\mathrm{s}')}\right]^{\frac{3}{2}} e^{-iS(t_\mathrm{s},t_\mathrm{s}')+i\omega t_\mathrm{s}} \\ \times \int_{-\infty}^{\infty} dt \int_{-\infty}^{\infty} dt'\, e^{\frac{1}{2}i(k_\mathrm{s}(t_\mathrm{s},t_\mathrm{s}')+A(t_\mathrm{s}))\left(\frac{k_\mathrm{s}(t_\mathrm{s},t_\mathrm{s}')+A(t_\mathrm{s})}{t_\mathrm{s}-t_\mathrm{s}'}+E(t_\mathrm{s})\right)t^2} \\ e^{\frac{1}{2}i\left(-\frac{(k_\mathrm{s}(t_\mathrm{s},t_\mathrm{s}')+A(t_\mathrm{s}'))^2(k_\mathrm{s}(t_\mathrm{s},t_\mathrm{s}')+A(t_\mathrm{s}))}{(t_\mathrm{s}-t_\mathrm{s}')^2\left(\frac{k_\mathrm{s}(t_\mathrm{s},t_\mathrm{s}')+A(t_\mathrm{s})}{t_\mathrm{s}-t_\mathrm{s}'}+E(t_\mathrm{s})\right)}+(k_\mathrm{s}(t_\mathrm{s},t_\mathrm{s}')+A(t_\mathrm{s}'))\left(\frac{k_\mathrm{s}(t_\mathrm{s},t_\mathrm{s}')+A(t_\mathrm{s}')}{t_\mathrm{s}-t_\mathrm{s}'}-E(t_\mathrm{s}')\right)\right)t'^2}.\end{aligned} \tag{5.51}$$

For Gaussian integrals we know that

$$\int_{\infty}^{\infty} e^{-a\,t^2} dt = \sqrt{\frac{\pi}{a}} \qquad \text{for } \mathrm{Re}(a) \geq 0. \tag{5.52}$$

Before evaluating the time integrals, we should check if the condition $\mathrm{Re}(a) \geq 0$ in Eq. (5.52) is fulfilled for both integrals. At least we know that for $\gamma = 0$ this condition should be fulfilled since the exponent is purely imaginary in this case. Starting with the integration over the return time t, we wish to determine $\mathrm{sgn}(\mathrm{Re}(a))$. We rewrite a using Eq. (5.33) and then expand the resulting expression in a Taylor series around $\gamma = 0$ as

$$\begin{aligned} a &= -\frac{1}{2}i(k_\mathrm{s}(t_\mathrm{s},t_\mathrm{s}')+A(t_\mathrm{s}))\left(\frac{k_\mathrm{s}(t_\mathrm{s},t_\mathrm{s}')+A(t_\mathrm{s})}{t_\mathrm{s}-t_\mathrm{s}'}+E(t_\mathrm{s})\right) \\ &= -\frac{1}{2}i\left(\frac{v_\mathrm{rec}^2}{t_\mathrm{s}-t_\mathrm{s}'}+E(t_\mathrm{s})\,v_\mathrm{rec}\right) \\ &= -\frac{1}{2}i\left(\frac{v_\mathrm{rec}^2}{t_0+\frac{1}{2}b_2\gamma^2-t_0'-a_1\gamma-\frac{1}{2}a_2\gamma^2}+E(t_0+\frac{1}{2}b_2\gamma^2)\,v_\mathrm{rec}\right)+\mathcal{O}(\gamma^3). \end{aligned} \tag{5.53}$$

Now we use that b_2 is real, to write

$$\mathrm{Re}(a) = \mathrm{Im}\left(\frac{1}{2}\frac{v_\mathrm{rec}^2}{t_0+\frac{1}{2}b_2\gamma^2-t_0'-a_1\gamma-\frac{1}{2}a_2\gamma^2}\right)+\mathcal{O}(\gamma^3). \tag{5.54}$$

In general, we can rewrite the fraction $\mathrm{Im}\left(\frac{c_1}{c_2+c_3 i}\right)$ for $c_1, c_2, c_3 \in \mathbb{R}$ as

$$\mathrm{Im}\left(\frac{c_1}{c_2+c_3 i}\right) = \mathrm{Im}\left(\frac{c_1\,(c_2-c_3 i)}{c_2^2+c_3^2}\right) = -\frac{c_1 c_3}{c_2^2+c_3^2}. \tag{5.55}$$

Inserting this equality into Eq. (5.54) using

$$c_1 = \frac{1}{2} v_{\mathrm{rec}}^2 > 0, \tag{5.56a}$$

$$c_3 = -a_1\gamma/i = \frac{S_{\mathrm{Ip}} 2\sqrt{U_{\mathrm{p}}}}{E(t_0')}\gamma, \tag{5.56b}$$

leads to $\mathrm{sgn}(\mathrm{Re}(a))$ being determined up to second order in γ as

$$\begin{aligned}\mathrm{sgn}(\mathrm{Re}(a)) &= \mathrm{sgn}\left(-\frac{c_1 c_3}{c_2^2+c_3^2}\right) = \mathrm{sgn}(-c_3) = \mathrm{sgn}\left(\frac{-S_{\mathrm{Ip}}}{E(t_0')}\gamma\right) \\ &= \begin{cases} -\mathrm{sgn}(E(t_0'))S_{\mathrm{Ip}} & \text{for } \gamma > 0 \\ 0 & \text{for } \gamma = 0. \end{cases}\end{aligned} \tag{5.57}$$

We see that the condition $\mathrm{Re}(a) \geq 0$ is satisfied for $\gamma = 0$. We expect $\alpha(\omega)$ to change only infinitesimally when γ is infinitesimally small. That means that in that case the condition $\mathrm{Re}(a) \geq 0$ should still be fulfilled, otherwise the integration over t suddenly becomes singular. This leads to S_{Ip} being determined up to second order in γ for $\gamma > 0$ as

$$S_{\mathrm{Ip}} = -\mathrm{sgn}(E(t_0')). \tag{5.58}$$

Physically, this choice for S_{Ip} ensures that the integration over t does not explicitly depend on the value of the electric field at the birth time t'. We can see that it should not by considering a trajectory arising from a gerade molecule in a laser field. If we change the polarization of the laser pulse by 180°, the resulting harmonic will undergo a 180°-polarization shift too. For a classical plane-wave trajectory this shift stems entirely from the complex conjugation of the recombination matrix element. This means that the rest of the contributions to $a(\omega)$ should be unaltered, i.e., be independent of the sign of the electric field at the birth time t'. Using Eq. (5.58), the ambiguity in the γ-expansion of the saddle-point birth time t_s' is resolved and we can write

$$a_1 = -\frac{S_{\mathrm{Ip}} 2i\sqrt{U_{\mathrm{p}}}}{E(t_0')} = \frac{2i\sqrt{U_{\mathrm{p}}}}{|E(t_0')|}. \tag{5.59}$$

Similarly, the saddle-point condition for the birth time (Eq. (5.33a)) becomes

$$f(\gamma) \equiv k_{\mathrm{s}}(t_{\mathrm{s}}, t_{\mathrm{s}}') + A(t_{\mathrm{s}}') = -2i\,\mathrm{sgn}(E(t_0'))\,\sqrt{U_{\mathrm{p}}}\gamma. \tag{5.60}$$

Using the above value for S_{Ip} and evaluating the integral over the return time, we find

$$\begin{aligned}\int_{-\infty}^{\infty} dt\, e^{-at^2} &= \int_{-\infty}^{\infty} dt\, e^{\frac{1}{2}i(k_{\mathrm{s}}(t_{\mathrm{s}},t_{\mathrm{s}}')+A(t_{\mathrm{s}}))\left(\frac{k_{\mathrm{s}}(t_{\mathrm{s}},t_{\mathrm{s}}')+A(t_{\mathrm{s}})}{t_{\mathrm{s}}-t_{\mathrm{s}}'}+E(t_{\mathrm{s}})\right)t^2} \\ &= \sqrt{\frac{2\pi i}{\frac{v_{\mathrm{rec}}^2}{t_0+\frac{1}{2}b_2\gamma^2-t_0'-a_1\gamma-\frac{1}{2}a_2\gamma^2} + E(t_0+\frac{1}{2}b_2\gamma^2)\,v_{\mathrm{rec}}}} + \mathcal{O}(\gamma^3).\end{aligned} \tag{5.61}$$

In a numerical calculation one can use Eq. (5.60) to calculate $k_\mathrm{s}(t_\mathrm{s}, t'_\mathrm{s})$ efficiently, analogously to Eq. (5.35) for $k_\mathrm{s}(t_0, t'_0)$.

5.1.2.2 Complex laser fields

As a side-excursion, we determine the expansions around $\gamma = 0$ of the laser electric field. This expansion can be used to calculate the electric field at complex times. For the birth time, we have that

$$\begin{aligned} E(t'_\mathrm{s}) &= E(t'_0) + \left[\frac{dE(t'_\mathrm{s}(\gamma))}{d\gamma}\right]_{\gamma=0}\gamma \\ &\quad + \frac{1}{2}\left[\frac{d^2E(t'_\mathrm{s}(\gamma))}{d\gamma^2}\right]_{\gamma=0}\gamma^2 + \mathcal{O}(\gamma^3), \end{aligned} \tag{5.62a}$$

$$\left[\frac{dE(t'_\mathrm{s}))}{d\gamma}\right]_{\gamma=0} = \left[\frac{\partial E(t'_\mathrm{s})}{\partial t'_\mathrm{s}}\right]_{t'_\mathrm{s}=t'_0}\left[\frac{dt'_\mathrm{s}}{d\gamma}\right]_{\gamma=0} = a_1\left[\frac{\partial E(t)}{\partial t}\right]_{t=t'_0}, \tag{5.62b}$$

$$\begin{aligned} \left[\frac{d^2E(t'_\mathrm{s}(\gamma))}{d\gamma^2}\right]_{\gamma=0} &= \left[\frac{\partial E(t'_\mathrm{s})}{\partial t'_\mathrm{s}}\frac{d^2t'_\mathrm{s}}{d\gamma^2} + \frac{\partial^2 E(t'_\mathrm{s})}{\partial t'^2_\mathrm{s}}\left(\frac{dt'_\mathrm{s}}{d\gamma}\right)^2\right]_{\gamma=0} \\ &= \left[\frac{\partial E(t)}{\partial t}\right]_{t=t'_0} a_2 + \left[\frac{\partial^2 E(t)}{\partial t^2}\right]_{t=t'_0} a_1^2. \end{aligned} \tag{5.62c}$$

This leads to

$$E(t'_\mathrm{s}) = E(t'_0) + a_1E'(t'_0)\gamma + \frac{1}{2}(a_2E'(t'_0) + a_1^2E''(t'_0))\gamma^2 + \mathcal{O}(\gamma^3), \tag{5.63a}$$

and similarly to

$$E(t_\mathrm{s}) = E(t_0) + \frac{1}{2}b_2E'(t_0)\gamma^2 + \mathcal{O}(\gamma^3). \tag{5.63b}$$

5.1.2.3 Gaussian integral for birth time

For the integration over the birth time t' we define b as

$$\begin{aligned} b &\equiv \frac{1}{2}i\Bigg(\frac{(k_\mathrm{s}(t_\mathrm{s}, t'_\mathrm{s}) + A(t'_\mathrm{s}))^2(k_\mathrm{s}(t_\mathrm{s}, t'_\mathrm{s}) + A(t_\mathrm{s}))}{(t_\mathrm{s} - t'_\mathrm{s})^2\left(\frac{k_\mathrm{s}(t_\mathrm{s}, t'_\mathrm{s}) + A(t_\mathrm{s})}{t_\mathrm{s} - t'_\mathrm{s}} + E(t_\mathrm{s})\right)} \\ &\quad - (k_\mathrm{s}(t_\mathrm{s}, t'_\mathrm{s}) + A(t'_\mathrm{s}))\left(\frac{k_\mathrm{s}(t_\mathrm{s}, t'_\mathrm{s}) + A(t'_\mathrm{s})}{t_\mathrm{s} - t'_\mathrm{s}} - E(t'_\mathrm{s})\right)\Bigg) \\ &= \frac{1}{2}i\left(\frac{-4U_\mathrm{p}\gamma^2 v_\mathrm{rec}}{(t_\mathrm{s} - t'_\mathrm{s})^2\left(\frac{v_\mathrm{rec}}{t_\mathrm{s} - t'_\mathrm{s}} + E(t_\mathrm{s})\right)} + \frac{4U_\mathrm{p}\gamma^2}{t_\mathrm{s} - t'_\mathrm{s}} - 2i\sqrt{U_\mathrm{p}}\gamma\,\mathrm{sgn}(E(t'_0))\,E(t'_\mathrm{s})\right) \\ &= \frac{2(t_\mathrm{s} - t'_\mathrm{s})E(t_\mathrm{s})}{(t_\mathrm{s} - t'_\mathrm{s})\,(v_\mathrm{rec} + (t_\mathrm{s} - t'_\mathrm{s})E(t_\mathrm{s}))}iU_\mathrm{p}\gamma^2 + \sqrt{U_\mathrm{p}}\gamma\,\mathrm{sgn}(E(t'_0))\,E(t'_\mathrm{s}) \\ &= \left(\frac{E(t_0)}{v_\mathrm{rec} + (t_0 - t'_0)E(t_0)} + \frac{E'(t'_0)}{E(t'_0)}\right)2iU_\mathrm{p}\gamma^2 + \sqrt{U_\mathrm{p}}\gamma|E(t'_0)| + \mathcal{O}(\gamma^3). \end{aligned} \tag{5.64}$$

From this it can be easily seen that at least up to second order in γ we have that

$$\mathrm{sgn}(\mathrm{Re}(b)) \geq 0. \tag{5.65}$$

Evaluating the integral we reach

$$\begin{aligned}
&\int_{-\infty}^{\infty} dt'\, e^{-bt'^2} \\
&\quad = \sqrt{\frac{\pi}{\left(\frac{E(t_0)}{v_{\mathrm{rec}}+(t_0-t_0')E(t_0)} + \frac{E'(t_0')}{E(t_0')}\right) 2iU_{\mathrm{p}}\gamma^2 + \sqrt{U_{\mathrm{p}}}\gamma|E(t_0')|}} + \mathcal{O}(\gamma^3) \\
&\quad = \left(\sqrt{U_{\mathrm{p}}}\gamma\right)^{-\frac{1}{2}} \sqrt{\frac{\pi}{\left(\frac{E(t_0)}{v_{\mathrm{rec}}+(t_0-t_0')E(t_0)} + \frac{E'(t_0')}{E(t_0')}\right) 2i\sqrt{U_{\mathrm{p}}}\gamma + |E(t_0')|}} + \mathcal{O}(\gamma^3).
\end{aligned} \tag{5.66}$$

5.1.2.4 Expansion of the action

The final step in evaluating Eq. (5.51) is expanding $\exp(-i(S(t_{\mathrm{s}}, t_{\mathrm{s}}') - \omega t_{\mathrm{s}}))$ around $\gamma = 0$, so that we do not have to integrate the laser field over complex times. Moreover the expansion will prove physically insightful as it makes the factor describing the tunneling process appear explicitly. We also expand the $I_{\mathrm{p}} = 2U_{\mathrm{p}}\gamma^2$-term in the action. The expansion is easier performed by first expanding the new function

$$h(\gamma) \equiv S(t_{\mathrm{s}}(\gamma), t_{\mathrm{s}}'(\gamma), \gamma) - \omega t_{\mathrm{s}}(\gamma), \tag{5.67a}$$

with

$$S(t_{\mathrm{s}}, t_{\mathrm{s}}', \gamma) = \frac{1}{2}\int_{t_{\mathrm{s}}'}^{t_{\mathrm{s}}} dt''\, [k_{\mathrm{s}}(t_{\mathrm{s}}, t_{\mathrm{s}}') + A(t'')]^2 + 2U_{\mathrm{p}}\gamma^2(t_{\mathrm{s}} - t_{\mathrm{s}}'), \tag{5.67b}$$

around $\gamma = 0$ as

$$\begin{aligned}
h(\gamma) = h(0) &+ \left[\frac{dh}{d\gamma}\right]_{\gamma=0}\gamma + \frac{1}{2}\left[\frac{d^2h}{d\gamma^2}\right]_{\gamma=0}\gamma^2 + \frac{1}{6}\left[\frac{d^3h}{d\gamma^3}\right]_{\gamma=0}\gamma^3 \\
&+ \frac{1}{24}\left[\frac{d^4h}{d\gamma^4}\right]_{\gamma=0}\gamma^4 + \mathcal{O}(\gamma^5).
\end{aligned} \tag{5.68}$$

Here we introduced a three-argument version of the action. The three-argument action $S(t_{\mathrm{s}}, t_{\mathrm{s}}', \gamma)$ has the advantage that for all values of γ we can make use of the saddle-point equalities Eqs. (5.26) and other properties of the action derived before.

It should be noted that in Eq. (5.68) the expansion is up to fourth order in γ, whereas so far we have limited ourselves to second order in γ. Because $S(t_{\mathrm{s}}, t_{\mathrm{s}}', \gamma) - \omega t_{\mathrm{s}}$ is part of a rapidly varying phase factor in $\boldsymbol{\alpha}_\theta(\omega)$, we are especially interested in expanding it to the highest possible order in γ for better accuracy. For practical reasons, for the highest order expansion we perform we make use of *Mathematica*. In principle, for expansions above the second order in γ we have the problem that we expanded the saddle times t_{s} and t_{s}' only up to second order in γ. However, it turns out

that up to fourth order in γ we are in the lucky circumstance that all the terms containing higher order expansion coefficients of t_s or t'_s cancel, so that the higher order expansion can be done even without knowledge of these coefficients.

For the first order term of the expansion we have that

$$\begin{aligned}\left[\frac{dh}{d\gamma}\right]_{\gamma=0} &= \left[\frac{\partial h}{\partial t_\mathrm{s}}\frac{dt_\mathrm{s}}{d\gamma}\right]_{\gamma=0} + \left[\frac{\partial h}{\partial t'_\mathrm{s}}\frac{dt'_\mathrm{s}}{d\gamma}\right]_{\gamma=0} + \left[\frac{\partial h}{\partial \gamma}\right]_{\gamma=0} \\ &= \left[4U_\mathrm{p}\gamma(t_\mathrm{s}-t'_\mathrm{s})\right]_{\gamma=0} = 0,\end{aligned} \tag{5.69}$$

where we have used the saddle-point Eqs. (5.26). This means there is no contribution from the first order term.

For the second order term we have that

$$\begin{aligned}\frac{d^2h}{d\gamma^2}\Big|_{\gamma=0} &= \left[\left(\frac{dt_\mathrm{s}}{d\gamma}\frac{\partial}{\partial t_\mathrm{s}} + \frac{dt'_\mathrm{s}}{d\gamma}\frac{\partial}{\partial t'_\mathrm{s}} + \frac{\partial}{\partial\gamma}\right)\left(\frac{\partial h}{\partial t_\mathrm{s}}\frac{dt_\mathrm{s}}{d\gamma} + \frac{\partial h}{\partial t'_\mathrm{s}}\frac{dt'_\mathrm{s}}{d\gamma} + \frac{\partial h}{\partial\gamma}\right)\right]_{\gamma=0} \\ &= \Bigg[\frac{\partial^2 h}{\partial t_\mathrm{s}^2}\underbrace{\left(\frac{dt_\mathrm{s}}{d\gamma}\right)^2}_{=0} + 2\frac{\partial^2 h}{\partial t_\mathrm{s}\partial t'_\mathrm{s}}\underbrace{\frac{dt_\mathrm{s}}{d\gamma}}_{=0}\frac{dt'_\mathrm{s}}{d\gamma} + 2\frac{\partial^2 h}{\partial t_\mathrm{s}\partial\gamma}\underbrace{\frac{dt_\mathrm{s}}{d\gamma}}_{=0} \\ &\quad + \underbrace{\frac{\partial^2 h}{\partial t'^2_\mathrm{s}}}_{=0\ \text{(see Eq.(5.49c))}}\left(\frac{dt'_\mathrm{s}}{d\gamma}\right)^2 + 2\underbrace{\frac{\partial^2 h}{\partial t'_\mathrm{s}\partial\gamma}}_{=0\ (\sim\gamma)}\frac{dt'_\mathrm{s}}{d\gamma} + \underbrace{\frac{\partial h}{\partial t_\mathrm{s}}}_{=0\ \text{(SP)}}\frac{d^2t_\mathrm{s}}{d\gamma^2} + \underbrace{\frac{\partial h}{\partial t'_\mathrm{s}}}_{=0\ \text{(SP)}}\frac{d^2t'_\mathrm{s}}{d\gamma^2} + \frac{\partial^2 h}{\partial\gamma^2}\Bigg]_{\gamma=0} \\ &= 4U_\mathrm{p}\left(t_0 - t'_0\right).\end{aligned} \tag{5.70}$$

The equalities underneath the curly braces are partially taken already at $\gamma = 0$. With '(SP)' we denote that the equality follows from the saddle-point Eqs. (5.26). Up to second order the expansion is therefore given by

$$h(\gamma) = h(0) + 2U_\mathrm{p}\left(t_0 - t'_0\right)\gamma^2 + \mathcal{O}(\gamma^3) = S(t_0, t'_0, \gamma) - \omega t_0 + \mathcal{O}(\gamma^3),$$

(5.71a)

$$e^{-i(S(t_\mathrm{s},t'_\mathrm{s})-\omega t_\mathrm{s})} = e^{-i\left(S(t_0,t'_0,\gamma)-\omega t_0\right)} + \mathcal{O}(\gamma^3). \tag{5.71b}$$

For the third order term we need to act one more time with $\left(\frac{dt_\mathrm{s}}{d\gamma}\frac{\partial}{\partial t_\mathrm{s}} + \frac{dt'_\mathrm{s}}{d\gamma}\frac{\partial}{\partial t'_\mathrm{s}} + \frac{\partial}{\partial\gamma}\right)$ on everything inside the square brackets in Eq. (5.70), before taking the limit $\gamma \to 0$. If we immediately take into account that (Eqs. (5.26), (5.49), (5.43))

$$\frac{\partial h}{\partial t_\mathrm{s}}\Big|_{\gamma=0} = \frac{\partial h}{\partial t'_\mathrm{s}}\Big|_{\gamma=0} = \frac{\partial^2 h}{\partial t'^2_\mathrm{s}}\Big|_{\gamma=0} = \frac{\partial^2 h}{\partial t'_\mathrm{s}\partial t_\mathrm{s}}\Big|_{\gamma=0} = \frac{dt_\mathrm{s}}{\partial\gamma}\Big|_{\gamma=0} = 0, \tag{5.72}$$

we obtain

$$\begin{aligned}\frac{d^3h}{d\gamma^3}\Big|_{\gamma=0} = \Bigg[&\frac{\partial^3 h}{\partial t_\mathrm{s}'^3}\left(\frac{dt_\mathrm{s}'}{d\gamma}\right)^3 + 3\underbrace{\frac{\partial^3 h}{\partial t_\mathrm{s}'^2\partial\gamma}}_{=0}\left(\frac{dt_\mathrm{s}'}{d\gamma}\right)^2 + 3\frac{\partial^3 h}{\partial t_\mathrm{s}'\partial\gamma^2}\frac{dt_\mathrm{s}'}{d\gamma}\\ &+ 3\underbrace{\frac{\partial^2 h}{\partial t_\mathrm{s}\partial\gamma}}_{=0}\frac{d^2t_\mathrm{s}}{d\gamma^2} + 3\underbrace{\frac{\partial^2 h}{\partial t_\mathrm{s}'\partial\gamma}}_{=0}\frac{d^2t_\mathrm{s}'}{d\gamma^2} + \underbrace{\frac{\partial^3 h}{\partial\gamma^3}}_{=0}\Bigg]_{\gamma=0}.\end{aligned} \tag{5.73}$$

Using Eq. (5.49c) we find that

$$\left[\frac{\partial^3 h}{t_\mathrm{s}'^3}\right]_{\gamma=0} = -\left(E(t_0')\right)^2, \tag{5.74a}$$

$$\left[\left(\frac{dt_\mathrm{s}'}{d\gamma}\right)^3\right]_{\gamma=0} = a_1^3 = \frac{-8iU_\mathrm{p}^{3/2}}{|E(t_0')|^3}, \tag{5.74b}$$

$$\frac{\partial^3 h}{\partial t_\mathrm{s}'\partial\gamma^2} = -4U_\mathrm{p}. \tag{5.74c}$$

Plugging the results from Eq. (5.74) into Eq. (5.73) we obtain

$$\left[\frac{d^3h}{d\gamma^3}\right]_{\gamma=0} = \frac{-16i\,U_\mathrm{p}^{3/2}}{|E(t_0')|}. \tag{5.75}$$

That means that up to third order in γ the action is given by

$$h(\gamma) = S(t_0, t_0', \gamma) - \omega t_0 + \frac{-8i\,U_\mathrm{p}^{3/2}\gamma^3}{3|E(t_0')|} + \mathcal{O}(\gamma^4), \tag{5.76a}$$

$$e^{-i(S(t_\mathrm{s},t_\mathrm{s}')-\omega t_\mathrm{s})} = e^{-i(S(t_0,t_0',\gamma)-\omega t_0)}e^{-\frac{8U_\mathrm{p}^{3/2}\gamma^3}{3|E(t_0')|}} + \mathcal{O}(\gamma^4). \tag{5.76b}$$

With the help of *Mathematica*, we can continue the expansion a bit more. The result up to fourth order in γ is given by

$$\begin{aligned}e^{-i(S(t_\mathrm{s},t_\mathrm{s}')-\omega t_\mathrm{s})} = {}& e^{-i(S(t_0,t_0',\gamma)-\omega t_0)}e^{-\frac{8U_\mathrm{p}^{3/2}\gamma^3}{3|E(t_0')|}}\\ &\times e^{i\frac{2U_\mathrm{p}^2\left(\frac{E(t_0')(v_0E(t_0)-E(t_0')(2v_0+(t_0-t_0')E(t_0')))}{v_0(v_0+(t_0-t_0')E(t_0))}+E'(t_0')\right)\gamma^4}{(E(t_0'))^3}} + \mathcal{O}(\gamma^5).\end{aligned} \tag{5.77}$$

For an expansion up to fifth order in γ, only a_3 and b_3 and not a_4,a_5, b_4, or b_5 would be needed.

5.1.2.5 Final expression

Combining the results from the previous sections we can express the dipole acceleration $\boldsymbol{\alpha}_\theta(\omega)$ as

$$\begin{aligned}
\boldsymbol{\alpha}_\theta(\omega) = \frac{-\omega}{\left(\sqrt{U_\mathrm{p}}\gamma\right)^{\frac{1}{2}}} \sum_{t_0,t_0'} \mathbf{v}^*_{\mathrm{rec},\theta}(v_\mathrm{rec}) d_{\mathrm{ion},\theta}(-2i\,\mathrm{sgn}(E(t_0'))\,\sqrt{U_\mathrm{p}}\gamma, t_\mathrm{s}') \left[\frac{2\pi}{\epsilon + i(t_\mathrm{s}-t_\mathrm{s}')}\right]^{\frac{3}{2}} \\
\times e^{-i(S(t_0,t_0')-\omega t_0)} e^{i\left(\frac{E(t_0')(v_0E(t_0)-E(t_0')(2v_0+(t_0-t_0')E(t_0')))}{v_0(v_0+(t_0-t_0')E(t_0))}+E'(t_0')\right)\frac{2U_\mathrm{p}^2\gamma^4}{(E(t_0'))^3}} \\
\times e^{-\frac{8U_\mathrm{p}^{3/2}\gamma^3}{3|E(t_0')|}} \sqrt{\frac{2\pi i}{\frac{v_\mathrm{rec}^2}{t_0+\frac{1}{2}b_2\gamma^2-t_0'-a_1\gamma-\frac{1}{2}a_2\gamma^2}+E(t_0+\frac{1}{2}b_2\gamma^2)\,v_\mathrm{rec}}} \\
\times \sqrt{\frac{\pi}{\left(\frac{E(t_0)}{v_\mathrm{rec}+(t_0-t_0')E(t_0)}+\frac{E'(t_0')}{E(t_0')}\right)2i\sqrt{U_\mathrm{p}}\gamma+|E(t_0')|}} + \mathcal{O}(\gamma^3) \\
= -\omega\left(\frac{I_\mathrm{p}}{2}\right)^{-\frac{1}{4}} \sum_{t_0,t_0'} \mathbf{v}^*_{\mathrm{rec},\theta}(v_\mathrm{rec}) d_{\mathrm{ion},\theta}(-i\,\mathrm{sgn}(E(t_0'))\sqrt{2I_\mathrm{p}}, t_\mathrm{s}') \left[\frac{2\pi}{\epsilon + i(t_\mathrm{s}-t_\mathrm{s}')}\right]^{\frac{3}{2}} \\
\times e^{-i(S(t_0,t_0')-\omega t_0)} e^{i\left(\frac{E(t_0')(v_0E(t_0)-E(t_0')(2v_0+(t_0-t_0')E(t_0')))}{v_0(v_0+(t_0-t_0')E(t_0))}+E'(t_0')\right)\frac{I_\mathrm{p}^2}{2(E(t_0'))^3}} \\
\times e^{-\frac{(2I_\mathrm{p})^{3/2}}{3|E(t_0')|}} \sqrt{\frac{2\pi i}{\frac{v_\mathrm{rec}^2}{t_0+\frac{1}{2}b_2\gamma^2-t_0'-a_1\gamma-\frac{1}{2}a_2\gamma^2}+E(t_0+\frac{1}{2}b_2\gamma^2)\,v_\mathrm{rec}}} \\
\times \sqrt{\frac{\pi}{\left(\frac{E(t_0)}{v_\mathrm{rec}+(t_0-t_0')E(t_0)}+\frac{E'(t_0')}{E(t_0')}\right)i\sqrt{2I_\mathrm{p}}+|E(t_0')|}} + \mathcal{O}(\gamma^3),
\end{aligned} \tag{5.78a}$$

with

$$a_1 = \frac{2i\sqrt{U_\mathrm{p}}}{|E(t_0')|}, \tag{5.78b}$$

$$a_2 = \frac{4U_\mathrm{p}}{(E(t_0'))^2}\left(\frac{E(t_0)-E(t_0')}{v_0+(t_0-t_0')E(t_0)}+\frac{E'(t_0')}{E(t_0')}\right), \tag{5.78c}$$

$$b_2 = \frac{2v_0(t_0-t_0')\frac{U_\mathrm{p}}{\omega}+\frac{4U_\mathrm{p}}{E(t'0)}}{v_0+(t_0-t_0')E(t_0)}, \tag{5.78d}$$

$$v_0 = S_\mathrm{vrec}\sqrt{2\omega} = \pm\sqrt{2\omega}, \tag{5.78e}$$

$$v_\mathrm{rec} = S_\mathrm{vrec}\sqrt{2(\omega-I_\mathrm{p})} = \pm\sqrt{2(\omega-I_\mathrm{p})}, \tag{5.78f}$$

where for the last equality of $\boldsymbol{\alpha}_\theta(\omega)$ we inserted again I_p for $2U_\mathrm{p}\gamma^2$. It should be noted that the above expression is up to order $\mathcal{O}(\gamma^3)$, but the expansion of the action in it was up to $\mathcal{O}(\gamma^5)$. As mentioned before, the difference makes sense as the latter is a rapidly varying phase factor. Hopefully, this makes the whole expression reasonably accurate, although formally of course it is only so up to order $\mathcal{O}(\gamma^3)$.

5.1.3 Double saddle-point with only birth time equation expansion

The method described in section 5.1.2 has several advantages and disadvantages. It provides an intuitive expansion of the full trajectories in terms of γ, or alternatively, in terms of I_p, starting from the classical trajectories. The harmonic order generated by a classical trajectory is completely determined by its return momentum. One of the striking features of this procedure is therefore that the full solutions are expanded from classical trajectories associated with higher return momenta. As a consequence, the highest order harmonics cannot be calculated, as no classical returns with appropriate return momenta exist. Also, we do not calculate harmonics with an energy lower than I_p using our approaches based on classical trajectories. Although in principle this would be possible using the approach of section 5.1.2, we would expect very inaccurate results. The latter could be overcome by performing the integrations in Eq. (5.1) explicitly, or by solving the saddle-point conditions for imaginary return momenta, for which probably only solving them directly for complex times makes sense. Both of these would be accompanied by a substantial increase in numerical effort.

Concerning our current approach based on classical trajectories, we expect more accurate results from an expansion starting with trajectories that share the return momentum and are associated with the same harmonic as the full trajectory, because in that case the two trajectories will lie closer together. This can be achieved using an alternative approach for the expression of the full solutions in terms of solutions of real saddle-point equations. Instead of dividing both saddle-point equations by $2U_\mathrm{p}$ and expanding them in γ, or equivalently, in I_p, we will expand only the birth time equation, but keep the return time equation unmodified. This no longer corresponds to expanding I_p in the action in Eq. (5.1) and deriving the saddle-point conditions from there. Therefore the physical meaning of the expansion is lost and the expansion as treated in this section could be considered more artificial, i.e., a mathematical trick. In formulas, we find the solutions of the full equations

$$f(\gamma) \equiv k_\mathrm{s}(t_\mathrm{s}, t_\mathrm{s}') + A(t_\mathrm{s}') = -2i\,\mathrm{sgn}(E(t_0'))\sqrt{U_\mathrm{p}}\gamma, \tag{5.79a}$$

$$g(\gamma) \equiv k_\mathrm{s}(t_\mathrm{s}, t_\mathrm{s}') + A(t_\mathrm{s}) = v_\mathrm{rec} = \pm\sqrt{2(\omega - I_\mathrm{p})}, \tag{5.79b}$$

as expansions of the classical solutions of

$$f(0) \equiv k_\mathrm{s}(t_0, t_0') + A(t_0') = 0, \tag{5.80a}$$

$$g(0) \equiv k_\mathrm{s}(t_0, t_0') + A(t_0) = v_\mathrm{rec} \quad (\text{not } v_0!). \tag{5.80b}$$

Again we choose to expand in terms of γ and not I_p, because the expansion takes a lot simpler form then. This time we find the full expression on the basis of classical trajectories that satisfy $v_\mathrm{i} = 0$ (Eq. (5.80a)) and $\frac{v_\mathrm{rec}^2}{2} = \omega - I_\mathrm{p}$ (Eq. (5.80b)), i.e., in contrast to section 5.1.2 the full energy-conserving dispersion relationship is used. Appendix A.4.1 is devoted to finding the contributing classical trajectories.

As in section 5.1.2, we expand the saddle times $t_\mathrm{s}, t'_\mathrm{s}$ around t_0, t'_0 as

$$t'_\mathrm{s}(\gamma) = t'_0 + \sum_{n=1}^{\infty} \frac{1}{n!} a_n \gamma^n, \tag{5.81a}$$

$$t_\mathrm{s}(\gamma) = t_0 + \sum_{n=1}^{\infty} \frac{1}{n!} b_n \gamma^n. \tag{5.81b}$$

The coefficients a_i and b_i are determined by the expansion of the saddle-point equations $f(\gamma)$ and $g(\gamma)$ around $\gamma = 0$ as

$$f(\gamma) = f(0) + \sum_{n=1} \frac{1}{n!} \left[\frac{d^n f(\gamma)}{d\gamma^n}\right]_{\gamma=0} \gamma^n, \tag{5.82a}$$

$$g(\gamma) = g(0) + \sum_{n=1} \frac{1}{n!} \left[\frac{d^n g(\gamma)}{d\gamma^n}\right]_{\gamma=0} \gamma^n. \tag{5.82b}$$

By comparing Eqs. (5.79) and (5.80) with Eq. (5.82), we see that the coefficients a_i and b_i should be such that

$$\left[\frac{df(\gamma)}{d\gamma}\right]_{\gamma=0} = -2i \,\mathrm{sgn}(E(t'_0))\sqrt{U_\mathrm{p}}, \tag{5.83a}$$

$$\left[\frac{d^n f(\gamma)}{d\gamma^n}\right]_{\gamma=0} = 0 \qquad \text{for } n \geq 2, \tag{5.83b}$$

$$\left[\frac{d^n g(\gamma)}{d\gamma^n}\right]_{\gamma=0} = 0 \qquad \text{for } n \geq 1. \tag{5.83c}$$

Similarly as before, the first order conditions lead to

$$-a_1 \, E(t'_0) - \frac{b_1 \, v_\mathrm{rec}}{t_0 - t'_0} = -2i \,\mathrm{sgn}(E(t'_0))\sqrt{U_\mathrm{p}}, \tag{5.84a}$$

$$\left(-\frac{v_\mathrm{rec}}{t_0 - t'_0} - E(t_0)\right) b_1 = 0. \tag{5.84b}$$

Since the second condition must be fulfilled always, we again have that

$$a_1 = \frac{2i\sqrt{U_\mathrm{p}}}{|E(t'_0)|}, \tag{5.85a}$$

$$b_1 = 0. \tag{5.85b}$$

Using $b_1 = 0$, we verify that the second order derivatives of $f(\gamma)$ and $g(\gamma)$ are given by

$$\left[\frac{d^2 f(\gamma)}{d\gamma^2}\right]_{\gamma=0} = \frac{-b_2 v_\mathrm{rec}}{t_0 - t'_0} + \frac{-a_1^2 - a_2(t_0 - t'_0)}{t_0 - t'_0} E(t'_0) - a_1^2 E'(t'_0), \tag{5.86a}$$

$$\left[\frac{dg(\gamma)}{d\gamma^2}\right]_{\gamma=0} = -\frac{b_2(v_\mathrm{rec} + (t_0 - t'_0)E(t_0)) + a_1^2 E(t'_0)}{t_0 - t'_0}. \tag{5.86b}$$

Combining these equations with the requirements in Eq. (5.83) leads to

$$a_2 = \frac{4U_\mathrm{p}}{(E(t_0'))^2}\left(\frac{E(t_0)}{v_\mathrm{rec}+(t_0-t_0')E(t_0)}+\frac{E'(t_0')}{E(t_0')}\right), \tag{5.87a}$$

$$b_2 = \frac{4U_\mathrm{p}}{E(t_0')(v_\mathrm{rec}+(t_0-t_0')E(t_0))}. \tag{5.87b}$$

In comparison with the expansion of both saddle-point equations made in section 5.1.2, the first order expansion coefficients of the saddle-point times a_1 and b_1 are identical. However, the second order coefficients a_2 and b_2 take a simpler form.

5.1.3.1 Gaussian integrals

The next steps are identical to what was done in section 5.1.2. Taylor expanding $S(t,t')-\omega t$ around the saddle points $(t_\mathrm{s},t_\mathrm{s}')$ and shifting the integration variables leads to

$$\begin{aligned}\boldsymbol{\alpha}_\theta(\omega) \simeq -\omega \sum_{t_0,t_0'} \mathbf{v}^*_{\mathrm{rec},\theta}(v_\mathrm{rec}) d_{\mathrm{ion},\theta}(k_\mathrm{s}(t_\mathrm{s},t_\mathrm{s}')+A(t_\mathrm{s}'),t_\mathrm{s}')\left[\frac{2\pi}{\epsilon+i(t_\mathrm{s}-t_\mathrm{s}')}\right]^{\frac{3}{2}} e^{-iS(t_\mathrm{s},t_\mathrm{s}')+i\omega t_\mathrm{s}} \\ \times \int_{-\infty}^{\infty} dt \int_{-\infty}^{\infty} dt'\, e^{\frac{1}{2}i(k_\mathrm{s}(t_\mathrm{s},t_\mathrm{s}')+A(t_\mathrm{s}))\left(\frac{k_\mathrm{s}(t_\mathrm{s},t_\mathrm{s}')+A(t_\mathrm{s})}{t_\mathrm{s}-t_\mathrm{s}'}+E(t_\mathrm{s})\right)t^2} \\ e^{\frac{1}{2}i\left(-\frac{(k_\mathrm{s}(t_\mathrm{s},t_\mathrm{s}')+A(t_\mathrm{s}'))^2(k_\mathrm{s}(t_\mathrm{s},t_\mathrm{s}')+A(t_\mathrm{s}))}{(t_\mathrm{s}-t_\mathrm{s}')^2\left(\frac{k_\mathrm{s}(t_\mathrm{s},t_\mathrm{s}')+A(t_\mathrm{s})}{t_\mathrm{s}-t_\mathrm{s}'}+E(t_\mathrm{s})\right)}+(k_\mathrm{s}(t_\mathrm{s},t_\mathrm{s}')+A(t_\mathrm{s}'))\left(\frac{k_\mathrm{s}(t_\mathrm{s},t_\mathrm{s}')+A(t_\mathrm{s}')}{t_\mathrm{s}-t_\mathrm{s}'}-E(t_\mathrm{s}')\right)\right)t'^2}.\end{aligned} \tag{5.88}$$

Using the definition for a in Eq. (5.53), the integration over t gives us a prefactor

$$\begin{aligned}\int_{-\infty}^{\infty} dt\, e^{-at^2} &= \int_{-\infty}^{\infty} dt\, e^{\frac{1}{2}i(k_\mathrm{s}(t_\mathrm{s},t_\mathrm{s}')+A(t_\mathrm{s}))\left(\frac{k_\mathrm{s}(t_\mathrm{s},t_\mathrm{s}')+A(t_\mathrm{s})}{t_\mathrm{s}-t_\mathrm{s}'}+E(t_\mathrm{s})\right)t^2} \\ &= \sqrt{\frac{2\pi i}{\frac{v_\mathrm{rec}^2}{t_0+\frac{1}{2}b_2\gamma^2-t_0'-a_1\gamma-\frac{1}{2}a_2\gamma^2}+E(t_0+\frac{1}{2}b_2\gamma^2)\,v_\mathrm{rec}}}+\mathcal{O}(\gamma^3).\end{aligned} \tag{5.89}$$

With the appropriate new values for a_i and b_i, the laser field at complex times is still given by Eq. (5.63). Since b_2 is real, however, it is easier and better to calculate $E(t_\mathrm{s})$ directly as

$$E(t_\mathrm{s}) = E(t_0+\frac{1}{2}b_2\gamma^2). \tag{5.90}$$

The integration over t' gives the prefactor

$$\begin{aligned}
&\int_{-\infty}^{\infty} dt'\, e^{-bt'^2} \\
&\quad = \sqrt{\frac{\pi}{\left(\frac{E(t_0)}{v_{\mathrm{rec}}+(t_0-t_0')E(t_0)} + \frac{E'(t_0')}{E(t_0')}\right) 2iU_{\mathrm{p}}\gamma^2 + \sqrt{U_{\mathrm{p}}}\gamma|E(t_0')|}} + \mathcal{O}(\gamma^3) \\
&\quad = \left(\sqrt{U_{\mathrm{p}}}\gamma\right)^{-\frac{1}{2}} \sqrt{\frac{\pi}{\left(\frac{E(t_0)}{v_{\mathrm{rec}}+(t_0-t_0')E(t_0)} + \frac{E'(t_0')}{E(t_0')}\right) 2i\sqrt{U_{\mathrm{p}}}\gamma + |E(t_0')|}} + \mathcal{O}(\gamma^3).
\end{aligned} \tag{5.91}$$

5.1.3.2 Expansion of the action

To avoid the integration of the laser field over complex times, we need to expand $\exp(-i(S(t_{\mathrm{s}}, t_{\mathrm{s}}') - \omega t_{\mathrm{s}}))$ around the classical times t_0, t_0'. In contrast to section 5.1.2.4, this expansion is no longer equal to a full expansion around $\gamma = 0$. Effectively, we will expand the function

$$h(\gamma) \equiv S(t_{\mathrm{s}}, t_{\mathrm{s}}') - \omega t_{\mathrm{s}} = \frac{1}{2}\int_{t_{\mathrm{s}}'(\gamma)}^{t_{\mathrm{s}}(\gamma)} dt''\, [k_{\mathrm{s}}(t_{\mathrm{s}}(\gamma), t_{\mathrm{s}}'(\gamma)) + A(t'')]^2 + I_{\mathrm{p}}(t_{\mathrm{s}}(\gamma) - t_{\mathrm{s}}'(\gamma)) \tag{5.92}$$

as

$$h(\gamma) = h(0) + \left[\frac{dh}{d\gamma}\right]_{\gamma=0}\gamma + \frac{1}{2}\left[\frac{d^2h}{d\gamma^2}\right]_{\gamma=0}\gamma^2 + \frac{1}{6}\left[\frac{d^3h}{d\gamma^3}\right]_{\gamma=0}\gamma^3 + \frac{1}{24}\left[\frac{d^4h}{d\gamma^4}\right]_{\gamma=0}\gamma^4 + \mathcal{O}(\gamma^5). \tag{5.93}$$

For the purpose of the expansion, I_{p} in Eq. (5.92) is kept fixed and is not considered as a function of γ.

The first order term is given by

$$\left[\frac{dh}{d\gamma}\right]_{\gamma=0} = \left[\frac{\partial h}{\partial t_{\mathrm{s}}}\frac{dt_{\mathrm{s}}}{d\gamma}\right]_{\gamma=0} + \left[\frac{\partial h}{\partial t_{\mathrm{s}}'}\frac{dt_{\mathrm{s}}'}{d\gamma}\right]_{\gamma=0}, \tag{5.94a}$$

$$\frac{\partial h}{\partial t_{\mathrm{s}}} = \frac{1}{2}(k_{\mathrm{s}}(t_{\mathrm{s}}, t_{\mathrm{s}}') + A(t_{\mathrm{s}}))^2 + I_{\mathrm{p}} - \omega, \tag{5.94b}$$

$$\frac{\partial h}{\partial t_{\mathrm{s}}'} = -\frac{1}{2}(k_{\mathrm{s}}(t_{\mathrm{s}}, t_{\mathrm{s}}') + A(t_{\mathrm{s}}'))^2 - I_{\mathrm{p}}, \tag{5.94c}$$

$$\frac{dt_{\mathrm{s}}}{d\gamma} = b_2\gamma + \mathcal{O}(\gamma^3), \tag{5.94d}$$

$$\frac{dt_{\mathrm{s}}'}{d\gamma} = a_1 + a_2\gamma + \mathcal{O}(\gamma^3), \tag{5.94e}$$

leading to

$$\left[\frac{dh}{d\gamma}\right]_{\gamma=0} = -a_1 I_{\mathrm{p}} = -\frac{2i\sqrt{U_{\mathrm{p}}}I_{\mathrm{p}}}{|E(t_0')|}. \tag{5.94f}$$

From Eqs. (5.79a) and (5.94c) we see that here

$$\left[\frac{\partial h}{\partial t_\mathrm{s}'}\right]_{\gamma=0} \neq 0. \tag{5.95}$$

This is because for $\gamma = 0$ Eq. (5.79a) does not correspond to a saddle point of Eq. (5.92). Therefore the expansion of the action has to be calculated a bit more explicitly here compared to section 5.1.2.4.

The second order term is given by

$$\begin{aligned}\left[\frac{d^2h}{d\gamma^2}\right]_{\gamma=0} = \Bigg[&\frac{\partial h}{\partial t_\mathrm{s}}\frac{d^2t_\mathrm{s}}{d\gamma^2} + \frac{\partial^2 h}{\partial t_\mathrm{s}^2}\left(\frac{dt_\mathrm{s}}{d\gamma}\right)^2 + \frac{\partial h}{\partial t_\mathrm{s}'}\frac{d^2t_\mathrm{s}'}{d\gamma^2} + \frac{\partial^2 h}{\partial t_\mathrm{s}'^2}\left(\frac{dt_\mathrm{s}'}{d\gamma}\right)^2 \\ &+2\frac{\partial^2 h}{\partial t_\mathrm{s}\partial t_\mathrm{s}'}\frac{dt_\mathrm{s}}{d\gamma}\frac{dt_\mathrm{s}'}{d\gamma}\Bigg]_{\gamma=0}.\end{aligned} \tag{5.96a}$$

Using that (Eq. (5.49c))

$$\left[\frac{\partial^2 h}{\partial t_\mathrm{s}'^2}\right]_{\gamma=0} = 0, \tag{5.96b}$$

and that $b_1 = 0$ we arrive at

$$\left[\frac{d^2h}{d\gamma^2}\right]_{\gamma=0} = b_2\left(\frac{1}{2}v_\mathrm{rec}^2 + I_\mathrm{p} - \omega\right) - a_2 I_\mathrm{p} = -a_2 I_\mathrm{p}. \tag{5.96c}$$

Only including the first two order terms of the expansion, the action takes the form

$$\begin{aligned}S(t_\mathrm{s}, t_\mathrm{s}') - \omega t_\mathrm{s} &= S(t_0, t_0') - \omega t_0 - i\frac{4U_\mathrm{p}^{3/2}\gamma^3}{|E(t_0')|} \\ &\quad - \frac{4U_\mathrm{p}^2\gamma^4}{(E(t_0'))^2}\left(\frac{E(t_0)}{v_\mathrm{rec} + (t_0 - t_0')E(t_0)} + \frac{E'(t_0')}{E(t_0')}\right) + \mathcal{O}(\gamma^3) \\ &= S(t_0, t_0') - \omega t_0 + \mathcal{O}(\gamma^3).\end{aligned} \tag{5.97}$$

After having expressed I_p in terms of γ, we see that also using the approach of this section the action is given by the classical value up to third order in γ. However, unlike in section 5.1.2, the first and second order expansion terms are not zero but instead are of higher order in γ.

With the help of *Mathematica* we find that for the third order term

$$\left[\frac{d^3h}{d\gamma^3}\right]_{\gamma=0} = -2a_3 U_\mathrm{p}\gamma^2 + \frac{8iU_\mathrm{p}^{3/2}}{|E(t_0')|}. \tag{5.98}$$

The undetermined coefficient a_3 appears here, but it only contributes at fifth order in γ. The fourth order term is given by

$$\left[\frac{d^4h}{d\gamma^4}\right]_{\gamma=0} = \frac{48U_\mathrm{p}^2}{(E(t_0'))^2}\left(\frac{E(t_0)}{v_\mathrm{rec} + (t_0 - t_0')E(t_0)} + \frac{E'(t_0')}{E(t_0')}\right) + \mathcal{O}(\gamma^2). \tag{5.99}$$

When we combine the contributions from the different terms, we arrive at

$$\begin{aligned} S(t_\mathrm{s}, t'_\mathrm{s}) - \omega t_\mathrm{s} = S(t_0, t'_0) - \omega t_0 - \frac{8iU_\mathrm{p}^{3/2}}{3|E(t'_0)|} \\ - \left(\frac{E(t_0)}{v_\mathrm{rec} + (t_0 - t'_0)E(t_0)} + \frac{E'(t'_0)}{E(t'_0)} \right) \frac{2U_\mathrm{p}^2 \gamma^4}{(E(t'_0))^2} + \mathcal{O}(\gamma^5). \end{aligned} \tag{5.100}$$

Therefore we can write

$$e^{-i(S(t_\mathrm{s},t'_\mathrm{s})-\omega t_\mathrm{s})} = e^{-i(S(t_0,t'_0)-\omega t_0)} e^{-\frac{8U_\mathrm{p}^{3/2}\gamma^3}{3|E(t'_0)|}} e^{i\left(\frac{E(t_0)}{v_\mathrm{rec}+(t_0-t'_0)E(t_0)}+\frac{E'(t'_0)}{E(t'_0)}\right)\frac{2U_\mathrm{p}^2\gamma^4}{(E(t'_0))^2}} + \mathcal{O}(\gamma^5). \tag{5.101}$$

Compared to the result in section 5.1.2, the third order term describing tunnel ionization is identical. The fourth order term, a correction, takes a quite different but somewhat simpler form. The fifth order expansion term and the contribution to fifth order from the third order expansion term are such that the expression behaves even nicer than in the previous section, in the sense that for an expansion up to fifth order in γ, only a_3 and not even b_3, a_4, a_5, b_4, or b_5 would be needed.

5.1.3.3 Ionization matrix element

Unfortunately, evaluating Eq. (5.1) using the saddle-point approximation for both the birth and return times, as is done both here and in section 5.1.2, leads to an ambiguity in evaluating the ionization matrix element $d_{\mathrm{ion},\theta}(k,t)$. Clearly we cannot use the approximate classical starting momentum of 0 (from Eq. (5.35)) for $d_{\mathrm{ion},\theta}(k,t)$ as the result would be highly dependent on the symmetry of the molecule. Plugging $k = 0$ in Eq. (5.2a) shows that the result would even be equal to 0 for a gerade molecule.

On the other hand, the full saddle-point momentum $k = -i\,\mathrm{sgn}(E(t'_0))\sqrt{2I_\mathrm{p}}$ from Eq. (5.60) gives rise to $d_\mathrm{ion} \to \infty$ for a bound state with a Coulombic tail. As an illustration of the problem, consider a 3D hydrogen-like ground state. For such a state, $\psi \sim e^{-Zr}$ and $Z \simeq \sqrt{2I_\mathrm{p}}$ (see e.g. Bransden and Joachain [12]). Therefore on the x-axis the integrand is proportional to x for either positive or negative x and the integral diverges.

The singularity of the ionization matrix element at the solution of the saddle-point conditions Eq. (5.79) has to be taken into account somehow. Using the approach of section 5.1.1 where one performs the integration over t' numerically brings a clear advantage here. However, this approach brings less physical insight and does not allow us to relate ATI and HHG peaks in terms of contributing trajectories. Moreover it is computationally much more demanding. Sticking to an approach in terms of classical trajectories, formally the singularity of the ionization matrix element can be handled by taking into account the pole of the ionization matrix element analytically when performing the integration over t' (Chirilă [19]). However, this would only unnecessarily complicate things for our purposes as we are not interested in finding the overall amplitude of the HHG spectrum from the SFA calculations, but instead we are mostly interested in finding the relative contributions of the electronic trajectories

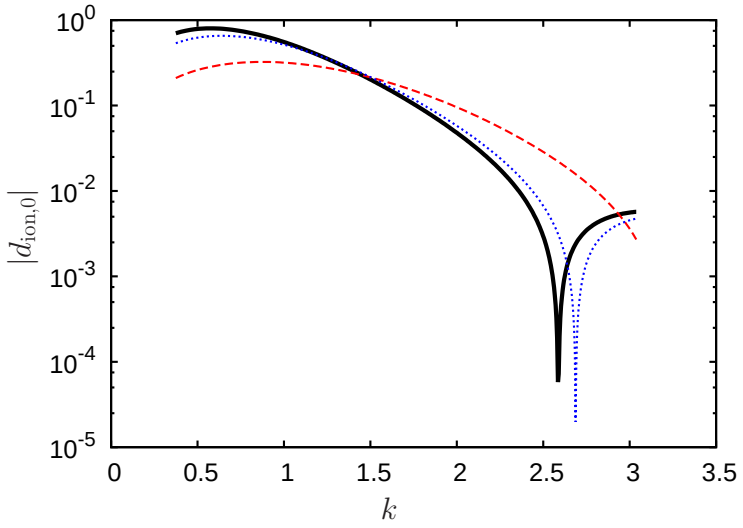

Figure 5.1: (Color online) Absolute value of $d_{\mathrm{ion},\theta}$ as a function of k for $E(t) = 1$. The black solid line is for $x_0 = \infty$ (effectively Eq. (5.2a)), the red dashed line for $x_0 = 2$ and the blue dotted line for $x_0 = 5$.

Instead, we insert a Gaussian filter in the definition of the ionization matrix element to cut off the long-distance contribution. In formula, Eq. (5.2a) becomes

$$d_{\mathrm{ion},\theta}(k,t) = \frac{1}{(2\pi)^{d/2}} \iint \psi_{0,\theta}(\mathbf{r})(E(t)\cdot x) e^{\frac{-\ln 2\,|\mathbf{r}|^2}{x_0^2}} e^{-ikx} d^2\mathbf{r}, \tag{5.102}$$

where x_0 is the radius at which the contribution to the ionization matrix element is attenuated by a factor 2. In our numerical calculations we use $x_0 = 5$. The number of dimensions, d, is set to $d = 2$ to reflect the fact that $\psi_0(\mathbf{r})$ is calculated as a true 2D state and not as a 2D projection of a 3D state as suggested by Eq. (4.53). As an illustration of the effect of the Gaussian filter, in Fig. 5.1 we plot the absolute value of d_{ion} for different values of x_0. The plot was created for the standard 2D model of H_2^+ with parallel alignment (see e.g., section 3.1). Although the curves are for real and not imaginary momenta, the figure suggests that using $x_0 = 5$ we obtain a reasonable approximation for the ionization matrix element.

Evaluated at the saddle points, the ionization matrix element is given by

$$d_{\mathrm{ion},\theta}(-i\,\mathrm{sgn}(E(t_0'))\sqrt{2I_\mathrm{p}}, t_\mathrm{s}') = \frac{1}{(2\pi)} E(t_\mathrm{s}') \iint \psi_{0,\theta}(\mathbf{r})\, x\, e^{\frac{-\ln 2|\mathbf{r}|^2}{x_0^2}} e^{-\mathrm{sgn}(E(t_0'))\sqrt{2I_\mathrm{p}}x} d^2\mathbf{r}, \tag{5.103}$$

where for $E(t_\mathrm{s}')$ we use Eq. (5.63a). From Eq. (5.103) we see that d_{ion} is given by a trajectory-dependent complex prefactor $E(t_\mathrm{s}')$ times one of two possible integrals depending on $\mathrm{sgn}(E(t_0'))$. For a symmetric molecule both these integrals are identical. This supports replacing Eq. (5.2a) by Eq. (5.102) for our purposes as $d_{\mathrm{ion},\theta}$ does not influence the relative contributions between trajectories.

5.1.3.4 Final expression

The final expression for the dipole acceleration $\boldsymbol{\alpha}_\theta(\omega)$ takes the form

$$\begin{aligned}\boldsymbol{\alpha}_\theta(\omega) = &-\omega\left(\sqrt{U_\mathrm{p}}\gamma\right)^{-\frac{1}{2}}\sum_{t_0,t_0'}\mathbf{v}^*_{\mathrm{rec},\theta}(v_\mathrm{rec})d_{\mathrm{ion},\theta}(-2i\,\mathrm{sgn}(E(t_0'))\,\sqrt{U_\mathrm{p}}\gamma,t_\mathrm{s}')\\
&\times\left[\frac{2\pi}{\epsilon+i(t_\mathrm{s}-t_\mathrm{s}')}\right]^{\frac{3}{2}}e^{-i(S(t_0,t_0')-\omega t_0)}e^{i\left(\frac{E(t_0)}{v_\mathrm{rec}+(t_0-t_0')E(t_0)}+\frac{E'(t_0')}{E(t_0')}\right)\frac{2U_\mathrm{p}^2\gamma^4}{(E(t_0'))^2}}\\
&\times e^{-\frac{8U_\mathrm{p}^{3/2}\gamma^3}{3|E(t_0')|}}\sqrt{\frac{2\pi i}{\frac{v_\mathrm{rec}^2}{t_\mathrm{s}-t_\mathrm{s}'}+E(t_\mathrm{s})\,v_\mathrm{rec}}}\\
&\times\sqrt{\frac{\pi}{\left(\frac{E(t_0)}{v_\mathrm{rec}+(t_0-t_0')E(t_0)}+\frac{E'(t_0')}{E(t_0')}\right)2i\sqrt{U_\mathrm{p}}\gamma+|E(t_0')|}}+\mathcal{O}(\gamma^3)\end{aligned}$$

or

$$\begin{aligned}= &-\omega\left(\frac{I_\mathrm{p}}{2}\right)^{-\frac{1}{4}}\sum_{t_0,t_0'}\mathbf{v}^*_{\mathrm{rec},\theta}(v_\mathrm{rec})d_{\mathrm{ion},\theta}(-i\,\mathrm{sgn}(E(t_0'))\sqrt{2I_\mathrm{p}},t_\mathrm{s}')\\
&\times\left[\frac{2\pi}{\epsilon+i(t_\mathrm{s}-t_\mathrm{s}')}\right]^{\frac{3}{2}}e^{-i(S(t_0,t_0')-\omega t_0)}e^{i\left(\frac{E(t_0)}{v_\mathrm{rec}+(t_0-t_0')E(t_0)}+\frac{E'(t_0')}{E(t_0')}\right)\frac{I_\mathrm{p}^2}{2(E(t_0'))^2}}\\
&\times e^{-\frac{(2I_\mathrm{p})^{3/2}}{3|E(t_0')|}}\sqrt{\frac{2\pi i}{\frac{v_\mathrm{rec}^2}{t_\mathrm{s}-t_\mathrm{s}'}+E(t_\mathrm{s})\,v_\mathrm{rec}}}\\
&\times\sqrt{\frac{\pi}{\left(\frac{E(t_0)}{v_\mathrm{rec}+(t_0-t_0')E(t_0)}+\frac{E'(t_0')}{E(t_0')}\right)i\sqrt{2I_\mathrm{p}}+|E(t_0')|}}+\mathcal{O}(\gamma^3),\end{aligned}\tag{5.104a}$$

with

$$t_\mathrm{s} = t_0+\frac{1}{2}b_2\gamma^2,\tag{5.104b}$$

$$t_\mathrm{s}' = t_0'+a_1\gamma+\frac{1}{2}a_2\gamma^2,\tag{5.104c}$$

$$a_1 = \frac{2i\sqrt{U_\mathrm{p}}}{|E(t_0')|},\tag{5.104d}$$

$$a_2 = \frac{4U_\mathrm{p}}{(E(t_0'))^2}\left(\frac{E(t_0)}{v_\mathrm{rec}+(t_0-t_0')E(t_0)}+\frac{E'(t_0')}{E(t_0')}\right),\tag{5.104e}$$

$$b_2 = \frac{4U_\mathrm{p}}{E(t_0')(v_\mathrm{rec}+(t_0-t_0')E(t_0))},\tag{5.104f}$$

$$v_\mathrm{rec} = S_\mathrm{vrec}\sqrt{2(\omega-I_\mathrm{p})} = \pm\sqrt{2(\omega-I_\mathrm{p})}.\tag{5.104g}$$

It should be noted that the above expression is up to order $\mathcal{O}(\gamma^3)$, but the expansion of the action in it was up to $\mathcal{O}(\gamma^5)$. As mentioned before, the difference makes sense as the latter is a rapidly varying phase factor. Hopefully, this makes the whole

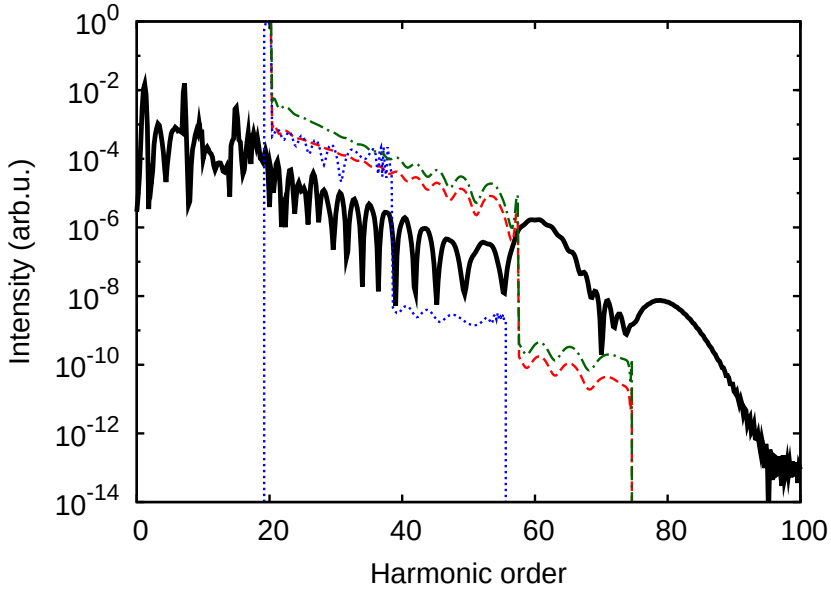

Figure 5.2: (Color online) Harmonic intensity polarized in the x-direction for a three-cycle $\sin^2$-pulse. The black solid line is for the exact TDSE result, the red dashed line is using Eq. (5.104) and the blue dotted line is using Eq. (5.78). The green dot-dashed line is for Eq. (5.104) in length form.

expression reasonably accurate, although formally of course it is only so up to order $\mathcal{O}(\gamma^3)$.

5.1.3.5 Spectra

For the 2D model of H_2^+ used in section 3.1 and other places in this thesis, we will compare HHG spectra from the TDSE (numerically exact) with SFA spectra calculated using Eqs. (5.78) and (5.104). The results for the three-cycle $\sin^2$- and fifteen-cycle trapezoidal pulses of section 3.1 are in Figs. 5.2 and 5.3, respectively. The plotted spectra are for an angle of $\theta = 45°$ between the laser polarization axis and the internuclear axis. We plot the exact result (black solid lines), the result from this section where I_p was expanded in the birth-time equation only (red dashed lines) and the result from section 5.1.2, where I_p was expanded in both saddle-point equations (blue dotted lines). Furthermore, the green dot-dashed lines are the result from this section after replacing $\mathbf{v}_{\mathrm{rec},\theta}(k)$ with a length-form expression (for details see section 5.1.3.6). In Fig. 5.2 the SFA results were shifted with respect to the TDSE result but not with respect to each other. In Fig. 5.3 all curves were shifted individually for clarity. Looking at the figures, one realizes that the SFA expressions for the harmonic intensity derived in this chapter are not that accurate. Obtaining accurate harmonic spectra was however not the purpose of this chapter. The curves for Eq. (5.104) (red dashed and green dot-dashed lines) do reproduce many of the features of the exact spectrum, including much of the interference patterns, indicating they can be used to assess the contributions of individual trajectories.

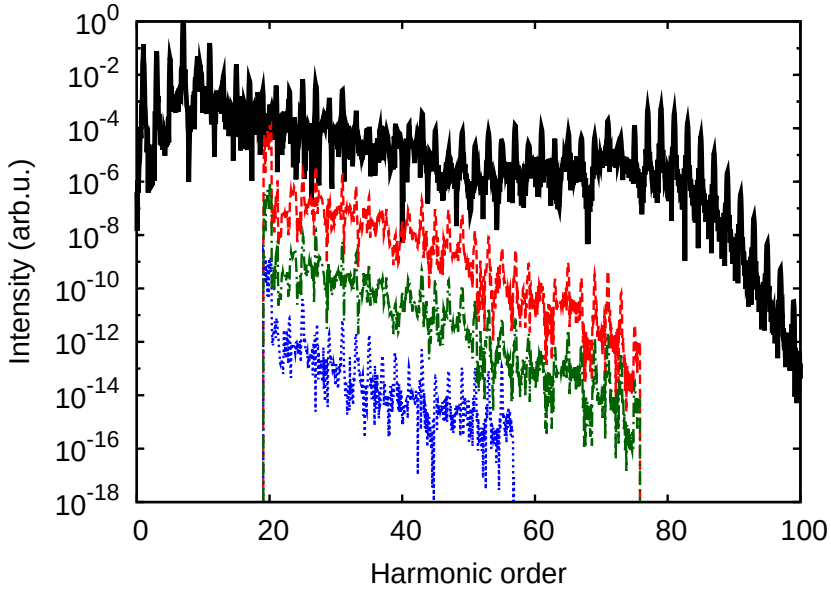

Figure 5.3: (Color online) Harmonic intensity polarized in the x-direction for a fifteen-cycle trapezoidal pulse. The black solid line is for the exact TDSE result, the red dashed line is using Eq. (5.104) and the blue dotted line is using Eq. (5.78). The green dot-dashed line is for Eq. (5.104) in length form.

For the extremely short pulse used in Fig. 5.2, the general trend of the spectrum is reproduced. The curves for Eq. (5.104) exhibit the double cutoff structure also present in the exact result. The physics behind the double cutoff can be understood from section 4.6.1; an electron returns most probably with negative momentum (for $\phi_{\mathrm{CEP}} = 1.25\pi$). However, returns with positive momenta can occur up to higher energies. Also the interference between the short and long trajectories is visible in all curves. Because the expansion from section 5.1.2 requires classical trajectories with higher energies than the full solution, the cutoff is underestimated for the blue dotted line. For the much longer pulse used in Fig. 5.3, the multi-cycle interference leading to the formation of harmonic peaks at only the odd harmonics is reproduced (Milošević and Becker [85]).

In Fig. 5.4 we plot the emission times for the short and long trajectories of a sin-pulse with $\lambda = 800$ nm and $I = 3 \times 10^{14}$ W/cm^2. We consider the emission times from the three-step model t_0, and the emission times t_{s} using the double I_{p}-expansion of section 5.1.2 and the single I_{p}-expansion of this section. The emission times are compared to the emission times from the quantum-orbital model (Chirilă et al. [20]), i.e., the real part of the exact solutions to the saddle-point Eqs. (5.27) and (5.29) on page 100. These were obtained by our former group member Ciprian Chirilă. As expected, we obtain much better results using the single-I_{p}-expansion approach of this section because the energy of the classical trajectories matches that of the expanded solution. The difference between the two will be smaller for a combination of laser and molecular parameters where I_{p} is a smaller fraction of the cutoff.

Furthermore, we observe that t_{s} from this section is a good approximation to the

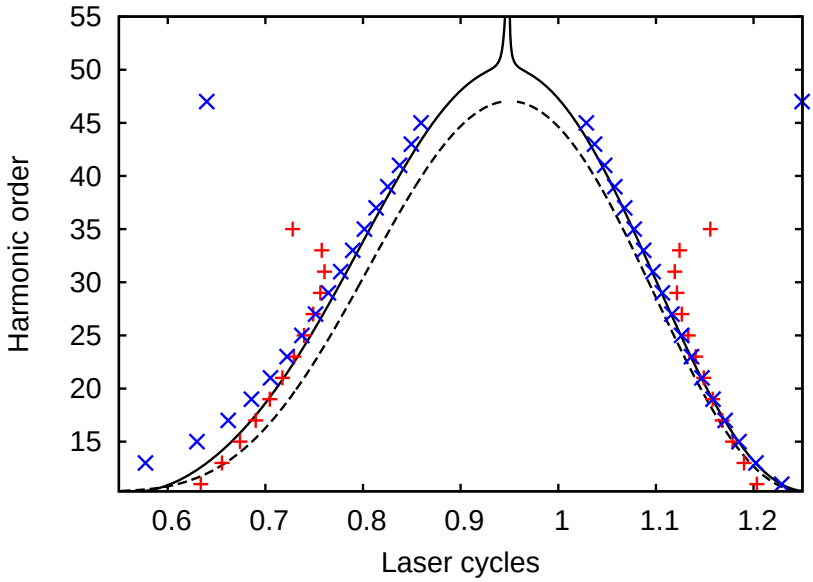

Figure 5.4: (Color online) Harmonic order as a function of emission time for the short and long trajectories of a sin-pulse. The black dashed curve represents the three-step model, the black solid curve represents the quantum-orbit model, the red plusses are t_s from section 5.1.2 and the blue crosses are t_s from section 5.1.3.

quantum-orbit emission time over most of the harmonic range for both the short and long trajectories. However, for the lowest-energy short trajectories we observe a significant deviation. In addition, the expanded saddle-point recombination times are completely off around the classically cutoff. This is partially due to the fact that the saddle-point approximation breaks down around the classical cutoff, as here two trajectories meet and the trajectories cannot be considered independently anymore (Figueira de Morisson Faria et al. [91]). Furthermore, our γ-expansion also does not seem to function when two trajectories meet as the direction of expansion for the classical trajectory is undetermined.

The SFA curves in the plots of this section show that using the approach based on classical trajectories taken in this chapter, the harmonic spectra cannot be calculated for harmonic energies smaller than I_p (except in principle using the approach taken in section 5.1.2) or above the semi-classical cutoff. The peaks for the SFA curves at the very low end of the harmonic spectra, just above I_p, are caused by electrons with very low momenta. Ignoring the Coulombic potential during the propagation of these electrons is a very bad approximation and therefore the Lewenstein model breaks down for these electrons. As a result, our SFA calculations are not reliable in this region.

5.1.3.6 Integration into molecular orbital tomography

In the short pulse case, where the momentum of the returning electron is always of the same sign (chosen negative), we have that

$$\begin{aligned}\boldsymbol{\alpha}_\theta(\omega) = -\omega\left(\frac{I_\mathrm{p}}{2}\right)^{-\frac{1}{4}} \mathbf{v}^*_{\mathrm{rec},\theta}(-\sqrt{2(\omega-I_\mathrm{p})}) \sum_{t_0,t_0'} d_{\mathrm{ion},\theta}(-i\,\mathrm{sgn}(E(t_0'))\sqrt{2I_\mathrm{p}}, t_\mathrm{s}') \\ \times \left[\frac{2\pi}{\epsilon + i(t_\mathrm{s}-t_\mathrm{s}')}\right]^{\frac{3}{2}} e^{-i(S(t_0,t_0')-\omega t_0)} e^{i\left(\frac{E(t_0)}{-\sqrt{2(\omega-I_\mathrm{p})}+(t_0-t_0')E(t_0)}+\frac{E'(t_0')}{E(t_0')}\right)\frac{I_\mathrm{p}^2}{2(E(t_0'))^2}} \\ \times e^{-\frac{(2I_\mathrm{p})^{3/2}}{3|E(t_0')|}} \sqrt{\frac{2\pi i}{\frac{2(\omega-I_\mathrm{p})}{t_\mathrm{s}-t_\mathrm{s}'} - E(t_\mathrm{s})\sqrt{2(\omega-I_\mathrm{p})}}} \\ \times \sqrt{\frac{\pi}{\left(\frac{E(t_0)}{-\sqrt{2(\omega-I_\mathrm{p})}+(t_0-t_0')E(t_0)}+\frac{E'(t_0')}{E(t_0')}\right) i\sqrt{2I_\mathrm{p}} + |E(t_0')|}} + \mathcal{O}(\gamma^3),\end{aligned} \tag{5.105a}$$

with

$$t_\mathrm{s} = t_0 + \frac{1}{2}b_2\gamma^2, \tag{5.105b}$$

$$t_\mathrm{s}' = t_0' + a_1\gamma + \frac{1}{2}a_2\gamma^2. \tag{5.105c}$$

$$a_1 = \frac{2i\sqrt{U_\mathrm{p}}}{|E(t_0')|}, \tag{5.105d}$$

$$a_2 = \frac{4U_\mathrm{p}}{(E(t_0'))^2}\left(\frac{E(t_0)}{-\sqrt{2(\omega-I_\mathrm{p})}+(t_0-t_0')E(t_0)}+\frac{E'(t_0')}{E(t_0')}\right), \tag{5.105e}$$

$$b_2 = \frac{4U_\mathrm{p}}{E(t_0')(-\sqrt{2(\omega-I_\mathrm{p})}+(t_0-t_0')E(t_0))}. \tag{5.105f}$$

In this case the summation over classical trajectories becomes a prefactor for the singly-occurring recombination matrix element, and it will be possible to rewrite this equation to express the orbital as a function of the harmonic yields and phases. Using Eq. (5.17), we can rewrite the SFA short-pulse result as

$$\mathbf{P}_\theta(\omega) = \frac{i\,\boldsymbol{\alpha}_\theta(\omega)}{\omega}. \tag{5.106}$$

When we compare this with the harmonic relationships for velocity-form reconstruction,

$$I_\theta(\omega) = \omega^2\left|\mathbf{P}_\theta(\omega)\right|^2,\ \mathbf{P}_\theta(\omega) = 2\pi\, a_\theta[-k(\omega)]\,\mathbf{p}_\theta(\omega), \tag{5.107a}$$

$$p_\theta(\omega) = \begin{pmatrix}\iint \psi_{0,\theta}(\mathbf{r})e^{-ik(\omega)x}d^2\mathbf{r}\\ 0\end{pmatrix}, \tag{5.107b}$$

and consider that the matrix element $\mathbf{v}^*_{\mathrm{rec},\theta}(-k) = \frac{1}{(2\pi)^{3/2}}\iint \psi_{0,\theta}(\mathbf{r})(i\nabla)e^{-ikx}d^2\mathbf{r} = \frac{k}{(2\pi)^{3/2}}\mathbf{p}_\theta[\omega(k)]$ we see that in the SFA the decomposition of the continuum wave

packet for velocity-form reconstruction is given by

$$
\begin{aligned}
a_\theta[-k(\omega)] = \frac{-ik(\omega)}{(2\pi)^{5/2}} \left(\frac{I_\mathrm{p}}{2}\right)^{-\frac{1}{4}} \sum_{t_0,t_0'} d_{\mathrm{ion},\theta}(-i\,\mathrm{sgn}(E(t_0'))\sqrt{2I_\mathrm{p}}, t_\mathrm{s}') \\
\times \left[\frac{2\pi}{\epsilon + i(t_\mathrm{s} - t_\mathrm{s}')}\right]^{\frac{3}{2}} e^{-i(S(t_0,t_0')-\omega t_0)} e^{i\left(\frac{E(t_0)}{-\sqrt{2(\omega-I_\mathrm{p})}+(t_0-t_0')E(t_0)} + \frac{E'(t_0')}{E(t_0')}\right)\frac{I_\mathrm{p}^2}{2(E(t_0'))^2}} \\
\times e^{-\frac{(2I_\mathrm{p})^{3/2}}{3|E(t_0')|}} \sqrt{\frac{2\pi i}{\frac{2(\omega-I_\mathrm{p})}{t_\mathrm{s}-t_\mathrm{s}'} - E(t_\mathrm{s})\sqrt{2(\omega-I_\mathrm{p})}}} \\
\times \sqrt{\frac{\pi}{\left(\frac{E(t_0)}{-\sqrt{2(\omega-I_\mathrm{p})}+(t_0-t_0')E(t_0)} + \frac{E'(t_0')}{E(t_0')}\right) i\sqrt{2I_\mathrm{p}} + |E(t_0')|}} + \mathcal{O}(\gamma^3).
\end{aligned}
\tag{5.108}
$$

In the above expression $k(\omega)$ is the dispersion relationship relating the emitted harmonic energy to the momentum of the returning electron used in the tomographic scheme. From a comparison of Eqs. (5.106) and (5.107) it can be seen that indeed for the SFA-calculations the dispersion relationship should be chosen as $k(\omega) = \sqrt{2(\omega - I_\mathrm{p})}$.

The overall result can still be quite accurately calculated using only the lowest order in γ for the prefactors in Eq. (5.108). The following expression is less accurate, but a lot simpler than Eq. (5.108),

$$
\begin{aligned}
a_\theta[-k(\omega)] \simeq \frac{-ik(\omega)}{2^{7/4}\pi^{3/2} I_\mathrm{p}^{1/4}} \sum_{t_0,t_0'} d_{\mathrm{ion},\theta}(-i\,\mathrm{sgn}(E(t_0'))\sqrt{2I_\mathrm{p}}, t_0') \\
\times \left[\frac{2\pi}{\epsilon + i(t_0 - t_0')}\right]^{3/2} e^{-i(S(t_0,t_0')-\omega t_0)} \\
\times e^{-\frac{(2I_\mathrm{p})^{3/2}}{3|E(t_0')|}} \sqrt{\frac{i}{\left(\frac{2(\omega-I_\mathrm{p})}{t_0-t_0'} - E(t_0)\sqrt{2(\omega-I_\mathrm{p})}\right)|E(t_0')|}} + \mathcal{O}(\gamma).
\end{aligned}
\tag{5.109}
$$

For the case of length-form reconstruction we need to replace the velocity-form recombination matrix element by a length-form one. Since the SFA-prefactor in front of the recombination matrix element (including the sum over electron trajectories) does not depend on the choice for the reconstruction form, we obtain the dipole

moment

$$\begin{aligned}\mathbf{D}_\theta(\omega) = -i\left(\frac{I_\mathrm{p}}{2}\right)^{-\frac{1}{4}} \mathbf{d}^*_{\mathrm{rec},\theta}(-\sqrt{2(\omega-I_p)}) \sum_{t_0,t_0'} d_{\mathrm{ion},\theta}(-i\,\mathrm{sgn}(E(t_0'))\sqrt{2I_\mathrm{p}}, t_\mathrm{s}') \\ \times \left[\frac{2\pi}{\epsilon + i(t_\mathrm{s}-t_\mathrm{s}')}\right]^{\frac{3}{2}} e^{-i(S(t_0,t_0')-\omega t_0)} e^{i\left(\frac{E(t_0)}{-\sqrt{2(\omega-I_\mathrm{p})}+(t_0-t_0')E(t_0)}+\frac{E'(t_0')}{E(t_0')}\right)\frac{I_\mathrm{p}^2}{2(E(t_0'))^2}} \\ \times e^{-\frac{(2I_\mathrm{p})^{3/2}}{3|E(t_0')|}} \sqrt{\frac{2\pi i}{\frac{2(\omega-I_\mathrm{p})}{t_\mathrm{s}-t_\mathrm{s}'} - E(t_\mathrm{s})\sqrt{2(\omega-I_\mathrm{p})}}} \\ \times \sqrt{\frac{\pi}{\left(\frac{E(t_0)}{-\sqrt{2(\omega-I_\mathrm{p})}+(t_0-t_0')E(t_0)} + \frac{E'(t_0')}{E(t_0')}\right) i\sqrt{2I_\mathrm{p}} + |E(t_0')|}} + \mathcal{O}(\gamma^3).\end{aligned} \tag{5.110}$$

where $\mathbf{d}^*_{\mathrm{rec},\theta}(-k) = \frac{1}{(2\pi)^{3/2}}\iint \psi_{0,\theta}(\mathbf{r})(-\mathbf{r})e^{-ikx}d^2\mathbf{r} = -\frac{1}{(2\pi)^{3/2}}\mathbf{d}_\theta[\omega(k)]$. Comparing with Eq. (5.24) for short pulses ($a(k) = 0$ for $k > 0$) we find that $a_\theta[-k(\omega)]$ is given by Eq. (5.108). That means that in the SFA the wave packet decomposition functions as defined in this paper for length- and velocity-form tomography are equal. Note that beyond the SFA the prefactors before the matrix elements in the expressions for $\mathbf{D}_\theta(\omega)$ and $\mathbf{P}_\theta(\omega)$ are different, e.g., because of differences in effects of the plane-wave approximation. Also note that in (van der Zwan et al. [140]) $a(k)$ has a prefactor of 2π compared to what is presented here.

5.2 Above Threshold Ionization

We consider here only direct ATI electrons, i.e., scattering at the nuclei after ionization is not taken into account. Assuming that $A(\infty) = 0$, i.e., we are dealing with a physical laser pulse, the SFA amplitude for the process is the so-called Keldysh-Faisal-Reiss amplitude (Faisal [30]; Keldysh [55]; Reiss [106]) and is given by

$$M(p) = -i\int_0^{T_p} dt\langle \mathbf{p} + \mathbf{A}(t)|\mathbf{r}\cdot\mathbf{E}(t)|\psi_0\rangle e^{iS(\mathbf{p},t)}, \tag{5.111a}$$

with

$$S(\mathbf{p},t) = \frac{1}{2}\int_0^t (\mathbf{p}+\mathbf{A}(t'))^2 dt' + I_\mathrm{p}t, \tag{5.111b}$$

where $\mathbf{p}$ is the momentum of the ATI electron.

Similar to what was done in section 5.1, using the saddle-point method one can find an expression for the transition amplitude M_p in terms of classical trajectories. For linear polarization and emission (anti-)parallel to the polarization axis, it is given by (Milošević et al. [86, 87, 88])

$$M(p) \simeq -i\sum_{t_\mathrm{s}^{(A)}} \left(\frac{2\pi i}{E(t_\mathrm{s}^{(A)})(p+A(t_\mathrm{s}^{(A)}))}\right)^{1/2} \langle p + A(t_\mathrm{s}^{(A)})|xE(t_\mathrm{s}^{(A)})|\psi_0\rangle e^{iS(p,t_\mathrm{s}^{(A)})}. \tag{5.112}$$

The saddle-point times $t_s^{(A)}$ satisfy the equation

$$\frac{(p + A(t_s^{(A)}))^2}{2} = -I_p. \tag{5.113}$$

This leads to

$$f(\gamma) \equiv p + A(t_s^{(A)}) = S_{ATI} i\sqrt{2I_p} = S_{ATI} 2i\sqrt{U_p}\gamma, \tag{5.114}$$

where we have redefined $f(\gamma)$ and $S_{ATI} = \pm 1$.

The solutions $t_s^{(A)}$ of Eq. (5.114) are complex, requiring analytical representations of the laser pulse in the complex plane. In the general case, these will not be available. Therefore we will proceed similarly as before for the HHG process, finding the solutions of Eq. (5.114) as expansions around classical solutions as

$$f(\gamma) = f(0) + \sum_{n=1} \frac{1}{n!} \left[\frac{d^n f(\gamma)}{d\gamma^n}\right]_{\gamma=0} \gamma^n. \tag{5.115}$$

In this case the classical equation, for which the solutions can easily be found, reads

$$f(0) = p + A(t_0^{(A)}) = 0. \tag{5.116}$$

To solve Eq. (5.114), the expansion coefficients should be given by

$$\left[\frac{df(\gamma)}{d\gamma}\right]_{\gamma=0} = S_{ATI} 2i\sqrt{U_p}, \tag{5.117a}$$

$$\left[\frac{d^n f(\gamma)}{d\gamma^n}\right]_{\gamma=0} = 0 \qquad \text{for } n \geq 2. \tag{5.117b}$$

To find the saddle times $t_s^{(A)}$ that satisfy Eq. (5.117), we also expand $t_s^{(A)}$ around $\gamma = 0$ as

$$t_s^{(A)}(\gamma) = t_0^{(A)} + \sum_{n=1}^{\infty} \frac{1}{n!} a_n^{(A)} \gamma^n. \tag{5.118}$$

For the first order term in Eq. (5.117), we have that

$$\left[\frac{df(\gamma)}{d\gamma}\right]_{\gamma=0} = \left[\frac{dt_s^{(A)}}{d\gamma}\frac{\partial f(\gamma)}{\partial t_s^{(A)}}\right]_{\gamma=0} = -a_1^{(A)} E(t_0^{(A)}). \tag{5.119}$$

Combining this with Eq. (5.117) leads to

$$a_1^{(A)} = -\frac{S_{ATI} 2i\sqrt{U_p}}{E(t_0^{(A)})}. \tag{5.120}$$

The imaginary part of $t_s^{(A)}$ represents ionization. Since $M(p)$ in Eq. (5.111a) is proportional to $\exp(-I_p \operatorname{Im}(t_s^{(A)}))$, $\operatorname{Im}(t_s^{(A)})$ should be positive. Therefore we have that

$$S_{ATI} = -\operatorname{sgn}(E(t_0^{(A)})). \tag{5.121}$$

That means that we can write

$$a_1^{(A)} = \frac{2i\sqrt{U_\mathrm{p}}}{|E(t_0^{(A)})|}, \tag{5.122}$$

and we can rewrite the saddle-point condition as

$$f(\gamma) \equiv p + A(t_\mathrm{s}^{(A)}) = -i\,\mathrm{sgn}(E(t_0^{(A)}))\,\sqrt{2I_\mathrm{p}} = -2i\,\mathrm{sgn}(E(t_0^{(A)}))\,\sqrt{U_\mathrm{p}}\gamma. \tag{5.123}$$

The second order term is given by

$$\left[\frac{d^2 f(\gamma)}{d\gamma^2}\right]_{\gamma=0} = -a_2^{(A)} E(t_0^{(A)}) - \left(a_1^{(A)}\right)^2 E'(t_0^{(A)}). \tag{5.124}$$

When we combine this with Eq. (5.117), we derive

$$a_2^{(A)} = \frac{4U_\mathrm{p} E'(t_0^{(A)})}{(E(t_0^{(A)}))^3}. \tag{5.125}$$

Because we are dealing with only one saddle-point time, it is easy to go beyond second order. With the help of *Mathematica*, we derive

$$a_3^{(A)} = \frac{8iU_\mathrm{p}^{3/2}}{|E(t_0^{(A)})|^3}\left(-3\frac{|E'(t_0^{(A)})|^2}{|E(t_0^{(A)})|^2} + \frac{E''(t_0^{(A)})}{E(t_0^{(A)})}\right), \tag{5.126}$$

$$a_4^{(A)} = \frac{16U_\mathrm{p}^2(-15(E'(t_0^{(A)}))^3 + 10E(t_0^{(A)})E'(t_0^{(A)})E''(t_0^{(A)}) - (E(t_0^{(A)}))^2 E'''(t_0^{(A)}))}{(E(t_0^{(A)}))^7}. \tag{5.127}$$

When we compare the expansion coefficients derived in this section, with those presented for the HHG process in Eq. (5.104), we see that the first order term for the birth time is identical. The second order term is also identical if we take $t_0 = \infty$, reflecting the fact that an ATI electron never recombines. In this case

$$[a_2]_{t_0\to\infty} = \frac{4U_\mathrm{p}}{(E(t_0'))^2}\frac{E'(t_0')}{E(t_0')} \tag{5.128}$$

becomes equal to $a_2^{(A)}$ if we set equal the two birth times.

Inserting equation(5.123) into Eq. (5.112), we arrive at

$$\begin{aligned} M(p) &\simeq -i\sum_{t_\mathrm{s}^{(A)}}\left(\frac{-2\pi}{E(t_\mathrm{s}^{(A)})\,\mathrm{sgn}(E(t_0^{(A)}))\,\sqrt{2I_\mathrm{p}}}\right)^{1/2} \\ &\quad\times\langle -i\,\mathrm{sgn}(E(t_0^{(A)}))\,\sqrt{2I_\mathrm{p}}|xE(t_\mathrm{s}^{(A)})|\psi_0\rangle e^{iS(p,t_\mathrm{s}^{(A)})} \\ &= -i\sum_{t_\mathrm{s}^{(A)}} d_{\mathrm{ion},\theta}(-i\,\mathrm{sgn}(E(t_0^{(A)}))\sqrt{2I_\mathrm{p}}, t_\mathrm{s}^{(A)}) \\ &\quad\times\left(\frac{-2\pi}{E(t_\mathrm{s}^{(A)})\,\mathrm{sgn}(E(t_0^{(A)}))\,\sqrt{2I_\mathrm{p}}}\right)^{1/2} e^{iS(p,t_\mathrm{s}^{(A)})}. \end{aligned} \tag{5.129}$$

To evaluate this expression, we need to know how to calculate $E(t_\mathrm{s}^{(A)})$ and $S(p, t_\mathrm{s}^{(A)})$. With the help of *Mathematica*, we find that the laser pulse at complex birth times is given by

$$\begin{aligned}E(t_\mathrm{s}^{(A)}) = E(t_0^{(A)}) &+ a_1^{(A)}E'(t_0^{(A)})\gamma + \frac{1}{2}\left(a_2^{(A)}E'(t_0^{(A)}) + \left(a_1^{(A)}\right)^2 E''(t_0^{(A)})\right)\gamma^2 \\ &+ \frac{1}{6}\left(a_3^{(A)}E'(t_0^{(A)}) + 3a_1^{(A)}a_2^{(A)}E''(t_0^{(A)}) + \left(a_1^{(A)}\right)^3 E'''(t_0^{(A)})\right)\gamma^3 \\ &+ \frac{1}{24}\big(a_4^{(A)}E'(t_0^{(A)}) + \left(3\left(a_2^{(A)}\right)^2 + 4a_1^{(A)}a_3^{(A)}\right)E''(t_0^{(A)}) \\ &\quad + 6\left(a_1^{(A)}\right)^2 a_2^{(A)}E'''(t_0^{(A)}) + \left(a_1^{(A)}\right)^4 E''''(t_0^{(A)})\big)\gamma^4 + \mathcal{O}(\gamma^5).\end{aligned} \tag{5.130}$$

Also with the help of *Mathematica*, we expand the action around $\gamma = 0$ to avoid integrating the laser field over complex times. With knowledge of the saddle-time expansion coefficients up to fourth order in γ, this expansion can be done up to sixth order in γ. The result expressed in terms of I_p is

$$\begin{aligned}e^{iS(p,t_\mathrm{s}^{(A)})} = e^{iS(p,t_0^{(A)})} &e^{-\frac{(2I_\mathrm{p})^{3/2}}{3|E(t_0^{(A)})|}} e^{i\frac{E'(t_0^{(A)})I_\mathrm{p}^2}{2\left(E(t_0^{(A)})\right)^3}} e^{\frac{2\sqrt{2}\left(3\left(E'(t_0^{(A)})\right)^2 - E(t_0^{(A)})E''(t_0^{(A)})\right)I_\mathrm{p}^{5/2}}{15|E(t_0^{(A)})|^5}} \\ &\times e^{i\frac{\left(-15\left(E'(t_0^{(A)})\right)^3 + 10E(t_0^{(A)})E'(t_0^{(A)})E''(t_0^{(A)}) - \left(E(t_0^{(A)})\right)^2 E'''(t_0^{(A)})\right)I_\mathrm{p}^3}{18\left(E(t_0^{(A)})\right)^7}} + \mathcal{O}(\gamma^7).\end{aligned} \tag{5.131}$$

The expansion of the action for the ATI process is very similar to that of the HHG process in Eq. (5.104). In both cases the action is stationary up to second order in γ, and the third order term gives the tunneling ionization factor. The fourth order term is identical if we take $t_0 \to \infty$ in Eq. (5.104). This is the same kind of relationship between HHG and ATI as we saw for a_2 versus $a_2^{(A)}$, reflecting the fact that the fourth order term of the action seems to depend physically on the second order term of the birth time.

We can now evaluate Eq. (5.129) by using the approximations made in Eqs. (5.130) and (5.131). The fifth order term of the expansion of the action is imaginary, leading to $\exp(iS)$ containing the exponent of a real number in Eq. (5.131). The numerator of this number can have both signs and its denominator can become arbitrarily small. Therefore evaluating this term sometimes amounts to taking the exponent of a division close to 0, which is associated with significant numerical problems and errors. It is for this reason that we do not use the fifth and sixth order terms of Eq. (5.131), i.e., the last two terms of the expression are ignored in numerical calculations. It is not very surprising that the expansion does not work for the trajectories that start at very small values of the electric field, because the underlying strong-field approximation is not applicable in this situation.

5.3 Suitability of laser pulse

In the sections 5.1.3 and 5.2 we saw that the HHG and ATI spectra of a molecular system can be expressed as sums over contributions from classical trajectories. In this section we will use these SFA results to calculate the suitability of a given laser pulse to perform molecular tomography.

5.3.1 Suitability of laser pulse for standard tomography

In section 2.3 it was shown that the tomographic reconstruction equation can only be derived for the general case of an unsymmetric molecule if $a(k) = 0$ for either $k > 0$ or $k < 0$. The extent to which this requirement is fulfilled for a particular laser pulse can be checked by comparing the contributions with negative return momentum to those with positive return momentum in Eq. (5.104). It will be interesting to compare the result of this calculation with the results of the simplified calculations in section 4.6.1.

Let c_{ni} be the i-th contribution to harmonic n with frequency ω_n. It is given by everything after $\mathbf{v}^*_{\mathrm{rec},\theta}(v_{\mathrm{rec}})$ in Eq. (5.104) evaluated for that specific trajectory. As a measure of the contribution of trajectories with negative return momentum to harmonic ω_n, we introduce the measure

$$Q^{(h)}_{\mathrm{NVR}}(\omega_n) = \begin{cases} \left(\sum_{v_{\mathrm{rec}}<0} |c_{ni}|\right) \Big/ \left(\sum_{i=1}^{N_n} |c_{ni}|\right) & \text{if } N_n > 0 \\ 0.5 & \text{else.} \end{cases} \tag{5.132}$$

Here N_n is the total number of trajectories contributing to ω_n. The contribution of trajectories with negative return momentum to the complete harmonic spectrum is then given by

$$Q_{\mathrm{NVR}} = \frac{1}{N} \sum_{n=1}^{N} Q^{(h)}_{\mathrm{NVR}}(\omega_n), \tag{5.133}$$

where N is the number of harmonic frequencies considered. Q_{NVR} will be equal to 1 if all trajectories that contribute to the harmonic spectrum return with negative momentum, and 0 if all the contributing trajectories return with positive momentum.

Instead of finding a single laser pulse that has $Q_{\mathrm{NVR}} = 1$ (or 0) for the system studied, of course also a small collection of different pulses can be used for the reconstruction. The system would be subjected to the different pulses independently. The harmonic ranges for which the individual pulses have $Q^{(h)}_{\mathrm{NVR}}(\omega_n)$ close to 1 or 0 can be combined before performing the reconstruction.

In theory, for a tomographic reconstruction regions of the spectrum where $Q^{(h)}_{\mathrm{NVR}}(\omega)$ is close to 0 can be combined with regions where $Q^{(h)}_{\mathrm{NVR}}(\omega)$ is close to 1, by taking the complex conjugate of the reconstruction matrix elements lying in the first category of regions. However, as we saw in section 4.6, in practice this does not work very well because the orbital is reconstructed with a global complex phase. Therefore it is impossible to use the regions where $Q^{(h)}_{\mathrm{NVR}}(\omega) = 0$ and instead we have to resort to recording the spectrum also for a pulse with opposite polarity.

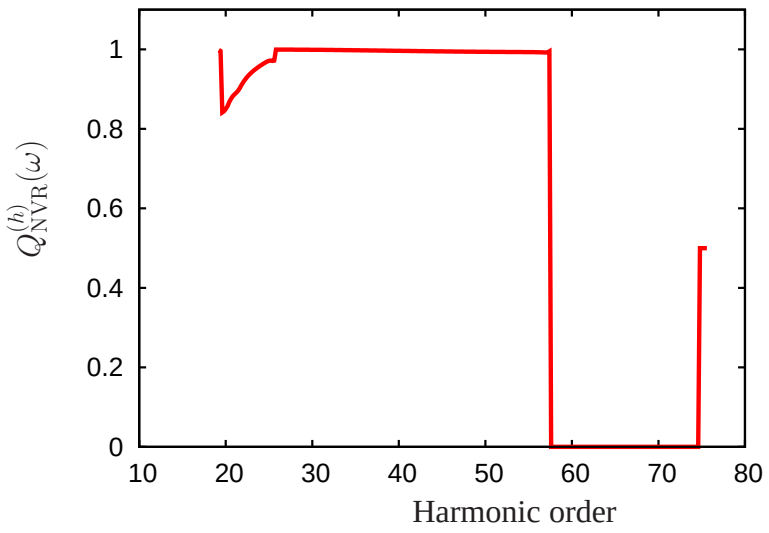

Figure 5.5: (Color online) $Q^{(h)}_{\mathrm{NVR}}(\omega)$ for a three-cycle $\sin^2$-pulse with $\phi_{\mathrm{CEP}} = 1.25\pi$. The laser intensity is $I = 5 \times 10^{14}$ W/cm^2 and the laser wavelength is $\lambda = 780$ nm.

5.3.1.1 Results

For a linearly polarized three-cycle $\sin^2$-pulse with a carrier-envelope-phase of $\phi_{\mathrm{CEP}} = 1.25\pi$ we plot $Q^{(h)}_{\mathrm{NVR}}(\omega)$ in Fig. 5.5. We use $I = 5 \times 10^{14}$ W/cm^2, $\lambda = 780$ nm, and we assume a 3D world. We can compare the result with Fig. 4.13b that was calculated for exactly the same laser pulse, a pulse that was also used for most of the numerical tomographic simulations presented in chapter 4. Note that in Fig. 4.13b we plotted the result for $\phi_{\mathrm{CEP}} = 0.25\pi$ though, which means that we must replace $k \rightarrow -k$ in that plot to compare it with Fig. 5.5. If we do so, we observe that Fig. 5.5 contains much of the same information as Fig. 4.13b, although more accurately because the full SFA expression including trajectory interferences and the effect of finite γ was used to calculate it. However, the absolute probabilities of the returns are not reflected in Fig. 5.5. Both curves convey that the spectrum associated with a three-cycle laser pulse with $\phi_{\mathrm{CEP}} = 1.25\pi$ is strongly dominated by electron returns with negative momenta up to around harmonic 57, and for the high end of the spectrum much weaker returns with positive momenta dominate the spectrum.

In Fig. 5.6 we copy from Fig. 4.15 the red plusses that indicate the fraction of electrons that return with negative momenta as a function of ϕ_{CEP} for three-cycle $\sin^2$-pulses. In addition we plot Q_{NVR} in the same figure for comparison (black triangles). The reason why the Q_{NVR}-values for the three-cycle $\sin^2$-pulses do not look very promising, whereas in section 4.6.1 we came to the conclusion that these pulses are very suitable for molecular tomography, is that Q_{NVR} is given by the average $Q^{(h)}_{\mathrm{NVR}}(\omega_n)$ over the entire harmonic range. As we saw in Fig. 5.5 for the $\phi_{\mathrm{CEP}} = 1.25\pi$-pulse, the high-end of the spectrum might be dominated by weak returns with momenta with the opposite sign as the returns that dominate the main part of the spectrum. In Fig. 4.15 these weak high-energy returns hardly contribute toward the result as here the total amplitudes of returns with negative and positive

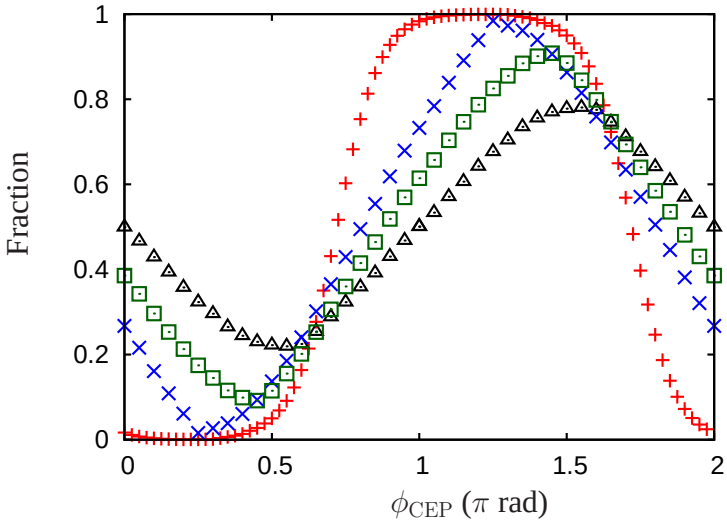

Figure 5.6: (Color online) The red plusses are taken from Fig. 4.15. The black triangles are Q_{NVR} for the same pulses. The green squares and blue crosses also show Q_{NVR}, but for the frequency range up to harmonic orders 57.6 and 65, respectively.

momenta are compared.

If instead of letting the sum in Eq. (5.133) run up to the classical cutoff (harmonic 76), we let the sum run up to harmonic 57.6 or 65, we obtain the green squares and blue crosses in Fig. 5.6, respectively. These curves show that some of these pulses are very suitable for molecular tomographic reconstructions of general molecules if we use a cutoff that is a bit lower than that predicted by the classical cutoff law ($3.17U_{\mathrm{p}} + I_{\mathrm{p}}$). Alternatively, as discussed just before section 5.3.1.1, we could combine a pulse with $\phi_{\mathrm{CEP}} = 1.25\pi$ for the main part of the spectrum with a pulse with $\phi_{\mathrm{CEP}} = 0.25\pi$ for the high-end part of the spectrum to obtain an even better reconstruction. However, as the numerical simulations in chapter 4 show, simply using the $\phi_{\mathrm{CEP}} = 0.25\pi$-pulse for the entire harmonic range produces already good results.

5.3.1.2 Multiple pulses

Instead of using a single laser pulse to perform the tomographic reconstruction, it is also possible to combine the data from many different laser pulses to improve the reconstruction. This is an advantage for extremely short pulses that may provide favorable conditions only for a small harmonic range. Therefore this has the most relevance for asymmetric molecules.

If multiple pulses are used for the reconstruction, we select the pulse for each harmonic ω_n using the following procedure. First we select the pulses that fulfill

$$Q_{1-\mathrm{sided}}(\omega_n) \geq q_{\mathrm{NVR}} = 0.999 \tag{5.134a}$$

and

$$I(\omega_n) \geq q_I \, I_{\max}(\omega_n) = 10^{-3} I_{\max}(\omega_n), \tag{5.134b}$$

where $Q_{1-\text{sided}}(\omega_n) = \max\left(Q^{(h)}_{\text{NVR}}(\omega_n), 1 - Q^{(h)}_{\text{NVR}}(\omega_n)\right)$ and $I_{\max}(\omega_n)$ is the maximum harmonic intensity at ω_n of all pulses considered. From these pulses we select the one associated with the highest harmonic intensity at frequency ω_n. If no pulses are found for which Eqs. (5.134a) and (5.134b) are fulfilled, we instead select the pulse that fulfills Eq. (5.134b) and is associated with the highest value of $Q_{1-\text{sided}}(\omega_n)$.

If no contributing trajectories could be found for ω_n for any of the pulses, $Q^{(h)}_{\text{NVR}}(\omega_n)$ is undefined for all the pulses. In this case we select the same pulse for ω_n as for ω_{n-1}, or if this is not possible, as for ω_{n+1} and we also transfer the $Q^{(h)}_{\text{NVR}}$-value from the neighboring harmonic. This way we extend the procedure into the classically forbidden region and there also reasonable pulses are selected based on surrounding classically allowed regions. Although $Q^{(h)}_{\text{NVR}}(\omega_n)$ is irrelevant for a symmetric molecule, the above procedure will improve the tomographic reconstruction of a symmetric molecule if extremely short pulses are used to reconstruct it. The reason is that it ensures that over the entire harmonic range pulses are used that give rise to a high harmonic intensity at that frequency and thereby good correspondence with the three-step model.

For asymmetric molecules we encounter problems in the tomographic reconstruction if at some harmonics we use dipole matrix elements retrieved from tomographic experiments where the short laser pulse effectively had the opposite polarity as for the other harmonics, i.e., when the wave packet came from the opposite side for those harmonics. In such a scenario, we retrieved $\mathbf{d}_{\theta+\pi}(\omega_n)$ or $p_{\theta+\pi}(\omega_n)$ for those harmonics for which $Q^{(h)}_{\text{NVR}}(\omega_n) < 0.5$. This means we have to rotate the orientation of the affected dipole matrix elements by π rad.

In Fig. 5.7 we plot the pulse selected by our selection procedure in case we consider ten different three-cycle $\sin^2$-pulses at a wavelength of 2000 nm and an intensity of 2×10^{14} W/cm^2. Here we consider the 1D world used for the simulations in section 4.9. The pulses have ϕ_{CEP}-values of 0.0–0.9. The plot shows that the procedure makes use of all the pulses to achieve one-sided recombinations over the entire harmonic range.

5.3.2 Suitability of laser pulse for tomography with ATI

In section 4.8.1 it was argued that if there exists a one-to-one mapping between each harmonic peak and an ATI peak, ATI electrons can be used to improve the molecular tomographic reconstruction. For this mapping to exist, each harmonic peak must be predominately determined by a single trajectory. At the birth time of that harmonic trajectory, an ATI trajectory that dominates the ATI spectrum for some momentum p must start. In this section we will derive measures that quantify how well the one-to-one mapping is satisfied, i.e., how suitable the laser pulse is for using ATI electrons to improve the molecular reconstruction.

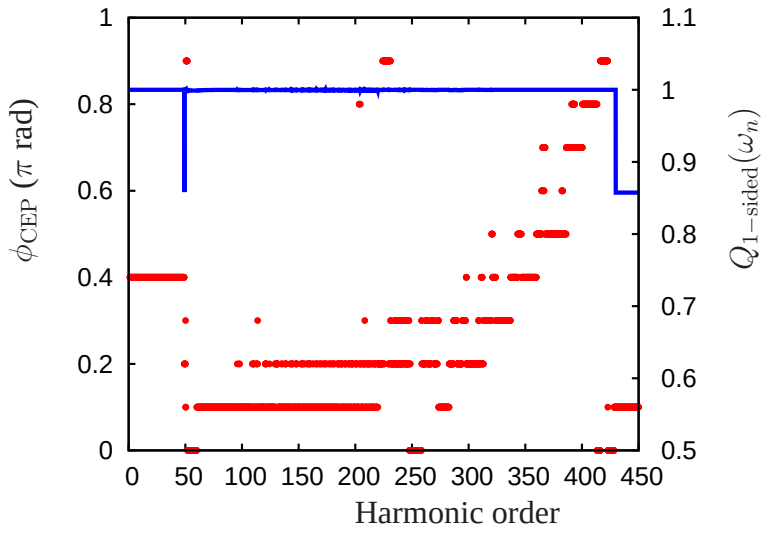

Figure 5.7: (Color online) The ϕ_{CEP} used for the reconstruction as a function of harmonic order when ten three-cycle pulses are considered (red dots). Also plotted is the value of $Q_{1-\mathrm{sided}}(\omega_n)$ (blue line).

The extent to which trajectory n_i determines harmonic ω_n, is given by

$$Q_{\mathrm{HHG}}(\omega_n, i) = |c_{ni}| \Big/ \left(\sum_{j=1}^{N_n} |c_{n_j}| \right) . \tag{5.135}$$

If the trajectory uniquely determines the harmonic, $Q_{\mathrm{HHG}}(\omega_n, i) = 1$, if it has no influence at all, $Q_{\mathrm{HHG}}(\omega_n, i) = 0$.

Let an ATI trajectory with the same birth time as harmonic trajectory n_i contribute with d_{ni} to ATI peak p_{ni}. Since we are making a classical comparison between the two trajectories, we set their classical birth times equal, not their full birth times or the real part of their full birth times. For the HHG trajectory, the return time has a direct influence on the expansion of the classical birth time to the full birth time. This shows that in the full birth times they are factors that go beyond the simple picture used here, and we should not consider the full birth time for this purpose. The contribution d_{ni} is given by everything after the sum in Eq. (5.129) for that trajectory. The uniqueness of that trajectory in determining ATI peak p_{ni} is given by

$$Q_{\mathrm{ATI}}(\omega_n, i) = |d_{ni}| \Big/ \left(\sum_{t_0^{(A)} \to p_{ni}} |d(t_{\mathrm{s}}^{(A)})| \right) , \tag{5.136}$$

where $d(t_0^{(A)})$ is the contribution to Eq. (5.129) from the trajectory with birth time $t_0^{(A)}$, and the sum is over all birth times that lead to an ATI peak at momentum p_{ni}. Since for non-cw pulses p_{ni} is not restricted to any discretized values, a dedicated search for other trajectories that lead to p_{ni} has to be performed.

Putting equations (5.135) and (5.136) together, the amount of one-to-one linking for

each HHG trajectory is defined as

$$Q^{(t)}_{1\text{to}1}(\omega_n, i) = Q_{\text{HHG}}(\omega_n, i) \times Q_{\text{ATI}}(\omega_n, i). \tag{5.137}$$

Here $Q^{(t)}_{1\text{to}1}(\omega_n, i) = 1$ means that the one-to-one linking is perfect for harmonic trajectory n_i and $Q^{(t)}_{1\text{to}1}(\omega_n, i) = 0$ means the link is not possible. The amount of one-to-one linking to an ATI peak for an harmonic peak ω_n is given by the best link provided by one of its contributing harmonic trajectories. In formula,

$$Q^{(h)}_{1\text{to}1}(\omega_n) = \begin{cases} \max\left(Q^{(t)}_{1\text{to}1}(\omega_n, 1), \ldots, Q^{(t)}_{1\text{to}1}(\omega_n, N_n)\right) & \text{if } N_n > 0 \\ 0 & \text{else.} \end{cases} \tag{5.138}$$

The total measure for the whole harmonic range is then given by

$$Q_{1\text{to}1} = \frac{1}{N} \sum_{n=1}^{N} Q^{(h)}_{1\text{to}1}(\omega_n). \tag{5.139}$$

If $Q_{1\text{to}1} = 0$, the pulse cannot be used to determine the continuum wave packet according to Eq. (4.57). If, however, $Q_{1\text{to}1} = 1$, the pulse is perfect for the incorporation of ATI electrons into the tomographic reconstruction scheme.

Besides playing a role in determining the suitability of the laser pulse for the molecular reconstruction, $Q^{(t)}_{1\text{to}1}(\omega_n, i)$ also provides us with the prescription of how to do the reconstruction. It can be used to determine $p^{(\text{A})}(\omega)$ in Eq. (4.57), i.e., it provides us with the information which harmonic peak to link to which ATI peak. Namely, the ATI peak that corresponds to the birth time of the trajectory n_k with the highest value $Q^{(t)}_{1\text{to}1}(\omega_n, k)$ for harmonic ω_n should be used. In formulas,

$$p^{(\text{A})}(\omega_n) = p_{nk}, \tag{5.140a}$$

with k such that

$$Q^{(t)}_{1\text{to}1}(\omega_n, k) \geq Q^{(t)}_{1\text{to}1}(\omega_n, l) \quad \text{for } 1 \leq l \leq N_n. \tag{5.140b}$$

If $Q_{1\text{to}1} = 1$ but Q_{NVR} is not equal 0 or 1, the condition that returns from one side only contribute to $a(k)$ is fulfilled in a complicated frequency-dependent manner. This means that in principle the pulse can still be used for the reconstruction of asymmetric molecules. However, attention should be paid to from which side the continuum wave packet approached the core for every harmonic and the measurement should be repeated with an oppositely polarized pulse for those harmonics where the return was originally from the opposite side.

As before, instead of considering a single pulse, a small collection of pulses can be used that perform well in different harmonic ranges. The results can then be properly combined to achieve an even better reconstruction.

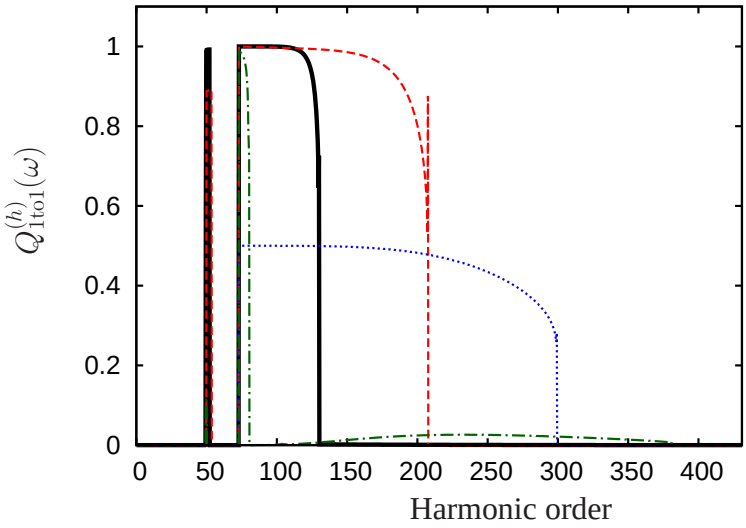

Figure 5.8: (Color online) $Q^{(h)}_{1\text{to}1}(\omega)$ for two-cycle $\sin^2$-pulses with $\phi_{\text{CEP}} = 0\pi$ (black solid line), $\phi_{\text{CEP}} = 0.25\pi$ (red dashed line), $\phi_{\text{CEP}} = 0.5\pi$ (blue dotted line) and $\phi_{\text{CEP}} = 0.75\pi$ (green dot-dashed line). The laser intensity is $I = 2 \times 10^{14}$ W/cm^2 and the laser wavelength is $\lambda = 2000$ nm.

5.3.2.1 Results

In this section we consider a 1D world as the simulations for molecular tomography including ATI electrons in this thesis are in 1D. This means that we adapt the wave-packet-spreading factor accordingly, as described below Eq. (5.5). We consider linearly polarized $\sin^2$-pulses with an intensity of $\lambda = 2000$ nm at an intensity of $I = 2 \times 10^{14}$ W/cm^2. For two-cycle and three-cycle pulses we plot $Q^{(h)}_{1\text{to}1}(\omega)$ for different ϕ_{CEP} in Figs. 5.8 and 5.9, respectively. The lowest energy ATI electrons are strongly perturbed by the Coulombic potential and we do not use them for tomographic reconstructions. Therefore we accept only those HHG-ATI links for which

$$\left|p^{(\text{A})}(\omega)\right| \geq p_{\text{min}}. \tag{5.141}$$

We arbitrarily set $p_{\text{min}} = \sqrt{2(0.2U_{\text{p}})} \simeq 1.05$ a.u. in Figs. 5.8 and 5.9. In Fig. 5.9 we additionally plot $Q^{(h)}_{1\text{to}1}(\omega)$ for $\phi_{\text{CEP}} = 0.25\pi$ using $p_{\text{min}} = 0$ (brown dot-dot-dashed versus red dashed line).

From Fig. 5.8 we observe that for extremely short pulses—even shorter than required for normal tomographic reconstructions of general molecules—over a broad harmonic range ATI peaks are available that can be used to improve the tomographic reconstruction. The observed one-to-one linking between HHG and ATI peaks is unique and has not been observed or predicted so far. Unfortunately the relationship between HHG and ATI peaks exists only for extremely short pulses. Already if we move to the three-cycle pulses of Fig. 5.9 we can find a usable one-to-one relationship between the two processes only for a narrow harmonic range. From the brown dot-dot-dashed lines in Fig. 5.9 we observe that this is the case because of the low momenta of the linked ATI peaks. Setting $p_{\text{min}} = 0$ or $p_{\text{min}} = \sqrt{2(0.2U_{\text{p}})}$

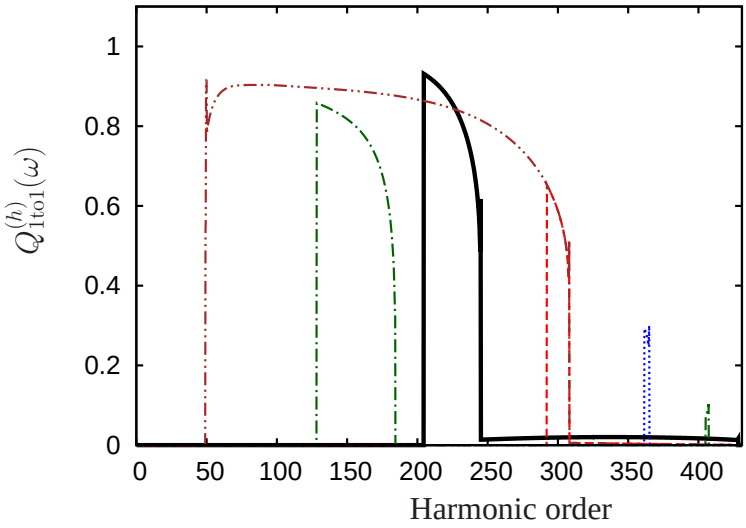

Figure 5.9: (Color online) $Q^{(h)}_{1\text{to}1}(\omega)$ for three-cycle $\sin^2$-pulses with $\phi_{\text{CEP}} = 0\pi$ (black solid line), $\phi_{\text{CEP}} = 0.25\pi$ (red dashed line), $\phi_{\text{CEP}} = 0.5\pi$ (blue dotted line) and $\phi_{\text{CEP}} = 0.75\pi$ (green dot-dashed line). Additionally $Q^{(h)}_{1\text{to}1}(\omega)$ for $p_{\text{min}} = 0$ is shown (brown dot-dot-dashed line). The laser intensity is $I = 2 \times 10^{14}$ W/cm^2 and the laser wavelength is $\lambda = 2000$ nm.

hardly makes a difference for the curves plotted in Fig. 5.8 (not plotted).

There is a straightforward physical explanation for the phenomenon that only extremely short pulses can give rise to significant usable one-to-one linking between HHG and ATI. Ionization takes predominantly place at the peaks of the electric field of the laser pulse. From Eq. (5.116) we see that the energy of an ATI peak is given by minus the value of the vector potential at the birth time. Since the vector potential is given by the integral of the electric field of the laser pulse, $A(t)$ tends to be exactly out of phase with the sinusoidal carrier of $E(t)$. Therefore the ATI trajectories born at the same time as the HHG trajectories, just after the peak of the electric field, tend to have low energies. This effect is broken for the two-cycle pulses of Fig. 5.8 as the very short envelope destroys the phase relationship between $A(t)$ and $E(t)$. For longer pulses also more trajectories contribute to each HHG and ATI peak, reducing the probability that one birth time has a significant influence on both an HHG and ATI peak.

In Figs. 5.10 and 5.11 we plot $Q_{1\text{to}1}$ as a function of ϕ_{CEP} for pulses with different lengths. The left plots are for an intensity of $I = 2 \times 10^{14}$ W/cm^2 at a laser wavelength of $\lambda = 2000$ nm whereas the right plots are for $I = 5 \times 10^{14}$ W/cm^2 and $\lambda = 780$ nm. In Fig. 5.11 we redefined Eq. (5.137) in accordance with Figs. 5.8 and 5.9 as

$$Q^{(t)}_{1\text{to}1}(\omega_n, i) = \begin{cases} Q_{\text{HHG}}(\omega_n, i) \times Q_{\text{ATI}}(\omega_n, i) & \text{if } |p_{ni}| \geq p_{\text{min}} \\ 0 & \text{else,} \end{cases} \tag{5.142}$$

before calculating $Q^{(h)}_{1\text{to}1}(\omega)$ and $Q_{1\text{to}1}$. Also here we use $p_{\text{min}} = \sqrt{2(0.2U_{\text{p}})}$, where p_{min} takes a different numerical value for the left and right plots because of the differ-

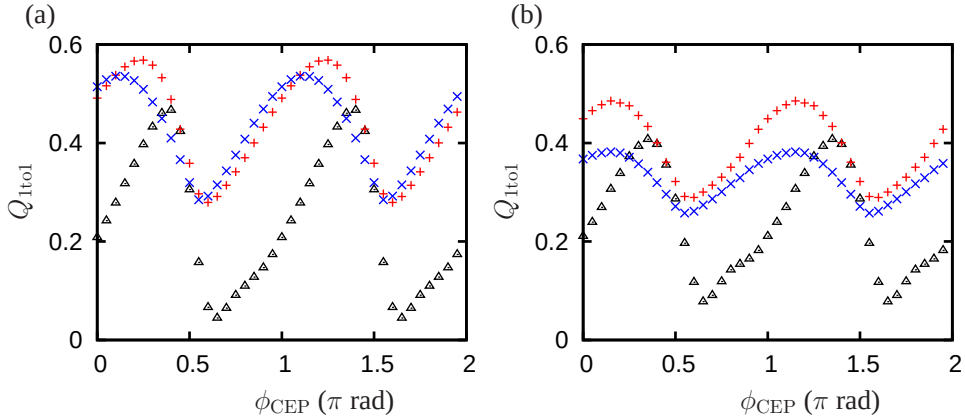

Figure 5.10: (Color online) Q_{1to1} as a function of ϕ_{CEP} for two-cycle $\sin^2$-pulses (black triangles), three-cycle $\sin^2$-pulses (red plusses), and four-cycle $\sin^2$-pulses (blue crosses); (a) $I = 2 \times 10^{14}$ W/cm^2 and $\lambda = 2000$ nm, (b) $I = 5 \times 10^{14}$ W/cm^2 and $\lambda = 780$ nm.

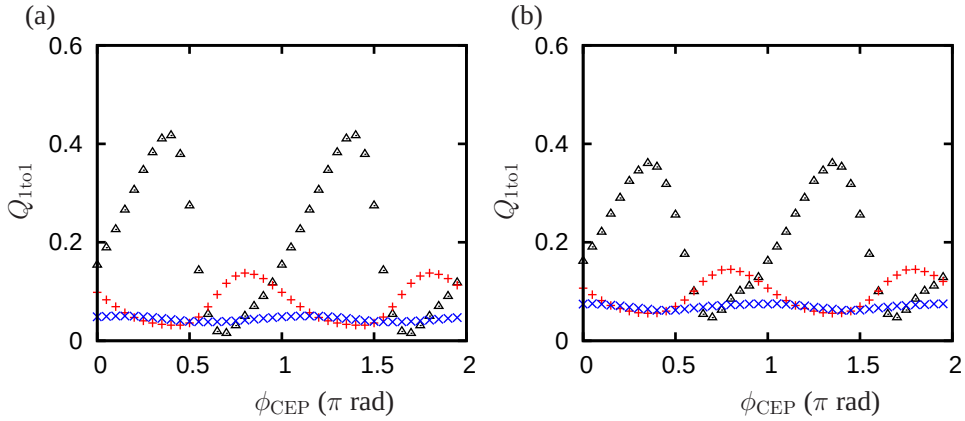

Figure 5.11: (Color online) Same as Fig. 5.10 with $p_{min} = \sqrt{2(0.2U_p)}$.

ence in laser parameters. If we accept $p_{min} = 0$ there is significant HHG-ATI linking for the investigated 2–4 cycle pulses. However, already using the relatively low $p_{min} = \sqrt{2(0.2U_p)}$ we observe there is hardly any possibility to use 3–4 cycle pulses to improve the tomographic reconstruction. Also visible is that longer wavelengths provide better opportunities for improving tomographic reconstructions using ATI electrons.

Experimentally the situation might be a bit better than depicted in this section because phase-matching leads to certain harmonic trajectories being selected (see section 2.3.3) (Gaarde and Schafer [38]; Hariharan and Robinson [47]; Salières et al. [110]). Because of the difference in propagation times, the short and long trajectories acquire different phases in the continuum. Therefore the contributions from a gas of atoms constructively add if the laser focus is placed either before or after the gas jet, and the short and long trajectories are emitted under different angles. (Balcou et al. [3]; Salières et al. [109]). For instance, in a standard experimental setup the long trajectories are suppressed relative to the short trajectories. The short trajectories

can also be selected by adding a weak third harmonic field to the generating pulse (Cao et al. [14]). For the very short pulses considered here the contributions of different trajectories depends on ϕ_{CEP}. Nonetheless some improvement might be possible when we block certain harmonic trajectories. We have not considered this possibility. Additionally the curves look slightly better for a physical 3D world as the wave-packet spreading tends to suppress unwanted trajectories.

5.3.2.2 Multiple pulses

As we saw in section 5.3.2.1, a single extremely short pulse only provides useful information over a narrow harmonic range. Therefore it makes sense to combine tomographic data from several pulses when incorporating ATI electrons into the tomographic reconstruction, both for symmetric and asymmetric molecules. Here we elaborate on the procedure to select the pulse to use for each harmonic frequency.

From all the pulses that fulfill

$$Q^{(h)}_{\mathrm{1to1}}(\omega_n) \geq q^{(1)}_{\mathrm{1to1}} = 0.8 \tag{5.143a}$$

and

$$|p^{(\mathrm{A})}(\omega_n)| \geq q^{(1)}_p = \sqrt{2(0.3U_{\mathrm{p}})}, \tag{5.143b}$$

we select the pulse that is associated with the highest momentum $p^{(\mathrm{A})}$ at frequency ω_n. If no such pulse exist, instead we select the pulse with the highest $Q^{(h)}_{\mathrm{1to1}}$-value under the conditions that

$$Q^{(h)}_{\mathrm{1to1}}(\omega_n) \geq q^{(2)}_{\mathrm{1to1}} = 0.5 \tag{5.144a}$$

and

$$|p^{(\mathrm{A})}(\omega_n)| \geq q^{(2)}_p = \sqrt{2(0.2U_{\mathrm{p}})}. \tag{5.144b}$$

In the case that no pulse can be found that fulfills Eq. (5.144), we do not use information from ATI electrons for the tomographic reconstruction and we resort to the procedure outlined in section 5.3.1.2.

Analogous to Fig. 5.7, in Fig. 5.12 we plot the pulse selected by our selection procedure for tomographic reconstruction including ATI electrons. In Fig. 5.12 we plot only those harmonics for which ATI electrons are incorporated into the reconstruction. Here we consider two-cycle and not three-cycle $\sin^2$-pulses, but the wavelength of 2000 nm and the intensity of 2×10^{14} W/cm^2 remain the same. The plot shows that there is good-quality information from ATI electrons available over a significant fraction of the harmonic range.

Also if the pulse was selected using Eq. (5.143) or Eq. (5.144), we need to consider the value of $Q^{(h)}_{\mathrm{NVR}}(\omega_n)$ for the harmonic considered. If $Q^{(h)}_{\mathrm{NVR}}(\omega_n) < 0.5$ for asymmetric molecules the reconstruction matrix elements between orientations θ and $\theta + \pi$ are switched around as described at the end of section 5.3.1.2.

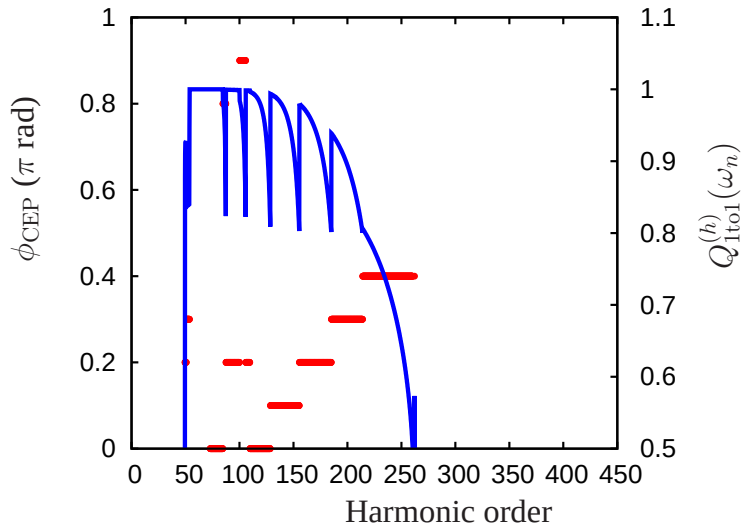

Figure 5.12: (Color online) The $\phi_{\rm CEP}$ used for tomographic reconstruction including ATI electrons as a function of harmonic order when ten two-cycle pulses are considered (red dots). Also plotted is the value of $Q_{\rm 1to1}(\omega_n)$ for those harmonics (blue line).

Chapter 6

Post-processing reconstructions

In this chapter we will occupy ourselves with the optimization of reconstructed orbitals obtained from the molecular tomographic scheme. This chapter is not devoted to optimizing the experimental scheme itself, but instead we focus on removing errors from the reconstructed orbitals numerically afterwards. The reconstruction errors can be partially removed in an iterative process. At each iteration step we will apply filters to the reconstructed orbital that represent *a priori* knowledge about either the orbital or the molecular tomographic scheme.

6.1 Error causes

Only for the simplest of orbitals and/ or optimal laser parameters does the tomographically reconstructed orbital closely resemble the real orbital of the target molecule. In contrast typically quite large errors are present. These errors either disturb the molecular reconstruction in the core region or present themselves as artifacts outside the core region. Very typical for the latter are the ring-like structures present in most tomographic reconstructions.

One of the main sources of error for the tomographic reconstruction are systematic errors of the Lewenstein model. Contributions from the orbital shape on the ionization process, and more importantly from the Coulomb field on the propagation and the recombination processes, and from the laser field on the recombination process all destroy the plane-wave character of the returning wave packet. Therefore the plane-wave approximation (PWA) that was used in the derivation of the reconstruction equations is not fully fulfilled and errors are introduced. Furthermore, only a finite range of frequencies can be determined, depending on both the laser wavelength and intensity and limited by the depletion of the bound state. Both low and high frequencies are missing, the former because the PWA becomes worse for the lowest harmonics and these are therefore normally ignored, and the latter because of the harmonic cutoff. Clearly molecular features at too low or too high frequencies cannot be recovered, but the limited range of frequencies present also causes artifacts in the reconstruction that can be removed.

In addition—and arguably the most important source of errors—using a reference atom we do not obtain the optimal $a_\theta[-k(\omega)]$. Despite all the problems mentioned above, an almost perfect reconstruction is often still possible using the optimal $a_\theta[-k(\omega)]$, as the $a_\theta[-k(\omega)]$-entries under the PWA are nothing more than Fourier components. Even if $a_\theta[-k(\omega)]$ does not accurately reflect the physical process behind HHG, if we find a good way to approximate $a_\theta[-k(\omega)]$, we can still attain an almost perfect reconstruction.

6.2 Error filters

The main notion behind the error reduction algorithm is that a physical orbital has a tight support, i.e., that it is nonzero only in a relatively small area around the origin. Furthermore we use that the error superimposed on the reconstructed orbital has limited θ- and k-dependence. In other words, we assume that the error introduced by the tomographic process does not change much on a small change of the momentum k or the angle θ. While we search for variations of the orbital that make it fulfill the requirement of the tight support and other requirements, at the same time we make sure that the introduced variations—the presumed error—fulfill the property of limited θ- and k-dependence. All requirements on the orbital or the error are expressed in terms of filters that are iteratively applied to the orbital.

The filters take the form of projection operators that project the current orbital onto the closest orbital that fulfills the condition expressed by the filter. Because the images of the filters are not orthogonal, together the filters are not a projection and the orbital keeps changing on iteratively applying the filters. Ideally it moves toward the point where the filter images overlap, i.e., the optimal point where all *a priori* requirements are met and that represents the physical orbital. This is illustrated geometrically in Fig. 6.1. In reality, such a point might not exist, meaning the true physical orbital cannot be found but only approximated. Moreover, because some constraint subspaces associated with the filters are nonconvex, the algorithm can get stuck in a fixed point that only fulfills a subset of the physical constraints (Elser [29]). The projection onto a concave image might be undefined, as the image can be orthogonal to the vector from the current orbital at a whole family of points. An extreme example that illustrates the problem is given by a circular image around a point that represents the current orbital. If one of the two images is concave, the algorithm can get stuck around a point where the distance between the two images has a local maximum.

6.3 Error reduction algorithm

A schematic of the error reduction algorithm is depicted in Fig. 6.2. It is largely based on the hybrid input-output algorithm (HIO) for phase retrieval developed by Fienup (Elser [29]; Fienup [34]). The HIO algorithm deals with the problem of recovering the phases if only the amplitudes of the Fourier transform of an object are

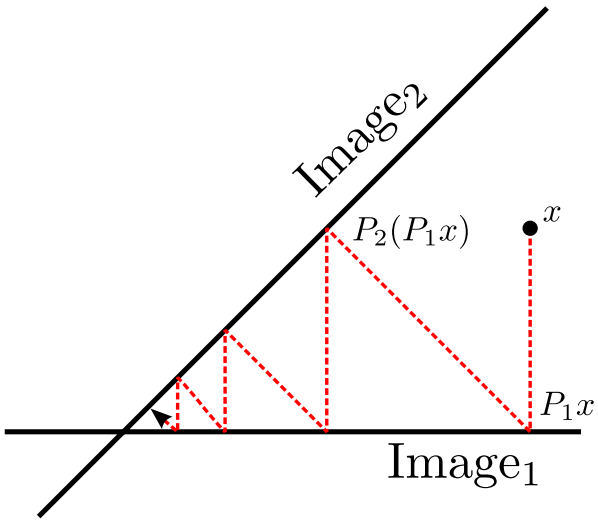

Figure 6.1: (Color online) Illustration of the effect of two non-orthogonal filters. Starting at point x, projection operators P_1 and P_2 are iteratively applied. The orbital converges slowly toward the intersection point of the filter images.

known. Such a problem is often encountered in for instance astronomy or crystallography. It works by iteratively Fourier transforming the object to the momentum domain. In each domain those filters representing physical knowledge about the orbital are applied that are best expressed in that domain. Most importantly, in the momentum domain the amplitudes of the Fourier components are set to the measured values. In the real domain it is used that the object is assumed to have a tight support. Although for the HIO algorithm nothing has been proven about the rate of convergence, it has been applied successfully in many different problems (Elser [29]). Depending on the complexity of the problem, convergence can take more than 1,000 iterations (see e.g. Marchesini et al. [82]).

The removal of errors from the tomographic reconstruction of a molecular orbital is not exactly the same as the phase-retrieval problem. Instead of having to retrieve the phases to the (approximately) exactly known amplitudes in the momentum domain, we have information about both the amplitudes and phases, but both with considerable errors. Since we assume that ψ is nonzero only in a relatively small area around the origin, we have adapted the HIO algorithm to look for variations of both the amplitudes and phases in the momentum domain with little θ- and k-dependence that make it fulfill the tight-support requirement in the real domain. In the following we will explain the different components of the error reduction algorithm as depicted in Fig. 6.2.

In Fig. 6.2 the circles represent states and the boxes represent operations or filters. At every iteration n we Fourier transform the orbital ψ to Ψ in the momentum domain and back, indicated by the boxes labeled 'FT' and 'FT^{-1}', respectively. After the momentum-domain filters have been applied to Ψ and the orbital has been transformed back into the real domain, we label it ψ'. The box labeled 'norm' represents the renormalization we perform on ψ' once every iteration.

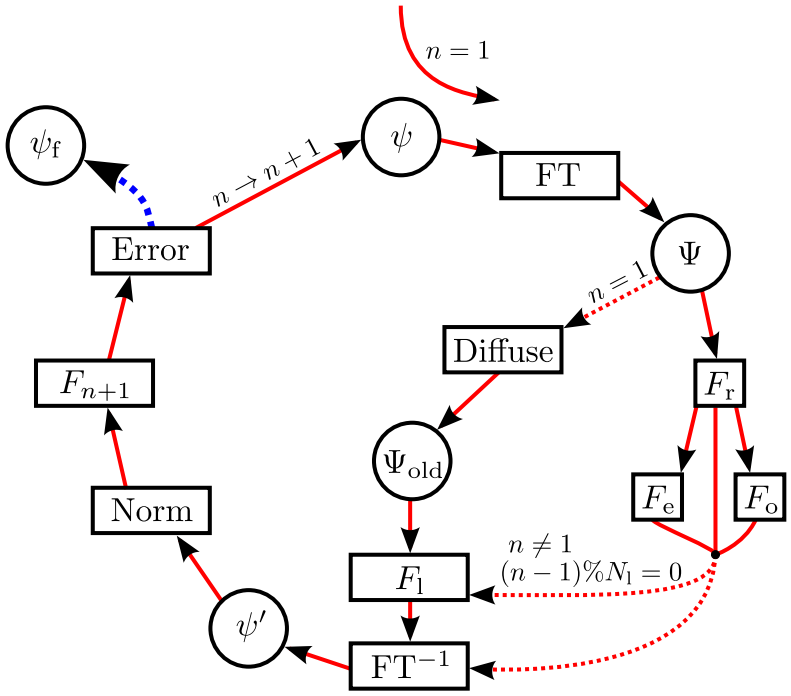

Figure 6.2: (Color online) The iterative error reduction algorithm. Start is at the top with $n = 1$. For an explanation of the different components see the text.

6.3.1 Filters

We assume that the orbital is real. Before we use the reconstructed orbital as input to the error reduction algorithm, we therefore rotate it in the complex domain to maximize its real density as explained in section 4.2.3. Projection operator F_r enforces the realness of the position-space orbital by projecting out the imaginary part as[1]

$$(F_r\Psi)(k_1, k_2) = 0.5\,(\Psi(k_1, k_2) + \Psi^*(-k_1, -k_2))\,. \tag{6.1}$$

If we know that we are dealing with a gerade or ungerade orbital, the projection operators F_e or F_o will enforce this as[2]

$$(F_e\,\Psi)(k_1, k_2) = \mathrm{Re}\,(\Psi(k_1, k_2))\,, \tag{6.2a}$$
$$(F_o\,\Psi)(k_1, k_2) = i\,\mathrm{Im}\,(\Psi(k_1, k_2))\,. \tag{6.2b}$$

6.3.1.1 Variation limitation

The filter that ensures the limited k- and θ-dependence of the imposed variation is labeled 'F_l'. For the first time during iteration $n = N_l+1$ and then every N_l iterations

[1] The Fourier transform of a real function $f(x, y)$ satisfies $F^*(-k_1, -k_2) = F(k_1, k_2)$.

[2] The Fourier transform of a real and symmetric function is purely real. The Fourier transform of a real and antisymmetric function is purely imaginary.

the current orbital Ψ_n is compared with Ψ_1. Here $N_\mathrm{l} \geq 1$ and normally $N_\mathrm{l} = 1 \ldots 10$. Beforehand Ψ_1 is smoothened slightly by convolution with a narrow Gaussian labeled as 'Diffuse' in Fig. 6.2. The Gaussian is such that in both dimensions grid points N_g steps away from the center point have a weight that is $\frac{1}{100}$th of the weight of the center point. If not specified differently, $N_\mathrm{g} = 5$ is used to smoothen out only the worst spikes in Ψ_1.

The first step of F_l is to represent $\Psi_n(k_1, k_2) - \Psi_1(k_1, k_2)$ on a (θ, k)-grid as

$$f(\theta, k) = \Psi_n(k_1(\theta, k), k_2(\theta, k)) - \Psi_1(k_1(\theta, k), k_2(\theta, k)), \tag{6.3}$$

where $k_1(\theta, k) = k \cos\theta$ and $k_2(\theta, k) = -k \sin\theta$. Here θ has the range $[0, 2\pi)$ and k has the range $[-1.26k_\mathrm{max}, 1.26k_\mathrm{max}]$, where k_max is the maximum momentum associated with the quantum mechanical cutoff (Lewenstein et al. [71])

$$U_\mathrm{max} = 3.17U_\mathrm{p} + 1.32I_\mathrm{p}. \tag{6.4}$$

Note that every point on the (k_1, k_2)-grid is represented twice on the (θ, k)-grid and therefore the values for negative k are copied from those with positive k. In the k-direction a $\cos^2$-window with a width of $0.2N_k$ is used, where N_k is the number of grid points in the k-direction. We choose the number of grid points such that at $k = k_\mathrm{max}$ the variation of the momentum vector is given by $\tau_\mathrm{v}\,\Delta k_1$ for both θ and k. We typically use $\tau_\mathrm{v} = 0.005$–0.025. The increased resolution on the (θ, k)-grid is necessary because otherwise the coordinate transformation back to the (k_1, k_2)-grid at the end of the procedure will introduce errors. For an intensity of 5×10^{14} W/cm^2 at a wavelength of 780 nm this leads for instance to $N_\theta = 9246$ and $N_k = 3710$ for $\tau_\mathrm{v} = 0.01$.

Secondly, $f(\theta, k)$ is Fourier transformed to reach $g(\Theta, r)$. Thirdly, the Fourier components of the variation $f(\theta, k)$ that are above the set limits are set to 0 as

$$g(\Theta, r) = 0 \qquad \text{for } |\Theta| \geq \tau_\Theta, \tag{6.5a}$$

$$g(\Theta, r) = 0 \qquad \text{for } |r| \geq \tau_r \frac{2\pi}{L_k}, \tag{6.5b}$$

where L_k is the length of the grid in the k-direction. Here τ_Θ and τ_r are the number of Fourier components that are allowed for the θ- and k-dependence of the imposed variation. To prevent introducing artificial high-frequency components, in practice the variation is not limited as abruptly as suggested by Eq. (6.5), but instead $\cos^2$-transitions with widths corresponding to $\frac{1}{5}$th of τ_Θ and τ_r are used, respectively.

Fourthly, $g(\Theta, r)$ is Fourier transformed back to $f(\theta, k)$ and fifthly $\Psi'_n(k_1, k_2)$ is

calculated using $k = \sqrt{k_1^2 + k_2^2}$ and $\tan\theta = -\frac{k_2}{k_1}$ as

$$\Psi'_n(k_1,k_2) = \begin{cases} \Psi_1(k_1,k_2) + f(\theta,k) & \text{for } \tau_2 \le k \le \tau_3 \\ \left(1 - \dfrac{k-\tau_1}{\tau_2-\tau_1}\right)\Psi_n(k_1,k_2) & \\ \qquad + \dfrac{k-\tau_1}{\tau_2-\tau_1}\left(\Psi_1(k_1,k_2) + f(\theta,k)\right) & \text{for } \tau_1 < k < \tau_2 \\ \dfrac{k-\tau_3}{\tau_4-\tau_3}\Psi_n(k_1,k_2) & \\ \qquad + \left(1 - \dfrac{k-\tau_3}{\tau_4-\tau_3}\right)\left(\Psi_1(k_1,k_2) + f(\theta,k)\right) & \text{for } \tau_3 < k < \tau_4 \\ \Psi_n(k_1,k_2) & \text{for } k \ge \tau_4 \text{ or } k \le \tau_1. \end{cases} \tag{6.6}$$

Here $\tau_1 < \tau_2 < \tau_3 < \tau_4$, F_l is not applied for momenta lower than τ_1 or higher than τ_4 and F_l is applied fully for momenta higher than τ_2 and lower than τ_3. In between τ_1 and τ_2 and in between τ_3 and τ_4 a linear transition is used. Unless specified otherwise, we use $\tau_1 = 0.1k_\mathrm{max}$, $\tau_2 = 0.15k_\mathrm{max}$, $\tau_3 = 0.95k_\mathrm{max}$, and $\tau_4 = 1.0k_\mathrm{max}$.

Because the other filters introduce high-frequency components to the orbital, we finally calculate $F_\mathrm{l}\,\Psi_n(k_1,k_2)$ as

$$F_\mathrm{l}\,\Psi_n(k_1,k_2) = \begin{cases} \Psi'_n(k_1,k_2) & \text{for } k \le \tau_\mathrm{max} - \frac{\Delta\tau_\mathrm{max}}{2} \\ \cos^2\left(\dfrac{k-\left(\tau_\mathrm{max}-\frac{\Delta\tau_\mathrm{max}}{2}\right)}{\Delta\tau_\mathrm{max}}\dfrac{\pi}{2}\right) & \text{for } \tau_\mathrm{max} - \frac{\Delta\tau_\mathrm{max}}{2} < k < \tau_\mathrm{max} + \frac{\Delta\tau_\mathrm{max}}{2} \\ 0 & \text{for } k \ge \tau_\mathrm{max} + \frac{\Delta\tau_\mathrm{max}}{2}. \end{cases} \tag{6.7}$$

Here k-components higher than τ_max are set to 0 using a $\cos^2$-transition with a width of $\Delta\tau_\mathrm{max} = 0.1\tau_\mathrm{max}$.

Unfortunately, F_l is not a true projection operator in the sense that

$$F_\mathrm{l}(F_\mathrm{l}\,\psi_n) \neq F_\mathrm{l}\,\psi_n. \tag{6.8}$$

This is because of windows associated with τ_Θ, τ_r, and τ_max that are needed in a numerical calculation, and to a much lesser extent because of further numerical errors associated with the forward and backward coordinate transformation. If the number of grid points on the (θ,k)-grid is significantly reduced the coordinate-transformation errors start to dominate in the sense that at some point the error in the orbital increases again. It is probably due to the combined effect of these errors that best results seem to be obtained using $N_\mathrm{l} \neq 1$ but for instance using $N_\mathrm{l} = 4$. In the cases we looked at, convergence takes around a couple of hundred iteration steps.

The exact reasons why applying F_l is necessary are unclear at the moment. As we will see in section 6.4.1, the algorithm does not function properly without F_l. However, the bounds on the allowed variation in the form of τ_Θ and τ_r are set to allow hundreds or even thousands of Fourier components of the variation to survive. Intuitively one would not expect such high bounds if the main reason for applying F_l was that the reconstructed orbital has an error with limited θ- and k-dependence.

In a phase-retrieval algorithm, at every iteration the amplitudes are set to the measured values. For our problem F_I is the only part of the algorithm that inputs the original orbital at every iteration. Although arbitrarily large variations of the orbital are allowed if they have limited θ- and k-dependence, an important contribution of F_I might be that it suppresses some unphysical and unwanted variations induced by the other filters. In particular, it smoothens out spikes in (θ, k)-space introduced by the support. If none of the other filters makes the orbital deviate from the input orbital too dramatically in other ways, we can understand that through F_I the correspondence with the reconstructed orbital is satisfactorily ensured.

6.3.1.2 Support

At every iteration step the limited support of the wave function is enforced in the real domain by F_{n+1} as depicted in Fig. 6.2. Following the HIO algorithm (Fienup [34]), we do not simply set the wave function to 0 outside the support area, but we somewhat overcompensate the area outside the support. In formula, the orbital for the next iteration is given by

$$\psi_{n+1}(\mathbf{r}) = \begin{cases} \psi'_n(\mathbf{r}) & \text{for } \mathbf{r} \in S \\ \psi_n(\mathbf{r}) - \beta\psi'_n(\mathbf{r}) & \text{for } \mathbf{r} \notin S, \end{cases} \tag{6.9}$$

where S is the support area. Here β is a relaxation parameter usually chosen between 0.5 and 1.

For the error reduction problem to have a unique solution, the dimensionality of the constraint subspaces should not be bigger than the dimensionality of the problem. The dimensionality of the problem is given by the number of grid points of the grid on which ψ is represented, and the constraint subspace associated with F_{n+1} has a dimensionality equal to the size of the support area. The dimensionality of F_I is not trivial to find, and therefore the exact dimension of the constraints is unknown, unlike in the phase retrieval problem (Elser [29]). However, it is clear that S should not be too big with respect to the grid dimensions, i.e., the orbital should be reconstructed on a large grid. This is referred to as oversampling in the literature as in crystallography it corresponds to using a higher momentum resolution than that of the measurement apparatus. The spatial grid we use for the error reduction algorithm measures 29.76×29.76 a.u. and has 190×190 grid points, leading to a spatial resolution of 0.157×0.157 a.u.

6.3.2 Shrinkwrap

In an earlier version of the algorithm we chose the support S for the error reduction algorithm based on *a priori* considerations to extend 3–5 a.u. in all directions from the origin. There are three problems with such an approach; firstly, the final orbital gets influenced heavily by our subjective guess for S, and secondly, the algorithm has the tendency to 'fill the space' offered by the fixed support, leading to featureless blobs instead of accurate orbitals. Thirdly, ψ tends to adopt the symmetry of S, making the error reduction of asymmetric orbitals impossible without putting the

asymmetry in by hand. Therefore we decided to follow the approach introduced by Chapman to employ a dynamically shrinking support (Chapman et al. [16, 17]). In our case at every iteration step the support is redetermined to no longer incorporate areas that are no longer significantly occupied by the orbital.

We consider a reconstructed orbital that is roughly centered at the origin. The initial support is determined from the autocorrelation of the diffused reconstructed orbital as

$$\begin{cases} \mathbf{r} \in S & \text{if } |R(\mathbf{r})| \geq \tau_a R_{\max} \\ \mathbf{r} \notin S & \text{else,} \end{cases} \tag{6.10}$$

where the autocorrelation $R(\mathbf{r})$ is given by

$$R(\mathbf{r}) = \iint \left(F_{\mathrm{g}}\, \psi^*\right)(\mathbf{r}') \left(F_{\mathrm{g}}\, \psi\right)(\mathbf{r}+\mathbf{r}') d^2r', \tag{6.11}$$

and $R_{\max}$ is its maximum amplitude. Here F_{g} smoothens the wave function by convoluting it with a Gaussian that has a $1/e$-width of $2\tau_{\mathrm{g}}$. Normally we use $\tau_{\mathrm{g}} = 5$ a.u. Furthermore τ_a is a parameter that we set equal to $\tau_a = 0.25$ unless specified otherwise. Numerically we calculate $R(\mathbf{r})$ using the Wiener-Khinchin theorem as the inverse Fourier transform of the spectral density of the diffused wave function (Weisstein [133]), i.e.,

$$R(\mathbf{r}) = \iint \left| \iint \left(F_{\mathrm{g}}\, \psi\right)(\mathbf{r}') e^{-i\mathbf{k}\cdot\mathbf{r}'} d^2r' \right|^2 e^{i\mathbf{k}\cdot\mathbf{r}} d^2k. \tag{6.12}$$

At every iteration step, we recalculate the support by looking for grid points that no longer need to be in the support. To this end we smoothen ψ'_n by applying F_{g} to it, i.e., by applying the same smoothening Gaussian as was used for the autocorrelation function. Then we look for points that can be removed out of the support as

$$\mathbf{r} \notin S \quad \text{if } |\psi'_n(\mathbf{r})| < \tau_{\mathrm{s}}\, \phi_{\max}, \tag{6.13}$$

where $\phi_{\max}$ is the maximum amplitude of $\psi_1(\mathbf{r})$ and τ_{s} is a parameter in the range 0.001–0.1.

6.3.3 Error determination

We estimate the error at every iteration step by calculating the difference between the orbitals after applying the momentum and coordinate domain filters and dividing that by the fraction of grid points that lies outside the support. This is indicated by the filter labeled 'Error' in Fig. 6.2. In formula,

$$\epsilon_{\mathrm{d}} = \sqrt{\iint \left|\psi_{n+1}(\mathbf{r}) - \psi'_n(\mathbf{r})\right|^2 d^2r} \;/\; c_{\mathrm{s}}, \tag{6.14}$$

where we use the normalized version of ψ'_n and c_{s} is the fraction of grid points that lies outside of the support. In the beginning the support is still very big, leading to just a very small effect from the F_{n+1}-filter. In that case ϵ_{d} is artificially small and

this effect is somewhat counterbalanced by the division by c_s. Estimating the error using ϵ_d is based on the assumption that we are in the optimal point, i.e., closest to the exact orbital, when the distance between the images of the momentum and coordinate domain filters is minimal.

If ϵ_d at the current iteration is smaller than all previous errors, we keep ψ_{n+1} and the current support. We do not use the orbital and support from the final iteration, not only because of the reasons mentioned at the end of section 6.3.1.1, but also because after some time the Shrinkwrap procedure tends to overshrink the support area (Chapman et al. [17]). The algorithm is stopped if the best error has not been improved in 200 iterations, or after a smaller number for initial scans and the like. The final orbital ψ_f is obtained by setting the orbital equal to 0 outside the best support using the support filter F_s as

$$\psi_\mathrm{f}(\mathbf{r}) = F_\mathrm{s}\,\psi_{n+1}(\mathbf{r}) = \begin{cases} \psi_{n+1}(\mathbf{r}) & \text{for } \mathbf{r} \in S \\ 0 & \text{for } \mathbf{r} \notin S. \end{cases} \tag{6.15}$$

In addition to the F_{n+1}-filter, also F_l has very limited effect in its first applications because we are still close to ψ_1. Therefore we accept a low error as the best error only if it occurs in an iteration for which $n \geq N_\mathrm{l} + 4$. Of course only iterations during which F_l was applied are considered for the final orbital.

In our simulations, we can also calculate the exact error of the optimized orbital by comparing it with the exact orbital. This information cannot be used by the optimization algorithm, as it would amount to 'cheating'. However, it can be used to assess the performance of the error reduction algorithm. In formula, we define the exact error ϵ_e as

$$\epsilon_\mathrm{e} = \sqrt{\iint_S |\psi_{n+1}(\mathbf{r}) - \psi_0(\mathbf{r})|^2 \, d^2r}, \tag{6.16}$$

where $\psi_0(\mathbf{r})$ is the exact bound state orbital. The integration is over the support area, as the orbital is assumed to be localized in this region by the algorithm.

6.3.4 Optimization

To automatically search for the optimal set of parameters (N_l, β, τ_Θ, τ_r, τ_max, N_g, τ_g, τ_s) that minimizes the error, we have employed a primitive gradient approach. We try both multiplying and dividing each of the parameters by $1 + \delta$, where δ is a parameter that is initially set to $\delta = 0.5$. If the error is found to decrease, the gradient is calculated for moving in this direction. The parameters N_l and N_g are set to the closest integer to the value suggested by the δ-variation that is different from the old value. The algorithm then moves in the direction of the steepest gradient; the variable gets multiplied or divided by $1 + 2^{n_\delta}\delta$, where n_δ is either 0, 1 or 2 depending on what gives rise to the lowest absolute error.

Every time no parameter variation can be found that gives rise to a negative gradient, δ is reduced by a factor 5. Once a negative gradient is found, δ is restored to its

original value of $\delta = 0.5$. If $\delta < 0.003$ and no significant improvement can be found anymore, the algorithm is stopped. Experience has shown it is needed to put an artificial bound on some of the parameters or otherwise the algorithm will converge to nonphysical solutions. The bounds we use are $0.5 \leq \beta \leq 1$, τ_Θ and τ_r can be up to one-third times the number of Fourier components represented on the grid, N_g is not allowed to increase beyond the original value, $\tau_\mathrm{g} \leq 5$, and τ_max is not allowed to increase by more than 10% with respect to the original value.

6.3.5 RAAR

As an alternative to HIO algorithm, the relaxed averaged alternating reflection (RAAR) algorithm was introduced in 2005 for the phase retrieval problem (Luke [74]). It is distinct in several points from the HIO algorithm. Since it uses the nonnegativity of the object present in the typical phase retrieval problem, but that is not generally a characteristic of a molecular orbital, we can not implement the RAAR algorithm directly.

In the RAAR-version of our algorithm, two changes are made with respect to what was presented before. Firstly, F_{n+1} (Eq. (6.9)) is replaced by

$$\psi_{n+1}(\mathbf{r}) = \begin{cases} \psi'_n(\mathbf{r}) & \text{for } \mathbf{r} \in S \\ \beta\psi_n(\mathbf{r}) + (1-2\beta)\psi'_n(\mathbf{r}) & \text{for } \mathbf{r} \notin S. \end{cases} \tag{6.17}$$

Here we assumed there is a sign error in Eq. (14) of (Luke [74]). Secondly, at each iteration the support is not calculated using Eq. (6.13), but instead a grid point is considered to lie outside of the support if the momentum-domain filters increases the amplitude of the object at the point by more than a factor of 2. In formula,

$$\mathbf{r} \notin S \quad \text{if } \left|\frac{\psi_n(\mathbf{r})}{\psi'_n(\mathbf{r})}\right| < 0.5. \tag{6.18}$$

An aspect of the RAAR algorithm that was not implemented is a nonconstant β that increases from $\beta = 0.75$ to $\beta = 1$ during the iteration process. We feel that such a behavior is not needed for our problem because of the much lower number of iteration steps. Similarly, it has been reported that the best results for the phase retrieval problem are obtained when the parameters and/ or algorithms are varied during the iteration process (see e.g. Chapman et al. [17]; Fienup [34]). We have not tested such an approach yet.

6.4 Post-processing results

The error reduction parameters used for the reconstructions presented in this section were all derived using the procedure outlined in section 6.3.4. For every orbital we started with the parameters $N_\mathrm{l} = 4$, $\beta = 1$, $\tau_\Theta = 100$, $\tau_r = 100$, $\tau_\mathrm{max} = k_\mathrm{max}$, $N_\mathrm{g} = 5$, $\tau_\mathrm{g} = 5$, and $\tau_\mathrm{s} = 0.01$. For the optimization of the parameters we used a resolution of $\tau_\mathrm{v} = 0.01$, and for the final runs we used $\tau_\mathrm{v} = 0.005$. This means that we

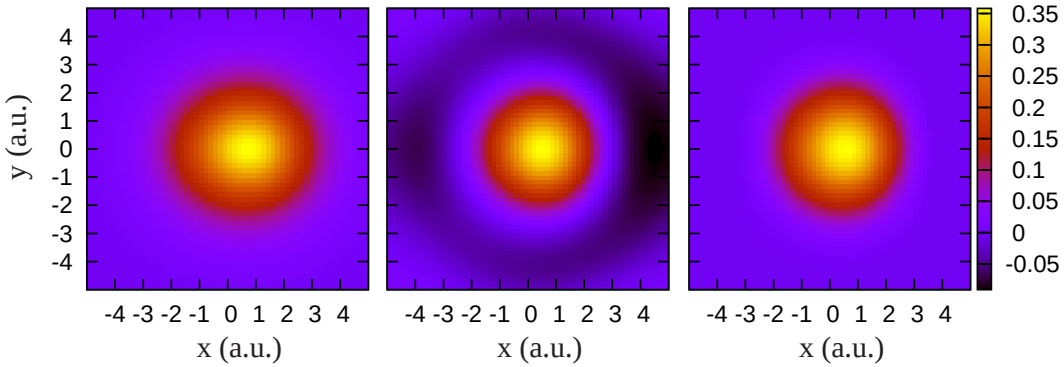

Figure 6.3: (Color online) Tomographic reconstruction of the ground state of 2D HeH^{2+}. From left to right the exact orbital, the real part of the reconstructed orbital using velocity-form reconstruction and the same orbital after postprocessing by the error reduction algorithm are shown.

did not manually tweak the algorithm for each of the orbitals. The only information that we put in the algorithm about the orbitals was their symmetry. Therefore a slightly more sophisticated algorithm would not need any extra information about the orbitals at all.

This section contains a lot of density plots. Just as for chapter 4, we ask the reader to view these in the color version of this thesis.

6.4.1 Helium-hydrogen cation

Firstly we consider the ground state of 2D softcore HeH^{2+} with $R = 2.5$ a.u., i.e., the same molecule as was considered in section 4.5.1. To set the ionization potential to 30.2 eV we use $a^2 = 2.56801$. The reference atom has $Z = 3$ a.u. and $a^2 = 3.33548$. The laser intensity for the tomographic reconstruction is 3×10^{14} W/cm^2 at a wavelength of 780 nm, and we used a three-cycle $\sin^2$-pulse with $\phi_{\mathrm{CEP}} = 1.25\pi$. The optimization procedure kept N_{l}, β, $N_{\mathrm{g}} = 5$, and $\tau_{\mathrm{g}} = 5$ constant. Furthermore, τ_Θ was set to 1310, τ_r was set to 432, $\tau_{\max}$ was set to 2.89 a.u., and τ_{s} was set to 0.0102. For τ_Θ and $\tau_{\max}$ this is equal to the maximum allowed. The results of the tomographic reconstruction and the postprocessing can be found in Fig. 6.3. We observe that the error reduction algorithm not only makes the reconstructed orbital go to 0 smoothly far away from the origin, but also in the inner region the postprocessed orbital corresponds better with the exact orbital. From a quadratic fit around the maximum value of the orbital at $y = 0$ the postprocessed orbital has its maximum at $x = 0.57$ compared with $x = 0.53$ for the reconstructed orbital and $x = 0.74$ for the exact orbital. Combined with the longer extension of the orbital for $x < 0$ the postprocessed orbital recovers the asymmetry of the exact orbital better and also the overall size of the orbital matches that of the exact orbital better.

In Fig. 6.4 we plot the results of runs of three adapted versions of the error reduction algorithm. On the left the output of the RAAR algorithm is shown. With respect to the Shrinkwrap algorithm presented in Fig. 6.3, for the RAAR algorithm τ_Θ was

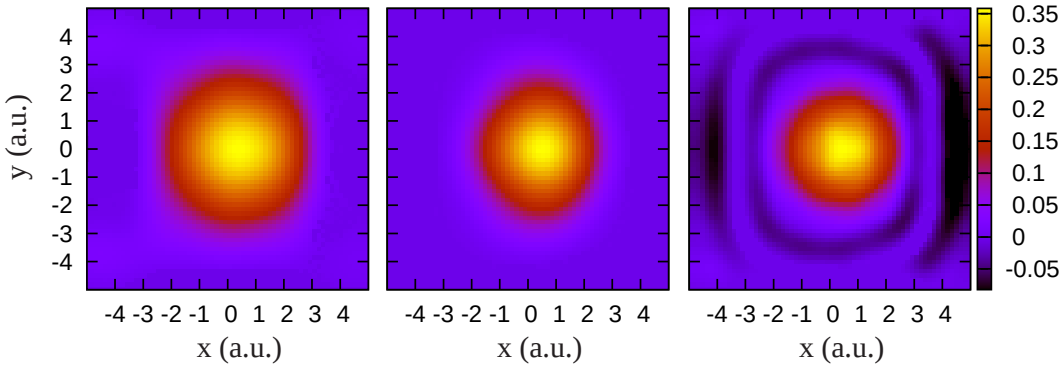

Figure 6.4: (Color online) Tomographic reconstruction of the ground state of 2D HeH^{2+}. From left to right the real part of the velocity-form reconstructed orbital after postprocessing using the RAAR algorithm, using the Shrinkwrap algorithm (same as Fig. 6.3) but without τ_Θ and τ_r, and using the Shrinkwrap algorithm but with $\tau_{\max} \to 2\tau_{\max}$ are shown.

set to 225 and τ_r was set to 307 as indicated by the optimization procedure. The postprocessed RAAR orbital is of bad quality, and we conclude that the RAAR algorithm as we implemented it does not seem to work for the current problem. The reason is probably more related to the way of determining the support than to the exact way in which the support is enforced in the algorithm.

The middle and right plots in Fig. 6.4 are the Shrinkwrap algorithm of the right plot in Fig. 6.3, but with changes in the parameters. For the middle plot τ_Θ and τ_r were not enforced. We observe that the resulting orbital looses the egg-like shape of the exact orbital, but instead becomes round and a lot more symmetric. Although the values of $\tau_\Theta = 1310$ and $\tau_r = 432$ seem very high and one might think that such high values have no significance, these limits are clearly necessary to recover the character of the exact orbital. For the right plot in Fig. 6.4 we doubled the value of $\tau_{\max}$ to $\tau_{\max} = 5.78$ a.u. This has a devastating effect on the postprocessed orbital and we conclude that it's very important that the high-frequency components introduced mainly by enforcing the support area are properly removed. Also one should realize that beyond the harmonic cutoff F_l cannot be applied anymore.

6.4.1.1 Convergence

In Fig. 6.5 we plot the convergence of the algorithm for the case of Fig. 6.3 as indicated by the error ϵ_d. We only plot those iterations during which F_l is applied. The algorithm performed 505 iterations, and the best orbital was obtained after 305 iterations (indicated by the vertical line). In the first few steps the convergence is very fast. Later on the convergence is a lot slower, and regularly the error even temporarily increases slightly. Just before the best error is found, one more big step is made. Afterwards no more progress is made but the error increases slowly because of the reasons mentioned in section 6.3.3. Also indicated is the size of the support area, i.e., the number of grid points it contains. We can see the support shrink gradually throughout the iterations until slightly before the best error is obtained,

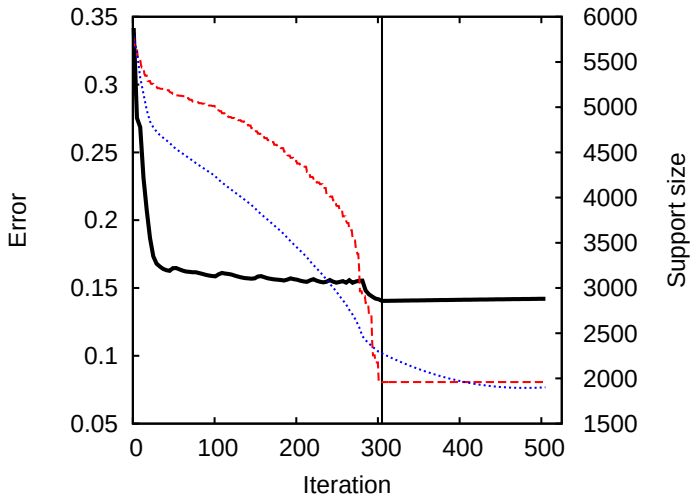

Figure 6.5: (Color online) The error measure ϵ_d (black solid line), exact error ϵ_e (blue dotted line), and the number of grid points inside the support (red dashed line) as a function of iteration n. For ϵ_d and ϵ_e only iterations during which F_l is applied are shown. The vertical line indicates the iteration at which the final orbital is determined. For clarity ϵ_e was multiplied with 0.5.

and then the support size remains constant.

The curve of the exact error ϵ_e in Fig. 6.5 shows that the algorithm successfully reduces the overall error in the reconstructed orbital. It also suggests that the best orbital is not reached after 305 iterations, but after around 475 iterations. From a visual inspection of the orbitals we conclude that the orbital in iteration 305 is closer to the exact orbital than the orbital in iteration 477, as the latter has grown too big in the y-direction (not shown). This illustrates the difficulty in finding the right point to stop the algorithm. Furthermore it shows that a minimum in ϵ_e not necessarily corresponds to best recovery of the orbital from a naked-eye point of view.

To give some insight into how the algorithm works, in the bottom row Fig. 6.6 we plot ψ'_n at different points in the procedure. In the top row of the same figure the initial support area and the support during two later points in the procedure are shown. At every iteration step, F_l introduces significant density mostly inside the current support area. If we look carefully, some density outside the current support can be observed for low n though. This shows that during the procedure the orbital changes slowly toward a solution while at the same time the set of solutions becomes smaller because of the shrinking support.

6.4.2 Hydrogen molecular cation

In this subsection we consider 2D softcore H_2^+ with $R = 2$ a.u., i.e., the same molecule that we occupied ourselves with through most of chapter 3. The reference atom has $Z = 2$ and $a^2 = 0.920747$ and therefore also $I_\mathrm{p} = 30.2$ eV. The laser parameters

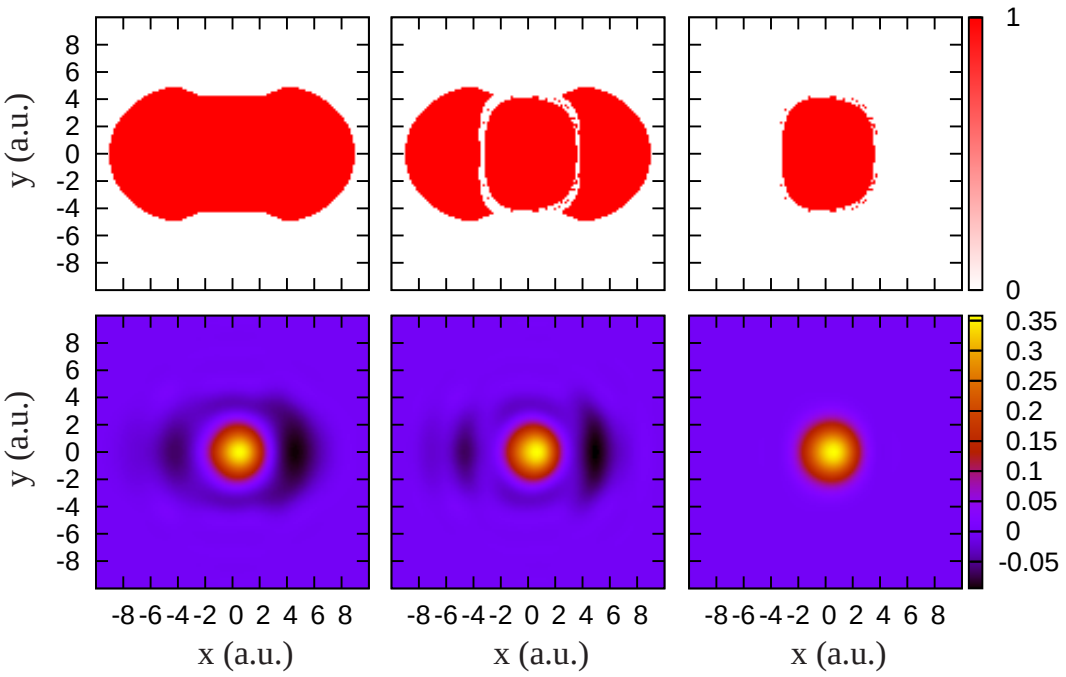

Figure 6.6: (Color online) Bottom row: from left to right ψ'_n at $n = 5$, $n = 13$, and $n = 305$. Top row: from left to right support area at $n = 1$, $n = 13$, and $n = 305$. Here the red (grey) area labeled '1' represents the support.

are the same as in section 6.4.1 except for the laser intensity, which equals 5×10^{14} W/cm^2 here. Firstly, we will consider the ground state. In Fig. 6.7 the results of a tomographic reconstruction and its postprocessing can be found. With respect to section 6.4.1 the following parameters were set differently by the optimization procedure: $N_\mathrm{l} = 5$, $\tau_\Theta = 1541$, $\tau_r = 618$, $\tau_\mathrm{max} = 3.40$ a.u., and $\tau_\mathrm{s} = 0.033132$. Here both τ_Θ and τ_r are set to the maximum value allowed. The postprocessing removes the errors at large r, but also the orbital itself appears slightly less longitudinal and therefore more accurately reconstructed. This is just a small effect as the reconstruction was already of very good quality.

Secondly and lastly we consider the first excited state. We change the softcore

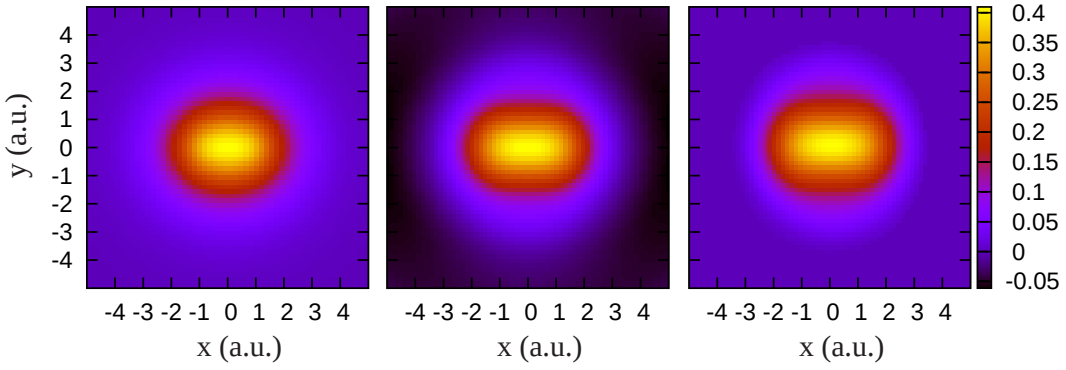

Figure 6.7: (Color online) Same as Fig. 6.3 for the ground state of 2D H_2^+.

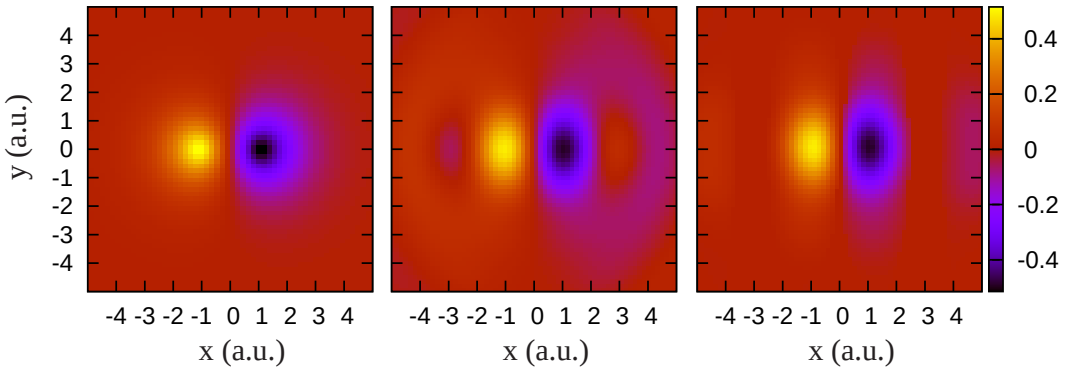

Figure 6.8: (Color online) Same as Fig. 6.3 for the first excited state of 2D H_2^+.

parameter to $a^2 = 0.06811$ in order to keep I_p at the same energy. The same reference state and the same laser pulse are used. The results of the tomographic simulation and the postprocessing can be found in Fig. 6.8. Instead of the previous parameters, now $N_l = 6$, $\tau_\Theta = 1504$ and $\tau_s = 0.0102$ are used, while all other parameters retain their value. We observe that the postprocessed orbital resembles the exact orbital better than the reconstructed orbital. Not only because some erroneous density further away from the origin has been removed, but also because the lobes extend further away from the origin in the x-direction, although not as far as for the exact orbital.

Chapter 7

Conclusion and outlook

In this chapter we summarize briefly the main conclusions of this thesis and give an outlook to future work. The main subject of this thesis is the relationship between molecular properties of simple molecules on one side, and their response to strong laser fields on the other side. We solve the time-dependent Schrödinger equation numerically to find the single-molecule response. Propagation and multi-electron effects are neglected throughout this thesis, i.e., we consider only the response of a single electron from a single molecule. We employ simple models to retrieve molecular characteristics from strong-field spectra.

By limiting ourselves to simple molecular models, a thorough understanding of the strong-field response is possible. This allows us to investigate single-particle and single-electron molecular imaging in great detail. The results are useful when interpreting molecular imaging results of more complicated molecules in experiments. We give special attention to the molecular orbital tomographic scheme, which can be used to image electronic orbitals using high-harmonic generation (HHG) (Itatani et al. [52]). Using theoretical analysis and semi-classical calculations involving the strong-field approximation (SFA), we provide the experimentalist with several enhancements to the scheme.

Molecular structure in high-harmonic generation

When a Gaussian wave packet collides with an aligned H_2^+-molecule, the resulting harmonic spectrum has a structural minimum from the two-center interference between the two lobes of the orbital. The position of this minimum points to an effective plane-wave momentum that transitions from the I_p-corrected $k(\omega) = \sqrt{2\omega}$ at low harmonics to the SFA-based $k(\omega) = \sqrt{2(\omega - I_\mathrm{p})}$ at high harmonics. A laser-induced HHG spectrum shows the same behavior if only a single electronic trajectory is taken into account, as is the case for a typical experimental setup. This justifies using HHG for molecular imaging as the laser field has no significant effect on the amplitude of the recombination matrix element. When a single set of short and long electron trajectories contributes to the spectrum, the interference between the two

trajectories causes a large but regular oscillation around the general trend. Introducing more and longer trajectories by using longer pulses has the effect of averaging out the oscillations to a smaller scattering around the Gaussian wave packet result and leads to a smoother interference minimum as a function of θ.

Our results show that the effect of the Coulomb potential can lead to significant ellipticity of the emitted radiation. At the interference minimum, the main polarization angle makes a π-jump and the ellipticity goes through zero. The Coulomb effects are less important at higher harmonics. Therefore we observe less overall ellipticity and a sharper jump in the polarization direction at the high end of the spectrum. We have shown that the two-center minimum is also visible in the emission time of the harmonics.

In a numerical calculation of a HHG spectrum the harmonic phases are retrieved with a rapidly oscillating time-translation phase superimposed on them. We have shown that when one removes this extra phase, the harmonic phase from a numerical calculation reveals the physics behind the generation process. The phase difference between two nearly degenerate state can be used to show that the continuum wave packet inherits the phase of the ionizing lobe upon ionization.

Tomographic reconstruction

It was demonstrated that one can use the HHG spectrum for different orientations of the molecule in the laser field combined with the HHG spectrum of a reference atom to reconstruct a molecular orbital (Itatani et al. [52]). We show that a necessary condition for accurate tomographic reconstruction of arbitrary molecular orbitals is that all recombining electrons return from the same direction. This can be achieved by using extremely short phase-stabilized laser pulses. Because of the exponential dependence of the tunnelling rate on the field amplitude, the choice of envelope shape is not very critical. A carrier-envelope phase of 0.25π rad seems to be optimal for either two- or three-cycle pulses. We present results from numerical simulations of the experiment for different molecular models. We introduce a velocity form for the reconstruction equation that recovers the internuclear distance more reliable than the conventional length-form formulation. The length-form reconstruction is associated with errors along the nodal planes of antisymmetric molecules and in asymmetric molecules. We have not found any method to remove these errors.

SFA calculations

The Lewenstein model is a quantum-mechanical model for the HHG process that employs the SFA. The HHG yield in the Lewenstein model can be expressed using a sum over electronic trajectories by performing the integrals over momentum and the birth and recombination times using the saddle-point method. We expand the resulting complex times from real-valued classical times. This allows us to calculate the contributions from individual trajectories to the full spectrum. We perform a similar calculation for the above-threshold ionization (ATI) spectrum also. We have

used this information to improve the characterization of the suitability of a pulse for conventional molecular tomography.

HHG-ATI correspondence

From the SFA calculation we also find that peaks from the HHG spectrum can be related to peaks in the ATI spectrum when extremely short pulses are used. The peaks are related through the common birth time of their dominant trajectories. We characterize the link between a HHG frequency and ATI momentum through the relative contributions of the relevant trajectories. We demonstrate the correspondence between HHG and ATI in 1D simulations. Because the plane-wave approximation for the returning electron does not seem to work well in 1D, we expect the correspondence between HHG and ATI to be stronger from 2D or 3D simulations or experiments. Performing 2D or 3D simulations for HHG and ATI to test this hypothesis will be an interesting future topic.

We propose a method to improve the tomographic reconstruction—that is so far based solely on HHG—by incorporating also ATI electrons into the reconstruction. The intensity of the ATI spectrum as a function of molecular orientation in the laser field can be used to improve the characterization of the continuum wave packet in the tomographic reconstruction scheme. Because molecular tomography does not function well in 1D, we have not been able to seriously test the method yet. At the moment lasers in the far-IR regime around 2000 nm are becoming available. There is also significant progress in the field of laser pulse shaping and laser pulses with a few optical cycles are becoming available. A combination of these techniques can be used to design pulses that are better suited for molecular tomography. Furthermore we believe that without much extra effort to the experimentalist the tomographic reconstruction can be moderately improved by using ATI electrons if one employs a suitable laser pulse.

Postprocessing

We have shown that it is possible to improve the tomographic reconstruction of a molecular orbital using a postprocessing algorithm. Filters that represent basic physical knowledge about the orbital or the reconstruction scheme are applied iteratively in the real and Fourier domain. In the real domain we use that the orbital is localized around the origin and in the Fourier domain we limit the variation from the input orbital. In the ideal case the algorithm converges to the exact orbital. We have shown that the algorithm recovers some of the features of a 2D HeH^{2+} cation and other molecules.

Future of molecular tomography

The future of the molecular tomographic scheme is unclear at the moment. So far experimentally the scheme has been proven to work for N_2 only. However, no experiments have been reported where laser wavelengths longer than that of a Ti:Sapphire laser were employed. Theoretically there should be a significant improvement from longer wavelengths, both from the increased harmonic range available and the associated better performance of the plane-wave approximation at high electron energies. Furthermore, additional methods to improve the reconstruction, such as the technique based on ATI electrons and the postprocessing proposed in this thesis, are being developed at the moment. The long-term goal of a molecular movie showing the full electronic wave function of the contributing electron(s) during a chemical reaction is still far away, but might be reached sooner than we think.

Appendix A

Numerics

A.1 TDSE solver

We wish to solve the time-dependent Schrödinger equation Eq. (2.1a) numerically. At $t = 0$ we start with an initial state $\psi(\mathbf{r}, 0)$, and we propagate the wave packet in time till $t = T_{\text{prop}}$. The evolution of the wave packet is given by

$$\psi(\mathbf{r}, t) = \Gamma\left(e^{-i\int_0^t \hat{H}(t')dt'}\right)\psi(\mathbf{r}, 0), \tag{A.1}$$

where the time-ordering operator Γ is needed because the Hamiltonian does not commute with itself at a different time. For a small time step Δt for which we take the Hamiltonian to be time-independent, this reduces to

$$\psi(\mathbf{r}, t + \Delta t) = e^{-i\hat{H}\Delta t}\psi(\mathbf{r}, t). \tag{A.2}$$

We split the Hamiltonian $\hat{H}$ as

$$\hat{H} = \hat{T} + \hat{V}, \tag{A.3}$$

where $\hat{T}$ is the momentum-dependent and $\hat{V}$ the space-dependent part. For ease, accuracy and mostly numerical speed, we would like to operate $\hat{T}$ on the wave function in momentum space, and $\hat{V}$ on the wave function in coordinate space. Because $\hat{T}$ and $\hat{V}$ do not commute we cannot apply them sequentially for arbitrarily large Δt. Instead, we use the Baker-Campbell-Hausdorff formula[1] to approximate the propagator in Eq. (A.2) using the split-operator method (Feit et al. [31]; Fleck et al. [35]) as

$$e^{-i\hat{H}\Delta t} = e^{-i\frac{\hat{V}}{2}\Delta t}e^{-i\hat{T}\Delta t}e^{-i\frac{\hat{V}}{2}\Delta t} + \mathcal{O}(\Delta t^3). \tag{A.4}$$

In between applying $e^{-i\frac{\hat{V}}{2}\Delta t}$ and $e^{-i\hat{T}\Delta t}$ we (inverse) Fourier transform the wave packet so that we can apply the respective operators in their own space, i.e., we

[1] The Baker-Campbell-Hausdorff formula for two noncommuting A, B reads

$$e^A e^B = e^{A+B+\frac{1}{2}[A,B]+\text{higher order commutators}},$$

where the commutator $[A, B] = AB - BA$.

avoid having to calculate gradients numerically. For the Fourier transforms we use the FFTw package (Frigo and Johnson [37]).

For the laser-induced HHG calculations the propagation time equals $T_{\text{prop}} = N_{\text{prop}}\, T$, where T is the laser period and N_{prop} is the number of laser cycles that we propagate the system. We choose $N_{\text{prop}} = N_{\text{cycles}} + 2$, where N_{cycles} is the number of cycles in the laser pulse. For the laser-free collisions of section 3.1, we propagate the system for the duration of one optical cycle of a 780-nm laser.

Normally we set the initial state $\psi(\mathbf{r}, 0)$ equal to a bound state $\psi(\mathbf{r}, 0) = \psi_0(\mathbf{r})$. For the laser-free results of section 3.1, the initial state is set equal to a bound state plus a Gaussian wave packet. We obtain the bound states by propagating a random initial state in imaginary time using the laser-field free Hamiltonian $\hat{H}_0$ (Kosloff and Tal-Ezer [57]). Replacing Δt by $-i\Delta\tau$, the evolution operator becomes $e^{-\hat{H}_0\,\Delta\tau}$. So how can we find a bound state using this operator? Expand the wave packet as

$$\psi(\mathbf{r}, \tau) = \sum_j a_j(\tau)\phi_j(\mathbf{r}), \tag{A.5}$$

where the $a_j(\tau)$ are complex coefficients of the $\phi_j(\mathbf{r})$. The $\phi_j(\mathbf{r})$ form a complete set of eigenstates of the Hamiltonian $\hat{H}_0$ with eigenenergies E_j. Now applying the imaginary-time propagator we obtain

$$e^{-\hat{H}_0\,\Delta\tau}\psi(\mathbf{r}, \tau) = \sum_j a_j(\tau)e^{-E_j\,\Delta\tau}\phi_j(\mathbf{r}). \tag{A.6}$$

This shows that eigenstates with energies higher than the ground state energy E_0 are exponentially suppressed.

The norm of the probability density is not conserved because the imaginary-time propagator is not unitary. After each imaginary-time step the norm is given by

$$N(\tau + \Delta\tau) = \iint \left|e^{-\hat{H}_0\,\Delta\tau}\psi(\mathbf{r}, \tau)\right|^2 d^2\mathbf{r} = \sum_j |a_j(\tau)|^2\, e^{-2E_j\,\Delta\tau}, \tag{A.7}$$

where we used the orthonormality of the $\phi_j(\mathbf{r})$. We renormalize the density to 1 after each imaginary-time step, such that

$$\psi(\mathbf{r}, \tau + \Delta\tau) = \frac{\sum_j a_j(\tau)e^{-E_j\,\Delta\tau}\phi_j(\mathbf{r})}{\sqrt{\sum_j |a_j(\tau)|^2\, e^{-2E_j\,\Delta\tau}}}. \tag{A.8}$$

As long as $\psi(\mathbf{r}, \tau) \neq \phi_0(\mathbf{r})$, but there is some contribution from the ground state in $\psi(\mathbf{r}, \tau)$ $(0 < |a_0(\tau)| < 1)$, after each imaginary-time step we can write for the coefficient of the ground state

$$|a_0(\tau + \Delta\tau)|^2 = \frac{|a_0(\tau)|^2\, e^{-2E_0\,\Delta\tau}}{\sum_j |a_j(\tau)|^2\, e^{-2E_j\,\Delta\tau}} > \frac{|a_0(\tau)|^2}{\sum_j |a_j(\tau)|^2} = |a_0(\tau)|^2\,. \tag{A.9}$$

Since $|a_0(\tau + \Delta\tau)|$ increases every imaginary-time step, $|a_0(\tau)|$ approaches 1 for $\tau \to \infty$. In words, if we propagate long enough in imaginary time, the initial state

will transform into the ground state. Theoretically, to obtain the ground state there should be some contribution of the ground state already in the initial state. Numerical errors can actually help here as they add a small fraction of all eigenstates to $\psi(\mathbf{x}, \tau)$ at each propagation step because of their random nature. The initial state is chosen completely randomly in our calculations, i.e., the value at every grid point is given by a random number.

Assuming that we have found the ground state, i.e., $|a_0(\tau)| = 1$ and $|a_k(\tau)| = 0$ for $k > 0$, the norm of the density after one propagation step is given by

$$N = e^{-2E_0\,\Delta\tau}. \tag{A.10}$$

We can invert this to obtain the ground state energy E_0 from the norm of the probability density after one propagation step as

$$E_0 = -\frac{1}{2\Delta\tau}\ln N. \tag{A.11}$$

Excited states can be obtained in either of two ways. Firstly, if the symmetry of the excited state is known and different from all states lower in energy, we can obtain the excited state by enforcing the symmetry at every propagation step. Also the symmetry can be helpful in separating (almost) degenerate states and to increase the numerical convergence and stability significantly for such systems. Therefore the almost degenerate states discussed in section 3.3 were obtained by taking advantage of their respective symmetries. Secondly, in general excited states can always be found by first finding the lower states one by one and then projecting these out during every propagation step. For example, to find the second excited state, we perform one run to find the ground state, then start again with a random initial state while projecting out the ground state at every time step, and then a final run where both the ground state and the first excited state are projected out at every time step. Projecting out a bound state is done according to the prescription

$$c_j = \langle \phi_j(\mathbf{r}) | \psi(\mathbf{r}, \tau) \rangle, \tag{A.12a}$$

$$\psi(\mathbf{r}, \tau) \to \psi'(\mathbf{r}, \tau) = \psi(\mathbf{r}, \tau) - c_j\,\phi_j(\mathbf{r}), \tag{A.12b}$$

where the complex conjugation guarantees that the prescription also works if the bound state is present in the wave packet with a complex global phase.

To increase the speed of conversion in finding bound states, we start the propagation with a relative big imaginary-time step equal to $\Delta\tau = 5$ a.u. Once the wave packet is converged, we reduce $\Delta\tau$ to continue the search using increased accuracy. We consider the bound state found if the wave packet is converged and $\Delta\tau < 10^{-5}$ a.u. If the wave packet does not converge to the ground state, which can happen for large $\Delta\tau$, we repeat the procedure using a smaller $\Delta\tau$.

The interaction between the electron and the laser can be described in either length or velocity gauge in the Hamiltonian. All Hamiltonians in this thesis presented so far—including e.g. Eq. (2.1b)—are written in length gauge because in length gauge the interaction with the laser takes a more intuitive form. In velocity gauge Eq. (2.1b) takes the form

$$\hat{H} = \frac{\left(\hat{\mathbf{p}} + \mathbf{A}(t)\right)^2}{2} + V(\mathbf{r}), \tag{A.13}$$

where $\mathbf{A}(t)$ is the vector potential of the laser, $\mathbf{A}(t) = -\int_{-\infty}^{t} \mathbf{E}(t')dt'$. Most of the numerical results presented in this thesis were calculated in velocity gauge. Physically the choice of gauge should not matter and we confirmed that this is the case for the numerical results presented in this thesis.

For the 2D calculations we performed for a wavelength of 780–800 nm we propagated the system for two more laser periods after the laser pulse. Some electrons might return to the nucleus after the laser pulse is already over. Furthermore, the temporal window would influence the HHG spectrum too much for extremely short pulses otherwise. For the 1D calculations (up to a wavelength of 2000 nm) we additionally inserted two extra laser periods before the start of the laser pulse into $\langle \boldsymbol{\alpha}(t) \rangle$. This has the effect of shifting the recombinations more towards the middle of $\langle \boldsymbol{\alpha}(t) \rangle$, thereby further reducing the influence of the temporal window.

A.1.1 Gaussian-wave-packet grid

In this section we describe how we select the parameters of the Gaussian-wave-packet calculations. For convenience, we copy here the definition of the Gaussian wave packet from Eq. (3.1b)

$$\psi_{\mathrm{G}}(\mathbf{r}) = \sqrt{C}\sqrt{\frac{c_x c_y}{\pi}} e^{-\frac{1}{2}\left(c_x^2\left(x-\frac{L_x}{4}\right)^2 + c_y^2 y^2\right) + ik_0 x}, \tag{A.14}$$

where c_x, c_y are the momentum spread of the wave packet in the x, y-directions and $k_0 < 0$ is the central momentum in the x-direction. The grid measures $L_x \times L_y$ a.u. and $\psi_{\mathrm{G}}(\mathbf{r})$ is centered at $(x_0 = L_x/4, 0)$ whereas the bound state is located at the origin. As described in section 3.1, we pick a parameter r_k that sets the momentum spread of the wave packet in the orthogonal direction as $c_y = r_k|k_0|$ to set one of the physically most relevant characteristics of the Gaussian wave packet. Furthermore we pick a laser intensity and wavelength that we want to compare the Gaussian wave packet with. We parameterize the Gaussian wave packet in terms of the U_{p} of this laser pulse. The other parameters are mostly set to guarantee the numerical accuracy of the calculation by limiting the size of the wave packet both in coordinate and momentum space, thereby preventing reflections at the boundaries. In addition, by limiting the frequency range of the Gaussian wave packet around the harmonic cutoff of a laser pulse with U_{p}, we can use the same spatial and temporal resolutions for the Gaussian-wave-packet calculation as for the corresponding HHG calculation. The other parameters are given by

$$k_{\max} = \sqrt{2(3.17U_{\mathrm{p}})}, \tag{A.15a}$$

$$e^{-r_x} = \left|\frac{\psi_{\mathrm{G}}(L_x/2, 0)}{\psi_{\mathrm{G}}(L_x/4, 0)}\right|, \qquad e^{-r_y} = \left|\frac{\psi_{\mathrm{G}}(L_x/4, L_y/2)}{\psi_{\mathrm{G}}(L_x/4, 0)}\right|, \tag{A.15b}$$

$$e^{-r_u} = \left|\frac{\hat{\psi}_{\mathrm{G}}(-k_{\max}, 0)}{\hat{\psi}_{\mathrm{G}}(k_0, 0)}\right|, \qquad e^{-r_d} = \left|\frac{\hat{\psi}_{\mathrm{G}}(0, 0)}{\hat{\psi}_{\mathrm{G}}(k_0, 0)}\right|, \tag{A.15c}$$

where $\hat{\psi}_{\mathrm{G}}(k_x, k_y)$ is the Fourier transform of $\psi_{\mathrm{G}}(x, y)$.

If we take into account that the propagation time T_{prop} must be chosen such that a classical particle with momentum k_0 moves from $(L_x/4, 0)$ to $(-L_x/4, 0)$ during the propagation as explained in section 3.1, the solution of Eq. (A.15) for k_0, c_x, L_x, L_y and T_{prop} is given by

$$k_0 = -\frac{k_{\max}}{1+\sqrt{\frac{ru}{rd}}}, \qquad c_x = \frac{k_{\max}}{\sqrt{2r_d}+\sqrt{2r_u}}, \tag{A.16a}$$

$$L_x = \frac{4\sqrt{2}\sqrt{r_x}}{c_x}, \qquad L_y = \frac{4\sqrt{2}\sqrt{r_y}}{c_y}, \tag{A.16b}$$

$$T_{\text{prop}} = \frac{L_x}{2\,|k_0|}. \tag{A.16c}$$

We use $r_x = r_y = r_d = 10$ and $r_u = 2$ for the calculations presented in this thesis. An additional requirement for T_{prop} is that it is given by $N_{\text{prop}}\,T$, where N_{prop} is an integer and T is the duration of one optical cycle of the equivalent laser pulse, such that the numerical energy data points lie on top of the harmonics of the equivalent laser pulse. That means that T_{prop} as prescribed by Eq. (A.16c) is extended to fulfill $T_{\text{prop}} = N_{\text{prop}}\,T$. To keep the collision at the middle of the propagation, L_x is then multiplied with the same factor. Also L_x, L_y are always set to at least 80 a.u. Therefore r_x, r_y should be considered minimum requirements, not absolute prescriptions.

For simulated laser parameters of $I = 5 \times 10^{14}$ W/cm^2 and $\lambda = 780$ nm and using $r_k = 0.01$, the grid dimensions are $L_x = 383$ a.u. and $L_y = 1006$ a.u. (the example in section 3.1). The spatial resolutions and grid characteristics such as the absorbing boundary are in line with what is prescribed for general HHG calculations in section A.1.2. For the above example we use 2304×6144 grid points, and the spatial resolution is 0.16–0.17 a.u. in both spatial dimensions.

A.1.2 Spatial grid in HHG calculations

The spatial grid needs to be big enough to represent all electrons that can play a role in the harmonic generation process. Solving the classical equations of motion Eq. (2.7) shows that classically the largest distance an electron can travel before returning to the core in a cw laser is $\pm 2\alpha$, where $\alpha = E_0/\omega^2$ and E_0 is the amplitude of laser electric field. If we consider a laser pulse with a finite length the envelope will reduce the effective amplitude of the electric field and the electron will stay closer to the core region before recombining. For the linearly polarized pulses considered in this thesis we adopt a spatial grid that covers $L_x = 8\alpha$ in the laser polarization direction. The 2D calculation uses $L_y = 0.3L_x$ in the orthogonal y-direction.

At every edge of the grid, 10% of the grid length in that dimension is used for an absorbing $\sin^2$-boundary. The purpose of the boundary is to absorb electron density moving outside the grid. The density moving outside the grid needs to be absorbed because technically a discretized grid is closed, i.e., density crossing the grid edge reappears at the opposing edge. The density at the edge cannot be removed too suddenly as that leads to artificial reflections. The effect of applying the absorbing boundary during the propagation is visualized in section A.1.4.

Unless mentioned otherwise, for all numerical calculations presented in this thesis we use spatial step sizes in the range $[0.15, 0.20]$ a.u. in each spatial dimension. This way the obtained spectra can be considered converged. In the past molecular characteristics were successfully calculated using significantly lower resolutions (see e.g. Lein et al. [67]), but modern day computers allow us to be on the safe side. For the typical case of a 2D calculation for $\lambda = 780$ nm at an intensity of $I = 5 \times 10^{14}$ W/cm^2 this then leads to a grid measuring 279.8×84.0 a.u. with 1536×512 grid points.

A.1.3 Spatial grid in ATI calculations

For combined HHG+ATI calculations, we keep the grid resolution identical to that used for a pure HHG calculation. However, the grid has to be lot larger since it has also hold electrons whose trajectories never return to the origin. For the tomographic procedure only direct ATI electrons are used, which means that classically the maximum kinetic energy we need to take into account is $E_{\max} = 2U_\mathrm{p}$. If we want to calculate the full ATI spectrum, also rescattering electrons with classical energies up to $E_{\max} = 10U_\mathrm{p}$ need to be considered. In formulas, in the laser polarization direction the grid needs to have the dimension

$$L_x = 2N_\mathrm{prop} T v_{\max}, \tag{A.17a}$$

$$v_{\max} = 1.2\sqrt{2E_{\max}} = 1.2\sqrt{2N_{U_\mathrm{p}} U_\mathrm{p}}, \tag{A.17b}$$

where N_{U_p} is a parameter that determines the highest kinetic energy the grid can hold in multiples of U_p. The factor 1.2 in Eq. (A.17b) represents the absorbing boundaries. The factor 2 in Eq. (A.17a) comes from the fact that the electron can travel the maximum distance in either direction. Especially for short pulses Eq. (A.17) overestimates the required grid dimension as we assumed that the electrons leave the nucleus at $t = 0$. To take into account quantum-mechanical effects, for direct electrons we use $N_{U_\mathrm{p}} = 3$ and for rescattering electrons we use $N_{U_\mathrm{p}} = 15$.

In an atom the maximum ATI energy is given by $10U_\mathrm{p}$. Only for a molecule that contains an internuclear distance comparable to the electron excursion length (35 a.u. for a pulse with 780-nm wavelength at 5×10^{14} W/cm^2), the cutoff energy is significantly higher (Chirilă and Lein [21]). For $N_{U_\mathrm{p}} = 15$ the absorbing boundary has practically no effect anymore as after the propagation virtually all density is still represented on the grid. As an example, for a three-cycle laser pulse ($N_\mathrm{prop} = 5$) with $\lambda = 2000$ nm and $I = 2\times10^{14}$ W/cm^2 we use $L_x = 13432$ a.u. for direct electrons and $L_x = 30034$ a.u. if we want to calculate the full ATI spectrum including rescattering electrons. For this we use 81920 and 179200 gridpoints, respectively.

A.1.4 Time step HHG calculations

The time step Δt is chosen such that the evolution operator $e^{-i\,E\,\Delta t}$ is close to unity for all energies E that we expect to occur during the propagation. For example, for the case of 780 nm and 5×10^{14} W/cm^2 we choose a minimum of 2000 time steps

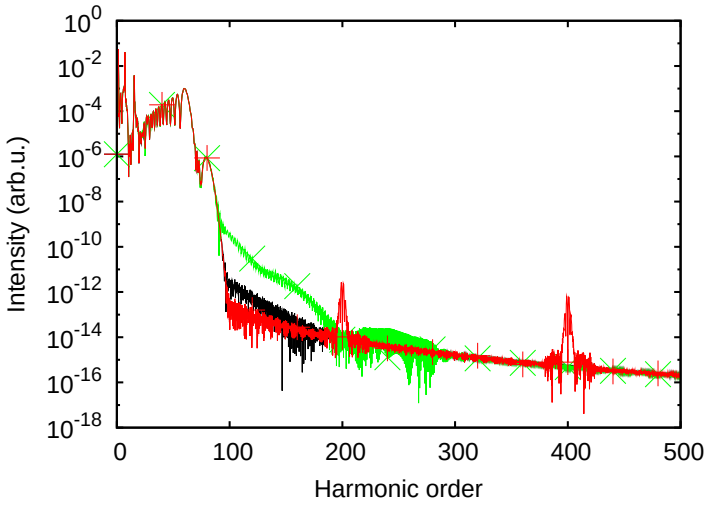

Figure A.1: (Color online) Effect of the absorbing boundary in the classically forbidden region. $N_{\text{mask}} = 1$ (green line with crosses), $N_{\text{mask}} = 8$ (black solid line) and $N_{\text{mask}} = 40$ (red line with plusses).

per laser cycle. For the 1D calculations we use significantly smaller time steps, as explained in the next paragraphs.

Every N_{mask} time steps the absorbing boundary is applied. If the system is such that the boundary absorbs some density, this creates artefacts at multiples of the angular frequency with which the boundary is applied, i.e., at multiples of $\frac{2\pi}{\Delta t}/N_{\text{mask}}$. This is illustrated in Fig. A.1. This plot was created from 1D solutions of the TDSE for a 3-cycle $\sin^2$-pulse with $\phi = 1.25\pi$ and 780 nm and 5×10^{14} W/cm^2. The molecule was 1D H_2^+ with $Z_1 = Z_2 = 0.7309$ and $a^2 = 0.5$ such that $I_{\text{p}} = 30.2$ eV. The number of time steps per laser cycle was 8000. The artefacts at multiples of harmonic 200 for $N_{\text{mask}} = 40$ in Fig. A.1 are therefore expected.

The choice of N_{mask} seems to affect the region beyond the cutoff in a pure HHG calculation. In particular, setting N_{mask} too low can cause the HHG spectrum to fall off less well right after the cutoff. This can be seen clearly from Fig. A.1 by considering the $N_{\text{mask}} = 1$-case. Therefore, care should be taken when selecting N_{mask} if one is interested in obtaining the cleanest numerical spectrum. Particularly, one should not forget to increase N_{mask} if the time resolution is increased.

A.1.5 Time step ATI calculations

For numerical ATI calculations on a simple grid as used by us, a higher time resolution is needed than for numerical pure HHG calculations. The grid also needs to be much larger. The reason is that we need to represent and propagate very fast electrons that do not contribute to HHG, but contribute to the ATI spectrum. These electrons are absorbed by the boundary on a pure HHG grid. Therefore the time resolution is chosen such that also these very fast electrons are properly propagated. One requirement we set is that rescattering ATI electrons with energies up to

$10U_\mathrm{p}$ (see section 2.2.2) are still correctly propagated. Here we ignore internuclear-distance effects (see the discussion below Eq. (5.4)). The second requirement is that no artifacts with the frequency of the inverse time step (from repeatedly applying the evolution operator) occur within the energy range represented on the grid. We require this because these artefacts seem to propagate to much lower energies, and then also influence the energy domain we are interested in. In formula the second requirement is that

$$\frac{2\pi}{\Delta t} \geq \frac{1}{2}\left(\frac{\pi}{\Delta x}\right)^2. \tag{A.18}$$

In practice, both requirements are usually fulfilled by a four times as small time step for a HHG+ATI calculation as for a pure HHG calculation, leading to e.g. 10,000 time steps per cycle for a calculation with a 2000-nm pulse at 2×10^{14} W/cm^2. In case we compare a tomographic reconstruction from an HHG+ATI calculation with a result from a pure HHG calculation we use the same higher time step for both calculations.

A.2 Pulse polarization

This section is about the inversion of Eq. (2.34). This allows us to express numerical HHG spectra in terms of physical parameters such as the orientation and ellipticity of the emitted radiation. If we split the equalities in Eq. (2.34) into real and imaginary parts explicitly and drop the angle dependence, we obtain

$$\mathrm{Re}(\alpha_x) = \frac{\mathrm{Re}(c)\cos\phi + \mathrm{Im}(c)\epsilon\sin\phi}{\sqrt{1+\epsilon^2}}, \tag{A.19a}$$

$$\mathrm{Im}(\alpha_x) = \frac{\mathrm{Im}(c)\cos\phi - \mathrm{Re}(c)\epsilon\sin\phi}{\sqrt{1+\epsilon^2}}, \tag{A.19b}$$

$$\mathrm{Re}(\alpha_y) = \frac{\mathrm{Re}(c)\sin\phi - \mathrm{Im}(c)\epsilon\cos\phi}{\sqrt{1+\epsilon^2}}, \tag{A.19c}$$

$$\mathrm{Im}(\alpha_y) = \frac{\mathrm{Im}(c)\sin\phi + \mathrm{Re}(c)\epsilon\cos\phi}{\sqrt{1+\epsilon^2}}. \tag{A.19d}$$

We add the squares of the four Eqs. (A.19) to obtain

$$\begin{aligned} |\boldsymbol{\alpha}|^2 &= |\alpha_x|^2 + |\alpha_y|^2 = (\mathrm{Re}(\alpha_x))^2 + (\mathrm{Im}(\alpha_x))^2 + (\mathrm{Re}(\alpha_y))^2 + (\mathrm{Im}(\alpha_y))^2 \\ &= \frac{((\mathrm{Re}(c))^2 + (\mathrm{Im}(c))^2)(\cos^2\phi + \sin^2\phi + \epsilon^2(\cos^2\phi + \sin^2\phi))}{1+\epsilon^2} \\ &= (\mathrm{Re}(c))^2 + (\mathrm{Im}(c))^2 = |c|^2. \end{aligned} \tag{A.20}$$

The 'mix'-terms between the real and imaginary parts of $\boldsymbol{\alpha}$ are given by

$$\mathrm{Re}(\alpha_x)\mathrm{Im}(\alpha_y) = \mathrm{Re}(c)\mathrm{Im}(c)\cos\phi\sin\phi + \frac{\epsilon\left((\mathrm{Re}(c))^2\cos^2\phi + (\mathrm{Im}(c))^2\sin^2\phi\right)}{1+\epsilon^2}, \tag{A.21}$$

$$\mathrm{Re}(\alpha_y)\mathrm{Im}(\alpha_x) = \mathrm{Re}(c)\mathrm{Im}(c)\cos\phi\sin\phi + \frac{\epsilon\left(-(\mathrm{Im}(c))^2\cos^2\phi - (\mathrm{Re}(c))^2\sin^2\phi\right)}{1+\epsilon^2}. \tag{A.22}$$

We can now define a new quantity σ as

$$\sigma \equiv \mathrm{Re}(\alpha_x)\mathrm{Im}(\alpha_y) - \mathrm{Re}(\alpha_y)\mathrm{Im}(\alpha_x) = \frac{\epsilon\left((\mathrm{Re}(c))^2 + (\mathrm{Im}(c))^2\right)}{1+\epsilon^2} = \frac{|\boldsymbol{\alpha}|^2\epsilon}{1+\epsilon^2}, \quad \text{(A.23)}$$

where for the last equality we used Eq. (A.20). Alternatively, using $\sin(a-b) = \sin a\cos b - \cos a \sin b$, we can express σ as

$$\sigma = |\alpha_x||\alpha_y|\sin\delta, \quad \text{(A.24)}$$

where δ is the phase difference between the two laboratory frame components, i.e., $\delta = \arg(\alpha_y) - \arg(\alpha_x)$.

From Eq. (A.23) we see that the numerically measurable quantity $\frac{\sigma}{|\boldsymbol{\alpha}|^2}$ is a measure for ϵ; $\frac{\sigma}{|\boldsymbol{\alpha}|^2} = 0$ for linear polarization ($\epsilon = 0$) and $\frac{\sigma}{|\boldsymbol{\alpha}|^2} = \pm\frac{1}{2}$ for circular polarization ($\epsilon^2 = 1$). It follows from Eq. (A.23) that

$$\frac{\sigma}{|\boldsymbol{\alpha}|^2}\epsilon^2 - \epsilon + \frac{\sigma}{|\boldsymbol{\alpha}|^2} = 0. \quad \text{(A.25)}$$

The solutions of this equation for ϵ for non-linear polarization are given by

$$\epsilon = \frac{1 \pm \sqrt{1 - 4\left(\frac{\sigma}{|\boldsymbol{\alpha}|^2}\right)^2}}{2\frac{\sigma}{|\boldsymbol{\alpha}|^2}}. \quad \text{(A.26)}$$

However, since for non-circular and non-linear polarization $-\frac{1}{2} < \frac{\sigma}{|\boldsymbol{\alpha}|^2} < \frac{1}{2}$ with $\frac{\sigma}{|\boldsymbol{\alpha}|^2} \neq 0$, it follows that $0 < \sqrt{1 - 4\left(\frac{\sigma}{|\boldsymbol{\alpha}|^2}\right)^2} < 1$. This means that the +-sign in Eq. (A.26) always give rise to unphysical solutions for ϵ, as $\left|\frac{1+\sqrt{1-4\left(\frac{\sigma}{|\boldsymbol{\alpha}|^2}\right)^2}}{2\frac{\sigma}{|\boldsymbol{\alpha}|^2}}\right| > 1$. Therefore we select the solution with the −-sign and write for the ellipticity

$$\epsilon = \frac{1 - \sqrt{1 - 4\left(\frac{\sigma}{|\boldsymbol{\alpha}|^2}\right)^2}}{2\frac{\sigma}{|\boldsymbol{\alpha}|^2}}. \quad \text{(A.27)}$$

Alternatively, using the trigonometric identities $\tan\left(\frac{1}{2}\arcsin a\right) = \frac{1-\sqrt{1-a^2}}{a}$ and $\sin(2\arctan a) = \frac{2a}{1+a^2}$, we express the ellipticity as

$$\epsilon = \tan\left(\frac{1}{2}\arcsin\left(\sin\left(2\arctan\left(\frac{|\alpha_y|}{|\alpha_x|}\right)\right)\sin\delta\right)\right), \quad \text{(A.28)}$$

as was for instance done in (Le et al. [63]).

Concerning the polarization direction, using Eq. (2.34) we can express the ratio between the two complex emission amplitudes in the laboratory frame as

$$\frac{\alpha_x}{\alpha_y} = \frac{\cos\phi - i\,\epsilon\sin\phi}{\sin\phi + i\,\epsilon\cos\phi} = \frac{1 - i\,\epsilon\tan\phi}{\tan\phi + i\,\epsilon}. \quad \text{(A.29)}$$

This equation can be solved for ϕ to obtain

$$\phi = \arctan\left(\frac{\alpha_y - i\,\epsilon\,\alpha_x}{\alpha_x + i\,\epsilon\,\alpha_y}\right). \tag{A.30}$$

The natural range of the arctan-function is $[-\pi/2, \pi/2]$. However, as we defined the range of ϕ to be $[0, \pi)$, we add π to ϕ if $\phi < 0$. Alternatively, as e.g. in (Le et al. [63]), ϕ can be expressed as

$$\phi = \frac{1}{2}\arctan2\left(\frac{\cos\delta}{1/\tan\left(2\arctan\left(\frac{|\alpha_y|}{|\alpha_x|}\right)\right)}\right), \tag{A.31}$$

where $\arctan2\left(\frac{y}{x}\right)$ is the arctan-function extended to the full 2π-complex domain by taking into account the signs of x and y. The fact that the arctan2-function is needed can be seen from the factor of $\frac{1}{2}$ in Eq. (A.31). Only in the presented—somewhat quaint—form with the double fraction is Eq. (A.31) numerically equal to Eq. (A.30).

Now using Eq. (2.34) again to determine the complex prefactor c, we find the two equivalent expressions

$$c = \frac{\sqrt{1+\epsilon^2}}{\cos\phi - i\,\epsilon\sin\phi}\alpha_x = \frac{\sqrt{1+\epsilon^2}}{\sin\phi + i\,\epsilon\cos\phi}\alpha_y. \tag{A.32}$$

A.2.1 Conversion algorithm

To perform the conversion, we need to distinguish between different cases. In particular, we have to exclude some special cases before we can use the general algorithm to obtain the pulse parameters, mostly to prevent divisions by 0 (especially $\frac{0}{0}$) from occurring. In the order listed, the special cases below are therefore checked for within some reasonable numerical limits.

A.2.1.1 Zero-pulse case

If the measured dipole moments $|\alpha_x|$ and $|\alpha_y|$ are equal to 0 within some numerical margin, the pulse has 0 amplitude. That means that c is set to 0, while ϕ and ϵ are undefined.

A.2.1.2 Linear polarization

This case is selected when the variable σ, defined in Eq. (A.23), is equal to 0 within numerical limits, as that amounts to $\epsilon = 0$ according to its definition. In addition, linear polarization ($\epsilon = 0$) is selected if $|\alpha_x|^2 \gg |\alpha_y|^2$ or $|\alpha_y|^2 \gg |\alpha_x|^2$ (in practice the condition is that one component is larger than 10^8 times the other). In other words, this is used as an alternative criterion for $\epsilon = 0$. The reason is that the above-mentioned requirement clearly amounts to the pulse being linear, as the electric

field is orientated along one direction only. The reason that we need to incorporate this second, in principle superfluous condition, is that for those pulses σ cannot be accurately determined numerically, as relatively small errors on the scale of the bigger component can be very big on the relatively scale of the small component. For the case of linear polarization, Eq. (A.30) simplifies to

$$\phi = \arctan\left(\frac{\alpha_y}{\alpha_x + \xi}\right), \tag{A.33}$$

where ξ, a very small number, was added to prevent division by 0. As indicated before, we add π to ϕ if $\phi < 0$. Using Eq. (A.32), we obtain the numerically most stable expression for c as

$$c = \begin{cases} \frac{\alpha_x}{\cos\phi} & \text{if } |\alpha_x| \geq |\alpha_y| \\ \frac{\alpha_y}{\sin\phi} & \text{else.} \end{cases} \tag{A.34}$$

A.2.1.3 Circular polarization

We select the circular polarization case if $\frac{\sigma}{|\boldsymbol{\alpha}|^2}$ is equal to $\pm\frac{1}{2}$ within numerical limits. Using Eq. (A.23) we set

$$\epsilon = \begin{cases} 1 & \text{if } \sigma > 0 \\ -1 & \text{else.} \end{cases} \tag{A.35}$$

In the case of circular polarization, the polarization angle ϕ is not uniquely defined, and changing it corresponds to multiplying c with a global complex phase factor. We arbitrarily set $\phi = 0$. Now Eq. (A.32) simplifies to

$$c = \sqrt{2}\alpha_x = -\sqrt{2}i\,\epsilon\,\alpha_y. \tag{A.36}$$

The best estimate for c is given by

$$c = \frac{1}{\sqrt{2}}\left(\alpha_x - i\,\epsilon\,\alpha_y\right). \tag{A.37}$$

A.2.1.4 General case

Using Eqs. (A.27), (A.30) and (A.32), the pulse parameters are determined as

$$\epsilon = \frac{1 - \sqrt{1 - 4\left(\frac{\sigma}{|\boldsymbol{\alpha}|^2}\right)^2}}{2\frac{\sigma}{|\boldsymbol{\alpha}|^2}}, \tag{A.38a}$$

$$\phi = \arctan\left(\frac{\alpha_y - i\,\epsilon\,\alpha_x}{\alpha_x + i\,\epsilon\,\alpha_y + \xi}\right), \tag{A.38b}$$

$$c = \begin{cases} \frac{\sqrt{1+\epsilon^2}}{\cos\phi - i\,\epsilon\sin\phi}\alpha_x & \text{if } |\alpha_x| \geq |\alpha_y| \\ \frac{\sqrt{1+\epsilon^2}}{\sin\phi + i\,\epsilon\cos\phi}\alpha_y & \text{else,} \end{cases} \tag{A.38c}$$

where ξ is again a very small number and for c we picked the numerically most stable expression. Again we add π to ϕ if $\phi < 0$.

A.3 Projected 3D orbital

In this section we show how to numerically convert a 2D projection of an orbital with rotational symmetry around the x-axis to the full 3D orbital. This section is the numerical appendix to section 4.7. Because of the rotational symmetry of the orbital, the following equality holds

$$\psi_0^{3D}(x,y,z) = \psi_0^{3D}(x,y,-z) = \psi_0^{3D}(x,\sqrt{y^2+z^2},0). \tag{A.39}$$

Let us now try to recover $\psi_0^{3D}(x,y,z)$ from $\psi_0(\mathbf{r})$. We take the orbital to be centered in the tomographic region $L_x \times L_y$, which means we can assume $\psi_0^{3D}(x,y,0) = 0$ for $|y| \geq L_y/2$. Therefore we have that

$$\begin{aligned}\psi_0(\mathbf{r}) &= \int_{-\frac{L_y}{2}}^{\frac{L_y}{2}} \psi_0^{3D}(x,y,z)dz = 2\int_0^{\frac{L_y}{2}} \psi_0^{3D}(x,\sqrt{y^2+z^2},0)dz \\ &= 2\int_y^{\sqrt{(\frac{L_y}{2})^2+y^2}} \frac{z'}{\sqrt{z'^2-y^2}}\psi_0^{3D}(x,z',0)dz',\end{aligned} \tag{A.40}$$

where $z' = \sqrt{y^2+z^2}$ and $\frac{z'}{\sqrt{z'^2-y^2}}$ is the Jacobian factor $\frac{dz}{dz'}$ associated with the change of integration variables in the last equality. Taking into account that $\psi_0(\mathbf{r}) = 0$ for $r \geq \sqrt{(\frac{L_y}{2})^2+y^2}$, this is an Abel transform (Weisstein [132]). Abel transforms are often encountered in the analysis of spherically or cylindrically symmetric functions and are Volterra integral equations of the first kind.

Because we want to solve the above equation discretely, we subtract the singularity at the lower integration boundary and calculate it analytically, so that

$$\begin{aligned}\psi_0(\mathbf{r}) = 2\int_y^{\frac{L_y}{2}} \frac{z'}{\sqrt{z'^2-y^2}} \left[\psi_0^{3D}(x,z',0) - \psi_0^{3D}(x,y,0)\right] dz' \\ + 2\int_y^{\frac{L_y}{2}} \frac{z'}{\sqrt{z'^2-y^2}} dz' \psi_0^{3D}(x,y,0),\end{aligned} \tag{A.41}$$

where we again used that the wave function is constrained to the tomographic region. The integral in the second part on the right hand side evaluates to $\sqrt{(\frac{L_y}{2})^2-y^2}$. Therefore we can write

$$\begin{aligned}\psi_0(\mathbf{r}) = 2\int_y^{\frac{L_y}{2}} \frac{z'}{\sqrt{z'^2-y^2}} \left[\psi_0^{3D}(x,z',0) - \psi_0^{3D}(x,y,0)\right] dz' \\ + 2\sqrt{(\frac{L_y}{2})^2-y^2}\, \psi_0^{3D}(x,y,0).\end{aligned} \tag{A.42}$$

To solve this equation numerically we will start at $y = L_y/2$ and work our way downwards. We define $\psi_{ij} = \psi_0(x_i,y_j)$ and $\psi_{ij}^{3D} = \psi_0^{3D}(x_i,z'_j,0)$. We also need to discretize the Jacobian prefactor. We will denote it by $K_{ij} = K(y_i,z'_j) = \frac{z'_j}{\sqrt{z'^2_j - y_i^2}}$.

Using the trapezoidal integration rule the discrete version of Eq. (A.42) is

$$\begin{aligned}\psi_{ij} &= 2\Delta y \left[\frac{K_{jj}}{2}(\psi_{ij}^{3D} - \psi_{ij}^{3D}) + \frac{K_{j,N_y-1}}{2}(\psi_{i,N_y-1}^{3D} - \psi_{ij}^{3D}) + \sum_{k=j+1}^{N_y-2} K_{jk}(\psi_{ik}^{3D} - \psi_{ij}^{3D}) \right] \\ &\quad + 2\sqrt{(\tfrac{L_y}{2})^2 - y^2}\, \psi_{ij}^{3D} \\ &= 2\Delta y \left[-\frac{K_{j,N_y-1}}{2}\psi_{ij}^{3D} + \sum_{k=j+1}^{N_y-2} K_{jk}(\psi_{ik}^{3D} - \psi_{ij}^{3D}) \right] + 2\sqrt{(\tfrac{L_y}{2})^2 - y^2}\, \psi_{ij}^{3D},\end{aligned} \tag{A.43}$$

where we made use of the fact that because of the boundary condition $\psi_{i0} = \psi_{i,N_y-1} = \psi_{i0}^{3D} = \psi_{i,N_y-1}^{3D} = 0$. In the actual calculation we can again use the rotational symmetry, so that we only have to calculate for $j > \frac{N_y-1}{2}$. In our calculations we consider grids with an even number of grid points because the FFT is faster then. That means we can go from the full 3D orbital to the projected orbitals using the equations

$$\begin{aligned}\psi_{ij} = 2 &\left[-\Delta y \left(\frac{K_{j,N_y-1}}{2} + \sum_{k=j+1}^{N_y-2} K_{jk} \right) + \sqrt{(\tfrac{L_y}{2})^2 - y^2} \right] \psi_{ij}^{3D} \\ &+ 2\Delta y \sum_{k=j+1}^{N_y-2} K_{jk}\psi_{ik}^{3D},\end{aligned} \qquad \text{for } j > \tfrac{N_y-1}{2} \tag{A.44a}$$

$$\psi_{i,-j} = \psi_{ij} \qquad \text{for } j < \tfrac{N_y-1}{2}. \tag{A.44b}$$

For going from the projected orbital to the full orbital the following equations can be used (starting at $j = N_y - 1$, and then going down)

$$\psi_{i,N_y-1}^{3D} = 0, \tag{A.45a}$$

$$\psi_{ij}^{3D} = \frac{2\Delta y \sum_{k=j+1}^{N_y-2} K_{jk}\psi_{ik}^{3D} - \psi_{ij}}{2\left[\Delta y \left(\frac{K_{j,N_y-1}}{2} + \sum_{k=j+1}^{N_y-2} K_{jk} \right) - \sqrt{(\tfrac{L_y}{2})^2 - y^2} \right]} \quad \text{for } \tfrac{N_y-1}{2} < j < N_y - 1, \tag{A.45b}$$

$$\psi_{i,-j}^{3D} = \psi_{ij}^{3D} \qquad \text{for } j < \tfrac{N_y-1}{2}. \tag{A.45c}$$

Because of the rotational symmetry, ψ_{ij}^{3D} contains all information about the three dimensional orbital, as

$$\psi_{ij}^{3D} = \psi_0^{3D}(x_i, y_j, 0) = \psi_0^{3D}(x_i, 0, z_j) = \psi_0^{3D}(x_i, y_j \cos\theta, z_j \sin\theta) \tag{A.46}$$

for all angles θ.

A.4 SFA calculations

A.4.1 Classical HHG trajectories

In section 5.1.3 we found an expression for the HHG amplitude (Eq. (5.104)) and also for $a_\theta[-k(\omega)]$ (Eq. (5.108)) as an expansion around $\gamma = 0$ on the basis of classical electron trajectories. Since we only consider linearly polarized pulses we consider one spatial dimension. The relevant classical trajectories ionize at time t_0' with initial momentum $v(t_0') = 0$ from position $x(t_0') = 0$, and return at time t_0 to their initial position $x(t_0) = 0$ with return momentum $v_{\mathrm{rec}} = \pm\sqrt{2(\omega - I_{\mathrm{p}})}$ (see Eq. (5.80)). To find the contributing classical trajectories for frequency ω, we solve the equations of motion Eq. (2.7) in two steps. First we perform an initial rough scan of all birth times to find the rough birth times of the contributing trajectories, and then we perform a more accurate calculation to find the exact times.

For the initial rough scan we solve the equations of motion for $N_{t'}$ birth times t' per laser cycle by discretely propagating Eq. (2.7c) from t' to two laser cycle periods after the laser pulse is over. For the propagation we discretize Eq. (2.7c) using the trapezium rule and we use half the number of time steps that are used for the TDSE calculation for the same laser intensity and wavelength. If during the propagation we cross $x(t, t') = 0$ we estimate the time of the crossing t and the return momentum k using a linear fit to the trajectory around the crossing, and we store the return parameters (t', t, k) in a list. After finishing the initial scan this list is such that it contains a family of returns (t', t, k) for each trajectory $(t_0', t_0, v_{\mathrm{rec}})$ that contributes to the spectrum. For each trajectory we select that return that has k closest to $\pm\sqrt{2(\omega - I_{\mathrm{p}})}$, but only under the condition that for this trajectory we have found at least one return for which $|k| \geq |v_{\mathrm{rec}}|$ and at least one return for which $|k| \leq |v_{\mathrm{rec}}|$. This is to ensure that a contributing trajectory can be found for this family of returns. We checked that using the employed (relatively high) $N_{t'} = 10,000$ (20,000) for $\lambda < 900$ nm ($\lambda > 900$ nm) the algorithm is reliably converged, i.e., all contributing trajectories can be found from the list of returns.

We find the set of contributing trajectories $\{(t_0', t_0, v_{\mathrm{rec}})\}$ for each frequency ω using a secant procedure starting from the selected returns (t', t, k). For the propagation we now use the same time step as for a TDSE calculation for the same experimental parameters. For each trajectory we try to achieve a resolution that satisfies $\left|\frac{k - v_{\mathrm{rec}}}{v_{\mathrm{rec}}}\right| < 10^{-9}$, but if such a resolution cannot be achieved we do not reject the trajectory unless the achieved accuracy in k is higher than 10^{-4}. The secant procedure has some exceptions built in to make it more numerically robust and prevent it from getting stuck in loops; every iteration step the maximum step in t' allowed is chosen randomly in the range $[10^{-6}$ a.u., $T)$, where T is the laser period. Furthermore, if the error got bigger or no return could be found, first a smaller birth time step in the same direction, and then a birth time step in the opposite direction is found. If still the error got bigger or no return could be found, a new random birth time close to the originally found return is used. After confirming that each entry in $\{(t_0', t_0, v_{\mathrm{rec}})\}$ is unique, we use the set to evaluate Eq. (5.104).

Bibliography

[1] A. Apolonski, A. Poppe, G. Tempea, C. Spielmann, T. Udem, R. Holzwarth, T. W. Hänsch, and F. Krausz. *Controlling the phase evolution of few-cycle light pulses.* Phys. Rev. Lett. **85**, 740 (2000).

[2] S. Baker, J. S. Robinson, C. A. Haworth, H. Teng, R. A. Smith, C. C. Chirilă, M. Lein, J. W. G. Tisch, and J. P. Marangos. *Probing proton dynamics in molecules on an attosecond time scale.* Science **312**, 424 (2006).

[3] P. Balcou, P. Salières, A. L'Huillier, and M. Lewenstein. *Coherence control of high-order harmonics.* Phys. Rev. A **55**, 3204 (1997).

[4] A. Baltuška, T. Fuji, and T. Kobayashi. *Controlling the carrier-envelope phase of ultrashort light pulses with optical parametric amplifiers.* Phys. Rev. Lett. **88**, 133901 (2002).

[5] A. Baltuška, T. Udem, M. Uiberacker, M. Hentschel, E. Goulielmakis, C. Gohle, R. Holzwarth, V. S. Yakovlev, A. Scrinzi, T. W. Hänsch, and F. Krausz. *Attosecond control of electronic processes by intense light fields.* Nature **421**, 611 (2003).

[6] D. R. Bates and T. R. Carson. *Exact Wave Functions of HeH^{2+}.* Proc. R. Soc. A **234**, 207 (1956).

[7] I. Ben-Itzhak, J. P. Bouhnik, B. D. Esry, I. Gertner, O. Heber, and B. Rosner. *Mean lifetime measurement of HeH^{2+} ($2p\sigma$) isotopes.* Phys. Rev. A **54**, 474 (1996).

[8] I. Ben-Itzhak, Z. Chen, B. D. Esry, I. Gertner, O. Heber, C. D. Lin, and B. Rosner. *Mean lifetime mean lifetime of the bound $2p\sigma$ state of HeH^{2+}.* Phys. Rev. A **49**, 1774 (1994).

[9] I. Ben-Itzhak, I. Gertner, O. Heber, and B. Rosner. *Experimental evidence for the existence of the $2p\sigma$ bound state of HeH^{2+} and its decay mechanism.* Phys. Rev. Lett. **71**, 1347 (1993).

[10] S. Bohman, A. Suda, M. Kaku, M. Nurhuda, T. Kanai, S. Yamaguchi, and K. Midorikawa. *Generation of 5 fs, 0.5 TW pulses focusable to relativistic intensities at 1 kHz.* Opt. Express **16**, 10684 (2008).

[11] W. Boutu, S. Haessler, H. Merdji, P. Breger, G. Waters, M. Stankiewicz, L. J. Frasinkski, R. Taïeb, J. Caillat, A. Maquet, P. Monchicourt, B. Carré, and

P. Salières. *Coherent control of attosecond emission from aligned molecules.* Nature Phys. **4**, 545 (2008).

[12] B. H. Bransden and C. J. Joachain. *Quantum Mechanics.* Pearson Education Ltd, Harlow, England, Second edition (2000).

[13] K. Burnett, V. C. Reed, J. Cooper, and P. L. Knight. *Calculation of the background emitted during high-harmonic generation.* Phys. Rev. A **45**, 3347 (1992).

[14] W. Cao, P. Lu, P. Lan, W. Hong, and X. Wang. *Control of quantum paths in high-order harmonic generation via a $\omega + 3\omega$ bichromatic laser field.* J. Phys. B **40**, 869 (2007).

[15] J. P. Caumes, G. Sansone, E. Benedetti, M. Pascolini, L. Poletto, P. Villoresi, S. Stagira, C. Vozzi, and M. Nisoli. *Imaging of recombination events in high-order harmonic generation by phase-stabilized few-optical-cycle pulses.* J. Mod. Opt. **53**, 67 (2006).

[16] H. N. Chapman, A. Barty, M. J. Bogan, S. Boutet, M. Frank, S. P. Hau-Riege, S. Marchesini, B. W. Woods, S. Bajt, W. H. Benner, R. A. London, E. Plönjes, M. Kuhlmann, R. Treusch, S. Düsterer, T. Tschentscher, J. R. Schneider, E. Spiller, T. Möller, C. Bostedt, M. Hoener, D. A. Shapiro, K. O. Hodgson, D. van der Spoel, F. Burmeister, M. Bergh, C. Caleman, G. Huldt, M. M. Seibert, F. R. N. C. Maia, R. W. Lee, A. Szöke, N. Timneanu, and J. Hajdu. *Femtosecond diffractive imaging with a soft-x-ray free-electron laser.* Nature Phys. **2**, 839 (2006).

[17] H. N. Chapman, A. Barty, S. Marchesini, A. Noy, S. P. Hau-Riege, C. Cui, M. R. Howells, R. Rosen, H. He, J. C. H. Spence, U. Weierstall, T. Beetz, C. Jacobsen, and D. Shapiro. *High-resolution ab initio three-dimensional x-ray diffraction microscopy.* JOSA A **23**, 1179 (2006).

[18] S. L. Chin and P. A. Golovinski. *High harmonic generation in the multiphoton regime: correlation with polarizability.* J. Phys. B **28**, 55 (1995).

[19] C. C. Chirilă. *Analysis of the strong field approximation for harmonic generation and multiphoton ionisation in intense ultrashort laser pulses.* Ph.D. thesis, University of Durham, Durham, England (2004).

[20] C. C. Chirilă, I. Dreissigacker, E. V. van der Zwan, and M. Lein. *Emission times in high-order harmonic generation.* Phys. Rev. A **81**, 033412 (2010).

[21] C. C. Chirilă and M. Lein. *Strong-field approximation for harmonic generation in diatomic molecules.* Phys. Rev. A **73**, 023410 (2006).

[22] C. C. Chirilă and M. Lein. *Assessing different forms of the strong-field approximation for harmonic generation in molecules.* J. Mod. Opt. **54**, 1039 (2007).

[23] C. C. Chirilă and M. Lein. *Explanation for the smoothness of the phase in molecular high-order harmonic generation.* Phys. Rev. A **80**, 013405 (2009).

[24] M. F. Ciappina, C. C. Chirilă, and M. Lein. *Influence of Coulomb continuum wave functions in the description of high-order harmonic generation with H_2^+.* Phys. Rev. A **75**, 043405 (2007).

[25] P. B. Corkum. *Plasma perspective on strong-field multiphoton ionization.* Phys. Rev. Lett. **71**, 1994 (1993).

[26] P. B. Corkum, N. H. Burnett, and M. Y. Ivanov. *Subfemtosecond pulses.* Opt. Lett. **19**, 1870 (1994).

[27] P. Dietrich, N. H. Burnett, M. Ivanov, and P. B. Corkum. *Plasma perspective on strong-field multiphoton ionization.* Phys. Rev. A **50**, R3585 (1994).

[28] M. Drescher, M. Hentschel, R. Kienberger, G. Tempea, C. Spielmann, G. A. Reider, P. B. Corkum, and F. Krausz. *X-ray pulses approaching the attosecond frontier.* Science **291**, 1923 (2001).

[29] V. Elser. *Phase retrieval by iterated projections.* JOSA A **20**, 40 (2003).

[30] F. H. M. Faisal. *Multiple absorption of laser photons by atoms.* J. Phys. B **6**, L89 (1973).

[31] M. D. Feit, J. A. Fleck, Jr, and A. Steiger. *Solution of the Schrödinger equation by a spectral method.* J. Comp. Phys. **47**, 412 (1982).

[32] X. Feng, S. Gilbertson, H. Mashiko, H. Wang, S. D. Khan, M. Chini, Y. Wu, K. Zhao, and Z. Chang. *Generation of isolated attosecond pulses with 20 to 28 femtosecond lasers.* Phys. Rev. Lett. **103**, 183901 (2009).

[33] M. Ferray, A. L'Huillier, X. F. Li, L. A. Lompre, G. Mainfray, and C. Manus. *Multiple-harmonic conversion of 1064 nm radiation in rare gases.* J. Phys. B **21**, L31 (1988).

[34] J. R. Fienup. *Reconstruction of an object from the modulus of its Fourier transform.* Opt. Lett. **3**, 27 (1978).

[35] J. A. Fleck, Jr, J. R. Morris, and M. D. Feit. *Time-dependent propagation of high energy laser beams through the atmosphere.* Appl. Phys. A **10**, 129 (1976).

[36] B. Friedrich and D. Herschbach. *Alignment and trapping of molecules in intense laser fields.* Phys. Rev. Lett. **74**, 4623 (1995).

[37] M. Frigo and S. G. Johnson. *The design and implementation of FFTW3.* Proceedings of the IEEE **93**, 216 (2005).

[38] M. B. Gaarde and K. J. Schafer. *Space-time considerations in the phase locking of high harmonics.* Phys. Rev. Lett. **89**, 213901 (2002).

[39] M. B. Gaarde, J. L. Tate, and K. J. Schafer. *Macroscopic aspects of attosecond pulse generation.* J. Phys. B **41**, 132001 (2008).

[40] D. Gabor. *Theory of communication.* J. Inst. Elect. Eng. **93**, 429 (1946).

[41] E. Gershnabel, I. S. Averbukh, and R. J. Gordon. *Orientaion of molecules via laser-induced alignment.* Phys. Rev. A **73**, 061401(R) (2006).

[42] S. Gilbertson, Y. Wu, S. D. Khan, M. Chini, K. Zhao, X. Feng, and Z. Chang. *Isolated attosecond pulse generation using multicycle pulses directly from a laser amplifier.* Phys. Rev. A **81**, 043810 (2010).

[43] I. A. Gonoskov and M. Y. Ryabikin. *Two-center interference in high harmonic generation from diatomic molecule: detailed numerical study.* J. Mod. Opt. **55**, 2685 (2008).

[44] A. Gordon, F. X. Kärtner, N. Rohringer, and R. Santra. *Role of many-electron dynamics in high harmonic generation.* Phys. Rev. Lett. **96**, 223902 (2006).

[45] S. Haessler. *Generation of Attosecond Pulses in Atoms and Molecules.* Ph.D. thesis, Commissariat à l'Energie Atomique (CEA) Saclay, Gif-sur-Yvette, France (2009).

[46] S. Haessler, J. Caillat, W. Boutu, C. Giovanetti-Teixeira, T. Ruchon, T. Auguste, Z. Diveki, P. Breger, A. Maquet, B. Carré, R. Taïeb, and P. Salières. *High harmonic interferometry of multi-electron dynamics in molecules.* Nature Phys. **6**, 200 (2010).

[47] P. Hariharan and P. A. Robinson. *The Gouy phase shift as a geometrical quantum effect.* J. Mod. Opt. **43**, 219 (1996).

[48] M. Hentschel, R. Kienberger, C. Spielmann, G. A. Reider, N. Milosevic, T. Brabec, P. B. Corkum, U. Heinzmann, M. Drescher, and F. Krausz. *Attosecond metrology.* Nature **414**, 509 (2001).

[49] E. Hijano, C. Serrat, G. N. Gibson, and J. Biegert. *Orbital geometry determined by orthogonal high-order harmonic polarization components.* Phys. Rev. A **81**, 041401 (2010).

[50] C. Horn, M. Wollenhaupt, M. Krug, and T. Baumert. *Adaptive control of molecular alignment.* Phys. Rev. A **73**, 031401(R) (2006).

[51] C. Iaconis and I. Walmsley. *Spectral phase interferometry for direct electric-field reconstruction of ultrashort optical pulses.* Opt. Lett. **23**, 792 (1998).

[52] J. Itatani, J. Levesque, D. Zeidler, H. Niikura, H. Pépin, J. C. Kieffer, P. B. Corkum, and D. M. Villeneuve. *Tomographic imaging of molecular orbitals.* Nature **432**, 867 (2004).

[53] D. J. Jones, S. A. Diddams, J. K. Ranka, A. Stentz, R. S. Windeler, J. L. Hall, and S. T. Cundiff. *Carrier-envelope phase control of femtosecond mode-locked lasers and direct optical frequency synthesis.* Science **288**, 635 (2000).

[54] D. J. Kane. *Recent progress toward real-time measurement of ultrashort laser pulses.* IEEE J. Quantum Electron. **35**, 421 (1999).

[55] L. V. Keldysh. *Ionization in the field of a strong electromagnetic wave.* Zh. Éksp. Teor. Fiz. **47**, 1945 (1964). Sov. Phys.–JETP 20, 1307 (1965) (Engl. Transl.).

[56] M. Kitzler and M. Lezius. *Spatial control of recollision wave packets with attosecond precision.* Phys. Rev. Lett. **95**, 253001 (2005).

[57] R. Kosloff and H. Tal-Ezer. *A direct relaxation method for calculating eigenfunctions and eigenvalues of the Schrödinger equation on a grid.* Chem. Phys. Lett. **127**, 223 (1986).

[58] J. E. Kruse, P. Tzallas, E. Skantzakis, C. Kalpouzos, G. D. Tsakiris, and D. Charalambidis. *Inconsistencies between two attosecond pulse metrology methods: A comparative study.* Phys. Rev. A **82**, 021402 (2010).

[59] M. Y. Kuchiev and V. N. Ostrovsky. *Quantum theory of high-harmonic generation via above-threshold ionization and stimulated recombination.* J. Phys. B **32**, L189 (1999).

[60] M. Y. Kuchiev and V. N. Ostrovsky. *Effective ATI channels in high harmonic generation.* J. Phys. B **34**, 405 (2001).

[61] J. J. Larsen, H. Sakai, C. P. Safvan, I. Wendt-Larsen, and H. Stapelfeldt. *Aligning molecules with intense nonresonant laser fields.* J. Chem. Phys. **111**, 7774 (1999).

[62] A.-T. Le, R. R. Lucchese, and C. D. Lin. *Uncovering multiple orbitals influence in high harmonic generation from aligned N_2.* J. Phys. B **42**, 211001 (2009).

[63] A.-T. Le, R. R. Lucchese, and C. D. Lin. *Polarization and ellipticity of high-order harmonics from aligned molecules generated by linearly polarized intense laser pulses.* Phys. Rev. A **82**, 023814 (2010).

[64] A.-T. Le, R. R. Lucchese, S. Tonzani, T. Morishita, and C. D. Lin. *Quantitative rescattering theory for high-order harmonic generation from molecules.* Phys. Rev. A **80**, 013401 (2009).

[65] V.-H. Le, A.-T. Le, R.-H. Xie, and C. D. Lin. *Theoretical analysis of dynamical chemical imaging with lasers using high-order harmonic generation.* Phys. Rev. A **76**, 013414 (2007).

[66] M. Lein and C. C. Chirilă. *Signatures of Molecular Structure and Dynamics in High-Order Harmonic Generation.* In S. H. Lin, A. A. Villaeys, and Y. Fujimura (Editors), *Advances in Multi-Photon Processes and Spectroscopy*, volume 18, pages 69–106. World Scientific Publishing Co. Pte. Ltd., Singapore (2008).

[67] M. Lein, N. Hay, R. Velotta, J. P. Marangos, and P. L. Knight. *Interference effects in high-order harmonic generation with molecules.* Phys. Rev. A **66**, 023805 (2002).

[68] M. Lein, N. Hay, R. Velotta, J. P. Marangos, and P. L. Knight. *Role of the intramolecular phase in high-harmonic generation.* Phys. Rev. Lett. **88**, 183903 (2002).

[69] J. Levesque, Y. Mairesse, N. Dudovich, H. Pépin, J.-C. Kieffer, P. B. Corkum, and D. M. Villeneuve. *Polarization state of high-order harmonic emission from aligned molecules.* Phys. Rev. Lett. **99**, 243001 (2007).

[70] J. Levesque, D. Zeidler, J. P. Marangos, P. B. Corkum, and D. M. Villeneuve.

High harmonic generation and the role of atomic orbital wave functions. Phys. Rev. Lett. **98**, 183903 (2007).

[71] M. Lewenstein, P. Balcou, M. Y. Ivanov, A. L'Huillier, and P. B. Corkum. *Theory of high-harmonic generation by low-frequency laser fields.* Phys. Rev. A **49**, 2117 (1994).

[72] Y. Liang, S. Augst, S. L. Chin, Y. Beaudoin, and M. Chaker. *High harmonic generation in atomic and diatomic molecular gases using intense picosecond laser pulses - a comparison.* J. Phys. B **27**, 5119 (1994).

[73] B. B. A. Lichtenbelt. *Fourier volume rendering.* Hewlett Packard Laboratories, Palo Alto, United States (1995).

[74] D. R. Luke. *Relaxed averaged alternating reflections for diffraction imaging.* Inverse Prob. **21**, 37 (2005).

[75] C. B. Madsen, M. Abu-samha, and L. B. Madsen. *High-order harmonic generation from polyatomic molecules including nuclear motion and a nuclear modes analysis.* Phys. Rev. A **81**, 043413 (2010).

[76] Y. Mairesse, A. de Bohan, L. J. Frasinski, H. Merdji, L. C. Dinu, P. Monchicourt, P. Breger, M. Kovačev, R. Taïeb, B. Carré, H. G. Muller, P. Agostini, and P. Salières. *Attosecond synchronization of high-harmonic soft x-rays.* Science **302**, 1540 (2003).

[77] Y. Mairesse, N. Dudovich, J. Levesque, M. Y. Ivanov, P. B. Corkum, and D. M. Villeneuve. *Electron wavepacket control with elliptically polarized laser light in high harmonic generation from aligned molecules.* New J. of Phys. **10**, 025015 (2008).

[78] Y. Mairesse, N. Dudovich, D. Zeidler, M. Spanner, D. M. Villeneuve, and P. B. Corkum. *Phase sensitivity of high harmonic transient grating spectroscopy.* J. Phys. B **43**, 065401 (2010).

[79] Y. Mairesse, J. Higuet, N. Dudovich, D. Shafir, B. Fabre, E. Mével, E. Constant, S. Patchkovskii, Z. Walters, M. Y. Ivanov, and O. Smirnova. *High harmonic spectroscopy of multichannel dynamics in strong-field ionization.* Phys. Rev. Lett. **104**, 213601 (2010).

[80] Y. Mairesse and F. Quéré. *Frequency-resolved optical gating for complete reconstruction of attosecond bursts.* Phys. Rev. A **71**, 011401(R) (2005).

[81] Y. Mairesse, D. Zeidler, N. Dudovich, M. Spanner, J. Levesque, D. M. Villeneuve, and P. B. Corkum. *High-order harmonic transient grating spectroscopy in a molecular jet.* Phys. Rev. Lett. **100**, 143903 (2008).

[82] S. Marchesini, H. He, H. N. Chapman, S. P. Hau-Riege, A. Noy, M. R. Howells, U. Weierstall, and J. C. H. Spence. *X-ray image reconstruction from a diffraction pattern alone.* Phys. Rev. B **68**, 140101 (2003).

[83] H. Mashiko, S. Gilbertson, C. Li, S. D. Khan, M. M. Shakya, E. Moon, and Z. Chang. *Double optical gating of high-order harmonic generation with carrier-envelope phase stabilized lasers.* Phys. Rev. Lett. **100**, 103906 (2008).

[84] B. K. McFarland, J. P. Farrell, P. H. Bucksbaum, and M. Gühr. *High-order harmonic phase in molecular nitrogen.* Phys. Rev. A **80**, 033412 (2009).

[85] D. B. Milošević and W. Becker. *Role of long quantum orbits in high-order harmonic generation.* Phys. Rev. A **66**, 063417 (2002).

[86] D. B. Milošević, G. G. Paulus, D. Bauer, and W. Becker. *Above-threshold ionization by few-cycle pulses.* J. Phys. B **39**, R203 (2006).

[87] D. B. Milošević, G. G. Paulus, and W. Becker. *Phase-dependent effects of a few-cycle laser pulse.* Phys. Rev. Lett. **89**, 153001 (2002).

[88] D. B. Milošević, G. G. Paulus, and W. Becker. *Above-threshold ionization with few-cycle laser pulses and the relevance of the absolute phase.* Laser Phys. **13**, 948 (2003).

[89] P. Moreno, L. Plaja, and L. Roso. *Ultrahigh harmonic generation from diatomic molecular ions in highly excited vibrational states.* Phys. Rev. A **55**, R1593 (1997).

[90] C. Figueira de Morisson Faria, M. Dörr, and W. Sandner. *Importance of excited bound states in harmonic generation.* Phys. Rev. A **58**, 2990 (1998).

[91] C. Figueira de Morisson Faria, H. Schomerus, and W. Becker. *High-order above-threshold ionization: The uniform approximation and the effect of the binding potential.* Phys. Rev. A **66**, 043413 (2002).

[92] H. G. Muller. *Reconstruction of attosecond harmonic beating by interference of two-photon transitions.* Appl. Phys. B **74**, s17 (2002).

[93] H. Niikura, N. Dudovich, D. M. Villeneuve, and P. B. Corkum. *Mapping molecular orbital symmetry on high-order harmonic generation spectrum using two-color laser fields.* Phys. Rev. Lett. **105**, 053003 (2010).

[94] M. Nisoli and G. Sansone. *New frontiers in attosecond science.* Prog. Quantum Electron. **33**, 17 (2009).

[95] M. Nisoli, S. D. Silvestri, and O. Svelto. *Generation of high energy 10 fs pulses by a new pulse compression technique.* Appl. Phys. Lett. **68**, 2793 (1996).

[96] M. Nisoli, S. D. Silvestri, O. Svelto, R. Szipöcs, K. Ferencz, C. Spielmann, S. Sartania, and F. Krausz. *Compression of high-energy laser pulses below 5 fs.* Opt. Lett. **22**, 522 (1997).

[97] H. Ohmura, N. Saito, and M. Tachiya. *Selective ionization of oriented nonpolar molecules with asymmetric structure by phase-controlled two-color laser fields.* Phys. Rev. Lett. **96**, 173001 (2006).

[98] R. Paschotta. *Encyclopedia of laser physics and technology.* `http://www.rp-photonics.com/encyclopedia.html` (2010).

[99] S. Patchkovskii, Z. Zhao, T. Brabec, and D. M. Villeneuve. *High harmonic generation and molecular orbital tomography in multi-electrons systems: Beyond the single active electron approximation.* Phys. Rev. Lett. **97**, 123003 (2006).

[100] S. Patchkovskii, Z. Zhao, T. Brabec, and D. M. Villeneuve. *High harmonic generation and molecular orbital tomography in multielectron systems.* J. Chem. Phys. **126**, 114306 (2007).

[101] P. M. Paul, E. S. Toma, P. Breger, G. Mullot, F. Augé, P. Balcou, H. G. Muller, and P. Agostini. *Observation of a train of attosecond pulses from high harmonic generation.* Science **292**, 1689 (2001).

[102] G. G. Paulus, W. Becker, W. Nicklich, and H. Walther. *Rescattering effects in above-threshold ionization: a classical model.* J. Phys. B **27**, L703 (1994).

[103] G. G. Paulus, W. Nicklich, H. Xu, P. Lambropoulos, and H. Walther. *Plateau in above threshold ionization spectra.* Phys. Rev. Lett. **72**, 2851 (1994).

[104] M. D. Poulsen, T. Ejdrup, and H. Stapelfeldt. *Alignment enhancement by the combination of a short and a long laser pulse.* Phys. Rev. A **73**, 033405 (2006).

[105] E. Priori, G. Cerullo, M. Nisoli, S. Stagira, S. De Silvestri, P. Villoresi, L. Poletto, P. Ceccherini, C. Altucci, R. Bruzzese, and C. de Lisio. *Nonadiabatic three-dimensional model of high-order harmonic generation in the few-optical-cycle regime.* Phys. Rev. A **61**, 063801 (2000).

[106] H. R. Reiss. *Effect of an intense electromagnetic field on a weakly bound system.* Phys. Rev. A **22**, 1786 (1980).

[107] F. Rosca-Pruna and M. J. J. Vrakking. *Experimental observation of revival structures in picosecond laser-induced alignment of I_2.* Phys. Rev. Lett. **87**, 153902 (2001).

[108] H. Sakai, C. P. Safvan, J. J. Larsen, K. M. Hilligsoe, K. Hald, and H. Stapelfeldt. *Controlling the alignment of neutral molecules by a strong laser field.* J. Chem. Phys. **110**, 10235 (1999).

[109] P. Salières, B. Carré, L. Le Déroff, F. Grasbon, G. G. Paulus, H. Walther, R. Kopold, W. Becker, D. B. Milošević, A. Sanpera, and M. Lewenstein. *Feynman's path-integral approach for intense-laser-atom interactions.* Science **292**, 902 (2001).

[110] P. Salières, A. L'Huillier, and M. Lewenstein. *Coherence control of high-order harmonics.* Phys. Rev. Lett. **74**, 3776 (1995).

[111] R. Santra and A. Gordon. *Three-step model for high-harmonic generation in many-electron systems.* Phys. Rev. Lett. **96**, 073906 (2006).

[112] B. Schenkel, J. Biegert, U. Keller, C. Vozzi, M. Nisoli, G. Sansone, S. Stagira, S. D. Silvestri, and O. Svelto. *Generation of 3.8-fs pulses from adaptive compression of a cascaded hollow fiber supercontinuum.* Opt. Lett. **28**, 1987 (2003).

[113] T. Seideman. *Rotational excitation and molecular alignment in intense laser fields.* J. Chem. Phys. **103**, 7887 (1995).

[114] T. Seideman. *Revival structure of aligned rotational wave packets.* Phys. Rev. Lett. **83**, 4971 (1999).

[115] D. Shafir, Y. Mairesse, D. M. Villeneuve, P. B. Corkum, and N. Dudovitch. *Atomic wavefunctions probed through strong-field light-matter interaction.* Nature Phys. **5**, 412 (2009).

[116] O. Smirnova, Y. Mairesse, S. Patchkovskii, N. Dudovich, D. Villeneuve, P. Corkum, and M. Y. Ivanov. *High harmonic interferometry of multi-electron dynamics in molecules.* Nature **460**, 972 (2009).

[117] O. Smirnova, S. Patchkovskii, Y. Mairesse, N. Dudovich, and M. Y. Ivanov. *Strong-field control and spectroscopy of attosecond electron-hole dynamics in molecules.* PNAS **106**, 16556 (2009).

[118] O. Smirnova, S. Patchkovskii, and M. Spanner. *Direct XUV Probing of Attosecond Electron Recollision.* Phys. Rev. Lett. **98**, 123001 (2007).

[119] I. J. Sola, E. Mével, L. Elouga, E. Constant, V. Strelkov, L. Poletto, P. Villoresi, E. Bendetti, J.-P. Caumes, S. Stagira, C. Vozzi, G. Sansone, and M. Nisoli. *Controlling attosecond electron dynamics by phase-stabilized polarization gating.* Nature Phys. **2**, 319 (2006).

[120] A. Suda, M. Hatayama, K. Nagasaka, and K. Midorikawa. *Generation of sub-10-fs, 5-mJ-optical pulses using a hollow fiber with a pressure gradient.* Appl. Phys. Lett. **86**, 111116 (2005).

[121] E. J. Takahashi, P. Lan, O. D. Mücke, Y. Nabekawa, and K. Midorikawa. *Infrared two-color multicycle laser field synthesis for generating an intense attosecond pulse.* Phys. Rev. Lett. **104**, 233901 (2010).

[122] H. Tanji, S. Minemoto, and H. Sakai. *Three-dimensional molecular orientation with combined electrostatic and elliptically polarized laser fields.* Phys. Rev. A **72**, 063401 (2006).

[123] H. R. Telle, G. Steinmeyer, A. E. Dunlop, J. Stenger, D. H. Sutter, and U. Keller. *Carrier-envelope offset phase control: A novel concept for absolute optical frequency measurement and ultrashort pulse generation.* Appl. Phys. B **69**, 327 (1999).

[124] E. S. Toma, P. Antoine, A. d. Bohan, and H. G. Muller. *Resonance-enhanced high-harmonic generation.* J. Phys. B **32**, 5843 (1999).

[125] X. M. Tong, K. Hino, and N. Toshima. *Phase-dependent atomic ionization in few-cycle intense laser fields.* Phys. Rev. A **74**, 031405(R) (2006).

[126] R. Torres, T. Siegel, L. Brugnera, I. Procino, J. G. Underwood, C. Altucci, R. Velotta, E. Springate, C. Froud, I. C. E. Turcu, S. Patchkovskii, M. Y. Ivanov, O. Smirnova, and J. P. Marangos. *Revealing molecular structure and dynamics through high-order harmonic generation driven by mid-ir fields.* Phys. Rev. A **81**, 051802 (2010).

[127] V. Tosa, H. T. Kim, I. J. Kim, and C. H. Nam. *High-order harmonic generation by chirped and self-guided femtosecond laser pulses. I. Spatial and spectral analysis.* Phys. Rev. A **71**, 063807 (2005).

[128] R. Trebino. *Frequency-Resolved Optical Gating*. Kluwer Academic, Boston, USA (2000).

[129] P. Tzallas, D. Charalambidis, N. A. Papadogiannis, K. Witte, and G. D. Tsakiris. *Direct observation of attosecond light bunching*. Nature **426**, 267 (2003).

[130] C. Vozzi, G. Cirmi, C. Manzoni, E. Benedetti, F. Calegari, G. Sansone, S. Stagira, O. Svelto, S. D. Silvestri, M. Nisoli, and G. Cerullo. *High-energy, few-optical-cycle pulses at 1.5 μm with passive carrier-envelope phase stabilization*. Opt. Express **14**, 10109 (2006).

[131] Z. B. Walters, S. Tonzani, and C. H. Greene. *Limits of the plane wave approximation in the measurement of molecular properties*. J. Phys. Chem. A **112**, 9439 (2008).

[132] E. W. Weisstein. *Abel transform*. From MathWorld–A Wolfram Web Resource. `http://mathworld.wolfram.com/AbelTransform.html` (2010).

[133] E. W. Weisstein. *Wiener-khinchin theorem*. From MathWorld–A Wolfram Web Resource. `http://mathworld.wolfram.com/Wiener-KhinchinTheorem.html` (2010).

[134] T. G. Winter, M. D. Duncan, and N. F. Lane. *Exact eigenvalues, electronic wavefunctions and their derivatives with respect to the internuclear separation for the lowest 20 states of the HeH^{2+} molecule*. J. Phys. B **10**, 285 (1977).

[135] H. J. Wörner, J. B. Bertrand, P. Hockett, P. B. Corkum, and D. M. Villeneuve. *Controlling the interference of multiple molecular orbitals in high-harmonic generation*. Phys. Rev. Lett. **104**, 233904 (2010).

[136] Z. Zhao, J. Wu, and J. Yuan. *Toward tomographic imaging of single and triplet states using high-order harmonic generation*. J. Phys. B **41**, 155601 (2008).

[137] Z. Zhao, J. Yuan, and T. Brabec. *Multielectron signatures in the polarization of high-order harmonic radiation*. Phys. Rev. A **76**, 031404(R) (2007).

[138] X. Zhou, R. Lock, W. Li, N. Wagner, M. M. Murnane, and H. C. Kapteyn. *Molecular recollision interferometry in high harmonic generation*. Phys. Rev. Lett. **100**, 073902 (2008).

[139] X. Zhou, R. Lock, N. Wagner, W. Li, H. C. Kapteyn, and M. M. Murnane. *Elliptically polarized high-order harmonic emission from molecules in linearly polarized laser fields*. Phys. Rev. Lett. **102**, 073902 (2009).

[140] E. V. van der Zwan, C. C. Chirilă, and M. Lein. *Molecular orbital tomography using short laser pulses*. Phys. Rev. A **78**, 033410 (2008).

[141] E. V. van der Zwan and M. Lein. *Tomographic imaging of molecular orbitals in length and velocity form*. AIP Conf. Proc. **963**, 570 (2007).

[142] E. V. van der Zwan and M. Lein. *Control of recollision wave packets for molecular orbital tomography using short laser pulses*. J. Phys. B **41**, 074009 (2008).

[143] E. V. van der Zwan and M. Lein. *Two-center interference and ellipticity in high-order harmonic generation from H_2^+*. Phys. Rev. A **82**, 033405 (2010).

Erklärung

Hiermit versichere ich, dass ich die vorliegende Dissertation selbständig und ohne unerlaubte Hilfe angefertigt und andere als die in der Dissertation angegebenen Hilfsmittel nicht benutzt habe. Alle Stellen, die wörtlich oder sinngemäß aus veröffentlichten oder unveröffentlichten Schriften entnommen sind, habe ich als solche kenntlich gemacht. Kein Teil dieser Arbeit ist in einem anderen Promotions- oder Habilitationsverfahren verwendet worden.

Elmar V. van der Zwan